Mechanical Modulation of Indirect Repair Mechanisms for Improved Hematopoietic Recovery

by

Frances D. Liu

Sc.B., Biomedical Engineering
Brown University, 2012

Submitted to the Department of Biological Engineering
in partial fulfillment of the requirements for the degree of

Doctor of Philosophy in Biological Engineering

at the

MASSACHUSETTS INSTITUTE OF TECHNOLOGY

June 2018

Signature redacted

Author..... .....

Department of Biological Engineering
February 6, 2018

Certified by..... Signature redacted .....

Krystyn J. Van Vliet
Associate Provost
Michael and Sonja Koerner Professor of Materials Science and Engineering
and Biological Engineering
Thesis Supervisor

Signature redacted

Accepted by..... .....

Forest M. White
Professor of Biological Engineering
Chair, Biological Engineering Graduate Program

Mechanical Modulation of Indirect Repair Mechanisms for Improved Hematopoietic Recovery

by

Frances D. Liu

Submitted to the Department of Biological Engineering
on February 6, 2018 in partial fulfillment of the
requirements for the degree of Doctor of Philosophy in
Biological Engineering

Abstract

Hematopoietic stem cell or bone marrow transplantation is a curative treatment for multiple hematologic malignancies. However, the myeloablative conditioning regimens preceding cell delivery have rendered the rapid and sustained hematopoietic recovery after transplantation an outstanding challenge. Successful long-term engraftment of hematopoietic stem cells is dependent largely on the surrounding stroma components or hematopoietic niche. Cell types within this niche that support hematopoietic recovery include two adherent cell types, mesenchymal stromal cells (MSCs) and vascular endothelial cells (VECs). The niche also contains many biophysical and mechanical cues including cell contractility against other cells or the matrix, pulsatile fluid flow, differences in localized niche stiffness, and occupation of fluid volume by macromolecules. This thesis aims to understand how VECs and MSCs respond to these cues *ex vivo*, and how these cues can be used to engineer VEC and MSC phenotypes that can predictably support hematopoietic recovery *in vivo*.

VEC-mediated angiogenesis and angiocrine signaling are known to support hematopoietic recovery *in vivo*. In this thesis, we first explored how the biophysical cue of macromolecular crowding (MMC) and the mechanical cue of strain can regulate angiogenesis. The addition of synthetic MMC to *in vitro* cultures replicates the endogenous occupation of fluid space due to macromolecules. We explored how MMC affects the basement membrane formation of VECs, and determined that MMC can increase the deposition, areal spread, and alignment of basement membrane proteins. Even with the addition of biochemical signals from pericytes, this biophysical cue of MMC played a dominant role in the organization of the basement membrane. Pericytes that surround blood vessels and the basement membrane have been shown to exert contractile forces, which results in a hoop strain in the blood vessel wall. We translated this strain to *in vitro* VEC cultures by applying static, uniaxial strain to confluent VEC monolayers using a polydimethyl siloxane (PDMS) substrata, which allowed us to de-couple the mechanical cue of pericytes from their chemical signaling. The application of 10%

engineering strain was sufficient to induce cell-cycle re-entry in a quiescent monolayer. We then went on to demonstrate in a quasi-3D assay that straining the VECs also produced angiogenic-like sprouts. Together, these results show that biophysical and mechanical cues of the hematopoietic niche alone are sufficient to direct VEC-derived extracellular matrix formation and to induce angiogenic sprouting. Thus, future models of *in vitro* angiogenesis must include these cues to more comprehensively and accurately replicate the *in vivo* hematopoietic niche.

Paracrine signaling from MSCs is crucial in regulating the self-renewal capacity and differentiation of hematopoietic stem and progenitor cells (HSPCs) that re-populate the bone marrow compartment *in vivo*. Thus, we then explored if and how to modulate MSC paracrine signaling or the MSC secretome. Like VECs, MSCs are known to respond to microenvironment cues such as substratum stiffness. We developed tissue-culture compatible PDMS-based substrata with tunable viscoelastic properties to assay potential mechanosensitivity. We characterized the bulk and surface properties of this substrata to verify that we could tune stiffness across three orders of magnitude without altering material surface biochemistry. When we expanded the MSCs on compliant substrata (elastic modulus ~1 kPa), we found that we could increase the expression of osteopontin as well the expression of at least a dozen other secreted proteins without altering cell capacity for terminal differentiation. We observed changes in the MSC secretome that were significantly correlated to the viscoelastic properties (shear storage and loss moduli G' and G'', respectively, and the ratio of G''/G' as tan δ) of the substratum material. These results suggested that we could mechanically modulate the MSC secretome using the viscoelastic properties of the extracellular substrata.

Finally, we went on to explore how these mechanically modulated changes in MSC phenotype could regulate hematopoiesis *in vitro* and support hematopoietic recovery *in vivo*. To do so, we used statistical regression modeling (partial least squares regression or PLSR) to identify the components of the MSC secretome that were significantly correlated with improved radiation rescue and hematopoietic recovery in mouse models of hematopoietic failure. We then characterized the expression of these key secretome components in our mechanoprimed MSCs. The mechanoprimed MSCs expressed equal or higher concentrations of these proteins as a diameter-defined subpopulation of MSCs we previously identified to be therapeutically effective. Using the regression parameters from PLSR and the new expression data from our mechanoprimed MSCs, we then predicted how our mechanoprimed MSCs would elicit radiation recovery of the bone marrow compartment *in vivo*. From these computational predictions, we found that our mechanoprimed MSCs could potentially improve survival proportion in this *in vivo* model of hematopoietic failure. Thus, we tested mechanoprimed MSCs by expanding them in co-culture with HSPCs to determine if the MSCs could regulate hematopoiesis *in vitro*. We found that mechanoprimed MSCs could maximize the proliferation or expansion of HSPCs when co-cultured on top of our most compliant PDMS substrata (~1 kPa). When grown on stiffer PDMS substrata (~100 kPa), those MSCs could prime differentiation of the HSPCs down myeloid lineages, which include red blood cells. Together, these results demonstrate that these

mechanoprimed MSCs can be used to modulate the *ex vivo* expansion and differentiation of HSPCs. Lastly, we tested these mechanoprimed MSCs in our sub-lethally irradiated mouse models of hematopoietic failure. Our mechanoprimed MSCs significantly increased the survival of the mice. Interestingly, this increased survival and improved hematopoietic recovery outperformed the survival predicted from our regression model. We also observed recovery of red blood cells, white blood cells, and platelets in mice treated with mechanoprimed MSCs, suggesting complete recovery of all hematopoietic lineages.

In summary, we have explored how biophysical and mechanical cues can modulate VEC and MSC phenotype *in vitro*. In the case of VECs, the results presented in this thesis further the development of more accurate *in vitro* models of angiogenesis. Accurate *in vitro* models of angiogenesis are necessary to elucidate the mechanisms by which VECs regulate hematopoietic recovery *in vivo.* We also characterized the components of the MSC secretome correlated with improving hematopoietic recovery and demonstrated that we could engineer the expression of these same MSC secretome components using substratum viscoelastic properties. Lastly, we validated that these mechanically modulated MSCs led to improved survival outcome *in vivo*. The work presented in this thesis furthers our understanding of how biophysical and mechanical cues regulate hematopoietic niche components that participate in indirect repair of the bone marrow. We also demonstrated how these same cues can be applied *in vitro* to improve cell-based therapies for hematopoietic recovery *in vivo*.

Thesis Supervisor: Krystyn J. Van Vliet
Title: Associate Provost and Michael and Sonja Koerner Professor of Materials Science and Engineering and Biological Engineering

Acknowledgements

First and foremost, I would like to thank my thesis advisor, Prof. Krystyn J. Van Vliet. She has supported me throughout the course of my graduate career, even when I wanted to give up on it. She graciously allowed me to switch projects and pursue ideas of my own, which eventually became my thesis project. Prof. Van Vliet was also very accommodating to my needs and interests as a graduate student. She has taught me how to ask research questions with real-world applications and how to find the best ways to answer them. I am very grateful for her guidance throughout the course of my graduate degree.

My committee members were crucial to expanding the scope of my thesis work. I am grateful for their knowledgeable advice and constructive criticism on how to improve my thesis research. I am thankful for Professor Forest White, who as my committee chair provided direction on how best to drive this research forward. He helped to prioritize the necessary experiments and analysis to tell a complete story. I am also grateful to Professor Roger Kamm who not only allowed me to use equipment in his laboratory and collaborated with us, but also provided new perspectives and detailed insight as a committee member. In addition to serving as my committee member, I appreciate Prof. Kamm's patience who also had to bear with me as a student and teaching assistant for multiple terms. Lastly, I would like to thank Professor Doug Lauffenburger who was so interested in my research that I later added him to my committee. In addition to Prof. Lauffenburger's enthusiasm and technical support, he was always able to help come up with solutions whenever a problem arose.

The work conducted in this thesis was financially supported by the Singapore-MIT Alliance for Research and Technology (SMART). Specifically, I was fortunate to be a part of the the BioSystems and Micromechanics (BioSyM) interdisciplinary research group within SMART. As a member of SMART-BioSyM, I was given the opportunity to work in both labs at MIT and in Singapore (at the National University of Singapore). Two members of the Singapore-based BioSyM team have contributed immeasurably to the design and execution of many of the experiments contained herein. Starting from my second year in the lab, Dr. Zhiyong Poon has not only taught me many of the technical skills I have acquired, but also was always willing to discuss new ideas and help design experiments. Dr. Kimberley Tam joined our research group a few years later, but worked most closely with me on this thesis project. She executed the final experiments that enabled me to conclude my thesis work. More importantly, she was also willing to spend time with me outside of work when I was alone in Singapore, which made those work trips to Singapore much more enjoyable. I would not have been able to complete this thesis work without the help from Dr. Poon or Dr. Tam.

The members of the Van Vliet Laboratory for Material Chemomechanics are an amazing group of students and researchers. I am grateful for our endless conversations and academic support. In particular, I would like to thank Dr. Jessica Swallow who has sat next to me for the majority of our graduate careers. Her passion, brilliance and hard work inside and outside the lab never failed to inspire me. Whenever I had a question on life or work, I could always go to Jess for help. I would also like to thank Deena Rennerfeldt who was always willing to listen to my

complaints and could relate closely to me both inside and outside of work. She was the only one in our group who could fully understand my research. Both of these ladies were dedicated friends and brilliant researchers who have supported me emotionally, academically, and socially. Additionally, I would also like to thank current and former members of my office (8-236): Dr. Anna Jagielska, Daniela Espinosa-Hoyos, and Dr. John Maloney. Thank you for being meticulous researchers and for being willing to always lend a listening ear.

Throughout the course of this project, I have been fortunate enough to work with collaborators inside and outside of the Van Vliet group. During my first year at MIT, I was mentored by Dr. Adam Zeiger in our group, who guided me through the early angiogenesis projects of my thesis work. While working with Adam, we were also fortunate enough to collaborate with Dr. Ira Herman and his post-doctoral researcher, Dr. Jennifer T. Durham, at Tufts University. I am also grateful to Novalia Pishesha who is my classmate, friend, and collaborator at the Whitehead Institute. All of the work on hematopoietic stem and progenitor cells was conducted in collaboration with Nova. She taught me about an entire field I originally knew nothing about, and was willing to put in many extra hours to work with me. Her intelligence and passion for science never failed to impress me.

Amongst my classmates, there are many other people who I need to thank. I am grateful to my former roommates: Ryan Truby, Kelly Moynihan, Santiago Correa, Griffin Clausen, and Shawn Musgrave. For four years, our home at 9 Seattle St was a reprieve from the difficult work and stressful situations of being a graduate student. Our weekly dinners served as reminders of the world that existed outside of academic research. From watching television series together to helping me prepare presentations, my roommates were able to support me both emotionally and academically. The collective intelligence, passion, fun, and kindness of the 9 Seattle St house is something I will aspire to continue for the rest of my life. Amongst our cohort, I am most grateful to Ryan Kelly, who has supported me with patience and understanding throughout the entire course of my graduate career. Even from the other side of the country, Ryan was always willing to talk to and support me. Ryan made sure that my happiness and social life was maintained outside of lab work.

Last, but not least, I would like to thank my family members. I am grateful to my parents, James and Teresa, who have always supported and believed in me. Throughout my graduate program, we have been close both physically and emotionally. Even as an adult, thank you Mom and Dad for feeding me when I did not want to cook or myself or helping to take care of me when I was sick. Vivian, my older sister, has always pushed me to be the best version of myself. Even if I may disagree with her sometimes, I always appreciate her advice and always have looked up to her. Jackie, my younger sister, has been an emotional support who was always willing to spend time with me. We struggled through the worst months of her high school career, and my graduate career together.

Table of Contents

Chapter 1 Introduction: Background and Motivation 17
1.1 Hematopoietic recovery 17
1.2 Indirect repair mechanisms in hematopoietic recovery: the hematopoietic niche 18
1.3 Mechanical modulation of mesenchymal stromal cell support 22
1.3.1 Macromolecular crowding effects on MSC behavior 23
1.3.2 Substratum stiffness and MSC phenotype 24
1.3.3 Substrata viscoelasticity and time dependence 25
1.3.4 MSC paracrine signaling due to strain and stiffness 26
1.4 Mechanobiology of vascular endothelial cells 29
1.4.1 Shear stress and VEC paracrine signaling 29
1.4.2 Macromolecular crowding and ECM formation of VECs 31
1.4.3 The effects of stiffness on VEC behavior 31
1.4.4 Effects of strain on angiocrine signaling and angiogenic sprouting 32
1.5 Direct mechanical regulation of hematopoietic stem and progenitor cells 34
1.5.1 The effects of shear flow on developmental hematopoiesis 34
1.5.2 Extracellular stiffness and HSC phenotype 35
1.6 Outlook 36
1.7 Thesis goals and organization 38

Chapter 2 Time-dependent extracellular matrix organization and secretion from vascular endothelial cells due to macromolecular crowding 41
2.1. Acknowledgements 41
2.2 Introduction 41
2.3 Materials and Methods 43
2.3.1 Cell Culture 43
2.3.2 Immunocytochemistry 44
2.3.3 Image Analysis 44
2.4 Results and Discussion 45
2.4.1 ECM deposition: amount and areal density 45
2.4.2 ECM fiber alignment 46

2.4.3 Effects of seeding density 47
2.4.4. Effects of pericyte-conditioned media 49
2.5 Conclusions 50

Chapter 3 Static mechanical strain induces vascular endothelial cell cycle re-entry and sprouting 51
3.1 Acknowledgements 51
3.2 Introduction 51
3.3 Materials and Methods 53
3.3.1 Preparation of PDMS molds 53
3.3.2 Vascular endothelial cell culture and strain application 54
3.3.3 Immunocytochemistry 54
3.3.4 Sprouting assay 55
3.4 Results and Discussion 55
3.4.1 Static strain-induce cell-cycle re-entry 55
3.4.2. Endothelial cell sprouting in a quasi-3D model 58
3.5 Conclusions 61

Chapter 4 Engineering the mesenchymal stromal cell secretome using viscoelastic properties of extracellular materials 65
4.1 Acknowledgements 65
4.2 Introduction 65
4.3 Materials and Methods 68
4.3.1 Material formulation and mechanical characterization 68
4.3.2 PDMS culture surface preparation and characterization 69
4.3.3 Cell culture and characterization 70
4.3.4 mRNA and protein expression 70
4.3.5 MSC osteogenic induction and quantification 71
4.4 Results 72
4.4.1 Characterization of bulk and surface properties of cell culture substrata 72
4.4.2 Cell-material interactions and changes in cell diameter 74
4.4.3 Viscoelastic moduli correlated with changes in MSC expression 76
4.4.4 Mechanical modulation of isolated MSC subpopulations 78

4.4.5 Mechanical modulation of the MSC secretome 81
4.5 Discussion 82
4.6 Conclusion 86

Chapter 5 Regulating hematopoiesis *in vitro* and improving hematopoietic recovery *in vivo* using mechanically-modulated mesenchymal stromal cells 87
5.1 Acknowledgements 87
5.2 Introduction 88
5.3 Materials and Methods 89
5.3.1 Regression modeling 89
5.3.2 MSC Culture 90
5.3.3 Secretome Characterization 91
5.3.4 *In vitro* co-culture of MSCs and HSPCs 92
5.3.5 *In vivo* mouse model 93
5.4 Results 94
5.4.1 PLSR model predictions of survival 94
5.4.2 Secretome Modulation and Training Data 98
5.4.3 Non-contact co-culture 100
5.4.4 Contact co-culture 102
5.4.5 Mouse survival and weight recovery 104
5.4.6 Complete blood count 106
5.5 Discussion 107
5.6 Conclusion 111

Chapter 6 Conclusions 113
6.1 Contributions 113
6.1.1 Angiogenesis *in vitro* 113
6.1.2. Characterization and modulation of the MSC secretome 115
6.1.3. Improving hematopoiesis *in vitro* and hematopoietic recovery *in vivo* 116
6.2 Outlook and Perspectives 118
6.2.1. Outstanding Questions 118
6.2.2. Outlook 120

Appendix A Supplemental data 123
A.1 Viscoelastic characterization of polydimethyl siloxanes (PDMS) substrata (Chapter 4) 123
A.2 Further Characterization of PDMS Surfaces (Chapter 4) 126
A.3 PDMS Wrinkling (Chapter 4) 128
A.4 Changes in Cell Diameter on PDMS (Chapter 4) 131
A.5 Determining Relative Expression Using the $\Delta\Delta C_T$ Method (Chapters 4 & 5) 133
A.6 Expression Regulation Across Multiple Donors (Chapter 4) 135
A.7 Collagen Functionalization (Chapter 4) 137
A.8 Expression of Chondrogenic Genes (Chapter 4) 139
A.9 Contact co-culture of MSCs and HSPCs (Chapter 5) 141
A.10 Differentiation of HSPCs after co-culture (Chapter 5) 144

Appendix B Further predictive modeling and *in vivo* results (Chapter 5) 147
B.1 Variance Explained in PLSR Components (Chapter 5) 147
B.2 Weight Recovery (Chapter 5) 148
B.3 Engraftment after non-contact co-culture (Chapter 5) 151
B.4 Evaluating Individual Secretome Components of the PLSR Model (Chapter 5) 153

Appendix C Analyzing and Segmenting Images with and without Macromolecular Crowder (Chapter 2) 159
C.1 Acknowledgements 159
C.2 Identifying ECM Fiber Orientation in VEC Images 159
C.3 MATLAB Code used to analyze fiber orientation 162

Appendix D Detailed Protocol for Preparation of Cell Stretcher PDMS Molds and VEC Sprouting Assay (Chapter 3) 167
D.1 Acknowledgements 167
D.2 Materials 167
D.3 Preparation of PDMS Molds 168
D.4 VEC Culture on PDMS Molds 169

Appendix E Detailed MSC Subculture (Chapters 4 and 5) 171
E.1 Materials 171

E.2 Preparing Media (in 50ml aliquots) 171
E.3 Thawing Cells 172
E.4 Expansion 172
E.5 Passaging Cells 173
E.6 Freezing Cells 174

Appendix F Detailed Tunable PDMS Substrata Fabrication Protocol 175
F.1 Materials 175
F.2 PDMS Mix Preparation 175
F.3 Surface Treatment 176

Appendix G Detailed MSC/HSPC Co-Culture Protocol (Chapter 5) 177
G.1 Acknowledgements 177
G.2 Materials 177
G.3 Co-Culture Protocol 178
G.4 HSPC Thawing Protocol (Courtesy of Novalia Pishesha) 181

Appendix H Detailed MSC Spiral Microfluidic Sorting Protocol 183
H.1 Acknowledgements 183
H.2 Materials 183
H.3 Device Fabrication 184
H.4. Sorting Cells 186

Appendix I MATLAB Codes 189
I.1 MATLAB Code for Determining Suspended Cell Diameters 189
I.2 MATLAB Code for Analyzing Suspended Cell Diameter Distributions 192
I.3 MATLAB Code for Analyzing ELISA Data 200
I.4 MATLAB Code for Analyzing Luminex-Based Data 203
I.5 MATLAB Code for Modeling Luminex-Based Data and Survival 208

Bibliography 243

List of Figures

Figure 1-1. Cell types in the hematopoietic niche

Figure 1-2. Mechanical and biophysical cues in the hematopoietic niche

Figure 1-3. MSC response to biophysical and mechanical cues

Figure 1-4. VEC response to biophysical and mechanical cues

Figure 1-5. Mechanical cues to improve cell therapies for hematopoietic recovery

Figure 2-1. Angiogenic Sprouting and the ECM

Figure 2-2. Effects of MMC on amount and distribution of VEC-secreted collagen-IV matrix

Figure 2-3. Macromolecular crowding of the extracellular fluid promotes alignment of the extracellular matrix

Figure 2-4. Effect of cell seeding density on ECM coverage and alignment

Figure 2-5. Effects of pericyte-conditioned media (PCM) on collagen alignment

Figure 3-1. Static strain induces S-phase entry in quiescent retinal microvascular endothelial cells (ECs)

Figure 3-2. Static strain induces sprouting in capillary endothelial-derived monolayers

Figure 3-3. Imaging of sprouting assays

Supporting Movies S1-S2. Confocal videos of capillary endothelial sprouts

Figure 4-1. Mechanical and surface characterization of elastomeric substrata

Figure 4-2. Cell diameter changes in response to PDMS substrata

Figure 4-3. Biological response of unsorted MSCs on elastomeric substrata

Figure 4-4. Size-sorted MSC subpopulations

Figure 4-5. Secretome wide changes on all substrata

Figure 5-1. Co-culture experimental setup

Figure 5-2. Training data and regression modeling

Figure 5-3. Secretome characterization and test data

Figure 5-4. *In vitro* hematopoietic recovery: HSPC and MSC non-contact co-culture

Figure 5-5. *In vitro* hematopoietic recovery: HSPC and MSC Contact co-culture

Figure 5-6. *In vivo* hematopoietic recovery: Mouse survival

Figure 5-7. *In vivo* hematopoietic recovery: Complete blood count (CBC).\

List of Tables

Table 1-1. HSC response to mechanical cues

Table 5-1. Proteins significantly correlated with survival

List of Appendix Figures

Figure A-1. Determining linear viscoelastic range

Figure A-2. Additional viscoelastic characterization of PDMS substrata

Figure A-3. Protein gel of non-specifically adsorbed serum protein

Figure A-4. Phase contrast images of PDMS substrata

Figure A-5. Phase contrast images of cells on all PDMS substrata

Figure A-6. Distribution of cell diameters on PDMS substrata

Figure A-7. Expression data across five additional donors

Figure A-8. Expression data with collagen functionalization on PDMS substrata

Figure A-9. Expression of chondrogenic genes on elastomeric substrata

Figure A-10. Effects of the mechanically-modulated MSCs on HSPCs

Figure A-11. Chemical induction into erythrocyte lineage

Figure B-1. PLSR components and variance

Figure B-2. Weight recovery of sub-lethally irradiated mice

Figure B-3. Engraftment of HSPCs after non-contact co-culture

Figure B-4. Knocking out expression of correlative proteins independently in PLSR model predictions

Figure B-5. Survival due to expression of correlative proteins independently in PLSR model predictions

Figure B-6. Knocking out expression of all correlative proteins and incorporating BMP2 in PLSR model predictions

Figure C-1. Raw images stained for analysis

Figure C-2. Re-sized and filtered images

Figure C-3. Segmented images indentifying ECM fibers

Figure C-4. Representative histograms of local fiber orientation

List of Appendix Tables

Table A-1. List of Human MSC Donors and Vendors Used

Table B-1. Mean weight recovery at each week

Table B-2. Statistical comparisons of weight recovery across experimental groups

Chapter 1

Introduction: Background and Motivation

1.1 Hematopoietic recovery

Approximately 25,000-50,000 hematopoietic stem cell transplantations (HSCTs) are conducted annually worldwide for treatment of multiple blood and immune disorders [1,2]. HSCT can be used to treat nonmalignant disorders such as anemia, sickle cell disease, and immune deficiencies [2,3]. Alternatively, HSCT is adopted frequently as a curative treatment for hematologic malignancies such as leukemias, lymphomas, and myelomas [2,3]. The cells used in transplantation are hematopoietic stem cells (HSCs) that reside natively in the bone marrow and repopulate the lymphoid and myeloid lineages [4]. HSCs can be isolated autologously from the patient, syngeneically from a twin, or allogeneically from an HLA-matched donor [2,3,5]. HSCs can be harvested directly from the bone marrow, mobilized to be collected from peripheral blood, or obtained from cord blood [2,3,5]. To date, cord blood derived hematopoietic stem cells (HSCs) are the only U.S. Food & Drug Administration (FDA)-approved stem cell-based product for use in the United States [6]. After transplantation, HSCs can then home to and engraft in the bone marrow compartment, and proceed to proliferate and differentiate to repopulate the blood cell lineages of the bone marrow [7,8].

For hematologic malignancies, conditioning regimens including radiation, chemotherapy and antibody-based therapies are administered prior to HSCT [9–11]. These conditioning regimens are selected primarily to reduce tumor burden and to prevent immune rejection [9–11]. With increasing myeloablative conditioning there is increased toxicity, but lower graft versus tumor effect and a reduced chance of relapse [11,12]. Thus, the combination and intensity of these conditioning regimens vary depending on the patient's risk factors as well as the source of the cells [9,10,12]. Nevertheless, all of these treatments destroy both healthy and diseased cells and tissue, so HSCTs are administered to replace the diseased cells and repopulate the lost blood cell populations. However, conditioning regimens also destroy the bone marrow stroma and niche-associated cell types, and subsequent HSCTs do not replace those cellular components [13]. HSCTs can fail at either extreme of engraftment. The transplant can engraft and overtake the host, resulting in graft versus host disease (GVHD), which can be fatal [2,3,12,14,15]. In the short term, this effect may be desirable to elicit a graft versus tumor effect to minimize the chance of relapse [3,4,11,15,16]. Slow hematopoietic recovery, and poor long-term engraftment of allogeneic HSCT results in the patient's immune deficiency and susceptibility to infection

[17,18]. Graft failure can be caused by immune rejection, conditioning regimen toxicity, and viral infection [17]. Both failure to engraft and GVHD results in increased morbidity and mortality [2,3,17]. Mortality due to transplant-related complications that are non-relapse related is approximately 40-50%, [2,3] and thus HSCT with low post-transplantation morbidity and mortality still remains a challenge.

Successful, long-term engraftment of administered HSCs is dependent upon surrounding hematopoietic niche components such as signaling molecules and multiple surrounding cell types [7,19]. HSCs are typically injected intravenously for transplant, and then must home to the hematopoietic microenvironment, engraft within the bone marrow niche, and differentiate into the myeloid and lymphoid lineages to replace blood cell populations [2,7]. Stromal cell-derived factor-1 (SDF-1) acts as a chemoattractant to allow for successful homing of the HSCs [2,7]. SDF-1 enables the extravasation of HSCs out of the blood stream into the hematopoietic compartment [20,21]. SDF-1 is an example of a soluble factor that plays a role in HSC homing and engraftment; however, many different cell types can contribute to HSC homing and engraftment. For example, mesenchymal stromal cells (MSCs) express SDF-1, and its expression from MSCs supports hematopoietic recovery *in vitro* and *in vivo* [22,23]. Vascular endothelial cells express selectins that bind to HSCs, and their adhesion plays a role in trafficking HSCs and regulating their self-renewal capacity [24,25]. In this thesis, we specifically explore how MSCs and VECs can be modulated mechanically to potentially support hematopoietic recovery.

1.2 Indirect repair mechanisms in hematopoietic recovery: the hematopoietic niche

Successful hematopoietic recovery or reconstitution after HSCT is dependent upon regulation from the hematopoietic niche. Awaya et al. showed that the stroma comprises the hematopoietic niche is not re-constituted from donor cells after HSCT, suggesting that myeloablative conditioning regimens may cause irreversible damage that impairs indirect cellular support of improved graft function [13]. The hematopoietic niche regulates the balance between symmetric and asymmetric cell division, which corresponds with proliferation and differentiation of HSCs, respectively [26,27]. Kong et al. compared graft outcomes, such as pancytopenia and HSC differentiation, from over 50 allogeneic HSCTs, and demonstrated that increased numbers of surrounding cell types in the niche are correlated with improved graft function [19]. The importance of the hematopoietic niche in regulating HSC behavior has led to debate over the localization and specific heterotypic cell-cell interactions.

There are varied perspectives regarding precisely which niche(s) within the bone marrow support hematopoietic recovery: the endosteal niche, the perivascular niche, or the vascular niche [19,26,28,29]. The cell types corresponding to these distinct niches include osteoblasts, pericytes, and VECs, respectively [19,28]. The HSCs appear to reside in the bone marrow in the space between trabecular bone or endosteal niche, and endothelium-lined sinuses or the vascular

niche [26,28–30]. Ellis et al. demonstrated that transplanted HSCs will rapidly home to the endosteal niche in close association with blood vessels from 15 minutes to 15 hours after transplantation, demonstrating the importance of both niches [31]. HSCs have been shown to localize adjacent to blood vessels and are regulated through interactions with endothelial or perivascular cells [32,33]. Sugiyama et. al demonstrated that SDF1 signaling from perivascular cells or pericyte-like cells, what they call CXCL12-abundant reticular (CAR) cells, maintained the self-renewal capacity of HSCs [33]. On the other hand, others have demonstrated that the endosteal niche, where osteoblastic cells reside and secrete factors such as G-CSF and BMP, regulate HSC expansion [34,35]. Similarly, Calvi et al. demonstrated Notch-1 activation in HSCs through increased levels of Jagged-1 expression from osteoblasts, which suggests that heterotypic cell-cell interactions between osteoblasts and HSCs can directly regulate proliferation of HSCs [36]. In summary, these heterotypic cell-cell interactions can regulate the self-renewal capacity and differentiation of HSCs through indirect or direct ways [26,28].

Vascular endothelial cells (VECs) make up the endothelium that lines blood vessel walls in the vascular or perivascular niche. VECs have been shown to promote HSC expansion differentiation potential in *ex vivo* co-culture [37]. Subsequent transplantation of these co-cultures demonstrated improved short-term hematopoietic re-population in a lethally irradiated mouse model; however, outcome depended on the organs from which the VECs were derived [37]. Montfort et al. demonstrated that the transplantation of vascular tissue in a lethally irradiated mouse model demonstrated radioprotection and improved hematopoietic re-constitution, suggesting that VECs may play a role in regulating hematopoiesis in response to injury [38]. The same group went on to demonstrate that a specific population of microvascular VECs expressing CD31 can restore hematopoiesis following lethal doses of irradiation [39]. However, the mechanisms by which these transplanted VECs support HSC recovery are still currently unknown. Hooper et al. demonstrated that VEGFR2 expression and signaling from sinusoidal VECs were necessary for transplant engraftment and hematopoietic recovery in a lethally irradiated mouse model [40]. Winkler et al. suggested that E-selectin expressed on bone marrow endothelial cells in the vascular niche may be responsible for promoting HSC proliferation in cases of myeloablation [24]. E-selectin knockouts demonstrated HSC dormancy and enhanced self-renewal potential [24]. Butler et al. showed that inhibition of angiocrine signaling of VECs caused a decreased frequency of long-term HSCs in *in vitro* contact co-culture and poor engraftment of HSCs *in vivo* [41]. Multiple studies demonstrated that upregulation of multiple pro-angiogenic factors from VECs such as FGF2, IGFBP2, ANG-1, IL-6, and EGF may play a role in supporting hematopoietic recovery after irradiation injury [42–44]. Similar to how osteoblasts are proposed to interact with HSCs, they also showed that this angiocrine support of LT-HSCs was notch-signaling dependent [41]. All of these studies used mouse models of bone marrow injury or myeloablation, which suggests that VECs may play a crucial role during hematopoietic recovery but not developmental hematopoiesis.

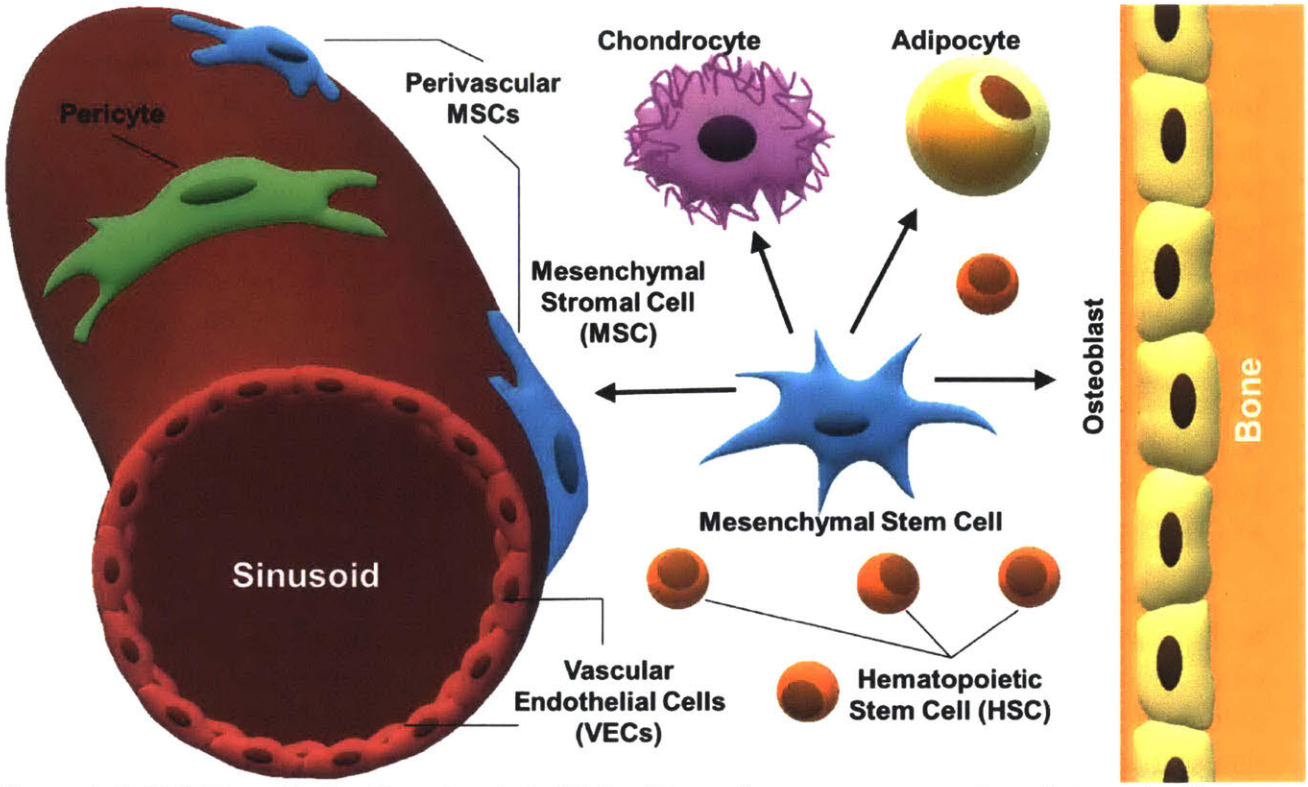

Figure 1-1. Cell Types in the Hematopoietic Niche. Blue cells represent mesenchymal stromal cells (MSCs). Orange cells represent hematopoietic stem cells (HSCs). Green cells represent the pericytes that surround the blood vessels. Vascular endothelial cells (VECs) are represented by red cells. Osteoblasts, chondrocytes and adipocytes are depicted as the three lineages which MSCs can differentiate into.

Mesenchymal stromal cells (MSCs) are another population of cells that natively reside in the bone marrow niche. MSCs contain a subset of multipotent stem cells that can differentiate into osteogenic, chondrogenic, and adipogenic lineages [45,46]. On the other hand, MSCs can be perivascular and are considered by some to be pericytes [28,47,48]. Whether or not pericytes are equivalent to or a subset of MSCs remains controversial, as pericytes do not exhibit endogenous multipotency *in vivo* [49]. The aggregate of these studies suggest that not all pericytes are MSCs and vice versa, but they may overlap in certain functional phenotypes [50]. Nevertheless, MSCs bridge an interesting gap, as they can exist as stromal cells in the perivascular space as well as osteoprogenitors in the endosteal niche. Sacchetti et al. demonstrated that subendothelial MSCs could generate ectopic bone and a new hematopoietic microenvironment when transplanted under the skin of immunodeficient mice [51]. Their work suggested that MSCs with osteogenic lineage potential, or osteoprogenitors, could be responsible for organizing the hematopoietic niche. Chan et al. then determined that a very specific subset of those subendothelial MSCs that proceeded as osteochondral progenitors, instead of just osteoprogenitors, was necessary for HSC niche formation and recruitment of LT-HSCs [52]. In both studies, MSCs acted in indirect ways to recruit other cell types and regenerate the bone marrow compartment in ectopic bone formation assays. Others have demonstrated that MSCs can directly support and maintain

hematopoiesis *in vitro* and *in vivo* via secreted factors such as SDF-1 and SCF [22,33,52–54]. MSCs that express high levels of SDF-1 have been shown to have adipogenic and osteogenic potential; this expression of SDF-1 has been shown to be necessary to promote HSC proliferation and maintain differentiation potential [54]. MSCs act as important cellular factories in the hematopoietic niche, secreting factors that regulate HSC proliferation and differentiation.

VECs and MSCs are important cellular components of the hematopoietic niche that regulate HSC behavior in the context of bone marrow repair after injury. Depicted in Figure 1-1 are the various cell types that are found in the hematopoietic niche. In this thesis, we focus on how these two distinct cell populations are each regulated by mechanical and biophysical cues. The *in vivo* mechanobiology can be used to improve *in vitro* models of these heterotypic cell interactions, and also to engineer these cells *ex vivo* to better improve HSC therapies. Figure 1-2 graphically represents many of these mechanical and biophysical cues in the hematopoietic niche.

In fact, endogeneous HSCs are not amenable to conventional labeling in their native 3D environment *in vivo* [50], so visualization of HSC interactions and mechanistic understanding of VEC support and angiocrine signaling in hematopoietic recovery remain challenging. Accurate *in vitro* models of angiogenesis in the hematopoietic niche can thus aid elucidation of the mechanisms through which angiogenic or angiocrine signaling regulates HSCs. VECs are presented with many mechanical and biophysical cues *in vivo* such as fluid shear stress, biophysical crowding, and contractile force or strain from other cell types. We can leverage the *in vivo* mechanobiology of VECs to better replicate models of angiogenesis *in vitro*. Once the mechanisms of VEC support of HSCs are elucidated sufficiently, these same mechanical and biophysical cues can then be used to engineer the paracrine signaling of the VECs to improve hematopoietic recovery *in vivo*.

MSCs have also been shown to alter aspects of differentiation potential in response to mechanical cues, including morphology and expression of lineage-specific proteins and extracellular components. For conditions under which differentiation potential or progenitor state appears correlated with MSCs' capacity to contribute to regeneration and reorganization of the hematopoietic niche [52,54], it is plausible that the mechanical modulation of MSCs can be used to engineer MSC capacity to support hematopoietic recovery. There has also been recent evidence suggesting that HSCs can also bind to their extracellular matrix and exhibit mechanosensitivity [55]. These mechanical cues can be used to leverage MSC or HSC phenotype to better improve hematopoietic recovery.

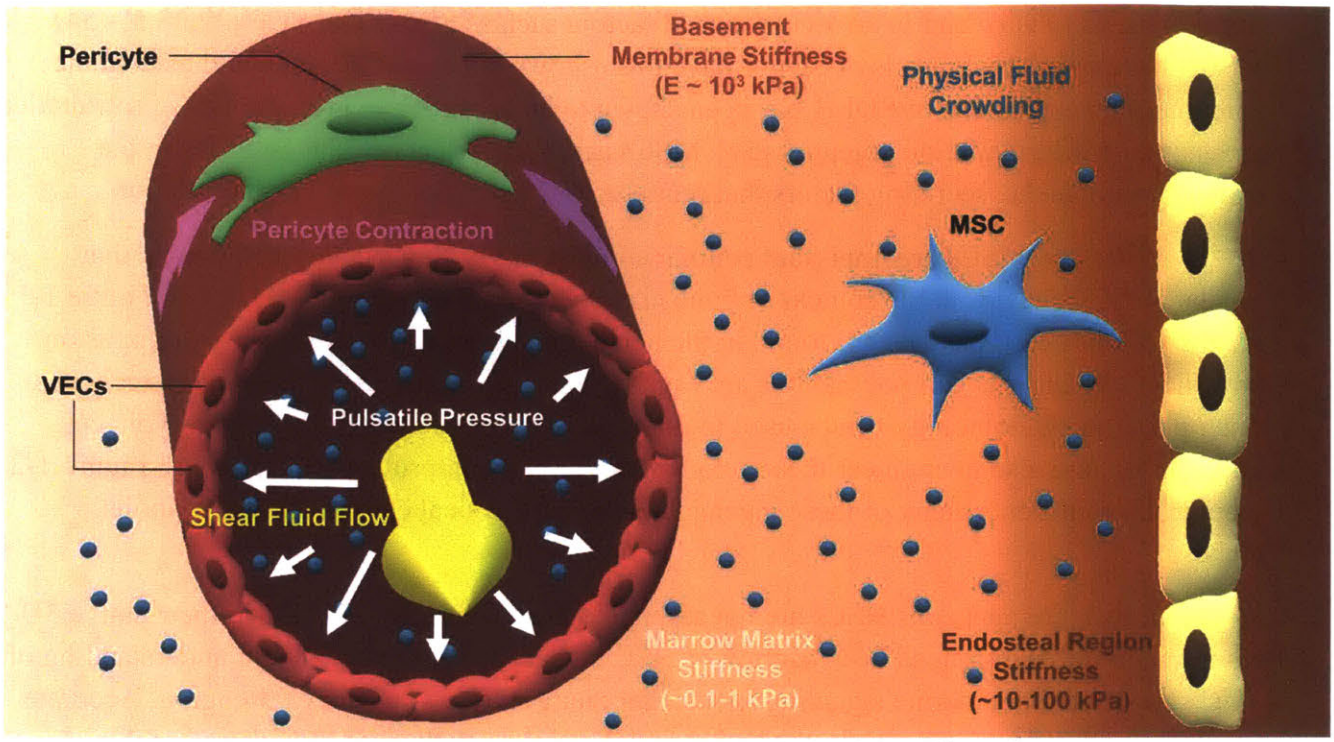

Figure 1-2. Mechanical and biophysical cues in the hematopoietic niche. Blue spheres represent physical fluid crowding macromolecular crowding (MMC). Orange background represents localized niche stiffness with more compliant regions represented by light orange and stiffer regions represented by dark orange. Hoop strain generated by contractile pericytes represented by purple arrows. Shear stress from fluid flow represented by yellow arrow. Pulsatile pressure presented by white arrows.

1.3 Mechanical modulation of mesenchymal stromal cell support

Mesenchymal stromal or stem cells are used as therapeutic agents in hundreds of registered clinical trials. However, there are currently no FDA-approved therapies, and this slow progression from safety to approved treatments is attributable in part to the heterogeneity of this cell population among donors and particularly after *ex vivo* expansion [56–59]. MSCs can vary depending on method of isolation, expansion technique and other *ex vivo* manipulation methods [59]. In order to address this heterogeneity, the International Society for Cellular Therapy (ISCT) has proposed a set of minimal criteria in terms of surface marker expression (expression of CD105, CD73, CD90, and lack of CD45, CD34, CD14, or CD11b, or CD19, and HLA-DR) and differentiation potential (along osteoblast, adipocyte, and chondroblast lineages *in vitro*) to define MSCs [60]. Despite this set of minimal criteria, we have shown that even though many populations (and subpopulations) of cells may appear immunophenotypically uniform, they can still be heterogeneous for *in vitro* and *in vivo* characteristics [61]. Others have also demonstrated that a very specific subset of perivascular MSCs that express CD146, Nestin, CXCL12 (or

SDF1) are those that can directly interact with HSCs and regulate hematopoiesis [28,62]. Thus, the ability to modulate MSC phenotype will play an important role in the translating these cells as a clinical therapy for improving hematopoietic recovery.

1.3.1 Macromolecular crowding effects on MSC behavior

A commonly overlooked extracellular cue for all cell types studied or expanded *in vitro* – including MSCs – is the biophysical occupation of fluid space due to macromolecules such as proteins, carbohydrates, lipids or glycosaminoglycans [63,64]. Traditionally, cells are cultured in dilute media and this macromolecular crowding (MMC) phenomenon has been considered chiefly in the intracellular space, where the decreased conformational organizations among molecules can drive reaction kinetics due to an excluded volume effect that results in entropic segregation [65–67]. *In vitro* culture media for MSCs are usually supplemented with serum proteins at concentrations around 1-10g/L, which is much lower than physiological protein concentrations that range about 30-80 g/L [63,68]. The fractional volume occupancy of physiological conditions is ~17-18% [63,68]. By supplementing the MSC media with synthetic, biologically inert MMC to recapitulate physiological crowding, extracellular matrix (ECM) deposition is increased [63,68]. We also demonstrated that in the presence of macromolecular crowding agents at such physiological fluid volume occupancies, MSC-derived ECM fibers (fibronectin and collagen IV) increased in alignment and increased the deposition and maturation of collagen I. In response to these changes in ECM organization and deposition, the MSCs also increased in proliferation and decreased in migration [68]. We and others have also demonstrated that the addition of MMC to *ex vivo* MSC cultures increases the rate and efficiency of differentiation induction into osteogenic or adipogenic lineages [63]. In a more recent study, Prewitz et al. used a higher fractional volume occupancy of ~28% for their MMC and explored how MMC interacted with other biochemical supplements such as ascorbic acid and osteogenic induction media [64]. In standard expansion and osteogenic induction conditions, they also observed an increase in sulfated glycosaminoglycan (GAG) deposition, which resulted in higher retention of growth factors such as VEGF and FGF-2 [64]. Prewitz et al. then went on to explore how MSC-derived ECM under MMC could affect HSC behavior. They expanded HSCs on top of de-cellularized ECM scaffolds (i.e., MSCs removed) that had been formed by cells in the presence or absence of MMC, and found that CD34+ hematopoietic stem and progenitor cell (HSPC) expansion increased on scaffolds formed under MMC [64]. Their results suggest that fluid macromolecular crowding is an important physiological cue to recapitulate the hematopoietic niche in order to promote HSPC expansion *in vitro*. In *ex vivo* culture, MMC also increased the stiffness of MSC-derived ECM and the subsequent stiffness of those adherent MSCs that exerted adhesion-mediated forces against that ECM [64,68]. As there are many different ranges of physiological stiffness in the bone marrow and hematopoietic niche, several studies have been dedicated to exploring how extracellular material or matrix stiffness can alter MSC behavior, typically in the absence of MMC considerations, as outlined below.

1.3.2 Substratum stiffness and MSC phenotype

MSCs contain a subset of stem cells that are a multipotent cell type that can be derived from adult tissues such as bone marrow and can be induced to differentiate along osteogenic, adipogenic, and chondrogenic lineages [46]. Due to their multipotency, MSCs were originally thought to be a promising cell type for applications in direct tissue repair. In these cases, MSCs would home to and engraft in sites of injury and replace damaged tissues of which they could differentiate into [69,70]. Because of this characteristic trilineage differentiation potential, early studies of MSC mechanobiology focused on modulating the differentiation potential of MSCs.

Substratum stiffness is an extracellular mechanical cue that has been explored widely regarding modulation of MSC differentiation potential. For example, Engler et al. used a polyacrylamide-based hydrogel as a cell-culture substratum to explore the effect of matrix stiffness [71]. They varied the stiffness of the polyacrylamide-based hydrogel across two orders of magnitude (from ~0.1 to 40 kPa) by modifying polymer cross-linking density, and compared various attributes of MSCs adhered to those materials (mechanical cues) after addition of differentiation induction media (chemical cues). They claimed that the most compliant to the stiffest hydrogels correspond with the stiffness of brain tissue, muscle, and osteoid tissue, respectively. Engler et al. showed that MSCs became more spread out on stiffer substrata, and were more branched on more compliant substrata. However, their claims on these changes in MSC morphology were based on images and quantification of select cells from a heterogeneous population of MSCs. Using microarray analysis, they showed that these changes in morphology were associated with neurogenic markers on compliant substrata and ostegeonic markers on stiff substrata. These researchers also added neurogenic and myogenic induction media and demonstrated that substrate stiffness could act synergistically with chemical cues to promote differentiation. While that study propelled forward the idea that substrate elastic modulus was a cue that that directed MSC differentiation capacity, many of its comparisons therein lacked statistical significance and the proposed trends were fitted using limited data and for cells obtained from a single donor. Further, that study did not verify whether the MSCs exhibited a terminally differentiated, functional phenotype upon chemical induction of differentiation, as the scope of that approach was based on morphology, gene expression, and expression of a small set of phenotypically correlated proteins or metabolites. In the decade following that study, differentiation of MSCs into myogenic and neurogenic lineages *in vivo* still remains controversial [72]. Moreover, their comparisons included multiple distinct material systems (i.e., polyacrylamide vs. glass) that not only differ in mechanical properties, but also in surface chemistry and topography. Thus, some of those findings based on comparisons between observations on polyacrylamide and glass substrata conflated the mechanical properties of bulk materials with the substrata surface properties that can also affect matrix protein adsorption and cell adhesive interactions. In short, that study did not demonstrate mechanical correlations conclusively nor intend to demonstrate causation, despite the inference that substratum stiffness directed lineage commitment. Nevertheless, that study demonstrated importantly that variation of

extracellular stiffness – in concert with chemical cues of induction media – can be concurrent with changes in some aspects of MSC morphology, gene expression, and metabolite expression that are consistent with progression toward commitment of tissue lineage cell phenotype.

In addition to stiffness of the material to which cells adhere, other cues such as the material surface nanotopography, ligand presentation, and substratum geometry (e.g., layer thickness) can alter the effective stiffness that MSCs sense upon adhesion and actomyosin contractility. These cues have been shown to influence MSC differentiation markedly, and may be conflated in early studies with the stiffness of the "bulk" material from which substrata layers were fabricated. As mechanosenstitivity is transduced through integrin-ligand interactions, it has become more widely appreciated that MSCs interpret stiffness as changes in adhesive ligand presentation [73–75]. Thus, the nanotopgraphy of the synthetic extracellular matrix is arguably more important to the differentiation potential of MSCs than the stiffness of the bulk material [73]. For example, nanopatterning of RGD ligands at high densities demonstrated increased focal adhesion and actin stress fiber formation, which corresponded with MSC osteogenic lineage commitment [74,76]. Fu et al. modified the effective stiffness or rigidity of the cell-culture substrata by restricting MSC binding to ligand-functionalized polydimethylsiloxane (PDMS) microposts. In this study, they increased micropost lengths to decrease pillar bending rigidity. They demonstrated increased osteogenic potential on stiffer substrata and increased adipogenic potential on more compliant substrata [77]. In a separate study, Trappmann et al. also suggested that the polyacrylamide hydrogel material system with tunable stiffness used in earlier studies also led to coupled changes in the substrata surface topography and in the presentation of the bound or tethered adhesion ligands at that surface [78]. In that particular study, they compared how MSC differentiation potential differed for cells adhered to a porous hydrogel (polyacrylamide) versus a nonporous elastomer (PDMS). Their study demonstrated how changes in mechanical properties of the bulk material need to be decoupled from other surface properties – such as porosity – that can alter the effective stiffness of the ligand to which the MSCs bind during cell-material adhesion. Recent studies have emphasized the importance of decoupling porosity of these hydrogel materials from the stiffness of these materials in order to better understand how substrata stiffness can influence MSC phenotype [79,80]. Together, these studies demonstrate that the effective stiffness of the substratum and ability of MSCs to form focal adhesion complexes and deform the surrounding microenvironment modulate differentiation capacity.

1.3.3 Substrata viscoelasticity and time dependence

In fact, most "soft" tissues in the body (e.g., brain, liver, and muscle tissue) do not deform mechanically as linear elastic or spring-like solids, but rather as time- or rate-dependent materials that exhibit both a time-independent stiffness and also viscous flow under certain deformation conditions and time scales. Bone marrow is among such materials that exhibit viscoelastic deformation [81]. Thus, recent studies have explored effects of viscoelastic properties of the extracellular materials on MSC behavior. Specifically, while Young's elastic

modulus E or storage moduli E' quantify material stiffness as an elastic parameter, recent studies have also explored how viscous or time-dependent parameters such as the loss moduli E'' or stress relaxation time τ of the cell culture substrata can affect MSC differentiation potential. Chaudhuri et al. demonstrated that stress relaxation in the cell culture substrata, not only stiffness, could regulate MSC differentiation potential [82]. They created alginate hydrogels with ionic cross-links with variable stress relaxation times, but approximately constant storage elastic moduli. In this study, they found that stiff hydrogels (initial Young's modulus, E_0, of ~17 kPa) with faster stress relaxation (short relaxation times) exhibited increased spreading, proliferation and osteogenic and chondrogenic differentiation potential. They also found that slower stress relaxation (long relaxation times) in more compliant gels (9 kPa) resulted in adipogenic differentiation potential. Their study demonstrated that a combination of both elastic and viscous parameters can modulate MSC differentiation potential. Yang et al. created PEG-based hydrogels that contained UV-degradable cross-links [83]. These allowed for the MSC culture substrata to switch from being stiff (~10 kPa) to more compliant (~2 kPa) with time. They found that depending how long ("dose") the MSCs were cultured on a stiff substratum, changes in MSC expression of osteogenic markers and osteogenic potential were either reversible (for short times) or irreversible (for long times) [83]. Their study showed that MSC differentiation outcomes could depend on how long a mechanical cue was administered to these adherent cells, and claimed that the MSCs could possess "memory." In this study, the authors also used mytomycin C to inhibit proliferation of the cells to limit differences in cell number. As they inhibited proliferation, the authors only explored one generation of MSCs and their sensitivity to mechanical environment changes. Thus, it is unclear if this mechanopriming is truly irreversible and would extend to future generations of MSCs after cell division. Nevertheless, this mechanical memory suggests that any *ex vivo* mechanopriming of MSCs could persist *in vivo* if MSCs were to be re-administered as a therapeutic *in vivo*.

1.3.4 MSC paracrine signaling due to strain and stiffness

As MSCs are not known to differentiate into hematopoietic lineages *in vivo*, MSCs participate in indirect repair during hematopoietic recovery by secretome-mediated interactions with HSCs [28,84]. The aforementioned studies all focused on how extracellular mechanical cues affected *differentiation potential* of MSCs. Although MSC ability to support hematopoietic recovery has been correlated with the MSCs' osteogenic differentiation potential or shift to osteoblast-like cells [34,36,52,85], the mechanisms through which MSCs support hematopoietic recovery proceed chiefly through soluble factors or *paracrine signaling* [28,53]. Majumdar et al. demonstrated that MSCs constitutively expressed cytokines and growth factors that support long-term repopulating HSCs [86]. Moreover, they found that growing MSCs in osteogenic induction medium instead of expansion medium decreased expression of certain cytokine [86]. Their study suggested that osteogenic differentiation potential of MSCs could be modulated *ex vivo* to differentially support HSC behavior. In a recent study, Qazi et al. used 3D porous scaffolds to enhance the secretory profile of MSCs to promote myoblast function [87]. They found that cell-

cell contact mediated by N-cadherin binding of MSCs in macroporous scaffolds enhanced the paracrine effects of MSCs [87]. Although the downstream application was not hematopoietic recovery, this study provided an example of how modification of physical parameters of the cell-culture material can affect cell-cell binding and subsequent MSC paracrine signaling. Very few published studies have explored how biomaterial mechanics can be leveraged to modulate MSC paracrine signaling and support hematopoietic recovery specifically.

In two separate studies, however, the mechanical microenvironment has been demonstrated to affect MSC paracrine signaling and downstream angiogenesis. Kasper et al. applied mechanical strain to MSCs and transferred the MSC conditioned media (MSC-CM) to VEC cultures. They found that the MSC-CM led to a significant increase in VEC proliferation and increased tube formation and sprout length indicative of improved angiogenesis. Kasper et al. also reported that mechanically loaded, or strained, MSCs led to an increased accumulation of MMP-2, TGF-β1 and bFGF in the CM derived from the MSCs [88]. They proposed that the upregulation of TGF-β1 and bFGF suggests that the FGFR signaling pathway instead of the VEGF pathway may play a role in how mechanically-loaded MSCs promote the VEC process of angiogenesis. They also suggested that MMP-2 could act indirectly to promote angiogenesis by enzymatic break down of mechanical barriers (e.g., matrix degradation) to facilitate microvessel sprouting [88]. In a similar study, Abdeen et al. also applied MSC-CM to cultures of VECs. However, instead of priming the MSCs with strain, Abdeen et al. mechanoprimed the MSCs by seeding them on to polyacrylamide hydrogels of varying stiffness (0.5, 10 and 40 kPa) that were first functionalized with different ligands (fibronectin, collagen I, and laminin) [89]. They observed maximum pro-angiogenic signaling (VEGF, angiogenin, IGF) from MSCs that had been grown on 40 kPa hydrogels. Abdeen et al. also verified increased tube formation, indicative of angiogenesis, with CM from MSCs grown on increasing stiffness. They noted that fibronectin seemed to exhibit the strongest stiffness dependence over other ligands, suggesting that ligand type is also important to the mechanosensitivity of MSC paracrine signaling. They could abrogate this effect by patterning fibronectin islands that restricted MSC spreading. These results suggested that increased MSC spreading in response to increase substratum stiffness may be necessary to improve MSC pro-angiogenic signaling [89]. In summary, their study demonstrated that MSC paracrine signaling is dependent upon both the mechanical microenvironment and also the biochemical cues presented by the ligand. Together, these two studies showed that mechanical strain, stiffness, and MSC spreading all play a role in altering MSC paracrine signaling and downstream angiogenesis.

We have studied how the viscoelastic properties of the cell culture substrata modulate MSC secretome components that can be applied to hematopoietic recovery [90]. In one recent study, we used PDMS to create cell culture substrata with tunable viscoelastic properties. We found that the decreased PDMS loss and storage moduli (G'', G') correlated with increased expression of important secreted proteins such as osteopontin, that has been implicated in maintaining hematopoiesis [91]. In our particular material system, we observed no differences in

terminal osteogenic differentiation potential. In addition to increasing osteopontin expression on compliant substrata, we also found that decreased stiffness correlated with increased expression of factors related to hematopoiesis such as IL-8, MCP-1, SDF-1α and more. Sieb et al. conducted a similar study with a polyethylene glycol diacrylate (PEGDA) based hydrogel with hyaluronic acid and gelatin incorporated as bioactive ligands at two stiffnesses (~1-2 kPa and ~15-20 kPa) [92]. Those researchers observed similar changes in cell spreading wherein the cells spread more on stiffer substrata. They assayed the expression of 28 different proteins on their stiff and compliant substrata at two different time points (2 and 14 days), and observed consistent upregulation of factors such as VEGF and urokinase plasminogen activator (uPA) over the course of two weeks. Contrary to our work, they observed over 100-fold upregulation of IL-8 on the stiffer substrata within two days, but the difference in expression on stiff and compliant substrata disappeared after 1 week. While the premise of the study was similar to our own, their results were phenomenological, lacked statistical significance, and not employed for downstream applications. Our results may differ due to the different material system and the adhesion ligand presentation (gelatin and hyaluronic acid) that Seib et al. used. However, their study did not go on to explore how the cytokine expression changes could be used for therapeutic applications. Similar to our work, Sieb et al. also showed that these changes in cytokine profile preceded detectable changes in expression of differentiation markers [92]. Together, these data suggest that the MSC secretome can be modulated mechanically, even prior to the point of detectable MSC lineage commitment (i.e., before differentiation). We have considered whether these changes in secretome expression could correlate with improved hematopoiesis. When our mechanoprimed MSCs were grown in non-contact co-cultures with HSPCs, HSPC proliferation increased significantly without altering HSPC differentiation potential. These data suggest that our mechanoprimed MSCs can maximize the proliferation of HSPCs without compromising HSPC differentiation potential, and that this paracrine signaling does not require MSC-HSPC contact [90]. Thus, mechanically modulated MSCs can promote HSPC proliferation *in vitro*, with important downstream applications in hematopoietic recovery *in vivo*.

Additionally, this same material system can be used to mechanoprime MSCs as a feeder layer than can be used to maximize expansion of naive HSPCs *ex vivo*. Thus, mechanobiology can play an important role in engineering MSC paracrine signaling to support hematopoiesis *in vivo*. A summary of the aforementioned biophysical and mechanical cues and the MSC responses is depicted in Figure 1-3.

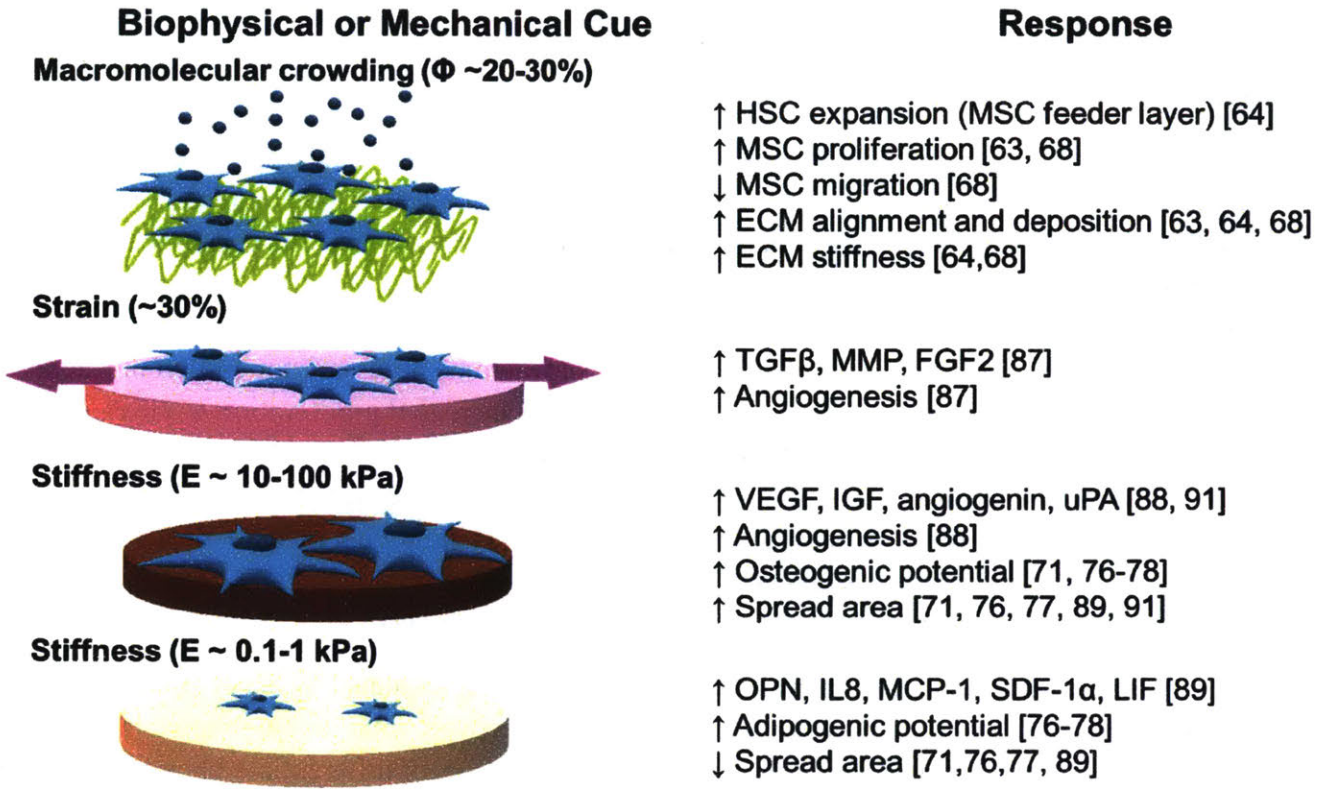

Figure 1-3. MSC response to biophysical and mechanical cues. Pictorial schematics of how biophysical and mechanical cues affect MSCs are depicted on the left. The MSC responses to these cues are summarized on the right.

1.4 Mechanobiology of vascular endothelial cells

1.4.1 Shear stress and VEC paracrine signaling

Blood flow through the vasculature can cause a frictional force that results in fluid shear stress on VEC-lined endothelium [93]. Almost 40 year ago, VECs were demonstrated to be sensitive to fluid shear stress whereby the VECs within the endothelium would preferentially align in the direction of shear flow [94]. More recent studies have explored how fluid shear flow changes the protein and cytokine expression by VECs. For example, Ando et al., demonstrated how VCAM-1 expression decreased in response to fluid shear stress [95]. VCAM-1 has also been proposed to be one of the adhesion molecules in which HSCs can interact with VECs [96]. Shear flow has also been demonstrated to increase the expression of IL-6 [97], which is an important *in vivo* regulator of HSCs self-renewal and differentiation potential [98]. GM-CSF is upregulated by shear stress [99] and has been shown to act with IL-3 to prevent apoptosis of HSCs and that it enables long term hematopoiesis [100,101]. Multiple studies from approximately two decades ago demonstrated that shear stress can increase the expression of a variety of VEC-derived growth factors including HB-EGF, bFGF (or FGF2), TGF-β [102–104].

However, very few of these studies in mechanobiology went on to explore how these changes in expression be useful for applications such as hematopoietic recovery, despite the fact that many of these cytokines are known regulators of hematopoiesis.

The lack of connection between those research communities conducting fluid shear stress studies using VECs with those developing approaches to speed hematopoietic recovery is due chiefly to the fact that the mechanisms by which these factors regulate hematopoiesis are only recently understood or are still being discovered. For example, EGF signaling was only recently demonstrated to be radioprotective of HSCs by reducing apoptosis of HSCs in irradiated mouse models [43]. Basic FGF (bFGF or FGF2) has been shown to be necessary for embryonic stem cell differentiation into hematopoietic lineages as well as increased proliferation of HSPCs derived from embryoid bodies [105]. In the last year, FGF2 has also been demonstrated to support osteblastic niche cells to support HSCs in response to bone marrow injury [106]. As understanding of how these growth factors are important for improving hematopoiesis grows, mechanical cues such as shear stress will become more widely understood and explored options for engineering VEC phenotype to optimize hematopoietic recovery.

Unlike bFGF and EGF, many of the factors that are upregulated by shear stress are not well understood in how they may impact hematopoietic recovery after myeloablative injury. Many of these factors may act in further downstream processes of differentiated hematopoietic lineages the may be implicated in hematopoietic recovery, instead of on HSCs directly. Shear stress-modulated VEC expression can serve as a model to recapitulate *in vivo* expression of these factors from VECs. It was established approximately 25 years ago that shear stress increased endothelial expression of PDGF [107,108]. However, the role of PDGF in normal human hematopoiesis is still unclear, but it acts on several downstream hematopoietic cell types *in vitro* such as megakaryocytes, platelets, macrophages, and lymphocyte subsets [109]. It has been reported to promote expansion of megakaryocyte progenitors from HSPCs, and enhances platelet recovery after irradiation in mice [109]. As the effects of PDGF on hematopoiesis are beginning to be understood, shear flow can be used to modulate this expression from VECs in *ex vivo* models. TGF-β is traditionally an inhibitor of HSC growth, suggesting that it is a regulator or HSC dormancy and quiescence [110]. However, this factor has also been determined to promote proliferation of certain HSC subtypes, such as myeloid-based HSCs, at certain concentrations [110]. Depending on the expression level, context, and differentiation stage of the target cell, TGF- β can have highly variable biological outcomes [110]. Thus, a means to tune this expression from VECs in an *in vitro* model that recapitulates key *in vivo* cues can be useful to understand how TGF-β regulates hematopoiesis.

It is well-established that shear stress can alter the secretory profile of VECs. These changes in cytokine and growth factor profiles may all have dramatic implications in hematopoietic recovery. However, signaling pathways of hematopoietic recovery are still being discovered, so to our knowledge there are no published reports that explore how mechanically-primed VECs can promote hematopoietic recovery. For those growth factors whose mechanisms

of action in regulating hematopoiesis are still unclear, shear stress may serve as an important cue in replicating *in vivo* VEC mechanobiology to better understand how VECs and their secretome interact with HSCs.

1.4.2 Macromolecular crowding and ECM formation of VECs

As angiocrine signaling plays a crucial role in maintaining the self-renewal capacity of HSCs, accurate *in vitro* models of angiogenesis are necessary to understand these regulatory mechanisms. Cellular interactions with the extracellular matrix (ECM) are important during angiogenesis as the VECs need to break down the basement membrane, form a provisional matrix where cell-cell contacts are absent, and then migrate to form new angiogenic sprouts [111]. The ECM provides guidance cues to regulate VEC migration, proliferation, and survival [111]. The ECM can serve to stabilize or enhance physiological angiogenesis or inhibit pathological angiogenesis [112]. As detailed in the previous section on MSCs, our group has demonstrated previously that MMC can preferentially align MSC-derived ECM and enhance the maturation of collagen I fibers in the absence of cells, suggesting that the effects of MMC on directing ECM organization are not cell-type dependent [63,68]. Importantly, these studies established a cell-matrix reciprocity, whereby MMC altered ECM organization that in turn affected cell morphology and functions including the amount of matrix protein production. Thus, we also explored how MMC affects the organization of basement membrane proteins secreted by the other key cell type in the hematopoietic niche, VECs [113]. Similarly, we observed increased alignment, spreading, and deposition of collagen IV in the presence of MMC [113]. Biophysical manipulation of the *in vitro* cell culture environment can more closely mimic the *in vivo* levels of crowding, in addition to manipulating the ECM organization and structure. Others have demonstrated that MMC increases the effective stiffness of the ECM produced by MSCs, which in turn led to improved HSPC expansion [64]. As VECs and MSCs occupy similar niches and MMC is not a cell-type specific phenomenon, we expect macromolecular crowding to increase the stiffness of the ECM surrounding VECs as well.

1.4.3 The effects of stiffness on VEC behavior

The effective stiffness of the blood vessels and surrounding ECM could also have important implications in hematopoietic recovery. Arterial stiffening is a result of cardiovascular disease, which has been shown to increase VEC contractility [114,115]. This contractility leads to de-stabilized cell-cell junctions, an increase in endothelial permeability, and subsequent leukocyte transmigration [115]. In contrast to these findings, *in vitro* studies have shown that compliant substrata (~140 or 200 Pa) promote spontaneous assembly of VEC capillary-like networks [116,117]. The pathological arterial stiffening that occurs *in vivo* has not been quantified mechanically; thus, the network formation on compliant substrata *in vitro* may occur at a range distinct from endogenous or *in vivo* stiffness values. HSCs are proposed to traffic in and out of the vasculature, similarly to leukocytes and lymphocytes [20]. Thus, the stiffness of VECs and the surrounding ECM can have important implications in HSC trafficking out of the

blood stream to home and engraft in the bone marrow. VECs are an epithelial cell type, not mesenchymal, so the VEC cell-cell junctions play an important role in their behavior. The behavior of sparse VECs vs. monolayers and how they respond to substrata of varying stiffness are different [118]. Yeung et al. created polyacrylamide-based substrata ranging in elastic moduli from ~2 Pa to 55 kPa, and demonstrated that isolated VECS develop stress fibers and increase in spread area at ~3 kPa. When the VECs are grown to confluence, however, they develop cell-cell contacts and these changes in VEC spreading and stress fiber formation are abrogated suggesting that signaling from cadherins may override cell-matrix adhesion complexes [118]. ECM stiffness plays a complex role in VEC contractility, VEC permeability, and capillary network formation.

1.4.4 Effects of strain on angiocrine signaling and angiogenic sprouting

Alternative to changes in extracellular stiffness, mechanical cues can take the form of extracellular, applied mechanical strain. Strain in VEC monolayers can be cyclic or static: pulsatile flow can impart a cyclic strain [93] whereas contractile cells such as pericytes can exert a static hoop strain on VEC monolayers [119,120]. In response to cyclic strains (20-40%), VECs increase in proliferation that is mediated by VE-cadherin junctions and Rac1 signaling [121]. Cyclic strain (10%) can also induce increased expression of VEC secreted factors such as tissue plasminogen activator (tPa) [122], which has been demonstrated to be important in fibrinolytic pathways that can regulate hematopoietic regeneration [123]. Yung et al. also demonstrated that cyclic tensile strain (~7%) could increase the expression of Ang-2 and PDGF-ββ by approximately five-fold when compared to no strain conditions [124]. These changes in signaling also resulted in increased VEC migration and sprout formation [124]. The pro-angiogenic factor Ang-2 is a ligand for Tie2 [124], which is also a receptor expressed on HSCs that promote a quiescent and anti-apoptotic state [44]. PDGF-ββ can act to indirectly regulate hematopoiesis by increasing erythropoietin production from stromal cells and subsequently promoting erythropoiesis [125]. Matrix metalloproteinase (MMP) expression from VECs is also regulated by cyclic strain [126,127], and MMPs may play in important role in ECM break down and increasing the number of circulating HSCs during hematopoietic recovery [128]. At static strains of 20~50%, Xiong et al. also demonstrated rapid exocytosis of Weibel-Palade Bodies from VECs, which resulted in increased secretion of von Willebrand factor (vWF) and interleukin-8 (IL-8) [129]. Those same levels of strain also increased selectin translocation and leukocyte adhesion [129]. Although Xiong et al. only explored leukocyte interaction with strained VECs, HSC dormancy is also regulated via selectin binding to VECs [24]. Together, these results demonstrate that not only does cyclic strain promote angiocrine signaling, but also regulates the translocation of VEC ligands to which HSCs can bind.

Pericytes that encircle VECs in microvascular environments such as capillary beds can exert actomyosin-mediate contractions that can result in a static hoop strain around VEC monolayers in a blood vessel wall [119,120]. For example, we applied static strain to VECs, of

magnitude comparable to pericyte contraction (~10%) in microvasculature on VEC monolayers. At these strains similar to those induced by pericyte contraction, the basement membrane of VECs exhibits strain stiffening due to its potential for nonlinear elastic stress-strain response over this range of strain [119,130]. This suggests that these changes in VEC behavior may not only be strain mediated, but also stiffness mediated. We found that these strains induced cell-cycle progression, translocation of nuclear transcription factors ($p27^{kip1}$), and angiogenic sprouting in 3D models [120]. This suggests that static mechanical strain can induce angiogenic sprouting. Physiological strains due to pulsatile flow or pericyte contraction can induce proliferation of VECs, enhance angiogenic sprouting, and increase the expression of VEC secreted factors. Thus, replicating physiological strains *in vitro* is necessary to mimic the perivascular niche that regulates hematopoiesis *in vivo*.

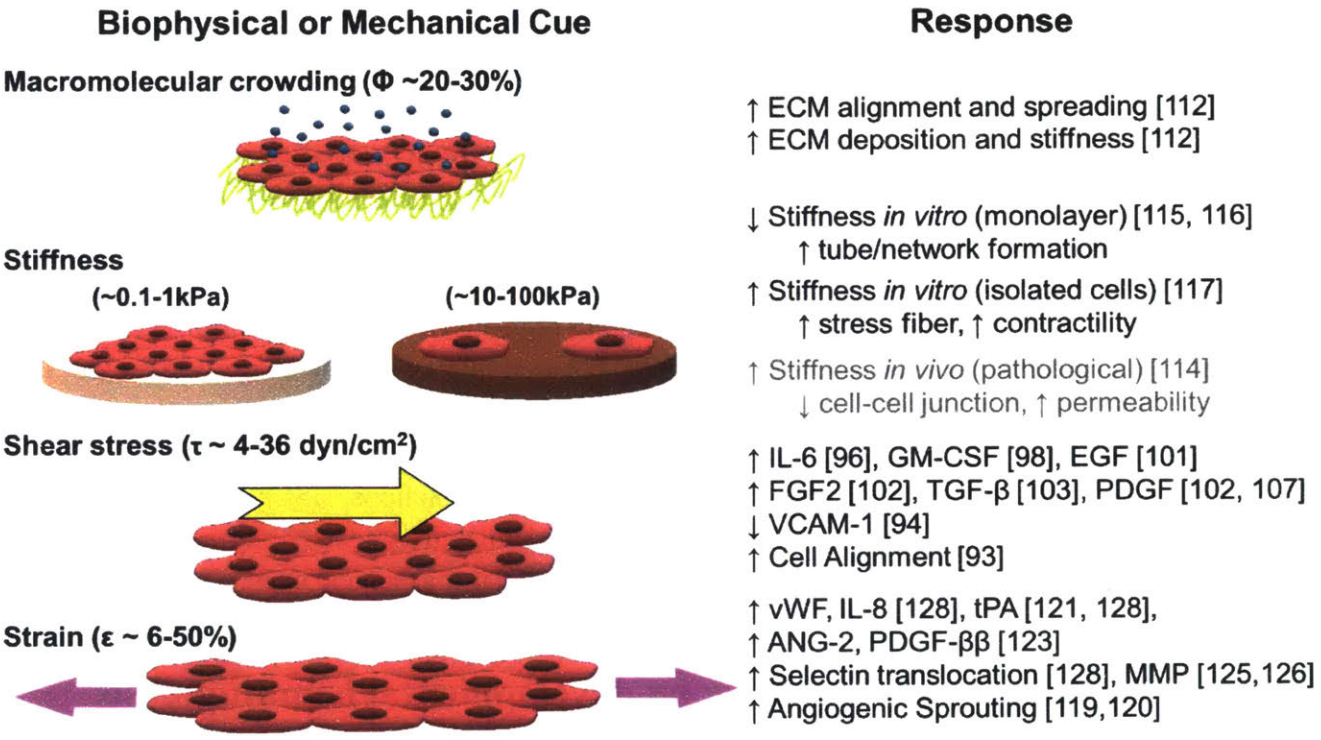

Figure 1-4. VEC response to biophysical and mechanical cues. Pictoral schematics of how biophysical and mechanical cues affect VECs are depicted on the left. The VEC responses to these cues are summarized on the right.

The biophysical cue of macromolecular crowding in the fluid space can also increase VEC-derived ECM deposition and organization that has the potential to influence VEC behavior such as proliferation and migration. Mechanical cues such as shear stress, extracellular stiffness, and cyclic or static strain can all regulate VEC behavior implicated in angiogenesis such as proliferation, migration, and capillary morphogenesis. These biophysical and mechanical cues are necessary tools to mimic the physiological vascular and perivascular niche accurately. Accurate recapitulation of the niche *ex vivo* is necessary to understand how VECs support hematopoiesis. These mechanical cues also regulate and enhance VEC paracrine signaling that

is implicated in hematopoietic recovery *in vivo*. These *in vitro* findings suggest that not only can these cues be used to mimic *in vivo* mechanobiology, but these cues can also be used to enhance VEC signaling. Using strain, shear, MMC, or stiffness, we can mechanoprime VECs to produce the cytokines and growth factors necessary for HSC expansion and self-renewal. Similar to MSCs, these VECs can be used to support HSC expansion *ex vivo* or as a transplantation therapy to promote hematopoiesis *in vivo* [38,39]. A graphical summary of how VECs respond to these biophysical and mechanical cues is depicted in Figure 1-4.

1.5 Direct mechanical regulation of hematopoietic stem and progenitor cells

HSCs express a variety of adhesion receptors that can interact with not only their surrounding ECM, but also ligands expressed on other cell types that can regulate HSC self-renewal, differentiation, and engraftment [131]. HSCs have been demonstrated to have heterotypic cell binding via the heterophilic SDF1α-CXCR4 axis and homophilic N-cadherin binding [132]. There has also been evidence of HSPC binding to various extracellular matrix proteins via integrin-ligand binding [55,133,134]. HSC expression of specific integrins (α4β1, α5β1, α4β7, α9β1, α6β1) have been demonstrated to regulate HSC adhesion, proliferation, migration and differentiation [20,131,135–137]. For example, one study demonstrated that HSC expression of the α4β7 integrin has been demonstrated to promote HSC homing and engraftment [138]. HSCs are proposed to sense their external environment via these integrin-mediated interactions [55]. Thus, through these adhesion-mediated interactions, HSCs could also potentially respond to their physical and mechanical microenvironment. Nevertheless, there has been limited exploration to date regarding how extracellular mechanical cues affect HSCs to date.

1.5.1 The effects of shear flow on developmental hematopoiesis

As the hematopoietic compartment develops in the embryo at similar times as vasculature, Adamo et al. proposed that biomechanical forces transduced via the developing vasculature could promote hematopoiesis [139]. They applied a shear stress of 5 dyn/cm^2 to isolated embryonic stem cells and observed increased expression of transcription factors associated with hematopoiesis, and accelerated differentiation of lymphocytes and erythroblasts, suggesting enhanced embryonic hematopoiesis [139]. They then went on to demonstrate loss of hematopoietic function *in vivo* by using a mouse model that lacked circulation, but maintained vasculature. From those mice, they isolated precursor cells, applied shear stress *ex vivo*, and observed recovery of hematopoietic potential via upregulation of transcription factor Runx1. Their study demonstrated that biomechanical force such as hemodynamic shear can enhance hematopoiesis.

1.5.2 Extracellular stiffness and HSC phenotype

In addition to shear flow, HSCs have also been shown to respond to extracellular stiffness or elastic modulus. Holst et al. used tropoelastin, a protein that extends under applied force, as an adhesion ligand for expanding HSCs and demonstrated enhanced *in vitro* expansion of naïve, undifferentiated HSCs by 2-3 fold, and cross-linking of the extracellular tropoelastin abrogated enhanced HSC expansion. By pharmacological inhibition of myosin activity, they also demonstrated that the mechanosensitvity of the HSCs depended on actomyosin contractility, but not necessarily integrin binding [140]. Shin et al. explored how HSPC expression of isoforms Myosin-IIA (MIIA) and Myosin-IIB (MIIB) changes during hematopoiesis [141]. They showed that MIIB polarization correlated with HSPC asymmetry and differentiation *in vitro*. This MIIB polarization was suppressed in compliant matrices, and enhanced in stiffer matrices and in areas of local stress, suggesting that MIIB transduces HSPC mechanosensitivity to their extracellular stiffness. They also found that MIIA is required for sustained engraftment *in vivo* and long-term hematopoiesis. They also explored how inactivation of both isoforms with blebbistatin treatment affected hematopoiesis *in vivo*. Shin et al. found that temporary blebbistatin treatment depleted progenitor cells but enriched the population for HSCs with multilineage reconstitution potential; thus, mechanosensitivity was necessary for *in vivo* differentiation of HSCs. In summary, that study showed that MIIB is expressed in HSPCs early on, but downregulated during differentiation, and that the isoform MIIA is required for sustained engraftment and hematopoiesis *in vivo* [141].

Another study attempted to decouple the effects of substrata stiffness, collagen functionalization density, and dimensionality on hematopoietic stem and progenitor cell (HSPC) behavior [142]. They explored the effects of stiffness by using 2D synthetic polyacrylamide-based substrata in the range of <1 kPa to >100 kPa with covalently functionalized collagen to promote binding. They purported to explore the effects of 2D culture vs. 3D culture with collagen hydrogels, but the material systems used for 3D culture did not include polyacrylamide. Moreover, their 3D hydrogels were more compliant than their 2D substrata by at least an order of magnitude, such that dimensionality and stiffness were not de-coupled in that experimental design. They only demonstrated changes in cell spread area and circularity once their 2D substrata exceeded 100 kPa, a stiffness that far exceeds any measurement of the hematopoietic compartment [142]. While that study was interesting in its aims, those particular results were phenomenological and lacked statistical significance or exploration of HSPC functional phenotypic consequences.

Lee et al. suggested that the stiffening of osteoblasts due to other paracrine signals in the endosteal niche could present mechanical cues to the HSPCs [143]. They demonstrated spreading and stiffening of osteoblasts and replicated this stiffening with UV-crosslinkable polyethylene glycol diacrylate (PEGDA) hydrogels. They demonstrated the osteoblast stiffening

in the range of tissue stiffness ~100-700 Pa, but their synthetic hydrogel system ranged from ~10-100 kPa, approximately 2-3 orders of magnitude stiffer than the endosteal niche. They also divided their PEGDA substrata in a binary way classifying them as "soft" vs. "hard" (which we refer to in terms of the elastic comparators, compliant vs. stiff) which corresponded with ~20 kPa and a range of ~40-100 kPa, respectively. Nevertheless, in their PEGDA system, they showed increased cell number and cell velocity with increasing stiffness [143]. This same group also explored how ligand patterning in 2D that probed RGD-integrin binding could affect HSPC adhesion and polarization. The authors found that a spacing distance of 20 nm maximized HSPC adhesion and lipid raft clustering indicative of outside-in signal transduction [133]. Lee et al. further extended those findings by using a PEGDA-based hydrogel with RGD (adhesive tripeptide integrin ligand) domains to create a 3D macroporous hydrogel with and cells such as MSCs to mimic the stromal microenvironment [144]. They maximized *ex vivo* HSPC expansion and maintenance of the differentiation potential using a biomaterials-based approach that mimicked this porous, cell adhesive aspect of the native microenvironment [144]. Together, these studies demonstrate that binding of HSPCs to their mechanical and physical microenvironment can modulate cell proliferative, migratory and differentiation potential.

In recent work, HSPCs have been shown to be mechanosensitive to cues such as extracellular shear stress and stiffness by altering their proliferation and differentiation capacity. Similar to other stem cells, HSC mechanosensitivity is also transduced via actomyosin contractility and integrin binding. As the understanding of how HSCs respond to their mechanical microenvironment expands, the community can use these cues to expand naive HSPCs *ex vivo* for HSCTs. A summary of how mechanical cues can alter hematopoiesis or HSC behavior is tabulated in Table 1-1.

Mechanical Cue	Response	Reference
Shear stress (5 dyn/cm^2)	↑ Embryonic hematopoiesis	[139]
Stiffness	↓ Stiffness (tropoelastin binding) → ↑ HSC expansion	[140]
	↑ Stiffness (0.3-34 kPa) → ↑ MIIB polarization & HSC differentiation	[141]
	↑ Stiffness (~10-50 kPa) → ↑ HSPC expansion, ↑ velocity	[143]

Table 1-1. HSC response to mechanical cues. Relative responses by HSCs to two distinct classes of mechanical cues.

1.6 Outlook

Due to myeloablative conditioning regimens, HSCTs with long-term engraftment and no relapse of disease remains challenging. Successful HSCT engraftment and subsequent hematopoietic recovery requires support from niche cells including VECs and MSCs. These niche cells can interact with HSCs directly (via cell-cell contacts) or indirectly (via paracrine signaling). MSC and VEC phenotypes can be modulated by mechanical stimuli or their physical microenvironment.

Current insights from cell-matrix mechanobiology can be applied to hematopoietic recovery to improve understanding of the hematopoietic compartment *in vivo* and to engineer HSCs for improved graft function. Mechanical and biophysical cues are necessary to accurately mimic the physiological perivascular and endosteal niches *ex vivo* in terms of paracrine signaling, cell behavior and ECM formation. Those *ex vivo* models can serve an important role in elucidating the mechanisms which VECs & MSCs interact with HSCs in the context of hematopoietic recovery. MSC differentiation potential, which is correlated with their paracrine signaling, can be modified by cues such as substratum stiffness. VEC angiocrine signaling and angiogenesis can also be enhanced by mechanical cues such as shear flow, extracellular stiffness, and strain. Many of these paracrine signals from MSCs and VECs have been correlated with improved hematopoietic recovery. Together, these studies suggest that MSCs and VECs can also be engineered with mechanical cues to exhibit the phenotypes necessary to support hematopoiesis. In recent work, mechanical cues such as shear stress and stiffness have also been shown to influence HSC proliferation and differentiation, suggesting that mechanical cues can also be used to directly influence HSC behavior *ex vivo*.

These related but separate fields of hematopoietic recovery and cell mechanobiology can now be bridged to develop improved therapies for HSCT. Understanding of *in vivo* mechanobiology in the hematopoietic niche allows for more accurate models of heterotypic cell-cell interactions *in vitro* that are necessary to determine what molecular components drive improved hematopoietic recovery *in vivo*. We can also leverage mechanical and physical cues to engineer MSC and VEC phenotype – and potentially also the HSC phenotype. Figure 1-5 illustrates several different approaches by which mechanical or biophysical cues can be used to promote hematopoietic recovery in humans. Indeed, this growing capacity to generate mechanoprimed VECs and MSCs provides the potential to either use these cells as feeder layers to expand HSCs *ex vivo,* or to inject these mechanoprimed support cell types *in vivo* as an adjuvant for co-transplantation therapies with HSCT.

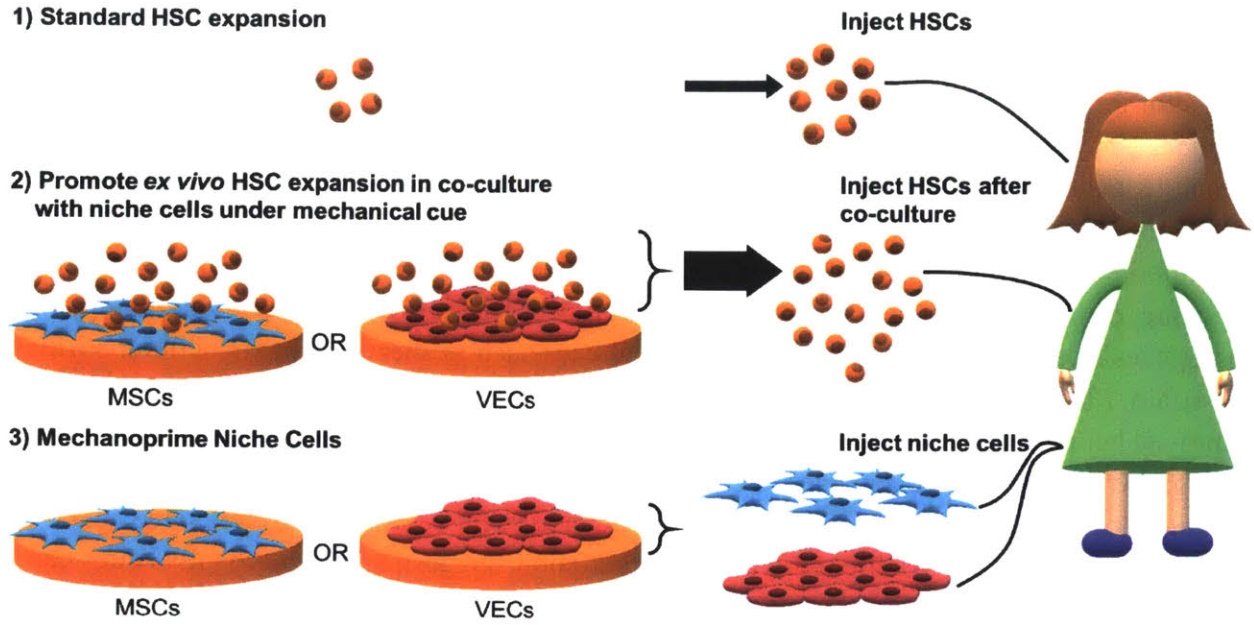

Figure 1-5. Mechanical cues to improve cell therapies for hematopoietic recovery. The first row represents how HSCs are typically expanded for HSC transplantation. Black arrow width represents expansion efficiency. The second row represents how VECs and MSCs can be engineered to promote increased *ex vivo* expansion of HSCs. The third row represents how VEC and MSC can be mechanoprimed and injected to serve as a co-transplantation therapy.

1.7 Thesis goals and organization

In this introduction, we have established the importance of hematopoietic recovery and how it is supported through the hematopoietic niche. Vascular endothelial cells (VECs) and mesenchymal stromal cells (MSCs) are two cell types contained in the hematopoietic niche that are crucial to supporting hematopoietic recovery through indirect repair mechanisms such as paracrine signaling. The aim of this thesis is to understand how biophysical and mechanical cues can regulate the VEC or MSC behavior and phenotype.

This work informs us of how to potentially develop improved cell-based therapies to promote hematopoietic recovery in three different ways. Firstly, replicating the mechanical and biophysical cues that exist in the hematopoietic niche *in vitro* is necessary to gain an accurate, mechanistic understanding of cellular interactions within the niche. Secondly, we can use these same cues to modulate the niche cells (e.g., mesenchymal stromal cells) to promote *ex vivo* expansion of hematopoietic stem cells used for transplantation. Lastly, these niche cells can also be administered as a separate adjuvant therapy to promote indirect repair *in vivo*. This thesis aims to bridge the two disparate fields of VEC or MSC mechanobiology and hematology to engineer and thus improve the outcome of hematopoietic stem cell (HSC) transplantations, which require proliferation and blood cell lineage differentiation of administered HSCs within the bone marrow niche.

- **Chapter 2** describes how the biophysical cue of **macromolecular crowding affects the kinetics of extracellular matrix (ECM) deposition and organization from vascular endothelial cells**. The basement membrane and ECM are important in regulating angiogenesis and angiocrine signaling. Thus, it is important to understand how the matrix is formed under physiological conditions. Macromolecular crowding is the occupation of fluid volume space due to macromolecules such as proteins, lipids, and carbohydrates. The occupation of fluid space creates an excluded volume effect that can drive the alignment of ECM fibers as well as speed up reaction kinetics. How does the MMC affect the alignment of VEC-derived basement membrane fibers? Can MMC increase the deposition of VEC-derived ECM? How is the distribution or spread of MMC altered in the presence of MMC? How quickly can MMC elicit these changes? How does this biophysical cue interact with other chemical cues such as paracrine signaling from pericytes? This chapter concludes that MMC is necessary *in vitro* to accurately replicate the endogeneous basement membrane architecture and ECM surrounding VECs and blood vessels *in vivo*.

- **Chapter 3** explores how applying the mechanical cue of **static, uniaxial strain can induce vascular endothelial cell cycle re-entry and angiogenic sprouting.** During myeloblative conditioning regimens, niche components such as blood vessels are also damaged. To decouple mechanical cues such as strain from chemical cues such as paracrine signaling, we developed a uniaxial strain device that could apply comparable strains to VECs and their basement membranes in a similar way as pericytes contract around VECs. This allowed us to address several questions about how mechanical cues such as pericyte-generated strains can regulate angiogenesis. Can static, uniaxial strain induce cell-cycle re-entry in a growth arrested monolayer of VECs? Is this mechanical cue sufficient to drive angiogenic sprouting *in vitro*? In this chapter, we conclude that static mechanical strain is an applied mechanical cue that is sufficient to promote angiogenesis alone. Thus, we can use it to engineer VEC behavior and phenotype. Moreover, understanding how microvascular angiogenesis is regulated by mechanical cues can help us to create better models of angiogenesis *in vitro*. These accurate *in vitro* models are a necessary prerequisite before we can begin to probe how angiogenesis and angiocrine signaling can support hematopoietic recovery.

- **Chapter 4** examines how the **viscoelastic properties of cell culture substrata can modulate the MSC secretome.** Mechanobiology of MSCs has been more typically focused on use of substratum mechanical properties (stiffness) to alter the differentiation potential of MSCs along mesenchymal tissue cell lineages. However, as the MSC secretome, not cell differentiation potential, is responsible for supporting hematopoietic recovery, we sought to explore how mechanobiology can be leveraged to engineer the MSC secretome prior to advanced phenotypic lineage commitment. We designed *in vitro*

systems and experiments to address several outstanding questions. Can we engineer cell culture substrata with tunable mechanical properties while keeping all biochemical properties constant? Are changes in shear loss and storage modulus across three orders of magnitude (~1 kPa, ~10 kPa to ~100 kPa) sufficient to cause changes in MSC behavior? How does the shear storage or loss modulus of the cell culture substrata affect the MSC secretome? Can these properties be used to engineer the MSC secretome? How is MSC terminal differentiation affected? In this chapter, we explore the answers to these aforementioned questions.

- **Chapter 5** presents how **mechanically modulated MSCs can be used to regulate hematopoiesis *in vitro* and improve hematopoietic recovery *in vivo*.** In previous studies, we had identified a specific subpopulation of MSCs that were effective in supporting hematopoietic recovery. In this chapter, we used the secretome expression of that specific subpopulation to identify the key factors that are correlated with and possibly support hematopoietic recovery. The questions of relevance here pivoted on prediction of *in vivo* outcomes from *in vitro* data on the biophysically sorted or mechanically modulated MSC population. What components of the secretome are correlated with improved hematopoietic recovery? Based on the expression of those identified factors, can we develop a regression model to predict survival of any MSC population? What are the expression levels of those key secretome components in our mechanically modulated MSCs? How do our mechanically modulated MSCs regulate hematopoiesis *in vitro* when co-cultured with HSPCs? Can our mechanically modulated MSCs support hematopoietic recovery *in vivo*? Can our regression model predict the *in vivo* outcomes of our engineered MSCs? Ultimately, this chapters aims to validate that we can improve the therapeutic efficacy of MSCs in indirectly supporting hematopoietic recovery using controlled and predictable means.

- **Chapter 6** concludes this thesis with a discussion of the most important findings of these studies, and their potential relevance in improving therapies for hematopoietic recovery. Additionally, the conclusion presents potential directions for future exploration, and how these studies can be expanded and translated for clinical relevance in hematopoietic recovery.

Chapter 2

Time-dependent extracellular matrix organization and secretion from vascular endothelial cells due to macromolecular crowding

In Chapter 1, we summarized how mechanical and biophysical cues can alter paracrine signaling or network formation from vascular endothelial cells (VECs) *in vitro*. Macromolecular crowding (MMC) has been explored in altering mesenchymal stromal cell (MSC)-derived extracellular matrix (ECM), but few studies have explored how the fractional volume occupancy of the fluid space can affect VEC matrix formation. In Chapter 2, we specifically explore how the biophysical cue of MMC organizes and directs basement membrane formation basal to VEC monolayers *in vitro*.

2.1. Acknowledgements

The work presented in this chapter was published as a conference proceedings article [113]. *Dr. Adam S. Zeiger mentored and conceived the initial design of this work. Frances D. Liu designed, conducted experiments, analyzed data, and wrote all of the results presented below. As noted in the methods, cells and conditioned media were provided originally by Prof. I.M. Herman and Dr. J. Durham (Tufts University), respectively.*

2.2 Introduction

Angiogenesis, the formation of new blood vessels extending from existing vasculature, is a complex process involving several potential cues at the molecular interfaces between cells and surrounding materials. Vascular endothelial cells (VECs) comprise the primary cell type that lines microvessel walls and secretes extracellular matrix (ECM) proteins [111], along with other vessel-associated cell types including pericytes (see Fig. 2-1). Although substantial previous work has explored biochemical and mechanical modulation of this process – including historical emphasis on therapies that modulate the type and amount of molecules the cells secrete or take up – there is increasing focus on direct manipulation of the cell-ECM microenvironment [112].

Here, we present and analyze a novel means to manipulate the organization of the VECs' extracellular matrix via macromolecular crowding of the aqueous fluid surrounding these cells *in vitro*. This approach provides one way to promote self-assembly of a microvessel ECM *in vitro* under conditions that more closely approximate those *in vivo*, and to explore how this one endogenous biophysical cue may modulate angiogenesis *in vivo*.

In vivo, the capillary microenvironment includes multiple cell types and their associated secreted molecules (the secretome), the basement membrane that is a collagen-IV rich ECM, and one characteristic that is rarely included in *in vitro* approximations of the microenvironment [3,4]. This characteristic is macromolecular crowding of the fluid inside and outside the vessel, which is packed densely with proteins, proteoglycans, and polysaccharides at concentrations of 30-70 g/L in interstitial fluid [5,6] and 80 g/L in blood plasma [147] that significantly exceed *in vitro* levels (<1-10 g/L) [67]. Macromolecular crowding increases intracellular protein folding, aggregation, reaction kinetics [66], and even gene expression in cell-free solutions [148]. However, MMC has been largely overlooked as a potential driver of changes in the *in vitro* extracellular environment. We have previously demonstrated that MMCs increase ECM protein production and promote ECM filament alignment *in vitro* for a mesenchymal cell type (mesenchymal stromal cells that are multipolar and motile *in vivo*), and that this crowding-induced change in matrix filament organization directly promotes increased cell adhesion and proliferation [68]. As capillary vessels are defined by polarized, planar arrays of nonmotile cells *in vivo*, it is not clear whether MMC will also significantly alter the matrix production and alignment in this cell type. In this study, we used MMC nanoparticles *in vitro* to mimic the excluded volume fraction occupied by these high protein concentrations surrounding the capillary *in vivo*, and indeed observed that such crowding *in vitro* significantly alters the amount and degree of self-assembled alignment of collagen-IV produced by VECs over several days.

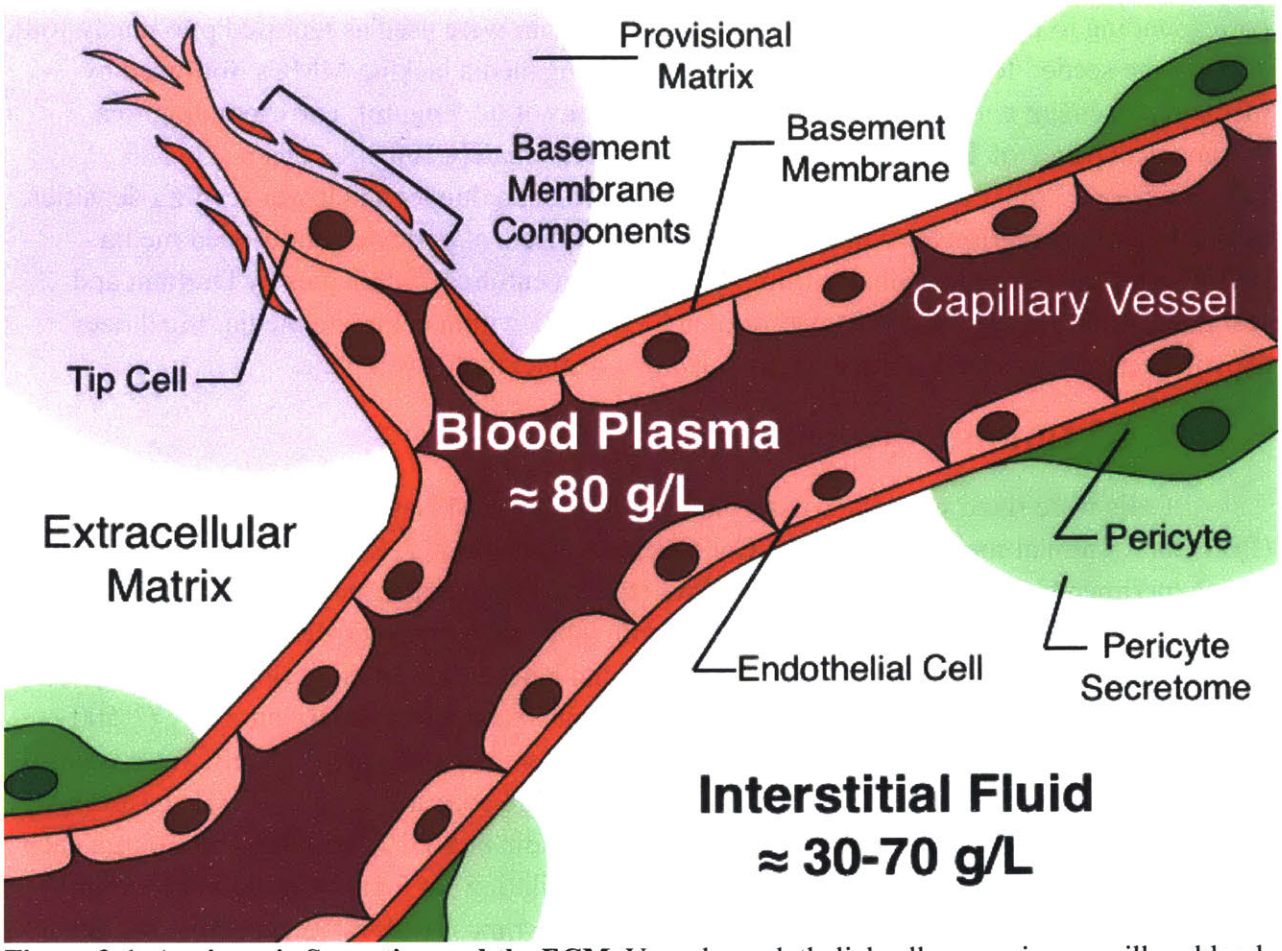

Figure 2-1. Angiogenic Sprouting and the ECM. Vascular endothelial cells comprise a capillary blood vessel, and can extend new branching vessels. Pericytes are embedded in the shared basement membrane; these cells can form gap junctions with VECs [10, 11] and secrete molecules. Approximate protein concentrations inside and outside the basement membrane significantly exceed *in vitro* concentrations, resulting in macromolecular crowding that may affect organization of extracellular matrix filaments in the intact vessel wall and at the sprouting region of new vessels.

2.3 Materials and Methods

2.3.1 Cell Culture

Vascular endothelial cells (VECs), derived originally from bovine retina by Herman et al., were cultured on glass-bottom 24-well dishes (In Vitro Scientific, P24-1.5H-N, Sunnyvale, CA) in Dulbecco's modified Eagle's Medium (DMEM) containing Bovine Calf Serum (BCS; #C8056, Sigma), with media exchange every three days, and maintained at 5% CO_2 and 37°C. For experiments <1 week, 10% BCS was used in complete media; for experiments >1 wk, 5% BCS was used to slow proliferation. Ficoll, a net-charge neutral epoxide-linked polysaccharide, was used as the macromolecular crowder [68]; a mixture of two Ficoll molecular weights

corresponding to hydrodynamic radii of ~4 nm and ~8 nm were used as reported previously [68]. VECs were seeded for at least 24 h in serum-containing media lacking MMCs, followed by media replacement containing MMCs at concentrations of 62.5 mg/mL corresponding to a volume occupancy of 17%. Cells were seeded at approximately 100,000 cells/mL (~530 cells/mm^2) or 37,500 cells/mL (~200 cells/mm^2) to compare higher and lower seeding densities, respectively. In experiments considering additional seffects of pericyte conditioned media (PCM) that was derived originally from 90% confluent cultures of pericytes by Durham and Herman (Tufts University), PCM was diluted to 10 vol% within complete media. In all data shown, each analysis time point corresponded to a distinct multi-well plate.

2.3.2 Immunocytochemistry

Cells were fixed with 4% paraformaldehyde in 150 mM NaCl phosphate buffered saline (PBS) for 15 min at room temperature. Cells were fixed at 1 day, 1, 2, 3, and 4 weeks (for long-term experiments); and at 1, 2, 3, 5, and 7 days (for short-term experiments) after +MMC-media replacement. Between steps, cells were rinsed with 0.05% Tween-20 or PBS. Cells were permeabilized with 0.1% Triton X-100 for 5 min, and blocked for 30 min prior to antibody staining using 3% goat serum in 1xPBS. Cells were incubated with primary antibody (1:500 dilution), rabbit polyclonal antibody to collagen IV (abcam ab6586), for 1 h. Cells were washed before incubating with secondary antibody, AlexaFluor488 goat anti-rabbit IgG (H+L) antibody (Life Technologies A11008) and AlexaFluor594 phalloidin at a 1:1000 dilution for 30 min each. Nuclei were stained with Hoechst 33342 at a 1:10000 dilution for 5 min. Cells and collagen IV were imaged via epifluorescence microscopy (IX-81, Olympus) with a 10x objective (Slidebook 5.0, Intelligent Imaging Innovations, Inc). Images within the same experiment were all acquired at the same lamp intensity and exposure duration.

2.3.3 Image Analysis

Relative protein amounts were estimated from image fluorescence intensity, quantified using CellProfiler (The Broad Institute). Collagen-IV alignment was determined using the metric of angular (or circular) standard deviation as described previously [68]. Angular standard deviation was quantified in MATLAB using a customized script to calculate the local orientation of simple neighborhoods. For further details on image analysis and segmentation, please refer to Appendix C.

2.4 Results and Discussion

2.4.1 ECM deposition: amount and areal density

Collagen IV is an extracellular matrix protein found primarily in the basal lamina, a thin layer of the capillary basement membrane. Here, we used collagen IV to monitor the development of this extracellular matrix over time. Figure 2-2 A-B illustrates the striking visual contrast in the amount and areal coverage of collagen IV secreted by VECs over four weeks, in the absence and presence of MMCs, respectively. Figure 2-2 C quantifies the relative amounts of collagen secreted per cell, in terms of fluorescence intensity. Clearly, MMCs within the in vitro fluid promote increased collagen production, as has also been observed for sparse cultures of mesenchymal stromal cells [68]. Figure 2-2 D quantifies matrix density and distribution, as the intensity is normalized per unit fluorescent area. Here, the apparent density of the self-assembled matrix is lower in the presence of MMCs. Together, Figs. 2-2 C-D suggest that the collagen fibers are more diffuse under macromolecular crowding conditions, which corroborates qualitative observations of representative images such as Figs. 2-2 A-B. These differences in amount and areal density of collagen-IV were significantly different by week 1 ($p<5x10^{-9}$ for total amount; $p<0.01$ for areal density) and were sustained for up to four weeks. Further, the increased amount and increased dispersion of the collagen fibers suggests a difference in the number of cell-ECM contacts, which may in turn plausibly alter cell behaviors of adhesion and migration that relate to angiogenesis. This biological consequence to the altered ECM organization induced by crowding was not explored directly in this study, and remains an opportunity for future work that seeks to recapitulate the *in vivo* ECM organization of the microvasculature *in vitro.*

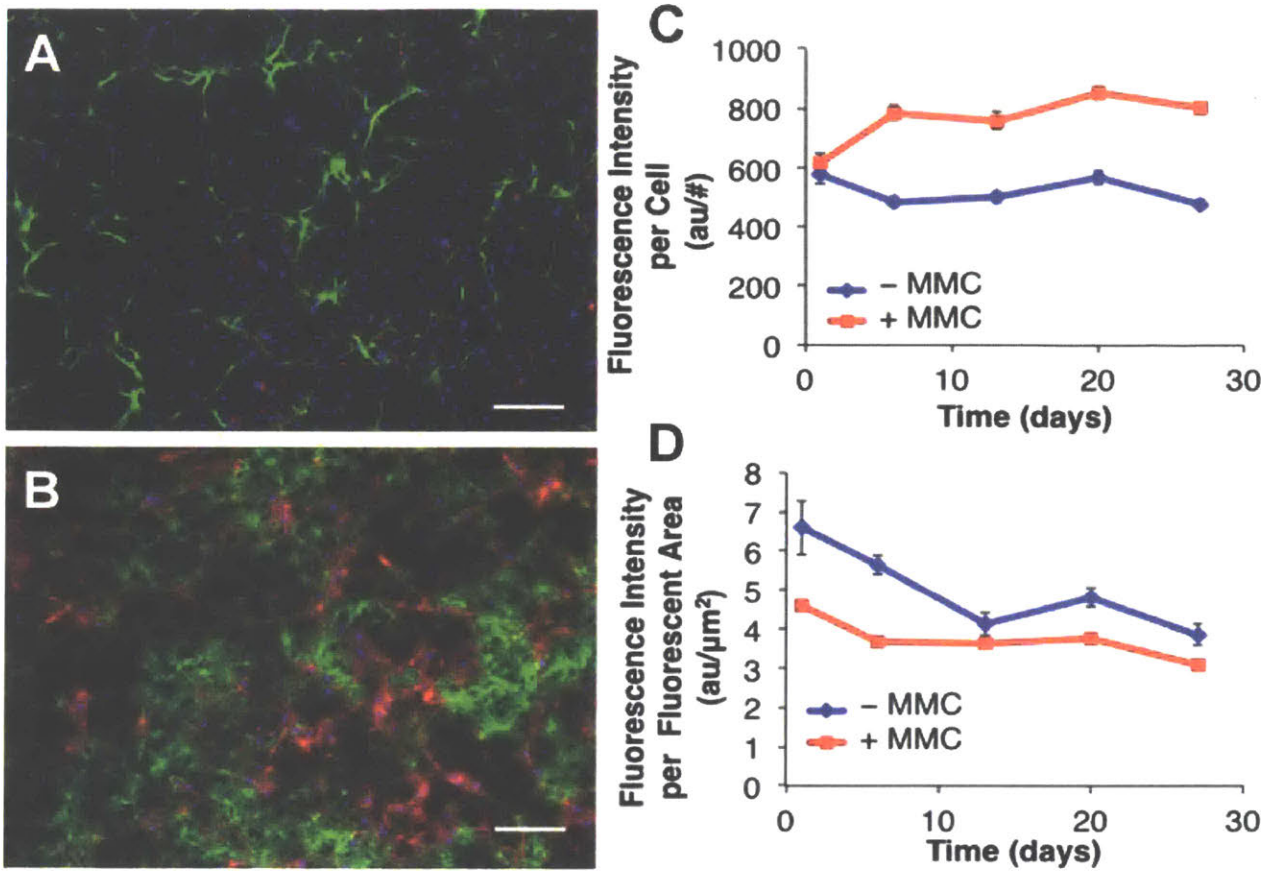

Figure 2-2. Effects of MMC on amount and distribution of VEC-secreted collagen-IV matrix. VECs cultured (A) without; and (B) with 62.5 mg/mL of Ficoll-based MMC nanoparticles exhibited distinct visual differences in collagen-IV (green), with cells visible by nuclei (blue) and F-actin cytoskeleton (red). (C) The amount of collagen-IV secreted per cell was greater in +MMC media over several weeks; and (D) the areal intensity of that coverage was lower in +MMC media due to the greater dispersion of that matrix network. Scale bars represent 100μm. Error bars represent standard error of measurement (SEM).

2.4.2 ECM fiber alignment

Relative alignment of the collagen IV fibers within this ECM was also evaluated. Alignment, or average angular standard deviation $\langle\alpha_{SD}\rangle$, provides an objective metric for ECM organization that does not depend on the orientation of the fibers with respect to the arbitrary image orientation. A lower $\langle\alpha_{SD}\rangle$ represents a more highly aligned network. Figure 2-3 shows that MMC promoted collagen network alignment within one week one ($p<5 \times 10^{-4}$), with $\langle\alpha_{SD}\rangle$ decreasing by ~50% with respect to the "uncrowded" dilute solutions of typical *in vitro* culture of VECs. As an alternative representation, inlaid corresponding histograms exhibited approximately normal distributions of relative matrix filament angle, with clearly narrowed dispersion of that angular distribution for matrix produced in the presence of MMCs. These data

indicate that the diffuse fibers formed under crowded conditions are also more highly aligned. As this matrix is organized *in vitro* under conditions that approximate the fractional volume occupancy of proteins *in vivo* (17%), it is plausible that this ECM organization may be indicative of the native structure of the basement membrane *in vivo*.

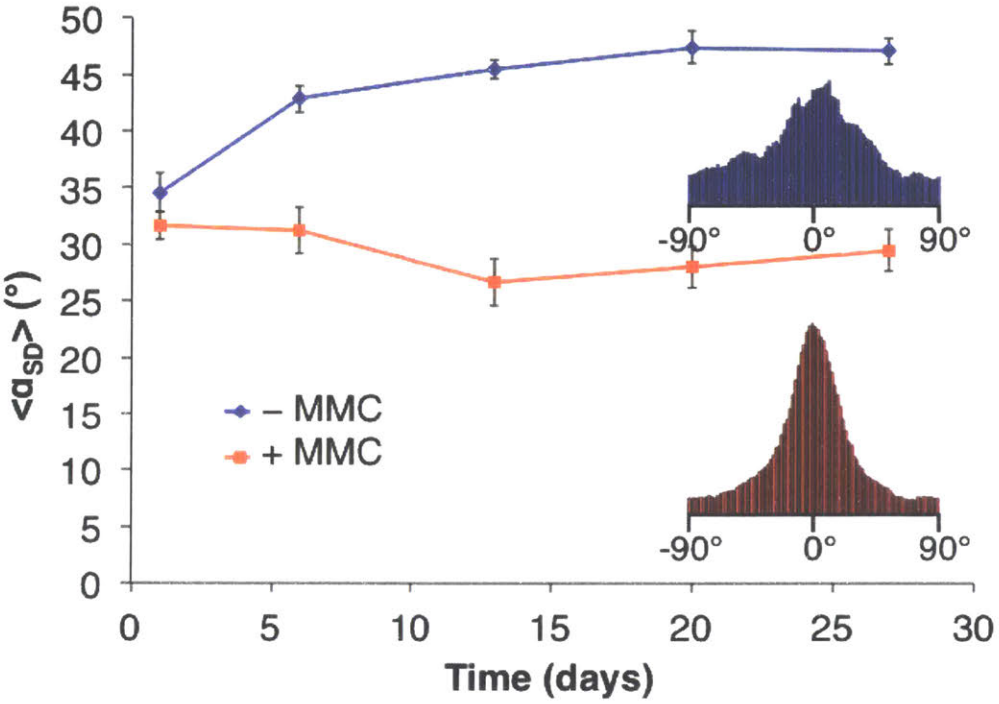

Figure 2-3. Macromolecular crowding of the extracellular fluid promotes alignment of the extracellular matrix. Average angular standard deviation $\langle\alpha_{SD}\rangle$ is lower for collagen-IV produced by VECs in the presence of MMCs within one week, and remains so for several weeks. Error bars represent SEM.

2.4.3 Effects of seeding density

To ascertain when this significant difference in matrix deposition and alignment emerged within the first week, this experiment was repeated at shorter time intervals. This understanding is required to identify temporal windows available to intervene in cases when matrix formation promotion may be desirable, as in the context of dysregulated wound healing. Separately, considerations of how the initial cell seeding density may affect this temporal response aids in understanding how disrupted vessels at wound or angiogenic sites may form structurally distinct ECM. Thus, adsorbed collagen-IV areal distribution (Fig. 2-4E) and filament alignment (Fig. 2-4F) were evaluated over the first 7 days, and two initial seeding densities were considered (lower, at 200 VECs/mm^2) and higher (530 VECs/mm^2). Two comparisons are enabled by Fig. 2-2 to 2-4: the effects of initial cell seeding density, and the effects of MMC for a given cell seeding density.

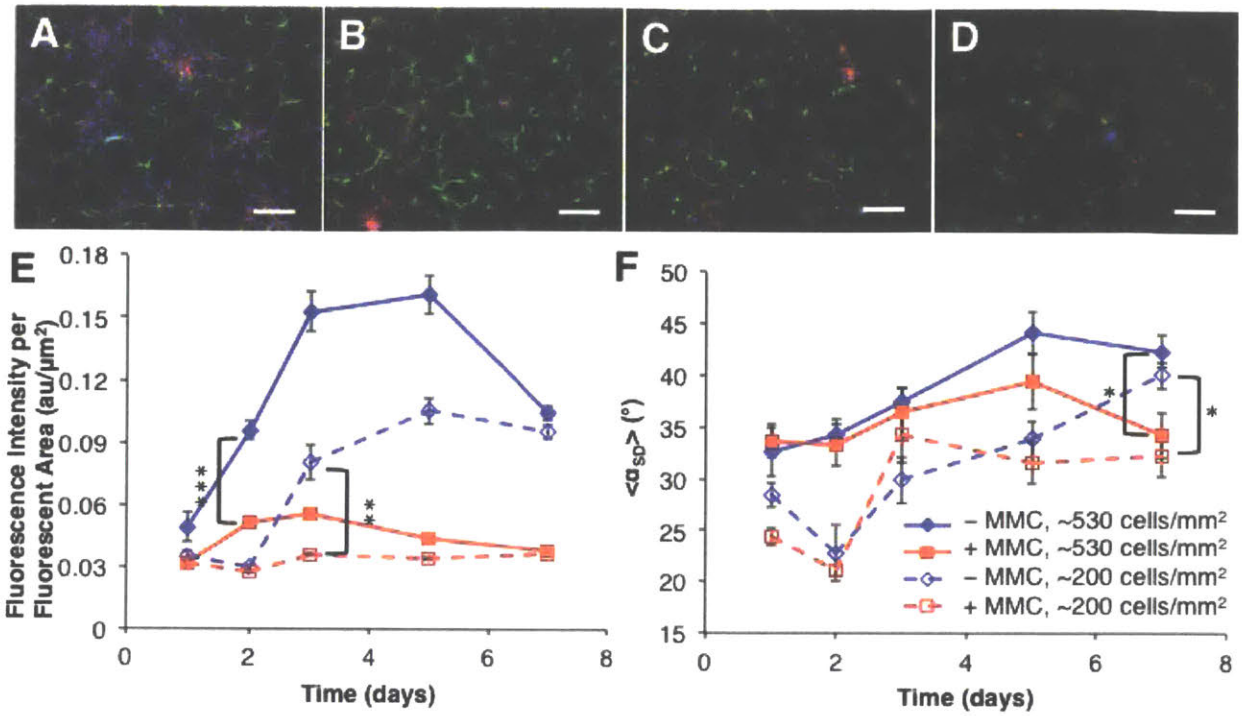

Figure 2-4. Effect of Cell Seeding Density on ECM Coverage and Alignment. (A) – (D): Fluorescent images of VECs at 2 days, without (A, C) and with (B, D) MMC in culture media. (A-B): VEC monolayers seeded at higher (~530 cells/mm^2) density; and (C-D): at lower density (200 cells/mm^2). (E) Average total fluorescence intensity for each condition normalized by fluorescent area. Solid and dashed lines represent higher and lower VEC seeding densities, respectively. (F) ECM alignment depends both on cell seeding density and macromolecular crowding by day 7. Square brackets indicate timepoints at which statistically significantly differences were observed as a function of MMC addition (** $p<0.0005$, *** $p<1x10^{-6}$). Error bars represent SEM.

Figure 2-4 E shows that this fluorescent area-normalized intensity was lower in the presence of MMC by day 2 for cells at higher seeding density, and by day 3 for cells at lower seeding density. By day 7, the effects of crowder on this matrix coverage were independent of the initial cell seeding density; this reflects in part that cell proliferation over that period rendered the final cells/mm^2 at day 7 indistinguishable. More importantly, this finding that the matrix was more uniformly spread among the VECs under crowded conditions (+MMC) was persistent up to day 7 for both cell seeding densities considered. (Note that fluorescence intensity maxima in Figs. 2-2D and 2-4E differ because these two experiments were performed independently and thus reflect differing exposure times, lamp intensities, and staining efficacy. However, relative trends over the first 7 days in these two independent experiments were comparable.) In contrast to these considerations of ECM amounts and areal densities, the effect of MMC on collagen fibril alignment was not significant until day 7 (Fig. 2-4F). This delayed observation of crowding-enhanced matrix alignment was independent of initial cell seeding density. This temporal analysis suggests that macromolecular crowding conditions for VECs promote self-

assembly of collagen-IV into aligned fibrils over the course of several days, at least for this MMC type and concentration. One would reasonably expect crowding-induced entropically driven alignment due to depletion forces to occur on faster time-scales than this (i.e., less than days). However, we speculate that our observations depart from this expectation for at least two reasons: (1) here, crowding of the ECM occurs with additional confinement between the cell basal surface and glass; and (2) the cell-secreted ECM proteins are of increasing but unquantified concentration over this duration, and crowding-induced alignment depends strongly on relative concentrations of MMC and ECM protein. Further, Fig. 4F shows that VECs seeded at lower cell density exhibit more aligned networks under crowding, as compared to those with initially greater cells per unit growth area.

2.4.4. Effects of pericyte-conditioned media

Finally, as noted in Fig. 2-1, macromolecular crowding competes with additional cues that may also affect the amount and organization of ECM. Another cue of interest in the microvasculature is potential paracrine signaling by pericytes that encircle and stabilize microvessels [151]. To consider whether pericyte-conditioned media (PCM) could also modulate the amount, distribution, or alignment of collagen-IV, we separately characterized the fibril alignment over 1 week. We considered both lower (10%) and higher (50%) concentrations of PCM within the media, in either the presence or absence of MMCs at 17% volume occupancy. Various concentrations were added to the basal culture media in addition to MMC media. The concentrations of PCM did not appear to affect the organization of the ECM. Figure 2-5 shows that PCM did not affect ECM fibril alignment at any PCM concentration considered. From this we infer that the presence of PCM in the crowded media did not interfere noticeably with crowding-induced collagen alignment. Addition of PCM also did not affect the amount or areal distribution of collagen under crowded or normal "dilute" media conditions (data not shown).

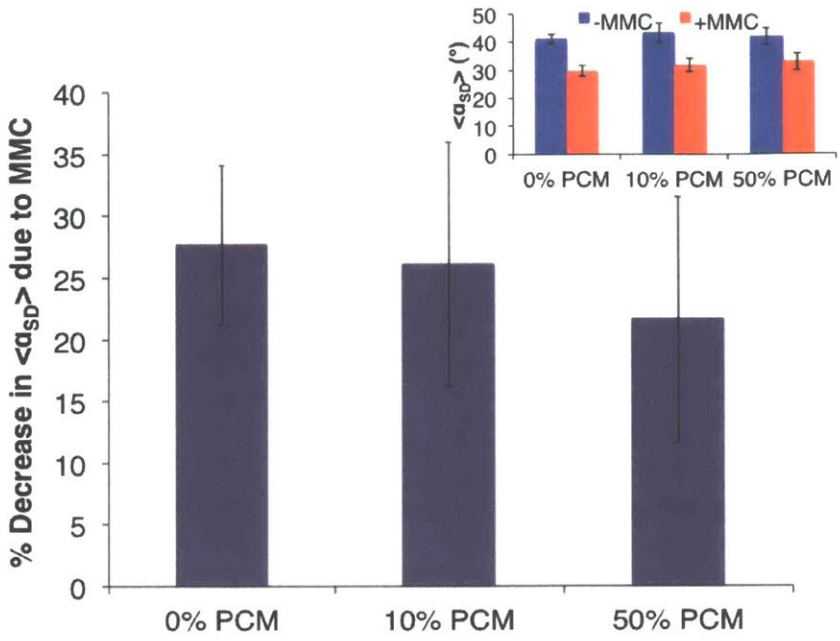

Figure 2-5. Effects of pericyte-conditioned media (PCM) on Collagen Alignment. Average angular standard deviation is unaffected by PCM at all concentrations, and MMC-induced alignment effects are retained. Inset: $\langle a_{SD} \rangle$ for +MMC (red) and –MMC (blue). Error bars are SEM.

2.5 Conclusions

Macromolecular crowding strongly modulates the amount and organization of collagen matrix networks produced by vascular endothelial cells *in vitro*. The speed of crowding-induced alignment depends in part on the local cell density, occurring over several days and then persisting over several weeks. This striking contrast in the organization of an extracellular structural network may directly modulate the number and collective strength of adhesive contacts between the VECs and the extracellular environment, with subsequent consequences for cell response that relate to angiogenic events. The present findings establish the capacity to tune these matrix structural parameters through facile addition of nanoscale neutral macromolecular particles to *in vitro* media solutions. For other cell types such as mesenchymal stromal cells (MSCs), the addition of MMC increased the effective ECM and cell stiffness, increasedd cell proliferation, and decreased cell migration [64,68]. In these studies, the changes in ECM deposition and alignment occur in the absence of cells suggesting that these changes in cell behavior may not be cell-type dependent. Thus, MMC could play a role in modulating VEC behavior and phenotype. Such biophysical manipulation of the cell culture environment can serve as a laboratory tool both to mimic *in vivo* crowding levels and to manipulate extracellular matrix structure.

Chapter 3

Static mechanical strain induces vascular endothelial cell cycle re-entry and sprouting

In Chapter 1, we described the importance of angiogenesis and angiocrine signaling in supporting hematopoietic recovery *in vivo*. In Chapter 2, we considered how the biophysical cue of macromolecular crowding alters the kinetics and deposition of basement membrane of vascular endothelial cells (VECs). To further understand how the angiogenic process is regulated, in Chapter 3, we explore how static, mechanical strain can promote angiogenic sprouting. Pericytes can exert contractile forces on the basement membrane or endothelial layer lining blood vessels, which results in a hoop strain around the circumference of the vessel wall. To translate this into a 2-D cultures system, we applied static, uniaxial strain to a confluent monolayer of VECs.

3.1 Acknowledgements

The work presented in this chapter is published as a full research article in Physical Biology [120]. *This study was a collaboration with Prof. Ira M. Herman and his post-doctoral researcher, Dr. Jennifer T. Durham. Dr Adam S. Zeiger was the primary author who initiated and pursued this study. Dr. Durham assisted with the initial design parameters of the quasi-3D sprouting assays. Frances D. Liu conducted replicate 2-D strain assays, further developed the quasi-3D assay, and executed and analyzed the results of the sprouting assay from confocal microscopy. Results on nuclear translocation of transcription factor p27kip1 are intentionally excluded from this thesis chapter as Liu did not participate in those studies. Prof. Krystyn J. Van Vliet and Liu were responsible for revisions and finalization of the work.*

3.2 Introduction

Microvascular endothelial cells (EC) are understood to respond to various extracellular mechanical cues. However, the role of sustained (static) mechanical tension to EC monolayers, as could be generated by adjacent cell types in the microvasculature, is less understood. For example, dynamic mechanical cues such as fluid shear stress [95,152,153] and cyclic strain from transmural or pulse pressure [122,124,127,154] have long been considered dynamic contributors to vascular cell (dys)function in larger vessels such as arteries and veins. Static tensile force and

strain [155–158] have also been shown to alter proliferation or migration of non-confluent EC cultures *in vitro*; however, such ECs are not in the growth-arrested state typical of the non-sprouting microvasculature. Other studies that include vessel fragments[155], multiple cell types, or *in vivo* implantation [159,160] suggest that either mechanical constraints to or cell-generated deformation of the extracellular matrix can modulate at least neovessel network formation; however, these approaches also obfuscate decoupling of mechanical cues from biochemical cues associated with inflammation, wound healing, and paracrine signaling. Thus, it has remained unclear whether and how well-controlled, simple strain states could induce a phenotypic transition in ECs to promote angiogenesis, the sprouting of new vessels from existing vasculature. In particular, it remains unknown how the static strains that have been reported to be generated by contractile microvascular pericytes may contribute to EC growth dynamics, including angiogenic sprouting from intact EC monolayers [151,161].

Pericytes are the predominant contractile cell type in microvessels, encircling venular and capillary ECs and communicating in close physical contact while embedded within the basement membrane [151,162]. Interactions between pericytes and associated EC are considered critical to microvasculature growth, stabilization, and survival, though most prior work has focused on biochemical aspects of this interaction [119,161]. Specifically, pericytes can inhibit vascular EC proliferation, foster microvascular stabilization and influence barrier function through cell contact- and paracrine mediator-dependent mechanisms [151,163]. These cells express cytoskeletal and contractile proteins [164]; and mechanical contraction by these cells has been quantified [119] and linked to the RhoGTPase effector pathway [163,165]. We have shown previously that pericytes can exert a sustained contractile force that results in the mechanical deformation of extracellular materials [119,151,163]; this mechanical cue can stiffen the basement membrane [119] and can presumably be transferred to adjacent ECs. Such contractile force *in vivo* may result in an effective tensile strain on adjacent ECs located distal to the pericytes surrounding the microvessel walls [119].

Interest in this potential for mechanical modulation of EC monolayers is twofold. First, understanding how and when a cue such as static extracellular tension is transduced to a cell response within EC monolayers informs our framework for physical biology of strain-induced cell cycle reentry and angiogenesis. Second, such findings can inform the debate of pericytes' role in vascular pathologies. Previous research has shown that the loss of pericytes, or "pericyte drop-out," is correlative with proliferative diabetic retinopathy [166–169]. However, other work suggests pericyte dysfunction – rather than death or loss – represents an early, initiating event in microvascular destabilization and pathological angiogenic activation [151,170]. Moreover, we have shown via *in vitro* co-culture that molecular manipulation, which increased pericyte contractility correlated with loss of EC quiescence [165,171], and can also promote angiogenic activation and microvascular sprouting [171]. To our knowledge, approaches have not been established to test the capacity for this isolated cue – sustained mechanical strain such as that generated by pericytes – to modulate capillary EC monolayer growth dynamics or angiogenic

switching. Here, we demonstrate that static uniaxial strain, of magnitudes shown previously to be exerted by microvascular pericytes [163], is sufficient to induce S-phase re-entry in confluent and growth-arrested capillary-derived EC monolayers within 15 minutes post-strain. We further show that this static mechanical strain is sufficient to induce angiogenic sprouting *in vitro*. These results indicate that mechanical deformation such as that initiated by pericyte contraction can signal EC cell cycle re-entry and potentially pathological angiogenic re-activation.

3.3 Materials and Methods

3.3.1 Preparation of PDMS molds

To construct PDMS multi-well molds, lids of 48-well tissue culture polystyrene plates (#677180, Greiner Bio-One) were lined with parafilm (Bemis, Neenah, WI); the lid served simply as a template on which to construct molds of precise position and spacing. Sixteen 1.25 cm-diameter mosaic mirrors (SKU8224, KitKraft, Studio City, CA) were adhered to parafilm using ethyl cyanoacrylate-based epoxy (Pacer Technology, Rancho Cucamonga, CA) to match the inscribed patterns in the four rows and columns in the center of multi-well tissue culture polystyrene lids (#677180, Greiner Bio-One). These mirrors served as a negative template or mold for a sixteen well-plate. After allowing the adhesive to cure for 15 minutes at room temperature, mirrors were gently wiped clean with Kimwipes (Kimberly-Clark, Roswell, GA) soaked in ethanol. Chemically curable PDMS (Sylgard 184, Dow Corning Corporation) was prepared at a weight ratio of 20:1 base to curing agent and stirred vigorously for 3 min. Mixed silicone of 25 mL volume was added to each of the prepared sixteen well-molds and allowed to spread under 0.08-0.09 MPa of vacuum pressure in a vacuum oven for 30-60 min to degas and remove air bubbles. After removing all air bubbles, vacuum was released and the PDMS was then cured at 45°C for 24-48 hours. After baking, molds were soaked in acetone at room temperature for 24 hours to remove any uncrosslinked PDMS, a modified version of the methods outlined by Vicker's et al. [172]. Molds were then placed in an oven for ~24 hours to evaporate and dry the acetone from the PDMS molds. PDMS molds were then sterilized for with ethanol and allowed to dry under UV light. After sterilization and drying, the surface of the PDMS mold was then plasma oxidized (handheld corona device #12051A-10, Electro-Technic Products, Inc., Chicago, IL) for 60 sec per mold, ensuring as uniform exposure to each well as possible. Such treatment allowed for the creation of hydrophilic PDMS for tissue culture (TC-PDMS) that retained hydrophilicity for at least 1 day in air and 14 days in fluids such as PBS or cell culture media. Note that cells can be seeded directly in these molded wells without the requirement of additional extracellular matrix proteins or surface functionalization chemistries [173]; this minimizes the potential for biased influence of exogenous adsorbed ECM proteins on cellular morphology or Src kinase and Rho GTPase activation [174].

3.3.2 Vascular endothelial cell culture and strain application

Capillary endothelial cells (ECs) were isolated from mammalian bovine retinas, similar to the isolation of pericytes outlined previously [164]. Cells were expanded until passage 12-15 and seeded onto prepared TC-PDMS molds, just after corona treatment, in Dulbecco's modified Eagle's Medium (DMEM) supplemented with 10% Bovine Calf Serum (BCS; #C8056, Sigma). Prior to cell seeding, the PDMS device was clamped at either end of a customized external strain device (Fig. 3-1 A), and extended manually with a micrometer to remove slack from the molded PDMS sheet and ensure that subsequent displacement of one end of the PDMS device would result in material strain within the PDMS molds. We refer to this as the clamped, unstrained configuration. Cells from post-confluent monolayers were trypsinized and then seeded onto these clamped, unstrained PDMS substrata. ECs were seeded at approximately 10^5 cells/cm^2 to ensure formation of a confluent monolayer within < 24 h, and maintained in growth medium (10% BCS in DMEM), at 5% CO_2 and 37°C. After visual verification of a monolayer, cells were then serum starved by exchanging the growth medium with reduced serum medium, 0.5% BCS in DMEM. Serum depletion facilitated growth arrest and cell cycle synchronization of the confluent monolayer within each well. After 24 h of serum starvation, tensile strain of the TC-PDMS substratum of each cell-seeded well was generated the by applying 10% increase in the length of the clamped TC-PDMS device. Cell response was monitored at constant (static) applied engineering strain of 10% for 15 min, 90 min, and 4 h, and cells were fixed (under strain) and stained (upon removal of strain) for subsequent analysis. These time points were selected to identify the earliest time point by which the strain cue resulted in statistically significant changes in cell cycle response, and 15 min was considered the earliest possible time point via the method of EdU incorporation. The two later time points then verified whether the system (cells and/or extracellular materials) significantly relaxed and mitigated a response to this mechanical cue on the timescale of hours. Each mold comprised 16 replicate wells per condition, as defined by strain magnitude and duration; Fig. 3-1 H comprises data from 12 such independent experiments.

3.3.3 Immunocytochemistry

To determine whether strain induced entry into S-phase of the cell cycle, an EdU assay was conducted (Click-iT® EdU Alexa Fluor 488 Imaging Kit, C10337, Molecular Probes). Briefly, cells were incubated for 90 min or 4 h at 37°C and 5% CO_2 with 5-ethynyl-2-deoxyuridine (EdU). For strain assays of 15 min duration that included EdU, cells were pre-incubated with EdU for 1 h before replacement with full media (10% BCS) and immediate application of strain. Cells were then fixed using 4% formaldehyde (#43368 AlfaAesar Ward Hill, MA) in PBS for 15 min at room temperature. Following fixation, cells were washed briefly with PBS, and permeabilized for 3 min at room temperature with 0.1% Triton X-100 (Fluka 93443, Switzerland). Cells were rinsed twice with 3% BSA and incubated for 30 min with the EdU Click-iT reaction cocktail, including the Alexa Fluor azide, as described by the manufacturer. Cells were washed three times (10 min each) with PBS and imaged by

fluorescence microscopy (IX-81, Olympus America, Inc.) and captured using Slidebook 5.0 (Intelligent Imaging Innovations, Inc. Denver, CO). Cell nuclei were also counterstained with 4',6-diamidino-2-phenylindole (DAPI) (Millipore 90229, 1:2000) before imaging. The fraction of cells in DNA synthesis, or S-phase, was characterized for each condition.

3.3.4 Sprouting assay

ECs were seeded onto TC-PDMS substrata at post-confluent densities, as described above. After 24 h post-seeding, the EC monolayer was serum depleted for an additional 24 h by removing the 10% BCS growth media and adding DMEM with 0.5% BCS. After serum depletion for 24 h, protein solutions in reduced serum media (0.5% BCS) were added to form a gel atop the cell monolayer. Monolayer stability was promoted by addition of 100 uL of 0.5% BCS in DMEM containing 3 μg/mL Collagen Type-I (Rat Tail BD Biosciences #354236) to each well and incubated at 37°C for 30 min. The collagen solution was carefully aspirated before the addition of 150 uL of a mixture that comprised 50 vol% Growth Factor Reduced Matrigel™ Matrix (BD Biosciences #354230), 16 vol% Collagen Type-I (Rat Tail BD Biosciences #354236), 4 vol% FITC-conjugated Collagen Type-I (AnaSpec #85111), and 30 vol% 0.5% BCS in DMEM. After 2 h of gelation, 100 uL of 10% BCS DMEM was added to each well. Either 0% or 10% uniaxial static strain was applied to the TC-PDMS devices and over 48 h under otherwise identical incubator conditions. After 48 h, gels were carefully fixed using a 2% paraformaldyhde:1% glutaraldehyde solution for 20 min. Gels were rinsed in 150 mM NaCl PBS (hereafter, PBS) before the addition of 0.1% Triton X-100 for permeabilization for 15 min. Gels were again rinsed in PBS before DAPI nuclear counterstaining and Alexa-Fluor 594 phalloidin (Life Technologies #A12381) in 3% bovine serum albumin in PBS. Gels were then rinsed twice in PBS before imaging. The number of sprouts and number of cells within each well was quantified using fluorescence microscopy (IX-81, Olympus America, Inc.) and captured using Slidebook 5.0 (Intelligent Imaging Innovations, Inc. Denver, CO). To visualize the sprouts in 3D, the sprouts in gels were taken to be imaged using confocal microscopy (Olympus FV-100, Olympus America, Inc.). The 3D stacks were then rendered using Fiji (or ImageJ, NIH).

3.4 Results and Discussion

3.4.1 Static strain-induce cell-cycle re-entry

To address whether mechanical strain consistent with pericyte contraction could influence endothelial growth and anigogenic activation, we designed and fabricated a device (Fig. 3-1 A) that applies uniform, uniaxial strain of duration and magnitude consistent with that measured previously for contractile pericytes [119]; see Methods for further details. This approach – by which cells adhere to hydrophilic, optically transparent, tissue-culture

polydimethylsiloxane multi-well membranes (TC-PDMS) – permits live imaging during strain, immunocytochemical characterization, and isolation of mechanical cues from other potential EC stimuli. Importantly, this approach also enables application of mechanical tension to EC in the absence of pericytes (or other cell types), and thus facilitates analysis of this mechanical deformation or strain in the absence of several competing factors possible in co-culture models (e.g., pericyte-secreted factors, EC-pericyte contact, ECM remodeling). To these ends, we seeded EC at post-confluent densities to achieve a growth-arrested population upon cell- and substratum-dependent contact (~10^5 cells/cm^2). We then applied a static, sustained tensile strain comparable to pericyte-generated deformation that has been quantified directly *in vitro* [119]. At the initiation of each experiment, the growth-arrest and post-confluent nature of the microvascular EC populations were confirmed via live cell and fluorescence imaging of cortical actin, collagen-IV [111] and VE-cadherin [174] (Fig. 3-1 B-D); previous studies have shown that EC growth inhibition and cell cycle arrest are induced by cell-cell contact [175]. Serum depletion 24 h post-plating promoted growth-arrest and cell cycle exit prior to the initiation of strain. Concomitant with strain induction, ECs were subjected to a media replacement and pulse-labeling with 5-ethynyl-2′-deoxyuridine (EdU); unstrained EC monolayers were prepared and manipulated identically and served as controls. As shown in Fig. 3-1, application of static strain rapidly induced a quantifiable and reproducible increase in endothelial S-phase entry, observed as a significant elevation in nuclear EdU incorporation (Fig. 3-1 E-G, $p < 0.001$). This shift occurred within 15 min post-strain and persisted over all strain durations considered ($n = 12$ independent experiments, with $N = 16$ wells per condition in each trial). For example, by 15 min post-strain, S-phase entry increased approximately three-fold, representing ~20% of the EC population. It should be noted that these results are for growth-arrested confluent ECs, and that subconfluent ECs absent of significant cell-cell contact did not exhibit such increases in post-strain endothelial S-phase entry.

Our finding that a modest (10%) static tensile strain can stimulate S-phase entry in microvascular ECs is consistent with recent studies demonstrating that non-physiologic, static strains of 40% could enhance 5-Bromo-2'-deoxyuridine (BrdU) incorporation in bovine pulmonary aortic ECs after 24 h; whether confluence was attained before strain application was not stated [174]. Our demonstration of EC S-phase entry within minutes following application of static uniaxial strain also aligns well with Xiong et al.'s recent finding that human umbilical vein and arterial ECs secreted Weibel-Palade bodies (WPBs) within 15 min post-equibiaxial strains of 20-50% (equal strain in both x- and y-directions) [129]. Further, Suzuma et al. noted that straining retinal microvascular ECs induced rapid ERK phosphorylation and mRNA expression of vascular endothelial growth factor receptor-2 [176,177]. To our knowledge this is the first direct demonstration that the application of static tensile strain induces endothelial S-phase re-entry in previously growth-arrested EC monolayers.

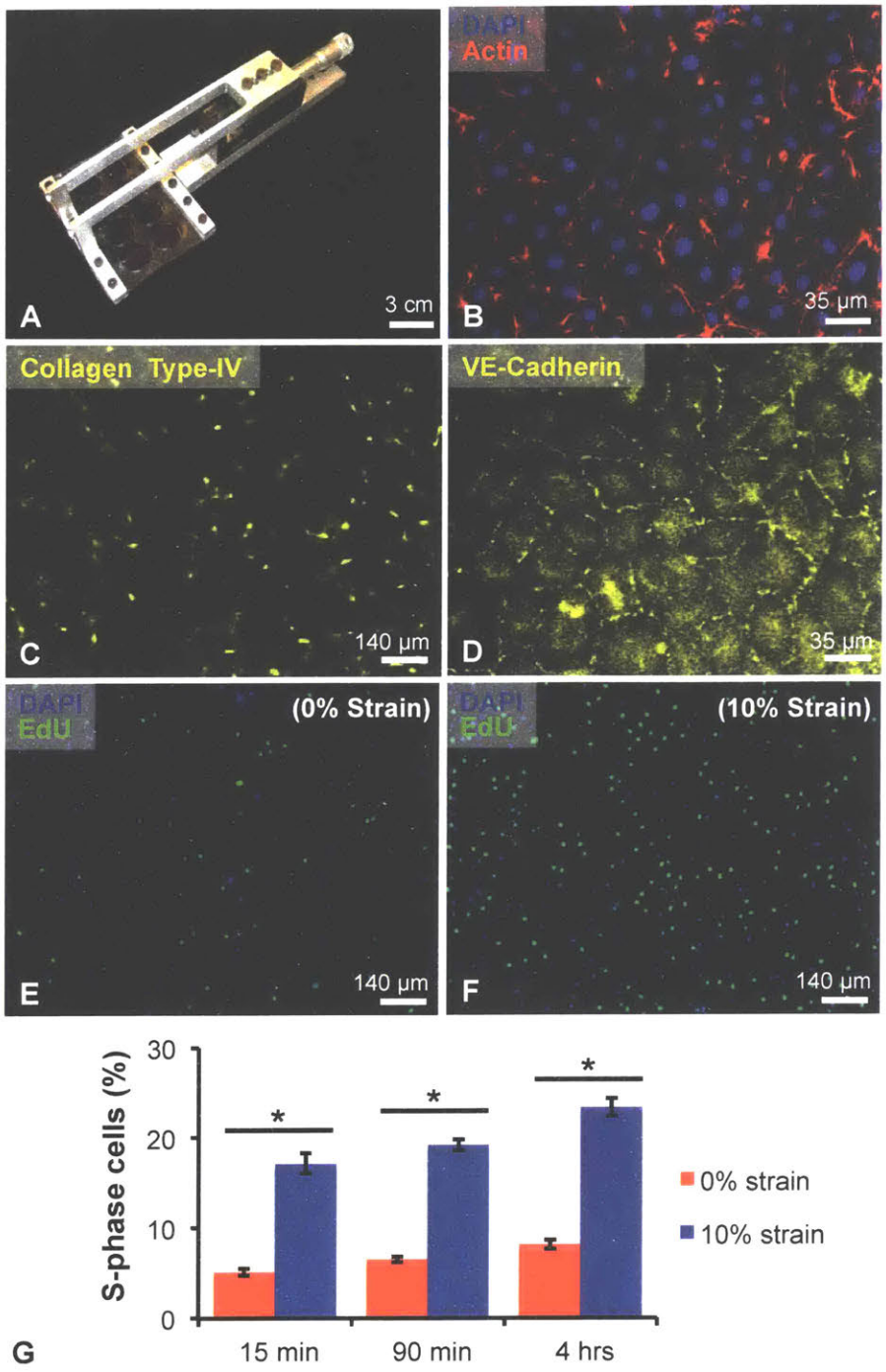

Figure 3-1. Static strain induces S-phase entry in quiescent retinal microvascular endothelial cells (ECs). (*A*) Multi-well elastomeric uniaxial strain device. (*B*) Bovine retinal ECs labeled nucleus via DAPI (blue) and F-actin via phalloidin (red). Antibody-stained ECs for (*C*) VE-cadherin confirmed confluence prior to strain application. (*D*) Type-IV collagen, an anticipated extracellular matrix component of ECs, visualized via antibody labeling. (*E-F*) 5-ethynyl-2′-deoxyuridine (EdU, green) incorporation and nucleus labeling via DAPI (blue) for control condition of (*E*) 0% strain and (*F*) 10% uniaxially strained EC monolayers. (*G*) Quantification of percent cells in S-phase after 15 min, 90 min, and 4 h. Values reported as mean ± standard error of measurement; * indicates statistically significant difference ($p < 0.001$).

3.4.2. Endothelial cell sprouting in a quasi-3D model

Strain-stimulated cell cycle progression is necessary but insufficient to demonstrate re-proliferation or angiogenic activation. To consider whether this static strain was also sufficient to induce angiogenic activation or "switching" in the absence of the pericytes, we applied 10% static strain to post-confluent EC monolayers within model ECM gels. In these assays, growth-factor reduced Matrigel provided a commonly used basement membrane analogue or extracellular matrix into which cells could extend from the monolayer, and this additional potential for biochemical cues was maintained constant in paired control experiments for which no strain was applied. Evidence of sprouting was quantified at 48 h for both post-strained and unstrained controls, via confocal microscopy following fixation and staining with nuclear- and cytoskeletal-specific markers. This strain resulted in 40% more sprouts from the post-confluent EC monolayer (Fig. 3-2 A-C), with a statistically significant increase compared with unstrained controls ($p = 0.0005$). This relative enhancement of sprouting in the strained wells is notable in that any increase in sprouting from the post-confluent EC monolayer can be attributed chiefly to the applied mechanical strain. Biochemical cues may also play a synergistic role in promoting sprouting due to the required use of extracellular matrix-based gels containing low but finite growth factor, but are kept constant across strained and unstrained conditions. Figure 3-2 D shows a representative image of sprouting cells from one of three replicate experiments (each with $N \geq 10$ wells per strained and unstrained condition).

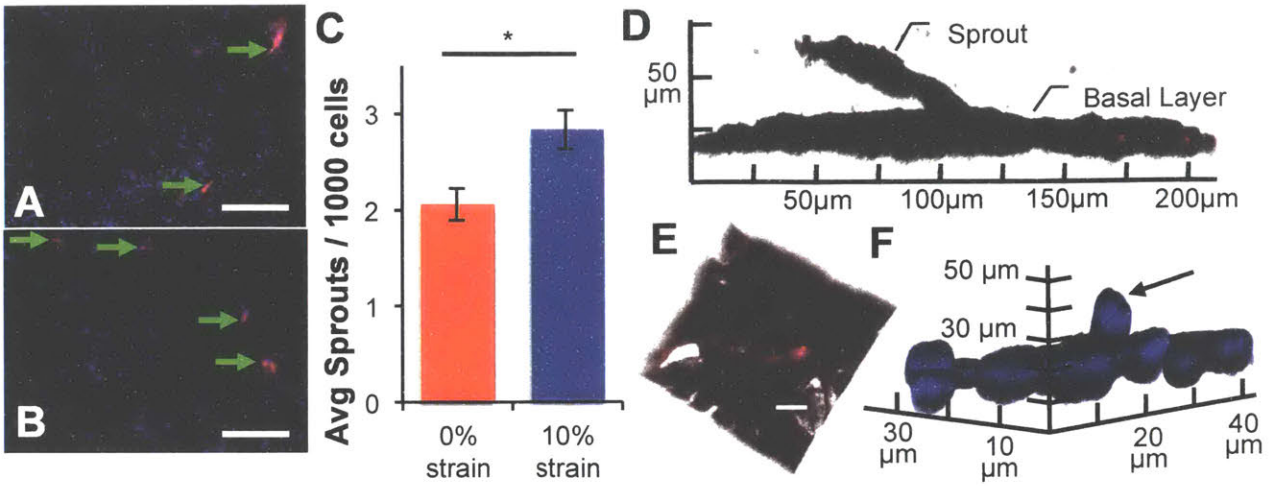

Figure 3-2. Static strain induces sprouting in capillary endothelial-derived monolayers. (*A-B*) Representative images of ECs demonstrate qualitatively increased sprouting into an overlying gel, after the application of (*B*) 10% uniaxial static strain as compared to (*A*) unstrained controls. (*C*) Quantification of sprouting images demonstrate a statistically significant increase in the average number of sprouts per 1000 DAPI-stained EC nuclei after 48 h of 10% static strain (* indicates significant difference, $p = 0.005$). Values reported as mean ± standard error of measurement. (*D-F*) Confocal renderings illustrating individual, out-of-plane sprout extension, visualized via *(D)* phalloidin-stained F-actin, *(E)* and composite with DAPI-stained nuclei show cellular process from sprouting tip cells extending into the gel; scale bar = 20 µm. *(F)* Out-of-plane nuclei can be seen extending from the monolayer (arrow) visualized with DAPI-stained nuclei and omission of actin for clarity.

The characteristic branched morphology of sprout-leading tip cells was noted consistently in strained conditions (Fig. 3-2 A-B, arrows), and confocal x-z analysis was conducted to confirm that ECs extended from the original growth substratum. Figure 3-2 D-E and Figure 3-3 A-B show endothelial sprouts that extended many cell lengths from the original, post-confluent EC monolayer; the most distant cells along that sprout exhibited protrusions often associated with angiogenic tip cells (Fig. 3-2 D-E). Nuclei were observed out-of-plane of the monolayer, suggesting that entire cells had begun to sprout upwards (Fig. 3-2 F). Renderings of data collected in z-stacks and as movies featuring 3D-rotation confirmed these observations: continuous and connected fluorescent signals track cells from the post-confluent monolayer along the sprout lengths (Supp. Movies S1 and S2 included in the last page of the chapter). In both z-stacks, a continuous signal was indicated in all z-planes, i.e., cells extended from the monolayer. These findings suggest that modest, static strain is sufficient to promote EC sprouting and angiogenic activation *in vitro*.

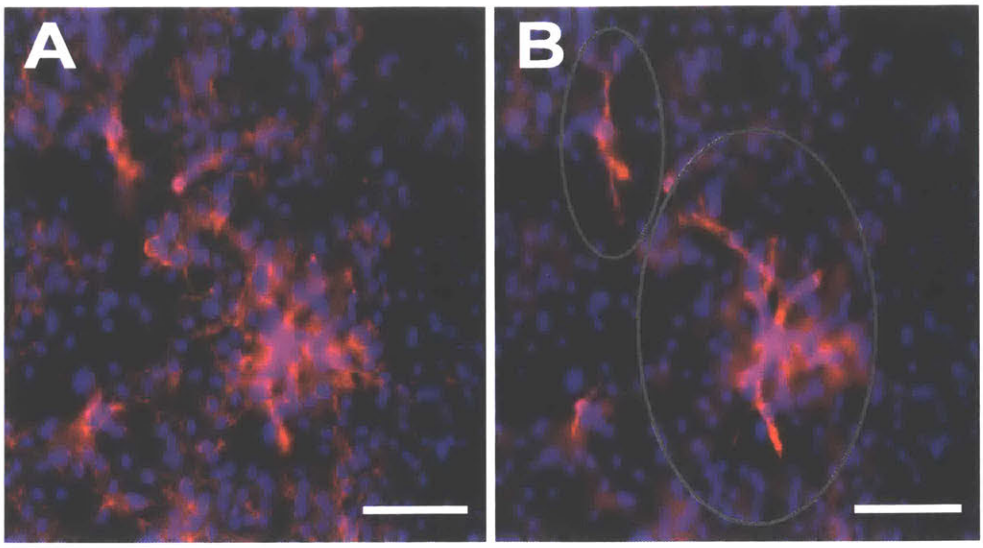

Figure 3-3. Imaging of sprouting assays. *(A-D)*, Bovine retinal ECs, with fluorescent cell nuclei (blue, DAPI) and F-actin (red, Alexa-Fluor 594-labeled phalloidin). *(A-B),* Epifluorescent imaging was used to quantify number of sprouts, defined by *(B),* out of plane cellular sprouts (outlines in grey circles) extending from and contiguous with the *(A)*, underlying cell monolayer (scale bar = 100 μm).

Angiogenesis is characterized fully by lumen-containing tube structures formed by the endothelial cells. Although we observed continuity of the multi-cell extensions from the strained monolayers, full confirmation of a patent lumen was not possible at such early sprouting timepoints. For 3D culture systems similar to our own, *in vitro* sprouting orthogonal to isolated endothelial cell monolayers typically requires longer time scales with patent lumen formation only observed after many days in culture [178–180]. However, we have previously demonstrated lumen formation in the same cell type [180], suggesting that our sprout-like structures may form observable lumens at longer time scales. In contrast, rapid formation of capillary-like structures with lumen containing regions has been demonstrated previously to occur within 2 days for purified ECs on top of (rather than within) Matrigel [181], or for more complex tissue explants [178,182]. Most studies that observe lumen-containing capillary structures use bioactive or exogeneous factors in order to induce, expedite, and stabilize angiogenic sprouting [178–182]. In order to decouple mechanical from chemical cues, we minimized exogeneous factors other than those contained in the Matrigel, and focused on independent effects of strain on early sprouting events including stable displacement of the tip cell and following cells from the intact VEC monolayer.

3.5 Conclusions

Initial vessel destabilization is generally attributed to a disrupted balance among several biochemical cues, including those derived from vascular and non-vascular cells. These include but are not limited to growth and survival factor (and cognate receptor) expression/release, protease activation/expression or cell-matrix receptor dynamics [183,184], which may coordinate angiogenic activation and microvascular morphogenesis. Indeed, we observe EC cell cycle re-entry and response to static strains consistent with that generated by capillary pericytes [119]. Our study is in agreement with previous *ex vivo* studies of whole vessels (arterial trunks and carotid arteries) demonstrating that excised capillaries and microvessels could be driven into proliferative states via uniaxial extension [185]. In other microvascular or macrovessel contexts, strain could be generated by other nearby non-vascular or vascular cell types such as fibroblasts or vascular smooth muscle cells [158–160], and others have shown that induced injuries *in vivo* can result in both interstitial fibroblasts contraction of gels and modulation of neovascularization [159,160]. However, in the context of microvascular remodeling and angiogenic activation considered here, pericytes do play a predominant role. The perivascular location of contractile pericytes that encircle the capillary presents the potential for cell-generated force to exert an effective tensile (hoop) strain on those ECs that are in close proximity or direct contact within the basement membrane [119]. Separately, unstrained co-cultures of ECs and pericytes within collagen gel punch-wound assays have demonstrated that increased pericyte contractility (via molecular manipulation of the myosin phosphatase RhoGTPase interacting protein) correlated with increased EC sprouting [171]. Durham et al. also showed that an increased number of heterotypic gap junctions between ECs and pericytes in co-culture does not in itself promote angiogenic sprouting [186]. This suggests that pro-angiogenic EC responses can be mediated by cell contact-dependent and soluble mechanisms, as well as by strain generated by adjacent cells such as contractile pericytes. Of course, it remains an important topic of future study whether and to what extent pericyte-generated strain may modulate angiogenic switching via cell-cell contact, non-vascular or vascular cell-cell type crosstalk, or release of angiogenic effectors from contractile pericytes and/or strained ECs. The present data suggest that pericyte contractility, reversal of endothelial growth arrest, and angiogenic activation are chemomechanically coupled.

Our results are distinct from and complement previous *in vitro* and *in vivo* studies, which have focused either on non-confluent (i.e., proliferating and migrating) ECs or in more complex *in vivo* settings. For example, static strain has been shown to alter extracellular matrix (ECM) organization and, thus, direct cell migration through contact guidance-dependent mechanisms [156–158], although it has been debated whether cells align in parallel [156,158] or are perpendicular [157] to the applied strain. Krishnan et al. inserted microvessel fragments (with ECs and perivascular cells) within gels and then applied strain *in vitro*; they found that neither applied static or cyclic strain of a lower magnitude (6%) than considered herein (10%) promoted a statistically significant increase in the number of vessels compared to unstrained constructs end-clamped in the same manner [155]. Boerkel et al. and Kilarski et al. reported *in vivo*

experiments of wound models that disrupted existing vasculature; neither study actively strained pre-encapsulated cells within the implanted gels. Boerkel et al. showed instead that propensity for vascular invasion into a gel depends on whether and how long a mechanical constraint (boundary condition) is imposed on the gels. Kilarski et al. showed that increased gel deformability (stiffness via varied gel composition) correlated with increased vascular invasion; the authors hypothesized that cell-mediated contraction (by fibroblasts) was necessary for vascular ingrowth and network remodeling, noting that they did not observe new sprouting. Such *in vivo* studies are interesting and interchangeably discuss "constraints" and "tension" as mediators of vascular remodeling, but were not designed to decouple mechanical cues from biochemical signals; the mechanical cues are not well-defined or controlled. Further, these previous studies have demonstrated increased cell alignment and in some cases, increased proliferation in response to constraints or strain, but none has shown the impact that straining a quiescent, post-confluent microvascular endothelial cell population can have on increasing or modulating angiogenic activation and sprouting dynamics. The simple strain state applied herein to confluent monolayers reflects the physiological stretch in microvessels. It is not intended to reflect further complexities such as distention or the fluid shear and cyclic deformation anticipated for larger vessels. This approach enables straightforward consideration of a key strain state anticipated in microvessels encircled by contractile cells such as pericytes.

We demonstrated that when mechanical strain applied to endothelial cells that are in a post-confluent and growth-arrested monolayer, ECs are activated and re-enter the cell cycle. This strain also promotes angiogenic activation and capillary-like endothelial sprouting. These findings that the isolated factor of static strain on post-confluent EC monolayers can induce such phenotypic changes also informs our understanding of pathological angiogenesis, such as that during diabetic retinopathy [187,188]. Pericyte loss is considered a hallmark of this condition, and pericyte dropout has been correlated with the onset of undesirable angiogenesis within the eye. However, our results suggest that pericyte contraction and attendant strain of the EC environment – rather than pericyte death or loss, and separately from any other pericyte signaling roles – can serve as an early mechanical cue that fosters re-activation of the endothelial cell cycle progression. Strain can be communicated to ECs via cell-generated contraction by pericytes in microvessels, and also by other contractile perivascular cell types such as vascular smooth muscle cells in more mature vessels. This mechanical form of an "angiogenic switch," due to contraction of nearby cells including but not limited to pericytes and independently of pulsatile fluid shear flow, prompts renewed consideration of how even modest and static mechanical strain can rapidly modulate EC growth dynamics and angiogenic status.

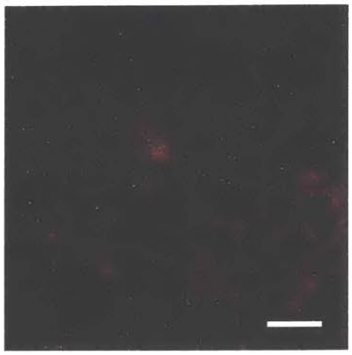

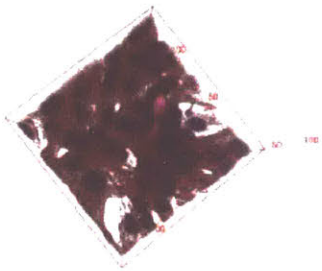

3DSproutingMovieStack.avi 3DSproutingMovieRotating.avi

Supporting movies S1-S2 | Confocal videos of capillary endothelial sprouts extending into overlaid gel. Animated z-stack (3DSproutingMovieStack.avi, Supp. Movie 1) and rendering of a sprout using 3D rotation (3DSproutingMovieRotating.avi, Supp. Movie 2) of a sprout shown in Supp. Figure 2. These movies are accessible by clicking on the movie snapshots above, which are hyperlinked to a dedicated Dropbox URL. Lateral scale bar shown = 20 μm, and the vertical z-stack extends up to 52.6 μm. These 3D renderings confirm the sprouted cells to be contiguous with the underlying monolayer. Sprout lengths included multiple cell lengths, e.g., 76.6 μm for the sprout indicated in Fig. 3D of the main text.

Supporting movie files can be accessed for review via direct Dropbox links, due to file size:

In this first movie, we observed a continuous signal in both the blue and red channels, which correspond with nuclei and actin cytoskeleton, respectively. This continuous signal suggested that cells are sprouting from the monolayer and not simply migrating out-of-plane.

3DSproutingMovieStack as .AVI (55MB) and .MP4 (1MB, lower resolution):

https://www.dropbox.com/s/x3nv5mjwbvbz7e8/3DSproutingMovieStack.avi?dl=0

https://www.dropbox.com/s/bqk58ypvd2d3x6n/3DSproutingMovieStack.mp4?dl=0

In this second movie, we observed nearly full coverage in the basal plane adjacent to the PDMS. This suggested that VECs were sprouting away from the quiescent monolayer and not simply forming spontaneous tube-like networks. Moreover, the z-axis extends beyond 50 μm, which is longer than a single cell length. In both movies, we also observed the presence of two out of plane nuclei, which suggests that it is a multi-cellular angiogenic sprout, and not extensions or processes of single cells.

3DSproutingMovieRotating as .AVI (142MB) and .MP4 (4MB, lower resolution):

https://www.dropbox.com/s/qrjctqfufzgo32j/3DSproutingMovieRotating.avi?dl=0

https://www.dropbox.com/s/ilpzahheeioiyc0/3DSproutingMovieRotating%20copy.mp4?dl=0

Chapter 4

Engineering the mesenchymal stromal cell secretome using viscoelastic properties of extracellular materials

In Chapters 2-3, we explored how the biophysical cue of macromolecular crowding and the mechanical cue of strain regulate angiogenesis *in vitro*. In addition to vascular endothelial cells, we also emphasized the importance of mesenchymal stromal cells (MSCs) in Chapter 1. As discussed in Chapter 1, MSCs support hematopoietic recovery through paracrine signaling. In Chapter 4, we explore how tuning the viscoelastic properties of the substratum material can regulate MSC paracrine signaling or the MSC secretome.

4.1 Acknowledgements

The work presented in this chapter is published as an original research article in ACS Biomaterials Science & Engineering [90]. *Frances D. Liu was responsible for design, execution, and analysis of the experiments discussed in this chapter. For thematic coherence, the section on hematopoietic stem and progenitor cell co-culture from that research article is located in Chapter 5.*

4.2 Introduction

Mesenchymal stem cells are a non-hematopoietic stem cell that can be obtained as a subset of bone marrow stromal cells [45]. As MSCs can be induced *in vitro* to differentiate along osteogenic, adipogenic, and chondrogenic lineages [46], these cells have long been considered for *in vitro* organoids or tissue-engineered constructs and for delivery for direct tissue repair [69,70]. These direct repair mechanisms would proceed *in vivo* presumably via MSC homing, engraftment, and differentiation into cell types required of the damaged tissue [189–192]. Indeed, most *in vitro* studies have focused on mechanical modulation of phenotypic lineage commitment, e.g., via population-level expression correlated with differentiation along at least one mesenchymal tissue cell lineage, as a function of elastic modulus or stiffness of the materials

to which the MSCs adhered [71,73,193–196]. However, *in vivo* studies of systemically administered MSCs have demonstrated repair following local injury due to thrombotic stroke [197,198], myocardial infarction [199–201], and bone marrow irradiation [202]. However, tissue repair can occur in some contexts even when MSC engraftment and differentiation are not detectable [202], and evidence for robust MSC differentiation at the injury sites remains a point of debate [202–206]. Such studies suggest that MSCs can play an important indirect repair role via paracrine signaling, through secretion of immunomodulatory and pro-angiogenic cytokines [72,89,207–213] to recruit and promote other cell types to repair the stroma of the injured tissue. Thus, there is growing interest in characterizing and manufacturing MSCs – in contrast to the progenitor or lineage-committed cells derived from MSCs – as a vehicle for indirect repair of bone marrow, neurological disorders, cardiovascular disease, liver failure, and immune disorders [206,207,211,214–220].

In our own work, we have exploited the indirect repair mechanisms of MSCs to support hematopoietic recovery *in vivo* [202]. MSCs constitute a heterogeneous population of cells, at least upon *in vitro* expansion conditions employed typically for bench-scale research or clinical administration of adult human bone marrow-derived MSCs. This emergent population heterogeneity results in multiple subpopulations of mesenchymal stromal cells that differ in biophysical, *in vitro*, and *in vivo* properties [57,59,61], despite undetectable changes in proposed immunophenotypic markers of stemness by the International Society for Cellular Therapy [60]. We leveraged microfluidic sorting to enrich cell diameter-defined subpopulations of these mesenchymal stromal cells [61,221], effectively separating human MSCs (*D^{lo} cells*) from osteochondral progenitors of more restricted differentiation potential. This osteochondral progenitor subpopulation, defined in part by its relatively larger cell diameter (*D^{hi} cells*) [61], homed to and promoted *in vivo* repair of the bone marrow compartment post-irradiation without sustained engraftment [202]. That subpopulation secreted increased concentrations of growth factors and cytokines (e.g., ANG-1, BMP2, IL-8, and VEGF-A) known to promote hematopoietic recovery, and was consistent with prior reports of osteoblast-like cells or osteoprogenitors priming and organizing the hematopoietic microenvironment for hematopoiesis [34,36,51,222]. Moreover, MSCs are not known to differentiate into or repopulate the hematopoietic cell lineages of the bone marrow, generally attributed instead to proliferation and differentiation of hematopoietic stem and progenitor cells (HSPCs). Those findings support the concept that putative MSCs – more accurately described as multipotent mesenchymal stromal cells or as MSC-derived progenitors – can promote bone marrow repair indirectly by acting as "cellular factories" that produce secreted factors promoting HSPC growth and differentiation.

The MSC secretome has been explored by various means summarized here, though not from the perspective of how mechanical cues can modulate that secretome directly. For example, the secretome and membrane proteins of MSCs have been analyzed at various timepoints during early adipocyte and osteoblast differentiation [223–225]. Various studies have also considered how certain biochemical stimulation of MSCs can alter its secretome. Lee et al. demonstrated

how TNFα stimulated the secretome of adipose-derived stem cells to secrete immune modulators such as IL-6, IL-8, MCP-1 and show how it affected monocyte migration [226]. Tasso et al. showed how bFGF stimulated MSCs to secrete molecules that promoted a regenerative microenvironment for ectopic bone formation [227]. Cheng et al. utilized genetic engineering to constitutively express CXCR4 in MSCs to create an optimal secretome for cardiac repair [201]. Other studies have considered differences in the secretome of MSCs derived from various sources including MSCs derived from human embryonic stem cells [228], bone marrow, umbilical cord, and placenta [229]. Many studies have also considered how hypoxia and expression of HIF-1a affect the secretion of angiogenic factors such as VEGF [230–233]. In addition to MSC-secreted factors, MSCs have also been shown to secrete microvesicles or exosomes that can carry these various growth factor, cytokines, and even pre-microRNAs [234–236]. MSC conditioned media alone has also been shown to mediate lasting effects in the cases of liver failure [218,219]. The MSC-conditioned media, containing only the secretome, have demonstrated efficacy in disease models including nerve regeneration, myocardial infarction, ischemia, hypoxia, wound healing, inflammation, bone regeneration, and organ failure [236]. The MSC secretome has been explored in many different disease states, under the influence of biochemical factors, during differentiation and across different tissue sources. However, very few studies have considered how microenvironment mechanics can alter the MSC secretome.

Obtaining sufficient numbers of microfludically isolated MSC-derived osteochondral progenitors, or D^{hi} cells of larger diameter ~20 μm, is inefficient because these cells constitute <20% of the total culture-expanded MSC population that ranges in diameter from 10-50 μm [202]. In this work, we aimed to bias the heterogeneous population of MSCs toward the D^{hi} cell phenotype, at least in terms of functional indicators such as secreted factors. This allowed us to circumvent the physical sorting that would reduce yield of culture-expanded cells for potential therapeutic indications. Thus, we leveraged microenvironment mechanical cues presented by the substratum material to modulate the MSC population toward secretome expression that could support hematopoietic recovery.

MSCs can also exert mechanical force on extracellular materials and, like many adherent cell types, exhibit mechanosensitive morphology and behavior. Prior studies have focused chiefly on how stiffness and topography of the material to which the cells adhere can modulate cell morphology and *in vitro* differentiation along mesenchymal tissue lineages of bone, cartilage, and fat [71,73,82,193–196,237–239]. Such mechanotransduction occurs through extracellular matrix binding chiefly via integrin-ligand interactions [240,241] and subsequent intracellular signaling including chromatin remodeling [242–245] and changes in transcription [246–248]. Mechanical regulation of cell-generated forces and ligand-receptor interactions at the cell-material interface, intracellular cytoskeletal organization and signaling, and transcriptional activation have each been explored in relation to stem cell differentiation potential [240–248]. Others have also reported correlations among viscoelastic time constants and MSC spread area, and differentiation [82,249]. For example, a recent study demonstrated that timescale of stress

relaxation rather than changes in elastic modulus is correlated with changes in cell spreading and MSC differentiation [82,249]. Whether and how the mechanical stiffness or stress relaxation of a material substratum causes (or simply correlates with) MSC lineage commitment *in vitro* remains an important clarification of active study [77–79]. Such understanding can be aided by use of cell culture materials for which mechanical and chemical properties can be varied widely and characterized quantitatively. Beyond heterogeneity of the culture-expanded cell population, the topography and surface chemistry of the material surface (including extracellular matrix ligand type, density, and configurational flexibility) can also modulate cell response or even act as the dominant cue. This coupling may conflate the effective stiffness of the ligand tether [239,250,251] with that of the bulk or film material [78,79,252]. Those prior studies prompt care in both design and characterization of the substratum surface and bulk properties, when the goal is to determine correlation of mechanical cues with MSC response.

Mechanical regulation of the MSC-secreted factors, or secretome, prior to terminal differentiation and lineage commitment of the cell population has been largely neglected. Multiple translational applications of MSCs do not anticipate or require *in vivo* differentiation of these cells into adipocytes, chondrocytes, or osteoblasts, but do require the capacity to produce large numbers of those cells *in vitro* with predictable therapeutic efficacy and cost efficiency. Thus, we focus here on mechanical modulation of the MSC secretome, prior to detectable terminal differentiation of the population. We show that viscoelastic properties of the adherent substratum material can alter or bias a heterogeneous population of MSCs to a phenotype that can stimulate bone marrow repair. This mechanical priming of MSCs is advantageous even when cells can be sorted (via biophysical or biochemical markers), in that the targeted subpopulations of such label-free sorting typically constitute <20% of the starting cell population [61]. These findings demonstrate how cell-material interactions *in vitro* can be engineered to more efficiently produce an MSC-derived cell population for *in vitro* HSPC production or for *in vivo* hematopoietic recovery.

4.3 Materials and Methods

4.3.1 Material formulation and mechanical characterization

Mechanically tuned cell culture substrata were fabricated from commercially available, two-component poly-dimethyl siloxane, PDMS (CY 52-276, Dow Corning). This particular PDMS formulation was selected instead of more commonly used Sylgard 184 (Dow Corning) formulations used by others [78,79] because fully cured polymers of low elastic moduli (<100 kPa) were more reliably attained with this CY two-component system. Distinct viscoelastic (mechanical) properties were obtained via systematic variation the ratio of the two components, a

pre-polymer base and cross-linking catalyst, Part A and B, respectively. PDMS mixtures of specific A:B ratios were cured for 24 h at 80°C in air.

Shear storage and loss moduli, *G'* and *G"*, were measured in the linear viscoelastic range via parallel plate shear rheometry (Anton Paar, 10 mm-diameter plate) at 1% strain from 0.1 to 100 rad/s. The linear viscoelastic range was determined by conducting an amplitude sweep from 0.01% to 10% strain at 1.6 Hz (10 rad/s). The linear viscoelastic range was determined to be about ~0.5% to ~10% strain (see Appendix A and Fig. A-1). Component A and B were varied in mass ratios from 3:2, 1:1, and 1:3 to obtain materials with shear storage modulus *G'*(1 Hz) of approximately 1 kPa, 10 kPa, and 100 kPa, respectively.

4.3.2 PDMS culture surface preparation and characterization

Pre-mixed PDMS liquids (0.2 mL) were aliquotted directly into wells of 2.2 cm diameter (within a 12-well plate); this fluid volume resulted in approximate thickness of the PDMS substrata of ~500 μm after curing. One column of wells was left blank to serve as a control (non-PDMS) substratum comprising tissue culture polystyrene (PS). Immediately after PDMS curing, plates were plasma treated for 5-10 min to render PDMS surfaces sufficiently hydrophilic for tissue culture. In contrast to prior recent studies [78,79], these PDMS surfaces were not further treated nor covalently functionalized prior to addition of cells and were rendered sufficiently hydrophilic and cytophilic by this surface treatment as described previously [120]. The only extracellular matrix proteins present on the PDMS would be non-specifically-adsorbed serum proteins or those secreted by the cells themselves. In a separate experiment described in the SI, PDMS surfaces were also modified to explore the effects of covalently binding a specific protein.

The following characterization (Figure 4-1 D-E) was performed to determine various surface properties that might affect cell-material interactions. Surface wettability was determined via water contact angle measurements in air (VCA200). Contact angle was measured before and immediately after plasma treatment of the PDMS substrata. Contact angle measurements of the surfaces were also obtained at 1, 2, and 3 days after exposure to air, to evaluate the time required before the cell-culture substrata become distinct due to hydrophobic recovery.

To determine degree of non-specific protein adsorption, small volumes (0.2 mL) of fetal bovine serum (FBS, Gibco 16000-044) were deposited immediately into wells after plasma treatment, incubated for 2 h at 37°C. Non-adsorbed serum was aspirated, and surfaces were washed twice with 150 mM NaCl phosphate buffered saline (PBS). Adsorbed proteins were then released with 0.05% Trypsin-EDTA (Gibco, 25300062), and fluorescently stained using the Qubit Protein Assay kit (ThermoFisher Scientific, Q33211,). Total protein was then assessed via fluorimetry using the Qubit (Qubit 2.0, Thermo Fisher Scientific).

4.3.3 Cell culture and characterization

Human bone marrow-derived MSCs (MSCs) were purchased from multiple commercial sources (Lonza, RoosterBio, and ReachBio) at what was stated by the vendor as a low passage number. MSCs were isolated from healthy-donor derived bone marrow aspirate. Cells were expanded in complete expansion media containing low-glucose Dulbecco's modified Eagle medium (DMEM, Gibco 11885-084), 10% FBS and 1% penicillin-streptomycin (pen-strep, Gibco 10378-016), in 5%CO2 at 37°C to passage 5-7 (up to approximately 14 population doublings) on commercial tissue culture polystyrene (Falcon, 353112) prior to plating in prepared PDMS wells. Expansion media was added to culture wells (1.0 mL/well) immediately after plasma treatment to maintain hydrophilic state of the substratum surfaces prior to the addition of MSCs at ~1000 cells/cm^2. Within each well, media was exchanged every 3-4 days for replacement with complete expansion media, and cells were characterized at approximately day 7.

Size-sorted subpopulations were obtained as described previously (detailed in Appendix H), using an inertia-based spiral microfluidic device with a trapezoidal channel cross-section and two outlets [61,202]. This resulted in two cell subpopulations enriched from the heterogeneous, putative MSC population, characterized by a larger and smaller mean cell diameter in suspension. These sorted subpopulations were grown on PDMS substrata in the same way as heterogeneous, unsorted populations.

Cells were imaged in phase contrast (Olympus IX-81), in both the attached state and suspended (i.e., post-trypsinization) states to determine cell spread area and suspended cell diameter, respectively. These geometric descriptors were obtained via image analysis with customized scripts in MATLAB and CellProfiler.

4.3.4 mRNA and protein expression

Culture-expanded MSCs were plated and grown on PDMS substrata as described above, prior to analysis of mRNA expression. Cells were lysed for mRNA extraction after 1 week in culture. mRNA expression levels were determined using qRT-PCR (EXPRESS SYBR GreenER qPCR, Life). The $\Delta\Delta C_T$ method was used to quantify relative mRNA expression levels across samples. Primer sequences for glyceraldehyde 3-phosphate dehydrogenase (gapdh), runt-related transcription factor 2 (runx2), osteopontin (opn), osteocalcin (ocn), peroxisome proliferator-activated receptor gamma (pparg), and hyaluronan and proteoglycan binding link protein 1 (hapln) are the same as published previously [202]. GAPDH was the reference gene for normalization of expression.

Cells were plated at a slightly higher density of 20,000 cells/cm^2 on PDMS (in a 60 mm-diameter Petri dish format), prior to analysis of secreted protein via a multiplexed antibody panel. After 4-5 days in complete expansion culture media, MSCs were serum starved and MSC-conditioned serum-free media was harvested after 24-48 h. Samples of 0.5ml each were concentrated 10-fold using Amicon Ultra-0.5 Centrifugal filter units (Millipore Catalog# UFC500324) to reduce the volume by 10 fold to 50ul. They were then assayed using a Bradford assay (Thermo Fisher Scientific Cat. #23236) to determine total protein concentration. All total protein concentrations were divided by the minimum concentration within each set of samples to calculate a normalization factor to account for differences in cell number. 10-fold concentrated samples were then assayed in technical duplicates using the ProcartaPlex 45-plex human cytokine/cytokine/growth factor panel (eBioscience, EPX450-12171-901) following manufacturer's instructions. Concentrations reported in Figure 4-5 are ten-fold concentrated and divided by the normalization factor calculated from the Bradford Assay.

Secreted ostepontin was analyzed via quantitative ELISA (eBioScience BMS2066). Cells were plated at a density of 10,000 cells/cm^2 and allowed to grow to confluence for 4-5 days in culture. A smaller volume of 1.0 mL/well of fresh expansion media was then added and MSC-conditioned media was harvested after another 4-5 days. The MSC conditioned media was used directly without dilution for ELISA quantification. ELISA was conducted following manufacturer's protocol.

4.3.5 MSC osteogenic induction and quantification

Cells were plated into 12-well plates at 25-30,000 cells/cm^2 in expansion media. After 24 h, expansion media was exchanged for osteogenic induction media (OIM), comprising high glucose DMEM (Gibco 11995-065), 10% FBS, 1% pen-strep, 10 mM beta-glycerophospphate disodium salt hydrate (Sigma G9422), 10 nM dexamethasone (Sigma D4902), and 0.2mM L-ascorbic acid 2-phsphate sesquimagnesium salt (Sigma A8960). Cells were induced in OIM for up to 1 week with OIM exchanges every 3-4 days.

Cells were fixed in 4% formaldehyde for 15 min at room temperature, and wells were gently washed with deionized water between fixing and staining steps. Cells were stained with Alizarin Red for ~15-20 min to identify mineral deposition, then rinsing excess stain. Stained mineral deposits were then completely dissolved with acetic acid, and those dissolved products added to ammonium hydroxide in a new 96-well plate. Absorbance at a wavelength of 405 nm (Tecan Infinite 200 Pro) was quantified in 96-well plate to compare extent of mineral deposition.

4.4 Results

4.4.1 Characterization of bulk and surface properties of cell culture substrata

Figures 4-1 A-C show that the three types of silicone materials used as MSC substrata differed substantially in viscoelastic properties. We varied these mechanical properties – spanning three orders of magnitude in shear storage modulus G' – via systematic variation in the extent of crosslinking while otherwise maintaining constant chemical composition within the silicone elastomer used as the cell culture substratum [78]. Polydimethylsiloxane (PDMS) is a nonporous elastomer, and provides a wide range of mechanical stiffness without conflating differences in ligand tethering spacing or flexibility, as may occur with other material systems such as relatively porous hydrogels [78]. As most reported studies consider only the linear elastic modulus of viscoelastic polymers used as cell culture substrata, we also report a single G' as a measure of mechanical stiffness for each of the three PDMS formulations used. We approximated G' at 1% strain and 1 Hz strain frequency of these three materials within the linear elastic regime: hereafter denoted as 1 kPa, 10 kPa, and 100 kPa.The viscoelastic damping factor, or ratio of shear storage and loss moduli, also differed substantially among these materials (see Appendix A and Fig. A-2 A).

Despite this wide variation in mechanical characteristics, we detected no significant differences in extent of extracellular matrix protein adsorption (Fig. 4-1 D) or in water contact angle that describes wettability or hydrophilicity (Fig. 4-1 E) among these PDMS substrata. All PDMS substrata were rendered equally hydrophilic immediately after plasma oxidation, and were more hydrophilic than tissue culture-treated polystyrene. This hydrophilicity decreased to levels commensurate with that of polystyrene within one day of storage in air, defining the optimal storage duration of such materials. After air exposure for one day, PDMS substrata became equally hydrophilic as tissue culture-treated PS. This suggests that the PDMS substrata can be used for up to one day after plasma treatment.

Note that we included tissue culture-treated polystyrene (PS) as an experimental control, representing the current standard substratum for *in vitro* expansion of MSCs and MSC/HSPC co-culture. This condition is indicated as black points or striped bars in all figures (e.g., Figs. 4-1 D-E), to make clear that we do not include this ubiquitous cell substratum material in our consideration of substrata mechanical effects. Polystyrene is a glassy polymer that is orders of magnitude stiffer than these PDMS materials (~1 GPa) [253], but also differs significantly from PDMS in surface topography and chemistry that can also act as cues to adherent cells [254].

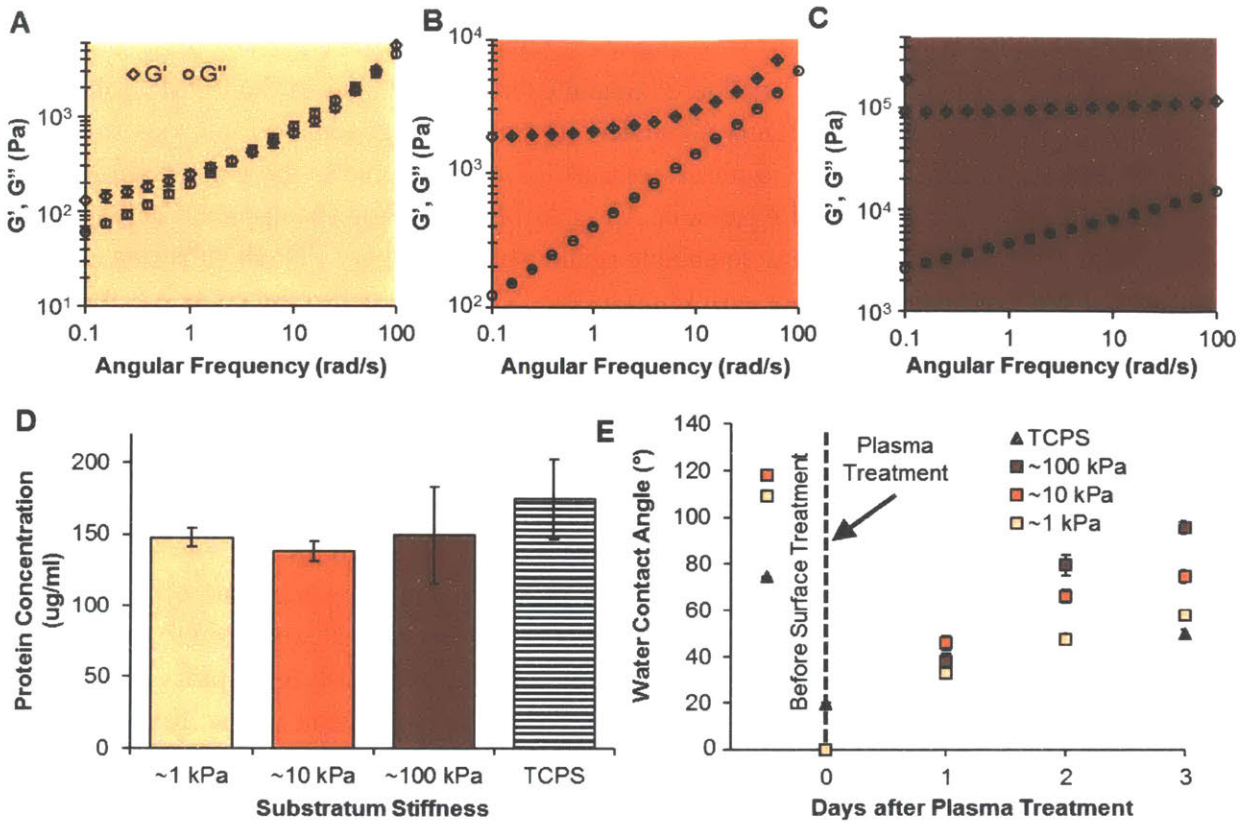

Figure 4-1. Mechanical and Surface Characterization of Elastomeric Substrata (A-C) Frequency sweeps at 1% strain of PDMS gels of varying prepolymer to crosslinker composition: (A) 3:2, (B) 1:1, and (C) 1:3. Equilibrium shear storage modulus ranges across three orders of magnitude corresponding to ~1 kPa, ~10 kPa, and ~100 kPa, respectively. (D) Concentration of non-specific serum protein adsorption to the substrata after incubation for two hours. (E) Surface wettability was determined using water contact angle measurements in air before and after plasma oxidation of cell culture substrata.

4.4.2 Cell-material interactions and changes in cell diameter

Figure 4-2 illustrates that cells adhered to and exerted force against the PDMS substrata, and that mean cell size increased slightly on stiffer substrata. Cell-generated force was sufficient to induce surface wrinkling visible via phase contrast for cells adhered to the more compliant substrata (Figs. 4-2 A for 1 kPa and Appendix A Fig A-5 for 10 kPa). The apparent cell spread area was larger but wrinkling was not detectable on the stiffest of these PDMS substrata (Fig. 4-2 B, 100 kPa). We verified that surface wrinkling on the PDMS was cell-induced as we observed no changes in the surfaces of the PDMS substrata prior to cell attachment (Appendix A Fig. A-4). We compared cell size shortly after cell adhesion (9 h) and after population doublings (5 days) on each material, in terms of suspended cell diameter immediately upon trypsinization. We detected no significant differences in cell size within 9 h after seeding (Fig. 4-2 C), indicating that larger cells did not preferentially attach to the stiffer substrata. However, cell progeny at day 5 exhibited a larger diameter on stiffer substrata (Fig. 4-2 C). Although this increase in geometric mean cell diameter was statistically significant ($p < 5 \times 10^{-15}$ comparing substrata of 1 to 100 kPa stiffness), cell diameters were greater by only 1 μm (5%) on the stiffest compared to the most compliant substrata. (See Appendix A Section 5 and Fig. A-6 for further descriptors of cell diameter distribution on PDMS substrata.) As conveyed in the Discussion below, this slight but detectable difference in mean cell diameter was an order of magnitude less than differences in mean cell diameter between physically sorted MSC subpopulations.

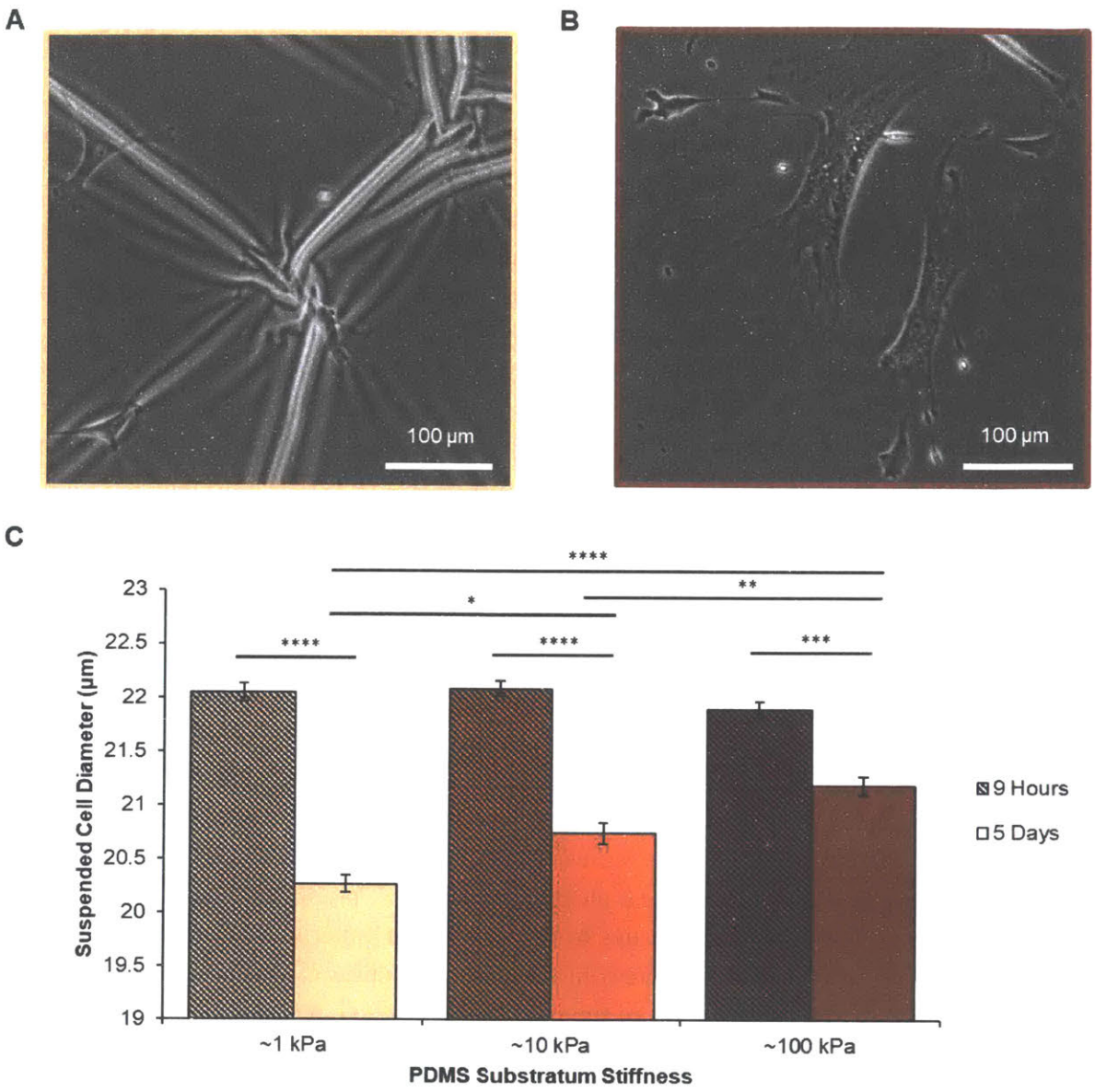

Figure 4-2. Cell Diameter Changes in Response to PDMS Substrata (A-B) Phase contrast images of hMSCs grown on PDMS of varying viscoelastic properties corresponding to increasing shear storage modulus (~1 kPa and ~100 kPa, respectively). (C) Geometric means +/- geometric SEM of suspended cell diameter was determined on substrata of varying stiffness. Suspended cell diameter was determined by trypsinization and image analysis (striped bars) nine hours after seeding and (solid bars) five days after seeding cells on substrata. Statistical differences in expression were determined using unpaired, two-tailed Student's t-test with unequal variance (*$p<0.0005$, **$p<0.0001$, ***$p<1e\text{-}9$, ****$p<5e\text{-}15$).

4.4.3 Viscoelastic moduli correlated with changes in MSC expression

More importantly, these changes in substrata stiffness also correlated with changes in mRNA and protein expression by MSCs, prior to detectable changes in terminal phenotypic differentiation along the osteogenic pathway. We considered mRNA expression changes via quantitative polymerase chain reaction (qPCR) for markers of adipogenesis (peroxisome proliferator-activated receptor gamma, pparγ), chondrogenesis (hyaluronan and proteoglycan link protein 1, hapln), and osteogenesis spanning early to later stage commitment, via quantitative polymerase chain reaction (qPCR): runt-related transcription factor 2 (runx2, early), ostepontin (opn, mid), and osteocalcin (ocn, late). Expression of runx2, ocn, pparg, and hapln did not vary significantly with substratum stiffness, relative to expression on tissue culture-treated PS. To detect the formation of osteochondral progenitors (or D^{hi} cells), we also paneled multiple chondrogenic markers but saw no correlations between any chondrogenic marker expression and substratum stiffness (Appendix A Fig. A-9). However, Fig. 4-3A shows that opn expression increased with decreasing PDMS stiffness, with > 2.5-fold increase on the most compliant substrata.

MSCs also exhibited upregulated osteopontin expression at the protein level as detected via ELISA, with up to a two-fold increase in secreted osteopontin for cells on PDMS (Fig. 4-3B) as compared to tissue culture-treated PS. Maximum expression of secreted osteopontin occurred on PDMS of intermediate stiffness (10 kPa), indicating a biphasic rather than monotonic correlation with substratum stiffness. This increase in osteopontin expression by MSCs on PDMS correlated with both increasing shear storage modulus G', proportional to substratum stiffness, and also with viscoelastic properties of the substratum material. For example, relative osteopontin expression increased with increasing shear loss modulus G'' (Fig. 4-3 C) and decreased with increasing damping factor of the material $\tan(\delta) = G''/G'$ (Fig. 4-3 D). However, we detected no difference in the extent of terminal osteogenic differentiation as a function of substratum stiffness at day 7 (Figs. 4-3 E-F), upon chemical induction of osteogenesis and Alizarin Red staining and quantification of mineral deposits. Taken together, these data show significant and stiffness-correlated increase in osteopontin production as a function of PDMS substrata stiffness and other viscoelastic parameters within one week *in vitro*, but not in late stage markers or metabolic profiles indicative of osteogenic lineage commitment.

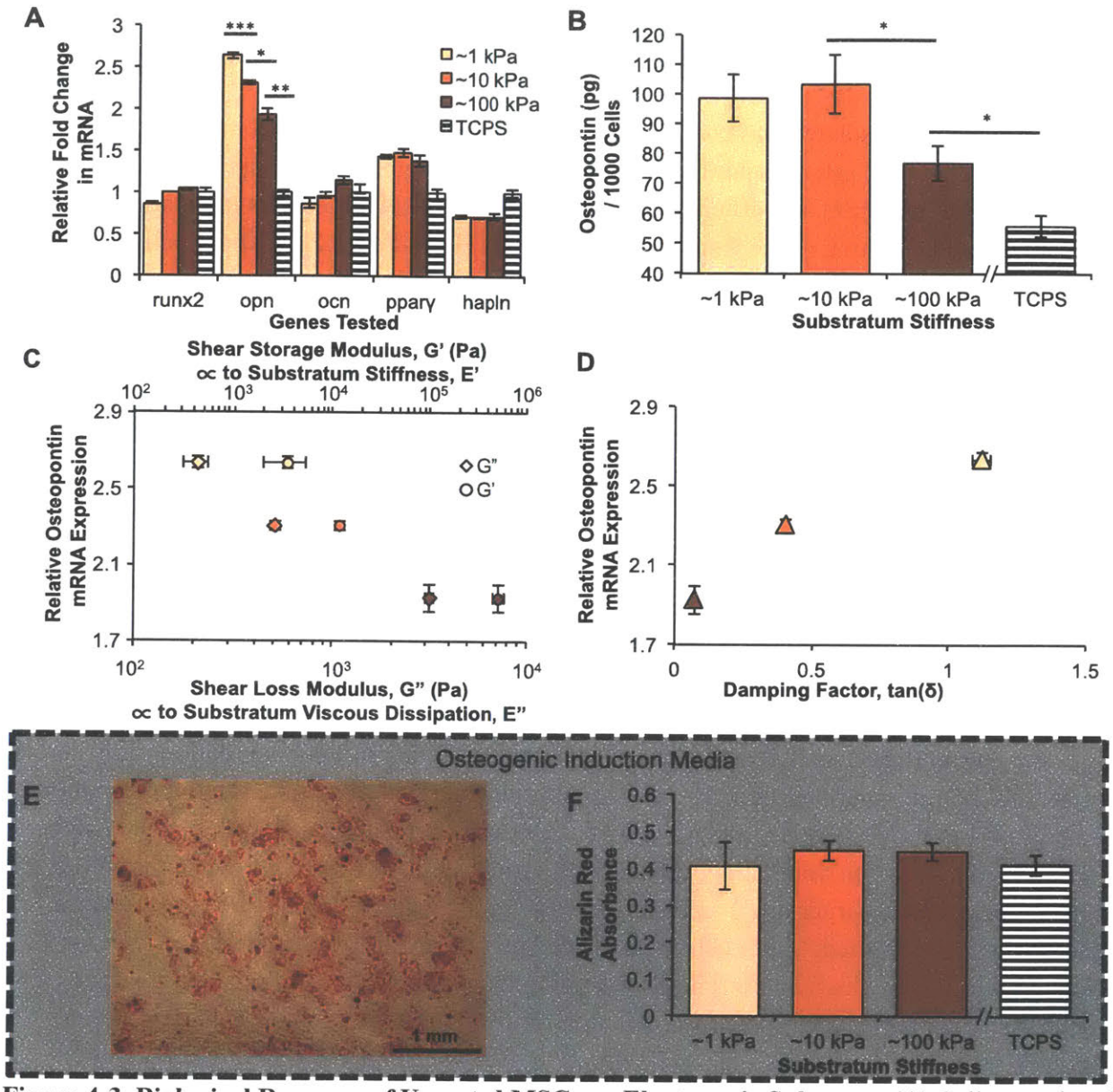

Figure 4-3. Biological Response of Unsorted MSCs on Elastomeric Substrata. (A) Cells were lysed and RNA was extracted and analyzed after one week in culture. First three genes are osteogenic markers (runx2, opn, ocn), fourth gene is a chondrogenic marker (hapln), and last gene is an adipogenic marker (pparγ). $\Delta\Delta C_T$ method was used for relative quantification of expression levels from qRT-PCR with normalization to expression levels of hMSCs grown on polystyrene (black striped bars) with error bars represent standard deviation. Statistical differences in expression were determined using unpaired, two-tailed student's t-test with unequal variance (*$p<0.005$, **$p<0.001$, ***$p<0.0005$). (B) Mean osteopontin protein measured via ELISA with error bars representing standard deviation (*$p<0.05$). (C) Relative osteopontin mRNA expression as a function of (C) shear storage modulus, G' (top horizontal axis), shear loss modulus, G'' (bottom horizontal axis) (D) and as the damping factor ($\tan(\delta) = G''/G'$). Note that G', G'', and $\tan(\delta)$ were determined at a shear oscillation frequency of ~1Hz (~6.31 rad/s). Error bars represent standard deviations. (E) Representative image of alizarin red stained MSC monolayer grown in the presence of osteogenic induction media for one week. Alizarin red stains for calcium deposits secreted by osteogenic MSCs. (F) Mineral deposition quantified using absorbance of dissolved alizarin red stain.

4.4.4 Mechanical modulation of isolated MSC subpopulations

We previously isolated and characterized ostechondral progenitors from a putative MSC population [202]. Those osteochondral progenitors were distinguished by biophysical markers including cell diameter [61] and efficiently separated from the heterogeneous population via inertial microfluidic sorting of the fluid-suspended cells (Fig. 4-4 A) [202]. These cells were the subset of putative MSCs that best supported indirect repair of the hematopoietic compartment *in vivo*, primarily through paracrine signaling and not engraftment. Because the osteochondral progenitors cells characterized through this biophysical sorting comprised <20% of the heterogeneous population of MSCs, available cells numbers are reduced drastically with respect to the total culture-expanded heterogeneous population. Osteopontin (opn) is a secretome component and osteogenic differentiation marker that serves as a key marker for the osteochondral progenitors. Using opn as a correlative marker for the therapeutically effective MSC phenotype, we then explored how PDMS substrata of varying mechanics could modulate both isolated MSC subpopulations and heterogeneous MSC populations. These experiments were designed to answer the following questions: (1) Can we further increase expression of known cytokines from the osteochondral progenitors? and (2) Can we bias the therapeutically ineffective subset of MSCs toward the osteochondral progenitor phenotype?

We thus enriched for osteochondral progenitors, resulting in a subpopulation of mean cell diameter of 22.6 μm, or approximately 5 μm larger diameter than that of the relatively smaller cells (Figs. 4-4 B-C). For brevity and to indicate that this sorted subset of larger diameter D^{hi} is not considered a stem cell population, these sorted groups derived from heterogeneous MSCs are designated hereafter as larger or D^{hi} cells and smaller or D^{lo} cells. We confirmed key baseline characteristics of the sorted, larger cells subcultured on tissue culture-treated polystyrene for 1 week, a duration over which approximately two population doublings occur. Cells of larger diameter also maintained a larger spread cell area for over 1 week in culture on tissue culture-treated polystyrene (Fig. 4-4 D) – the same duration over which are cells are grown on our PDMS substrata. Thus, even when expanded for a week in culture, the cells remained distinct in relatively larger spread area indicative of cell size. These sorted D^{hi} subpopulations expressed over two-fold more osteopontin (opn) than the unsorted population (labeled as control), and five-fold more opn than the sorted subpopulation of smaller cell diameter (Fig. 4-4 E). In addition to greater expression of opn, these larger cells also exhibited greater expression of other cytokines that participate in immune regulation and hematopoietic support, such as interleukin 8 (il8) and insulin-like growth factor binding protein 2 (igfbp2). The upregulation of these cytokines in the D^{hi} cells is what contribute to its therapeutic efficacy in supporting bone marrow regeneration *in vivo*.

Figure 4-4 F quantifies the effect of PDMS substratum stiffness on osteopontin expression for the microfluidically isolated D^{hi} and D^{lo} subpopulations. For both unsorted and

sorted subpopulations, opn expression increased with decreasing PDMS substratum stiffness, and always exceeded the expression levels obtainable for that group on tissue culture-treated PS. Remarkably, opn expression increased up to five-fold for D^{hi} cells on the most compliant PDMS (1 kPa), as compared to unsorted cells on the standard culture substratum of tissue culture-treated PS. Further, opn expression of D^{lo} cells cultured on compliant PDMS increased to similar levels as the D^{hi} cells grown on TCPS. In other words, we attained the same or greater levels of opn production for smaller (non-osteoprogenitor) cells on compliant substratum material as for the larger (osteoprogenitor) cells under currently standard *in vitro* conditions. In addition to this inverse correlation between PDMS substratum stiffness and opn expression, we also observed significant mechanical modulation of six other secreted proteins (IL-8, MCP-1, SDF-1a, IL-21, BDNF, and bNGF) (Fig. 4-5). Together, these data indicate that the mechanical characteristics of the PDMS substratum material – denoted succinctly but incompletely by the effective elastic moduli ranging 1 to 100 kPa – can be varied to modulate production of secretome components *in vitro* that have been correlated with improved *in vivo* outcomes.

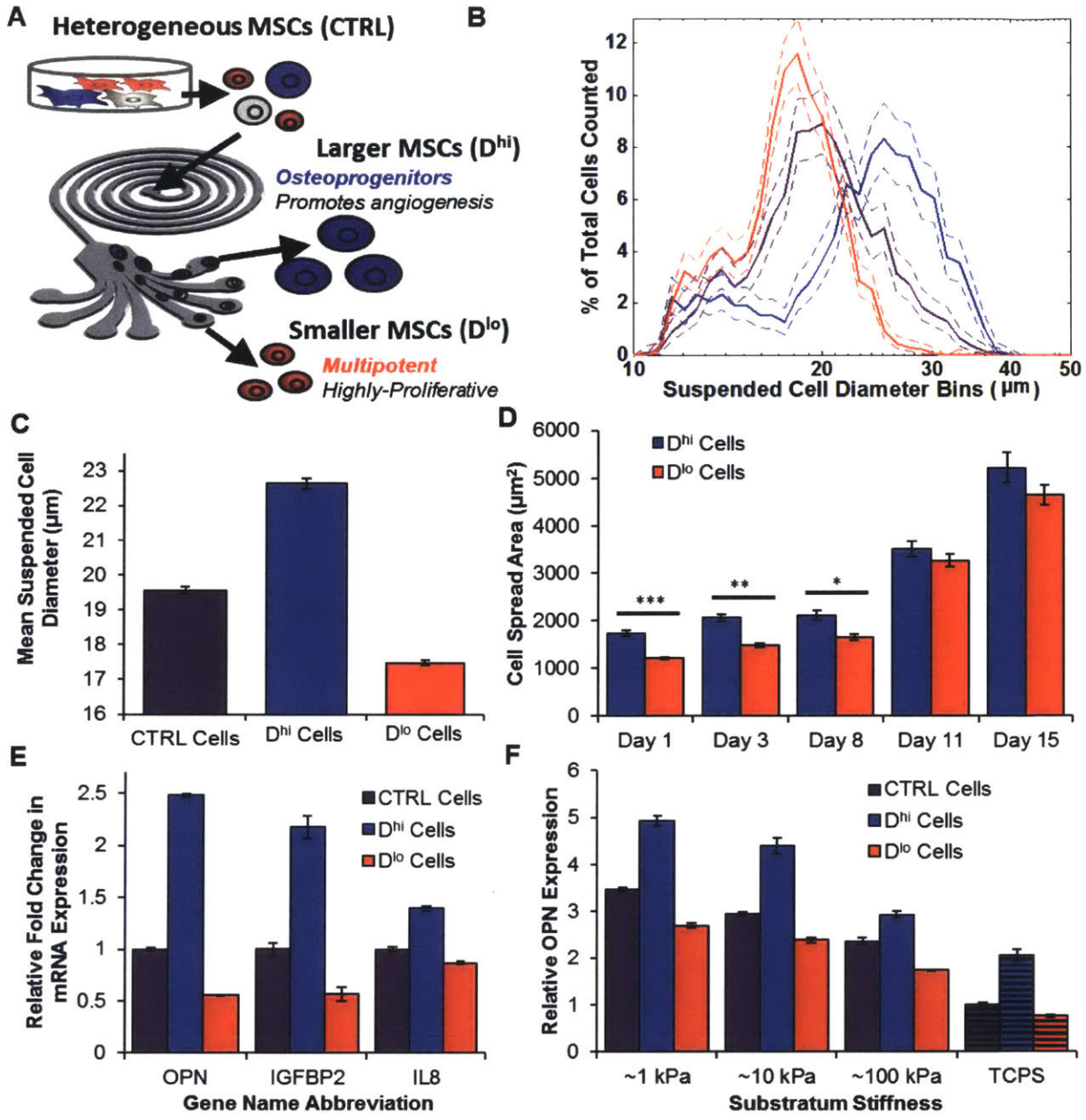

Figure 4-4. Size-Sorted MSC Subpopulations. (A) Schematic diagram of inertial spiral microfluidic device used for size-based sorting of hMSCs. Blue cells represent larger cells (D^{hi}), red cells represent small cells (D^{lo}), gray cells represent intermediate sized cells. CTRL cells (purple) as heterogeneous, unsorted cell population. Typical size distribution of sorted cells represented as a (B) log-distributed histogram with +/- 95% boot-strapped confidence intervals delineated with dotted lines and (C) bar chart representing the geometric mean of the suspended cell diameter with error bars representing the geometric SEM. (D) Tracking of geometric mean of attached cell spread area of sorted cells over the course of two weeks (*p<5e-5, *p<5e-12, ***p<1e-20) shows that sorted cell fractions remain statistically distinct in size after 1 week in culture on polystyrene. Error bars represent +/- geometric SEM. Statistical differences in expression were determined using unpaired, two-tailed student's t-test with unequal variance. (E) Large vs. small cell relative expression of genes correlated with bone marrow recovery after growth on polystyrene for 1 week. (F) Relative osteopontin expression of the unsorted (magenta) and sorted cell

populations (blue and red) after 1 week in culture on PDMS susbtrata of varying stiffness (~1 kPa, ~10 kPa, ~100 kPa) and on polystyrene (~GPa, PS, and black striped bars). Error bars for expression data (E,F) represent standard deviation.

4.4.5 Mechanical modulation of the MSC secretome

In our study, osteopontin (opn) acts as a correlative marker for our D^{hi} cell phenotype that is effective in hematopoietic recovery *in vivo*. However, we were also interested to learn what other secreted factors may also be co-regulated by our PDMS substrata. Using a Luminex-based multiplex antibody array, we paneled over 45-different secreted proteins and cytokines. We collected the secretome samples (i.e. hMSC-conditioned media) from cells grown on our PDMS substrata and on polystyrene. We found that there were 13 factors that exhibited significant trends or large changes in expression (>2fold change) across our substrata (Fig. 4-5). Of these thirteen factors, six of them (IL-8, MCP-1, SDF-1a, IL-21, BDNF, bNGF) exhibited significant rank-based correlations with PDMS stiffness when only looking at PDMS substrata and excluding the polystyrene condition (Fig. 4-5). These data suggest that we can mechanically modulate more than one factor or cytokine of the MSC secretome.

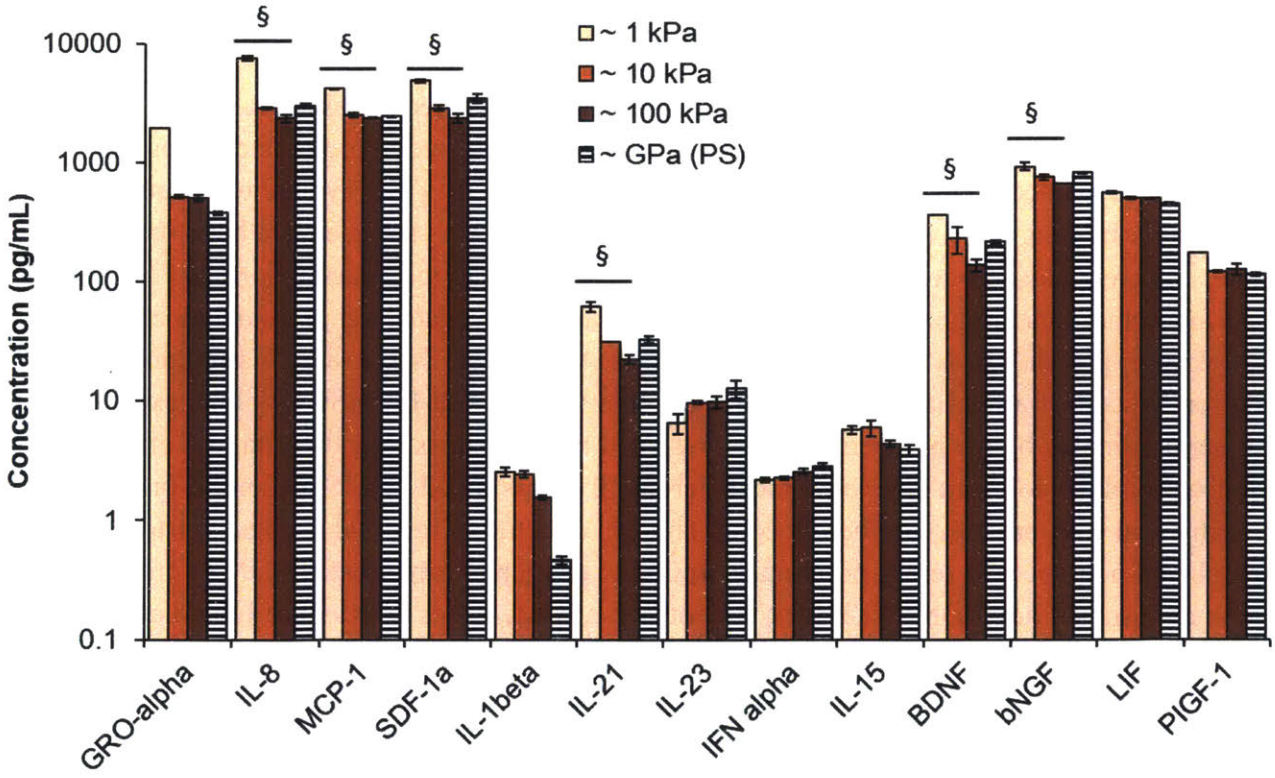

Figure 4-5. Secretome Wide Changes on All Substrata. Protein expression changes in the secretome were paneled using a multiplexed antibody array (ProcartaPlex Immunoassay 45-plex). Expression levels of secretome samples harvested from hMSCs grown on PDMS are shown in orange bars and polystyrene in black striped bars. Error bars represent standard deviation. Statistically significant trends on PDMS substrata only were determined by calculation the Spearman correlation and its corresponding p-value (§ Spearman $|\rho| > 0.8$, and $p<0.05$).

4.5 Discussion

Several previous studies have considered how mechanically compliant or deformable microenvironments can influence the terminal differentiation of MSCs along tissue cell lineages. In contrast, here we show that changes in expression of important cytokines such as osteopontin can be modulated significantly by varying the mechanical properties of cell culture substrata materials, prior to detectable differences in terminal differentiation indicators such as osteogenic mineral deposition. It remains debated how deformable cell-culture environments comprising different material types (e.g., hydrogels vs. silicone elastomers) may influence terminal differentiation [71,77–79]. On hydrogel-based materials, MSCs express more osteogenic markers when grown on substrata in the ~25-40 kPa range when compared to substrata of lower stiffness [71,78,79]. On PDMS substrata, previous studies have demonstrated an apparent insensitivity of human MSCs to substratum stiffness over the range of nominal elastic modulus 0.1 kPa to 2.3 MPa, in terms of chemically induced terminal differentiation assessed by alkaline phosphatase assay [78,79]. Here, we confirm those findings via a distinct assay for terminal osteogenic induction (alizarin red staining): no detectable changes in MSC mineral deposition associated with terminal osteogenic differentiation were observed for a stiffness range spanning three orders of magnitude (1 to 100 kPa).

Note that we varied mechanical properties using this silicone-based elastomer because it is non-porous (relative to typical hydrogels) and is not anticipated to promote differential tethering of extracellular matrix proteins to the material surface [78]. Typical techniques of covalently binding matrix ligands such as collagen to the PDMS surface have been unfruitful. In fact, collagen may self-crosslink rather than bind covalently to the material surface [79]. Indeed, we found that functionalization of PDMS with collagen I abrogated the pronounced changes in cytokine expression with substratum stiffness (see Appendix A Fig. A-8). This suggests that, for currently state-of-art collagen functionalization methods on PDMS, MSC cytokine expression is either dominated by the biochemical cue presented by this matrix ligand or that the effectively self-crosslinked collagen layer atop the differentially crosslinked PDMS presents a uniform mechanical environment to adherent cells. Thus, in our studies reported in Figs. 4-1 to 4-5 we employed non-specific serum protein adsorption to oxygen plasma treated PDMS (previously termed tissue culture PDMS [120]). We identified no differences in extent of ligand attachment, confirmed in Fig. 4-1 via surface hydrophobicity and protein adsorption comparisons. We also explored whether the adsorbed serum protein composition differed detectably across the PDMS substrata, and observed no differences in band patterns on a 1D SDS-PAGE gel (Appendix A Fig. A-3). These three points of comparison together support the claim that the total amount and types of serum proteins adsorbed to these substrata were indistinguishable, though these metrics do not rule out the possibility that the conformation of some protein(s) could differ among the three substrata types. Thus, the observed changes in cell behavior correlated more directly with the viscoelastic properties of these substrata materials, rather than these specific surface biochemical properties of these materials.

Others have posited that PDMS formulations are simply too stiff to elicit a mechanosensitive response by MSCs [79,255]. This suggestion is due in part to prior studies that reported similar results for cells on the stiffest hydrogels considered (10s kPa) as for cells on much stiffer glass (~70 GPa), and to reports that tissue environments in the mesenchymal lineage are less stiff than many PDMS compositions [71,79]. However, here we showed that sparse cultures of MSCs (i.e., fewer cells per unit area than used for our studies of mechanosensitive expression) can mechanically deform PDMS ranging in nominal elastic modulus from 1 to 100 kPa, and that the extent of visible deformations such as surface wrinkling increase with decreasing viscoelastic moduli of the bulk polymer (Figs. 4-1 A-C and 4-2 A-B; see Appendix A Fig. A-4 and A-5 for further discussion of this cell contractility induced surface wrinkling).

We also observed that mean cell diameter $\underline{D}$ increased with increasing substratum stiffness upon population doubling (Fig. 4-2 C, day 5). Although this general finding is in agreement with prior studies that indicated cells are more spread or appear larger on stiffer materials [71,77], here these changes were slight with only ~0.5 μm difference in mean cell diameter for an order of magnitude difference in nominal substratum stiffness (Fig. 4-2 C). We observed much greater differences in cell diameter between biophysically sorted MSC groups, with mean cell diameter differing by ~5 μm between the sorted subsets of D^{hi} and D^{lo} cell subpopulations (Fig. 4-4 A). Thus, PDMS stiffness did not alter the MSC biophysical phenotype or differentiation potential significantly (Figs. 4-3 E-F), but did correlate with changes in secretome components such as osteopontin (Figs. 4-3 A-D, and Fig. 4-5). These substratum stiffness-correlated changes in cell size were not apparent upon initial adhesion and spreading, indicating that cells responded to the mechanical cue over time and did not selectively adhere to materials of varying stiffness in a manner correlated with initial cell size. Together, the capacities of these cells to deform the substrata and to exhibit population shifts in cell size indicate that these cells, considered putative MSCs, can actively sense and respond to mechanical cues presented by these PDMS substrata.

We characterized these PDMS materials via macroscale shear rheology because they are viscoelastic materials that are dominated by the viscous component or loss modulus G" dominating as stiffness (storage modulus) decreases. As a result, the shear storage or elastic moduli (expressed as G') varied significantly with strain rate – and thus may plausibly also vary in effective stiffness as cells exert force against the substratum material at varying rates. Methods that infer mechanical stiffness, e.g., by simplifying material description to a linear elastic solid described by a single elastic modulus, can fail to identify accurately or completely the mechanical differences that may affect adherent cell responses (see Appendix A and Fig. A-2 A-C) [82,249,256]. Fuller descriptors of nonlinear elastic behavior of polymers utilized as cell culture substrata can be helpful in identifying such possibilities. For example, Chaudhuri et al. showed that MSCs exhibited increased cell spread area and expression of some osteogenic markers when cultured on polymers of shorter vs. longer stress relaxation time constants. In that set of polymers, the viscous component of substratum deformation exhibited larger differences

than the elastic components described by G' at a specific frequency, and thus the authors attributed the differential cell response to time-dependent deformation of the substrata [82,249]. While our present study utilized polymers for which G' and G'' were coupled and thus could not distinguish the independent roles of elastic and viscous contributions to MSC secretome modulation, Fig. 4-3 D shows clearly that OPN expression correlated with the ratio of these viscoelastic descriptors, tan δ. It thus remains an interesting vein of future studies to determine whether and how viscous characteristics of the cell culture substrata, independently of elastic properties of the material, can play a dominant role in modulating these MSC secretome expression levels. For both brevity and relation to prior studies, here we refer to these distinctly viscoelastic materials in terms of stiffness, ranging in nominal elastic moduli from 1 to 100 kPa at a shear frequency of 1 Hz.

Although within 1 week of chemical induction these mechanical cues were insufficient to elicit stiffness-dependent changes in extent of terminal differentiation, the viscoelastic properties of PDMS correlated with significant changes in osteopontin expression (Figs. 4-3 A-D). Others have argued that culturing MSCs on PDMS of varying stiffness does not elicit measurable changes in MSC spreading or differentiation [78,79]. Similar to these previous studies, we do not observe changes in terminal differentiation potential (Fig. 4-3 E-F), but we noted significant changes in MSC size (Fig. 4-2 C). More importantly PDMS stiffness is correlated with the modulation of the secretory profile through which the MSCs support indirect repair *in vivo* (Fig. 4-5). Most notably, osteopontin production was further increased on more compliant substrata, for a size-sorted subset of putative osteochondral progenitor MSCs that were already upregulated in osteopontin (Fig 4-4 F). Osteopontin was originally named and identified as an extracellular matrix protein important for calcium binding, biomineralization, osteoclast anchoring, and bone formation [257,258]. Thus, it serves as an important marker for osteogenic commitment in MSCs [73]. As osteopontin is a marker of osteogenic commitment, one might expect ostepontin expression to increase with increasing substratum stiffness, in keeping with prior reports that stiffer materials promote osteogenic commitment of MSCs [71,77]. However, we observed uniformly lower osteopontin expression for MSCs adhered to stiffer PDMS substrata, whether for the control heterogeneous population of putative MSCs or for biophysically sorted subsets. (At the mRNA level (Fig. 4-3 A), we observed a monotonic correlation of decreased osteopontin transcription with increased substratum stiffness. At the secreted protein level (Fig. 4-3 B), this correlation was not monotonic; secreted osteopontin levels were lowest for cells on PDMS of 100 kPa stiffness, but similar for cells on PDMS of intermediate and lowest stiffness. This discrepancy may be attributed to differences in processes such as protein translation, degradation, or adsorption.) Moreover, this contradiction to expectation can be understood by noting that osteopontin is not only or chiefly a lineage commitment marker, despite its name [259,260]. This cytokine serves a complex role as a paracrine signal, and can be found in several different isoforms and splice variants with many post- translational modifications of serine residues as phosphorylation sites. Osteopontin plays an important role in both secreted and intracellular forms [261], for example by promoting angiogenesis via direct interaction with

endothelial cells [262]. This glycoprotein also contains an integrin-binding RGD sequence and a cryptic binding site exposed by thrombin cleavage, and is a known ligand for another glycoprotein CD44, a receptor that is expressed on T-cells. This interaction with CD44 has been shown to regulate IL-12, IL10 and IFN-gamma production from macrophages in cell-mediated immunity [263]. More importantly, the expression of osteopontin has been linked directly with hematopoietic niche maintenance after damage or from aging *in vivo* [264–266]. Osteopontin has also been shown to regulate the location, differentiation and proliferation of HSPCs *in vivo* [91,267,268].

The mechanically correlated osteopontion expression that we observed was conserved across multiple MSC donor sources tested (Appendix A Fig. A-7), among subpopulations sorted from a single donor (Fig. 4-4), and also for many other cytokines and growth factors that contribute to hematopoietic recovery (Fig. 4-5). This robust response suggests an efficient means by which to mechanically prime the entire MSC population towards the D^{hi} cell phenotype that supports bone marrow repair. By engineering the substratum stiffness, with or without biophysical sorting of MSC subpopulations that adhere to that material, we can induce the cell population to produce more of these beneficial factors. This mechanical priming can be useful whether the cells or those secreted proteins are the administered therapeutic product. For example, the D^{hi} cells promote bone marrow repair and regeneration in lethally irradiated mice through its secretome but are limited in number [61,202]. Thus, we need to either engineer increased expression of the effective secretome components or more of the MSCs similar to the D^{hi} cell phenotype. Here, we demonstrated that osteopontin expression is increased up to five-fold with respect to current *in vitro* culture materials, when these D^{hi} cells are biophysically sorted and cultured on compliant PDMS substrata of nominal 1 kPa stiffness. As importantly, we showed that D^{lo} cells (the dominant subpopulation representing ~80% of the heterogeneous MSCs, of otherwise reduced therapeutic outcome) cultured on compliant PDMS substrata exhibit increased osteopontin expression to approach levels produced by those D^{hi} cells on polystyrene (Fig. 4-4 F). This finding shows that substratum materials can be designed to engineer a larger quantity of MSC-derived cells with desired phenotype, either by uniformly upregulating cytokine production by the heterogenous MSC population or by selectively increasing cytokine production in the dominant subpopulation.

In physically sorted cells, MSC production of osteopontin was co-regulated with other factors such as igfbp2 and il8 (Fig. 4-4 E), which both promote hematopoietic growth and immune regulation [269–271]. This co-regulation of other factors along with osteopontin was consistent in the unsorted population of MSCs grown on PDMS. Six other cytokines or growth factors (IL-8, MCP-1, SDF-1a, IL-21, BDNF, and bNGF, Fig. 4-5) exhibited significant trends at the protein level similar to osteopontin. That is, all of these secreted factors exhibited increasing protein expression on decreasing substratum stiffness. For example, IL-8, has been shown to support mobilization of HSPCs and the long-term repopulating ability of HSPCs *in vivo* [271]. Increased IL-8 expression in early passage MSCs was shown to be key in supporting *in vitro*

expansion of HSPC [272]. Another mechanically modulated factor, SDF-1a, is a bone marrow niche component necessary to maintain a primitive state of the HSPCs in long-term *ex-vivo* culture [22,273,274]. Although it may not directly affect HSPC expansion *in vitro,* MCP-1 (also known as CCL2) has been shown to promote trafficking of HSPCs to sites of inflammation *in vivo* [275,276]. IL-21 can regulate downstream differentiation of HSPCs such as accelerating NK cell maturation or inducing B cell maturation and apopotosis [277,278]. While IL-21 and MCP-1 may not be expected to improve *ex vivo* expansion of HSPCs directly, they may regulate hematopoiesis and inflammatory processes *in vivo*. Together, these cytokines and growth factors expressed by MSCs could play a role in influencing hematopoiesis both *in vitro* and *in vivo*.

The factors BDNF and bNGF are not known or thought to impact hematopoiesis, but upregulation of those factors could be useful for other applications. BDNF and bNGF promote growth and survival of neurons [279,280]. These results suggest other potential *in vitro* applications or indirect repair targets for such mechanically modulated MSCs. Such mechanical priming of the MSC secretome *in vitro* could plausibly support HSPC production *in vitro* and hematopoietic recovery in bone marrow upon *in vivo* administration, which is further explored in Chapter 5.

4.6 Conclusion

We developed and demonstrated a facile, mechanically tunable PDMS system that supports MSC proliferation and progenitor cell production. This material design serves as an adherent cell substratum that can induce expression changes in important cytokines and growth factors of the MSC secretome, even prior to terminal differentiation. To illustrate this material mechanics approach, we increased by five-fold the production of one important MSC-secreted cytokine, osteopontin, through modulating both the stiffness of PDMS substrata and the subpopulation of MSC-derived cells. Substratum stiffness also correlated with MSC production of six other secreted proteins, demonstrating a mechanically modulated MSC secretome that can now be explored further. Moreover, we showed that systematic changes in cell substratum mechanics can shift the entire cell population toward a subpopulation phenotype (defined in part by these secreted factors) of established *in vivo* efficacy but low prevalence on current substratum materials. For MSC therapy applications such as bone marrow recovery, this materials-mediated approach increases the available cell number five to six-fold, by shifting the population toward this expression profile within one week *in vitro*. These mechanically tunable cell culture substrata provide a simple and effective alternative to modulate the MSC secretome, as compared with biochemical induction and genetic modification. This approach is also more readily amenable to scaled manufacturing of cell therapies, in contrast to viral transfection or chemical induction. This MSC mechanopriming can be used to improve production of other cell types *in vitro* that can be subsequently used for *in vivo* applications such as hematopoietic recovery.

Chapter 5

Regulating hematopoiesis *in vitro* and improving hematopoietic recovery *in vivo* using mechanically-modulated mesenchymal stromal cells

In Chapter 4, we explored how to mechanically modulate the mesenchymal stromal cell (MSC) secretome. In Chapter 5, we determine whether these mechanoprimed MSCs can play a role in regulating hematopoiesis *in vitro* and hematopoietic recovery *in vivo*. To do so, we first developed a statistical regression model based on MSC secretome expression *in vitro* to predict MSC support of hematopoietic recovery *in vivo*. We then used *in vitro* co-culture models of MSCs with hematopoietic stem and progenitor cells (HSPCs) to evaluate the role of mechanoprimed MSCs in regulating hematopoiesis *in vitro*. Finally, we administered these mechanoprimed MSCs to our mouse model of hematopoietic failure to evaluate this cell population's therapeutic efficacy *in vivo.*

5.1 Acknowledgements

The results presented in this chapter were a collaboration with researchers in SMART BioSyM, including researchers located at MIT and in Singapore. All co-culture experiments with HSPCs were conducted at MIT in collaboration with Ms. Novalia Pishesha at the Whitehead Institute. The non-contact co-culture results were published previously in the ACS Biomaterials Science & Engineering research article [90]. *The raw data for developing the regression model was obtained from a previous and cited study conducted by Dr. Zhiyong Poon in Singapore, with results published originally in Stem Cells Trans Research* [202]. *Dr. Kimberley Tam conducted the in vivo mouse experiments included in this chapter, employing the mechanopriming protocols developed by Frances D. Liu and transferred via Dr. Tam's visit to MIT and Ms. Liu's visits to Singapore.*

5.2 Introduction

Hematopoietic stem cell (HSC) transplants are performed as curative treatments for hematological malignancies such as leukemias, lymphomas, and myelomas [2,3]. Successful HSC transplantation with rapid hematopoietic recovery and long-term HSC engraftment remains a challenge. HSCs can fail to engraft or can proliferate and differentiate too slowly, resulting in immune deficiency and infection susceptibility during post-transplantation recovery [17,18]. Of equal concern upon immune system suppression, the administered cells can overtake the recipient's cells, resulting in graft versus host disease [2,3,12,14,15]. These complications related to the HSC transplants, but non-cancer related, have a reported mortality as high as 40-50% [2,3]. Myeloablative conditioning regimens, such as radiation or chemotherapy, are used commonly to reduce tumor burden and to suppress immune rejection of the transplant [9–11]. Many of these regimens destroy both diseased and healthy cells of the hematopoietic compartment, including the stroma and niche-associated cell types. Subsequent HSC transplantation is necessary to replace the destroyed hematopoietic lineages, but HSCs do not repair the stromal or niche cells [13]. HSC engraftment and rapid, successful hematopoietic recovery are dependent on the hematopoietic niche components, including paracrine signaling and interactions with surrounding cell types [7,19,26,28,281].

Mesenchymal stromal cells (MSCs) are a subset of hematopoietic niche cells important in supporting, maintaining, and expanding hematopoietic stem and progenitor cells (HSPCs) *in vivo* and *in vitro* [28,282–285]. MSC support of hematopoiesis *in vivo* and *in vitro* is attributed to MSC secretion of soluble factors such as stromal derived factor 1 (SDF1) and stem cell factor (SCF) [22,33,52–54]. These cells natively reside in the bone marrow niche and also contain a subset of multipotent stem cells that can differentiate into osteogenic, chondrogenic, and adipogenic lineages [45,46]. Due in part to this capacity for multipotent differentiation potential and asymmetric division, the MSC population become morphologically and functionally heterogeneous under standard *ex vivo* expansion conditions [57,286]. We demonstrated previously that culture-expanded MSCs that are immunophenotypically indistinguishable can be isolated into biophysically distinct subpopulations that result in distinct functional phenotypes [61,202]. We found that the biophysical marker of suspended cell diameter correlated with varying ability of the MSCs to support hematopoietic recovery *in vivo* [202]. In that study, we systemically administered MSC populations or distinct MSC subpopulations (isolated by cell diameter via spiral microfluidics) into sub-lethally irradiated mouse models of hematopoietic failure analogous to irradiation used for myeloablative conditioning regimens [202]. We found that MSCs of larger cell diameter (D^{hi} MSCs) improved radiation rescue over any other isolated subpopulation or the heterogeneous MSC populations [202]. These D^{hi} MSCs had limited differentiation potential characteristic of osteoprogenitors [61,202], which have also been demonstrated to support hematopoietic recovery *in vivo* [51,86,106]. In our study, these D^{hi} MSCs or osteoprogenitors did not exhibit long term engraftment (>10 days), and mouse survival also improved (though less dramatically) with injection of conditioned media from the D^{hi}

MSCs, suggesting that the observed hematopoietic support was secretome-mediated [202]. These results suggested that the MSCs were capable of indirectly supporting hematopoietic recovery via paracrine signaling, as MSCs are not known to differentiate into hematopoietic lineages *in vivo*.

While such label-free biophysical sorting of MSCs is an effective approach to identify and isolate MSC subpopulations of therapeutic value, the D^{hi} MSCs were only a minor fraction of the culture-expanded population (20-30%). Correspondingly, the production yield of this osteoprogenitor phenotype was low. We have also demonstrated recently that the MSC secretome can be modulated by *in vitro* expansion on a viscoelastic polymer of tunable mechanical stiffness, polydimethylsiloxane (PDMS) [90]. By expanding MSCs on PDMS of decreasing stiffness, we increased the expression of various growth factors and cytokines such as osteopontin (OPN), interleukin-8 (IL-8), insulin-like growth factor binding protein 2 (IGFBP2), monocyte chemoattractant protein-1 (MCP-1), and SDF1α [90]. These secreted factors have been shown in the literature to maintain HSC self-renewal capacity *in vivo,* regulate HSC differentiation *in vivo*, or support *ex vivo* expansion of long-term re-populating HSCs [22,91,271–278]. Many of these secreted factors were also over-expressed in biophysically sorted D^{hi} MSCs. Thus, we hypothesized that by growing the MSCs on PDMS substrata of designed mechanical stiffness, we could predictively produce MSC populations that would support hematopoietic recovery *in vivo* to levels comparable to the minor subpopulation of D^{hi} MSCs.

In the current chapter, we constructed a regression model from the secretome expression of the MSC populations and subpopulations that support recovery after bone marrow irradiation (i.e., radiation rescue) including hematopoietic recovery to varying extents *in vivo* [202]. Those expression data served as training set to predict survival after hematopoietic failure, in response to administration of different MSC preparations. We then used the expression profile of the MSCs expanded on PDMS, or mechanoprimed MSCs, as test data to validate the regression model. We verified that our mechanoprimed MSCs could promote radiation rescue using our regression model, and could also promote expansion of hematopoietic stem and progenitor cells (HSPCs) under *in vitro* co-culture. Lastly, we then deployed our mechanoprimed MSCs in the same *in vivo* model to demonstrate improved hematopoietic recovery in similar ways predicted by the statistical regression model.

5.3 Materials and Methods

5.3.1 Regression modeling

We compiled all MSC secretome expression data that was acquired from previous studies using Luminex-based assays or ELISAs [202]. Expression data and survival curves were collected from five experimental groups: unsorted MSCs at passages 3, 6, and 9 (approximate population doublings of 6, 12, and 18); and two subpopulations of size-sorted MSCs (D^{hi} and D^{lo} MSCs) at passage 6. Survival curves were acquired over 21 time points during the 50-day experiment duration. We first calculated the Pearson's linear correlation coefficients among the

expression data of 35 secreted factors against the survival proportions at a single time point (e.g., survival proportions for each experimental group at day 18). We then applied this same analysis to every time point to determine all proteins or cytokines that were significantly ($p<0.05$), linearly correlated ($|\rho|>0.875$) with survival over the duration of the entire experiment.

As there is no *a priori* expectation that the relationship between cytokine expression and survival is linear, we also conducted partial least squares regression (PLSR) to determine what proteins and cytokines are most strongly correlated with survival. For PLSR, the expression data were input as a 5x35 matrix of predictors while the survival curve data were input as a 5x21 response matrix. For both predictor and response matrices, we z-score normalized each column to have a mean of 0 and standard deviation of 1; this approach obviated inappropriate weighting of variables based on their relative magnitude (i.e., concentration). Over 90% variance in both the predictor and response matrices was contained within a two-component model; thus, we chose to use 2-dimensional principal component space to project our loading vectors (see Appendix B, Fig. B-1). We determined which secreted factors correlated most strongly with survival by determining the loading vectors of the predictor and response matrices that were closest together. Using this PLSR model, we also obtained a 36x21 matrix of regression coefficients, with the top row as intercepts, that could be used to predict survival using new expression data of the 35 proteins and secreted factor included in the analysis. We conducted all computations in MATLAB and the Statistics and Machine Learning Toolbox.

5.3.2 MSC Culture

We prepared PDMS-based cell culture substrata with tunable viscoelastic properties as described previously [90]. Briefly, we mixed a two-component PDMS (CY 52-276, Dow Corning) at three different mass ratios to form substrata of shear elastic moduli varying over three orders of magnitude (~ 1 kPa, ~ 10 kPa, ~ 100 kPa). We then added the PDMS mixtures to polystyrene well-plates or Petri dishes at volumes sufficient to form PDMS layers of ~500 μm thickness and cured these at 80°C for ~24 hrs. We plasma-treated PDMS surfaces for 5 min to render them sufficiently hydrophilic for cell attachment. We then cultured human bone marrow-derived MSCs on these PDMS substrata as described previously [90]. Prior to using the MSCs for these experiments, the MSCs were commercially purchased (Lonza) and expanded on tissue culture polystyrene up to passage 5-7. All expansion media (for both HSPCs and MSCs) and growth conditions were prepared as described previously [90].

For secretome characterization and co-culture with HSPCs, we cultured MSCs on plasma-treated PDMS in 12-well plates. For both of these *in vitro* experiments, we plated MSCs at high densities (~10,000 cells/cm^2) to ensure MSC confluency and growth-arrest within 4-5 days to maintain approximately constant cell numbers across all experimental conditions. For secretome characterization in 12-well plates, smaller volumes of media (1 mL/well) were then added to the wells upon media exchange at day 4 or 5. We then allowed the MSCs to condition the smaller volume of fresh MSC expansion media for 4-5 days prior to harvesting the media

from the wells for secretome characterization. To account for potential differences in MSC number across conditions, we fixed and stained the cells for nuclei (Hoechst 33342) after harvesting the secretome samples. We imaged at least 10 locations in each well to verify that MSC numbers were approximately constant across all conditions. If they were not, we normalized the concentrations by cell number normalization factors as described previously [90].

For sufficient expansion of MSCs for mouse studies, we cultured the MSCs on dishes of larger growth area: 150 mm-diameter Petri dishes (Thermo Fisher Scientific, Cat. No. 157150). We plated MSCs at a seeding density of ~1500-2000 cells/cm^2 and allowed the MSCs to proliferate for 7-10 days with MSC expansion media replaced every 3-4 days. We expanded MSCs on two PDMS substrata of lowest and highest stiffness: 1 kPa and 100 kPa. As a comparison to our previous studies, we included additional experimental groups: MSCs expanded on tissue culture polystyrene dishes (unsorted MSCs) and also subsequently sorted biophysically (D^{hi} MScs) as described previously [202].

5.3.3 Secretome Characterization

For secretome characterization, we assayed five MSC conditions: D^{hi} MSCs and unsorted MSCS expanded on tissue culture polystyrene as well as unsorted MSCs that were culture-expanded on PDMS of ~1, 10, or 100 kPa stiffness. After allowing the MSCs to condition the smaller volumes of expansion media for 4-5 days, we harvested the MSC-conditioned media for secretome characterization. After harvesting secretome samples, we centrifuged them for 8 min at 500xg to remove any cells or cell debris. We then transferred the supernatant to new tubes and froze them down at -80°C prior to use.

We thawed the samples on ice prior to protein characterization and assayed their composition in technical duplicates using the ProcartaPlex 45-plex human cytokine/chemokine/ growth factor panel (Thermo Fisher Scientific, EPX450-12171-901) following manufacturer's instructions. We conducted washing steps using a microplate washer (BioTek) and subsequently read the concentrations with the FlexMap 3D (Luminex). To assay the secretome samples for concentrations of angiopoietin-1 (ANG-1), bone morphogenetic protein 2 (BMP-2), acidic fibroblast growth factor (FGF-1), and thrombopoietin (THPO), which were not included in the Luminex-based panel, we completed multiple ELISAs (R&D Systems, Cat #s DANG10, DBP200, DFA00B, and DTP00B). Concentrations of BMP-2 and THPO in our samples were below the detection limit. We used arithmetic mean across technical duplicates as representative concentrations for all experimental groups in our PLSR model predictions.

5.3.4 *In vitro* co-culture of MSCs and HSPCs

We co-cultured human MSCs with mobilized human bone marrow CD34+ cells, which we refer to as hematopoietic stem and progenitor cells (HSPCs) (the Fred Hutchinson Cancer Center). We first added MSCs to 24-well plates with PDMS substrata (or tissue culture PS controls), prepared as described previously [90]. We seeded MSCs onto PDMS and tissue culture PS wells at 10,000 cells/cm^2 and allowed them to grow for 4-5 days until full confluency on all substrata.

For non-contact co-culture conditions, we gently placed transparent, semi-permeable, cell culture inserts with 1.0 μm pores (Falcon 353103) on top MSC monolayers within each well to physically separate HSPCs from MSCs. The small pore size (1.0 μm) ensured no contact between the HSPCs (~10 μm in mean diameter) and MSCs (~20 μm in mean diameter) while still allowing for exchange of secreted cytokines and growth factors. We then added HSPCs on top of the semi-permeable inserts at a density of 5,000 HSPCs per well. For contact co-culture, we added HSPCs directly to the MSC layers with no insert. A graphical depiction of the two different co-culture experimental setups is shown in Figure 5-1. We included two control conditions: PS wells seeded with MSCs and MSC-free PDMS wells containing only HSPCs, as a representation of standard HSPC expansion conditions. We grew co-cultures in HSPC expansion media containing 100 ng/ml recombinant human (rh) FLT3 9 (Peprotech 300-19), 100 ng/ml rhSCF (Peprotech 300-07), 20 ng/ml rhIL6 (Peprotech 200-06), 20 ng/ml rhIL3 (Peprotech 200-03) and 100 nM Dexamethasone (Sigma Aldrich D2915) in Stemspan SFEM II medium for 7 days.

We harvested HSPCs via aspiration followed by collection of any remaining cells with two vigorous PBS washes and collections. We visually inspected wells under phase contrast to ensure removal of all HSPCs from on top of the inserts. We quantified HSPC proliferation using the Cellometer Auto T4 Cell Viability Counter (Nexcelom Bioscience) for all conditions. To prepare HSPCs for flow cytometry analyses, we washed cells once with PBS and re-suspended them in FACS buffer containing 2mM EDTA and 5% FBS in PBS. We then stained cells with anti-CD34-FITC (eBioscience 11-0349-42), anti-CD10-Pe/Cy7 (BioLegend 312214) and anti-CD123-eFluor450 (eBioscience 48-1238-42) for 30 min at 4°C. We washed the samples twice with FACS buffer prior to further analysis. We acquired all flow data on a FACS Fortessa flow cytometer (BD Biosciences) and analyzed using Flowjo software (Tree Star Inc. Ashland, OR).

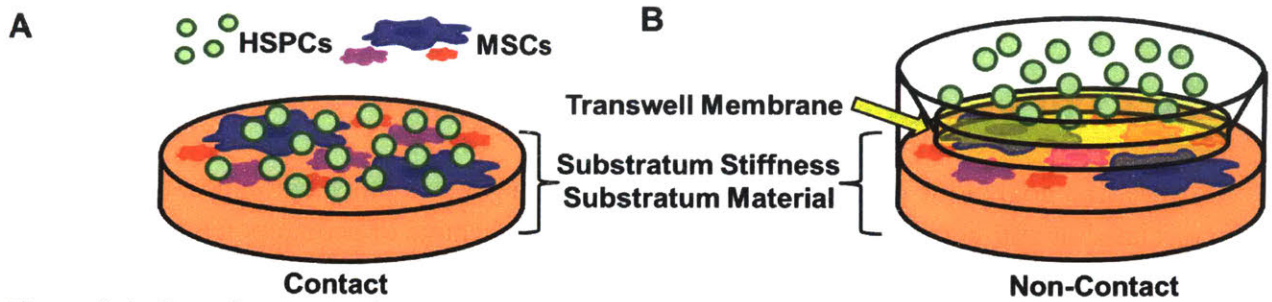

Figure 5-1. Co-culture experimental setup. (A-B) Schematic diagrams of (A) contact and (B) non-contact co-culture setups.

5.3.5 *In vivo* mouse model

Procedures involving animals and their care were conducted in conformity with all procedures approved by the National University of Singapore (NUS) Institutional Animal Care and Use Committee (IACUC), and all *in vivo* studies reported herein occurred in Singapore at NUS' animal housing facility. We compared *in vivo* responses for four distinct preparations of MSCs: unsorted MSCs expanded on tissue culture polystyrene; D^{hi} MSCs sorted from MSCs expanded on tissue culture polystyrene; and unsorted MSCs grown on 1 kPa PDMS or 100 kPa PDMS. All MSCs used for injection were derived from the same human donor (Lonza, commercially purchased lot) and expanded to the same passage number under identical culture conditions as described above.

We purchased and used 5-7 week old, female immune-compromised mice (NOD SCID, Jackson Laboratory) in irradiation studies as described previously [202]. We irradiated the mice using 4.0 Gy of gamma irradiation to induce hematopoietic failure. At 24 h post-irradiation, we injected MSCs (trypsinized and re-suspended at 10^6 MSCs/mL) via tail vein injection at a concentration of ~20,000 MSCs/g of mouse mass. As a negative vehicle control (no-treatment), we included a cohort injected with only saline, for a total of five condition cohorts. We tracked mouse survival and weight loss over the 50-day duration of the experiment. At weeks 1, 2, and 4 post-irradiation, we collected blood via cardiac puncture for complete blood counts (CBC), culling three randomly selected mice from the experimental groups injected with MSCs that were expanded on PDMS (1 kPa and 10 kPa). For the first two time points, we also culled and collected blood from mice in the no-treatment control cohort. We collected no data for the no-treatment control cohort beyond three weeks as there were no surviving mice. At week 5 (day 35), we also collected a small volume of blood (~0.1-0.3 mL) from at least 5 mice in the two experimental groups for CBC using a facial sub-mandibular bleed. We analyzed all *in vivo* data and their corresponding statistics using GraphPad Prism 7.

5.4 Results

5.4.1 PLSR model predictions of survival

The first goal of the present study was to identify any key factors, cytokines, or proteins that correlated or anti-correlated with improved survival indicative of hematopoietic recovery. We had characterized previously the secretome expression of five distinct MSC populations using targeted, antibody based assays including a Luminex-based panel and multiple ELISAs [202]. We had also tracked the survival of sub-lethally irradiated mice injected with those same MSC populations, as a model of hematopoietic failure and recovery [202]. Here, we related those previously acquired secretome expression data against the survival proportions of the mice at a given time point (i.e, at day 18, Fig. 5-2 A). From this 3-D graph, we visualized linear trends and calculated linear correlation coefficients where increased survival proportion increased with expression of a specific protein (indicated by black arrows, Fig. 5-2 A). However, the relative survival proportions of the mice across all five experimental groups varied throughout the 50-day duration of the experiment. Thus, we generated a similar 3D-plot for all 21 time points of the experiment. For each time point, we then calculated the linear Pearson correlation coefficient. Table 5-1 (column 1) indicates the cytokines and growth actors with significant ($p<0.05$) linear Pearson correlation coefficients ($|\rho|>0.875$). We considered several different passages of the MSCs, given our group's previous and ongoing work regarding the emergent heterogeneity of MSCs under typical *in vitro* culture expansion pressures; p6 represents passage 6 or approximately 12 population doublings *in vitro* under the expansion culture conditions at the time of that study used to acquire the mouse survival data, and as described previously [202].

As a linear correlation between MSC secreted factors and mouse survival is not anticipated *a priori*, we also conducted partial least squares regression (PLSR) as a separate statistical regression method to determine secreted factors significantly correlated with survival. A 2-component model was sufficient to capture over 90% of the variance in both the response (survival) and predictor (expression) variables (see Appendix B Fig. B-1). Figure 5-2 B shows the predictor and response loading vectors projected into the 2D principal component space calculated from PLSR. Each predictor loading vector represents the survival proportions at each time point of the study while each response loading vector represents the expression of each protein analyzed in the secretome. The predictor loading vectors closest to the response loading vectors were those growth factors and cytokines that were most strongly correlated with survival. In this model, we did not observe any secreted factors that were anti-correlated with survival. Table 5-1 (column 2) indicates the proteins most highly-correlated with increased survival as determined from PLSR. We calculated the regression coefficients and intercepts from PLSR to construct predicted survival curves. Using the same model data, we used PLSR to predict survival curves for the five groups considered in those previously reported *in vivo* experiments (Figs. 5-2 C-D). The predicted survival curves (dotted lines, Fig. 5-2 C) corresponded closely

with the original model data (solid lines, Fig. 5-2 C). Figure 5-2 D also indicates parity between our regression model and those experimental data, with a slope of approximately unity when graphing the predicted or fitted response from PLSR against the original training data.

Table 5-1 also indicates the cytokines and proteins that were identified from both statistical regression methods, suggesting strong correlations with improved survival. These secreted factors included interleukin-6 (IL-6), interleukin-8 (IL-8), bone morphogenetic protein 2 (BMP2), epidermal growth factor (EGF), fibroblast growth factor 1 (FGF1), regulated on activation, normal T cell expressed and secreted (RANTES), vascular endothelial growth factor A (VEGF-A), and angiopoietin-1 (ANG-1). We calculated significant Pearson correlations for Thrombopoietin (THPO) and interleukin-15 (IL-15), but these factors were not also identified in PLSR. On the other hand, monocyte chemoattractant protein 1 (MCP-1) was identified in PLSR, but not in linear Pearson correlations. For further analysis and exploration of individual proteins in the PLSR model, please refer to Appendix B, section B.4.

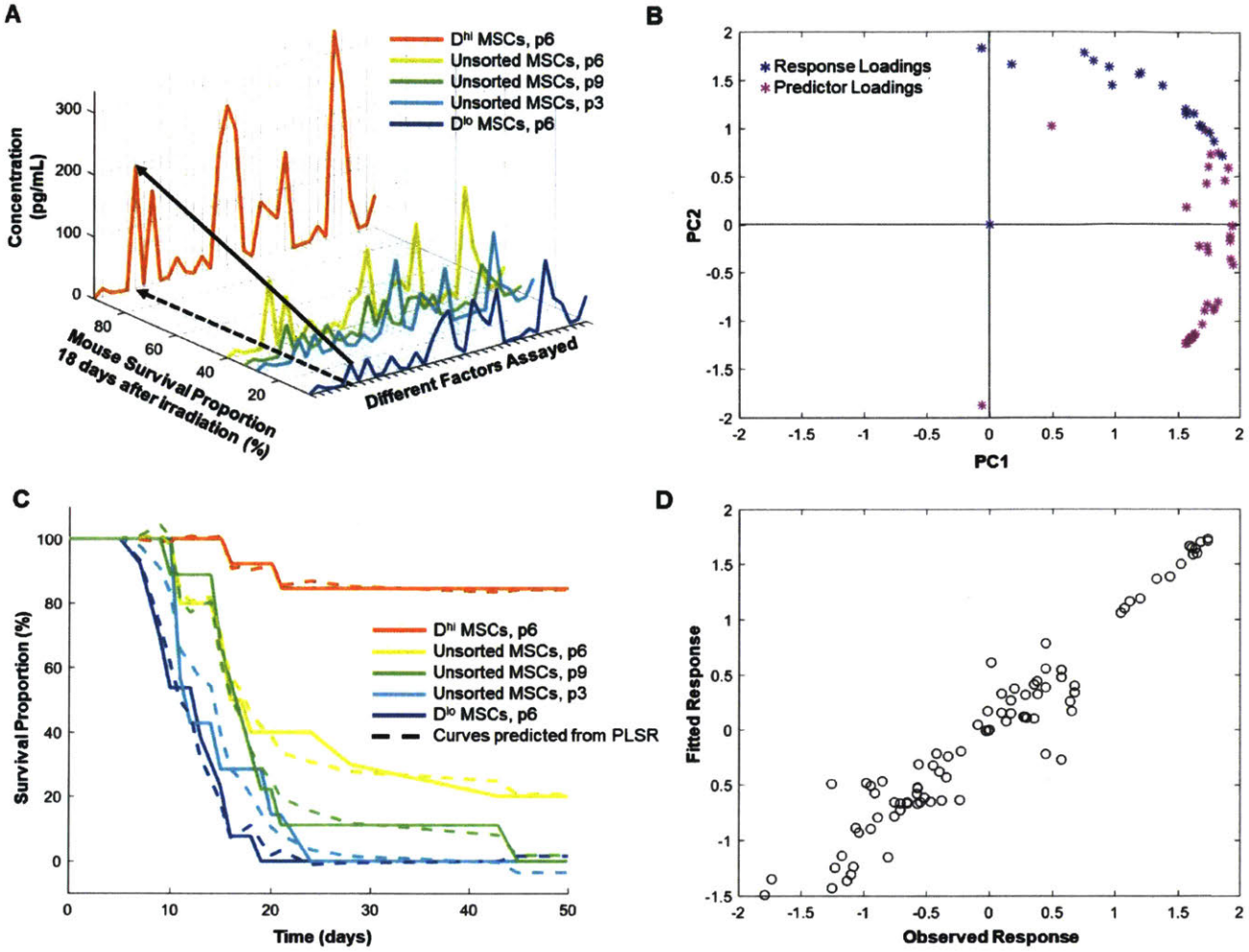

Figure 5-2. Training Data and Regression Modeling. A) Expression data of 35 secreted proteins are plotted against the mouse survival proportions at 18 days post-irradiation. Secreted protein concentrations were assayed prior to injection for five experimental MSC groups: D^{hi} MSCs (orange), unsorted MSCs at 3 different passages (yellow, green, cyan), and D^{lo} MSCs (blue). The small "p" indicates passage number of the cell population, e.g., p6 is passage 6 or approximately 12 population doublings *in vitro*. Black arrows visualize single protein's increasing concentration trending with increasing survival proportion. B) Loading vectors of predictor (purple stars) and response (blue stars) variables are plotted in 2-dimensional principal component plot from PLSR. C) Survival curves from all five experimental groups are plotted with survival curves predicted from PLSR model (dashed line). D) Every data point from the model is plotted as fitted data against the experimental or observed data.

Table 5-1. Proteins Significantly Correlated with Survival

Pearson Linear Regression	Partial Least Squares Regression	Overlapping Proteins
ANG-1	IL-6	IL-6
BMP2	IL-8	IL-8
EGF	BMP2	BMP2
FGF1	EGF	EGF
IL-15	FGF1	FGF1
IL-6	MCP-1	RANTES
IL-8	RANTES	VEGF-A
RANTES	VEGF-A	ANG-1
THPO	ANG-1	
VEGF-A		

ANG-1 = angiopoietin-1; BMP-2 = bone morphogenetic protein 2; EGF = epidermal growth factor; FGF-1 = fibroblast growth factor 1; IL-6 = interleukin 6; IL-8 = interleukin 8; IL-15 = interleukin 15; MCP- = monocyte chemoattractant protein 1; RANTES = regulated upon activation, normally T-expressed, and presumably secreted, also known as CC-Motif Chemokine Ligand 5; THPO = thrombopoieitin; VEGF-A = vascular endothelial growth factor A.

5.4.2 Secretome Modulation and Training Data

To obtain new training data for this model correlating the mechanically modulated MSC secretome with mouse survival, we expanded MSCs on PDMS substrata of stiffness varied across three orders of magnitude (shear elastic storage modulus G' (1 Hz) of 1, 10, or 100 kPa, as characterized previously [90]). We then characterized the resulting conditioned media using a Luminex-based panel and multiple ELISAs. We calculated the Spearman rank-based correlation between substratum stiffness and expression, and identified significant correlations ($p<0.001$) for the concentrations of a dozen different secreted proteins (Fig 5-3 A). Because we calculated correlations for every factor assayed, we corrected the critical p-value using a Bonferroni correction to account for multiple hypothesis testing. This analysis indicated that the concentrations of these dozen factors increased with decreasing substratum stiffness.

In addition to characterizing the MSCs grown on PDMS, we also characterized the secretome of MSCs grown on polystyrene in parallel, as a standard of comparison to our previous results and as a typical culture condition for MSCs used in preclinical studies. Specifically, we characterized the secretome of unsorted MSCs and D^{hi} MSCs from the same MSC donor grown on tissue culture polystyrene (TCPS). In all subsequent results, we indicated data for MSCs expanded on TCPS as black-striped bars, to emphasize that these MSCs are grown on a material with surface chemistry distinct from PDMS (Fig. 5-3 B). Of course, TCPS is also significantly stiffer (~ 1 GPa) than the PDMS substrata that we considered herein (1 – 100 kPa), but we do not draw inferences of mechanical cues from comparisons with TCPS due to the other marked differences between these polymeric surfaces.

Figure 5-3 B shows the concentrations of nine secretome factors identified through statistical analysis to be correlated with survival, for five experimental groups of MSC expansion conditions (Table 5-1). Similar to the expression data obtained in previous experiments [202], the D^{hi} cells exhibited higher expression of these factors than the unsorted MSCs on polystyrene (Fig. 5-3 B). For the factors statistically correlated with improved hematopoietic recovery, we observed that MSCs expanded on the most compliant PDMS substrata (1 kPa) exhibited expression levels similar to or greater than that of the D^{hi} MSC subpopulations (Fig. 5-3 B). We used these secretome data for subsequent model predictions.

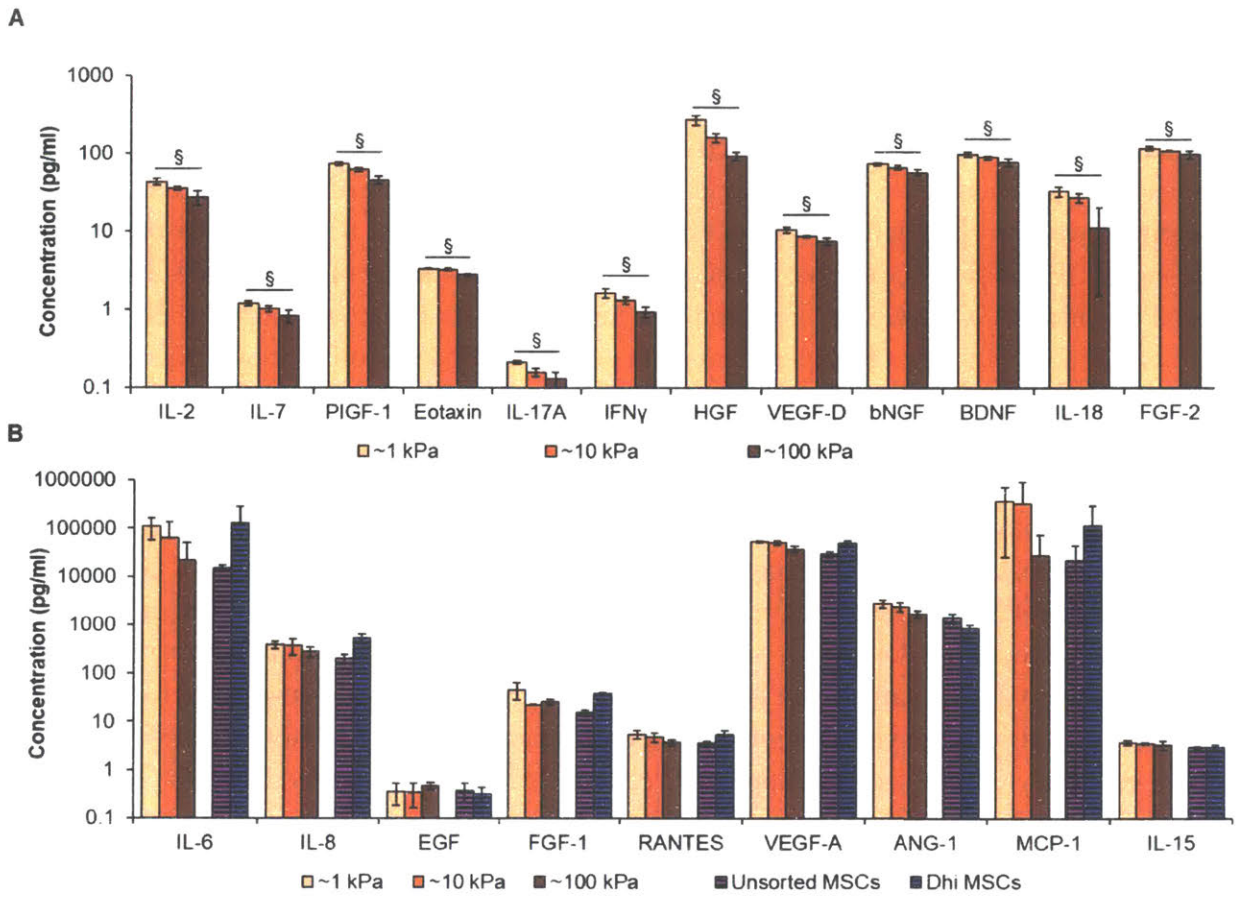

Figure 5-3. Secretome Characterization and Test Data. A) Unsorted MSCs were expanded on all PDMS substrata of varying stiffness (1, 10 and 100 kPa PDMS) for 7 days, represented by light, medium, and dark orange colors, respectively.) Expression of MSC secreted proteins that have significant trends (§ $p<0.001$) with cell culture substratum stiffness as determined from Spearman's rank-based correlation. B) As a comparison to MSCs on PDMS, unsorted and D^{hi} MSCs were also grown on TCPS and are represented by striped purple and blue bars, respectively. Expression of MSC secreted proteins identified in Table 1 were assayed across all five different culture conditions. All data are plotted with ±standard deviation.

5.4.3 Non-contact co-culture

To determine whether such a mechanically modulated secretome was sufficient to affect biologically relevant outcomes, we then co-cultured human HSPCs – a cell type that grows in suspension – with human MSCs adhered to PDMS of varied stiffness. As a standard of comparison, we also considered a typical HSPC expansion protocol, with no MSCs present in PS wells. Indeed, Fig. 5-4 A shows that HSPC proliferation depended strongly on the substratum material to which MSCs were adhered, and was maximized for the most compliant PDMS substratum (1 kPa). In separate experiments that quantified HSPC proliferation under contact co-culture with the MSCs that were adhered to the substrata, we observed similar increases in proliferation with decreasing PDMS stiffness (see Fig. 5-5 A and Appendix A Fig. A-10). Percentages of HSPCs expressing surface antigens indicating common myeloid and lymphoid progenitor commitment (CD123+ and CD10+, respectively) were not modulated by MSC substratum stiffness (Fig. 5-4 B). In contrast, we observed that HSPC expression of CD34+ increased and CD123+ decreased with decreasing PDMS stiffness, when in contact co-culture with MSCs (see section 5.4.4 and Appendix A Fig. A-10). Thus, the absolute numbers of HSPCs expressing either CD123+ or CD10+ (Fig. 5-4) were both maximized in co-culture for the most compliant MSC substrata. After co-culture and upon chemical induction of these HSPCs into terminal erythrocyte lineages, cells appeared red, enucleated and expressed CD235A (see Appendix A Fig. A-11 and associated discussion). This finding is consistent with the retention of the ability to terminally differentiate into red blood cells.

To confirm that the HSPCs retained their ability to differentiate and engraft *in vivo* after non-contact co-culture, these human HSPCs were subsequently injected into irradiated mouse models (see Appendix B, Section B.3 for further experimental details). We assayed chimerism in the blood of these mice, which was indicative of successful differentiation and engraftment (see Appendix B, Fig. B-3 for results).

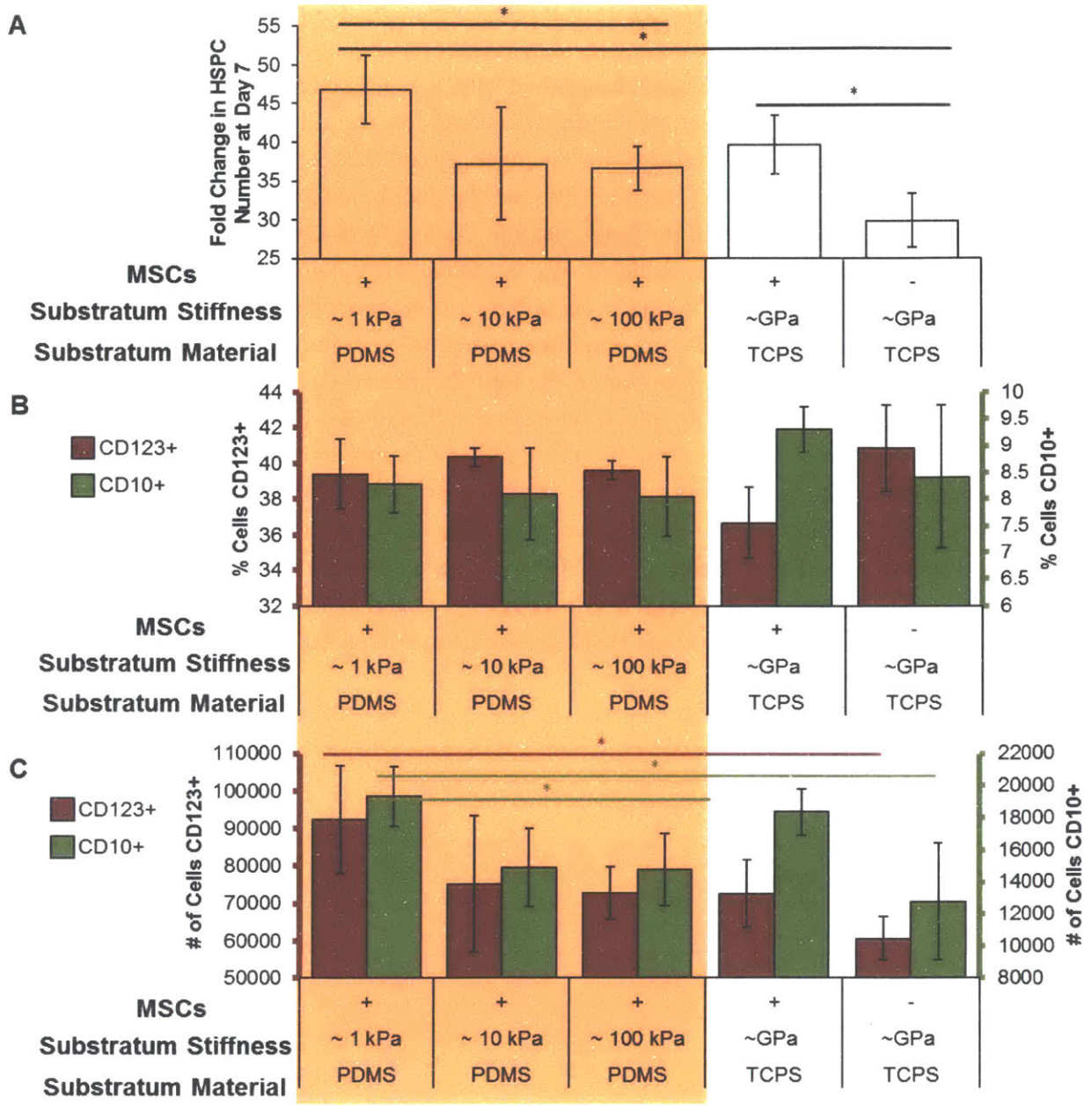

Figure 5-4. *In Vitro* Hematopoietic Recovery: HSPC and MSC Non-Contact Co-Culture. (A) HSPCs were counted 7 days after being in non-contact co-culture with MSCs on various substrata. Far right bars represent typical HSPC growth conditions with no hMSCs on tissue culture polystyrene. Conditions where cells were grown on PDMS substrata are highlighted in orange. (B-C) Surface marker expression of CD123 (maroon) and CD10 (dark green) were assayed using flow cytometry. (B) Percentage of positive CD123 expression is on the left, primary axis, percentage of positive CD10 expression is displayed on the right, secondary axis. (C) Number of positive CD123 expressing cells is on the left, primary axis, number of positive CD10 expressing cells is displayed on the right, secondary axis. Statistical differences were determined using unpaired, one-tailed Student's t-test with unequal variance (*$p<0.05$).

5.4.4 Contact co-culture

To determine whether these mechanoprimed MSCs could plausibly promote hematopoiesis *in vivo*, we first considered an *in vitro* assay for hematopoietic stem cell proliferation. Specifically, we co-cultured our mechanoprimed MSCs with human hematopoietic stem and progenitor cells (HSPCs). These HSPCs are the population of stem and progenitors that repopulate the blood cell lineages of the bone marrow. As a control and standard of comparison, we also expanded the HSPCs in monoculture. We found that HSPC proliferation was maximized when grown in co-culture with MSCs that were adhered to the most compliant PDMS substrata, both at day 4-5 in co-culture (Fig. 5-5 A) and after 1 week in co-culture (Fig 5-5 B). We also characterized the surface marker expression of the HSPCs after co-culture via flow cytometry. Figure 5-5 C shows representative dot plots, wherein quadrant 3 (the CD34+CD123- population) demonstrated a significant increase (**$p<0.005$) in CD34+ expression for HSPCs co-cultured on the more compliant of the two PDMS substrata (Fig. 5-5 D). When considering the common myeloid progenitor marker CD123, also known as IL-3Rα, we found that the CD123+CD34- expression was increased for co-culture with MSCs grown on either of those PDMS substrata as compared with the current standard, TCPS. Moreover, we found that this myeloid priming was maximized significantly (*$p<0.01$) when HSPCs were grown in co-culture with MSCs on 100 kPa PDMS (Fig. 5-5 E).

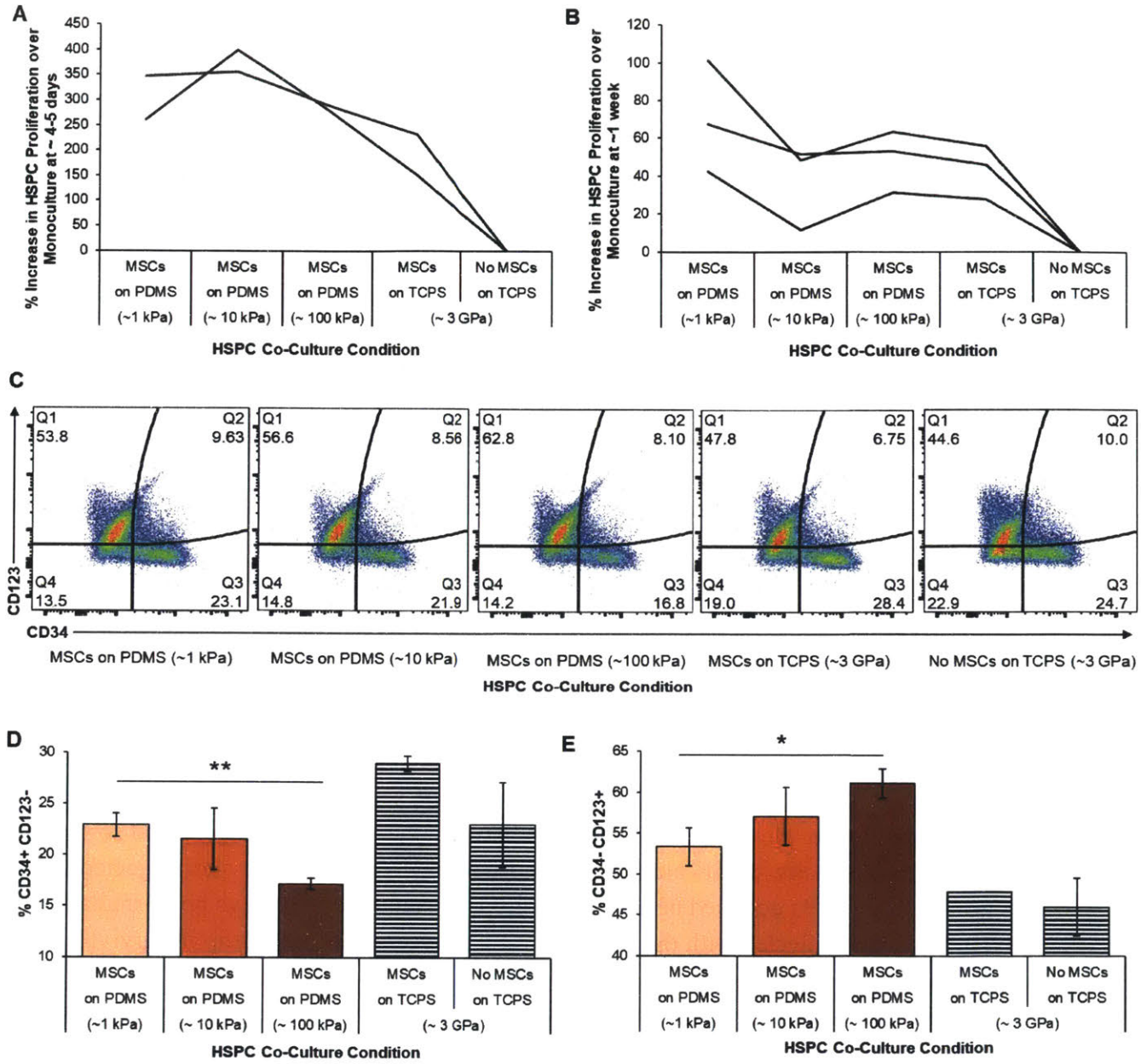

Figure 5-5. *In Vitro* Hematopoietic Recovery: HSPC and MSC Contact Co-Culture. Hematopoietic stem and progenitors (HSPCs) were grown in direct contact co-culture with MSCs grown on 1, 10, 100 kPa PDMS and TCPS. Proliferation of HSPCs in these co-culture conditions relative to monoculture were determined at A) 4-5 days and B) 1 week after co-culture. Individual lines represent replicate experiments. C) HSPC surface marker expression of CD123 and CD34 was assayed using flow cytometry. D) Mean % expression of CD34+ and CD123- cells are plotted with standard deviations (**$p<0.005$). E) Mean % expression of CD34- and CD123+ cells are plotted with standard deviations (*$p<0.01$). D-E) Co-culture on PDMS of increasing stiffness (1, 10, 100 kPa) are plotted in darkening shades of orange, respectively. Co-culture and monoculture of HSPCs are plotted with black- and white-striped bars. Data are plotted with ±standard deviation, N=3 across replicate wells.

5.4.5 Mouse survival and weight recovery

After observing increased HSPC proliferation and changes in HSPC surface marker expression *in vitro* (Figs. 5-4 and 5-5) when grown in co-culture with our mechanoprimed MSCs, we next considered how these mechanoprimed MSCs could affect hematopoietic recovery *in vivo*. Using our regression model (Fig. 5-2) and the characterized secretome expression of the mechanoprimed MSCs (Fig. 5-3), we first predicted the survival graphs using our PLSR model and measured expression data (Fig. 5-6 A). Injection of MSCs expanded on 1 kPa PDMS was predicted to exhibit the highest end-point survival of ~50% at day 50, the duration of the experiment (Fig. 5-6 A). When considering only the MSCs expanded on TCPS (blue and purple lines), as expected, the D^{hi} cells were predicted to exhibit higher survival than the unsorted cells over the entire experiment duration (Fig. 5-6 A). Among the PDMS substrata (three orange lines), mice were predicted to exhibit higher survival percentages when injected with MSCs grown on PDMS substrata of decreasing stiffness (Fig. 5-6 A). In other words, mouse survival was predicted to be maximized for unsorted MSCs grown on PDMS of stiffness 1 kPa.

We observed that some of these predicted relative trends were replicated in our animal model experiment (Fig. 5-6 B). For example, the MSCs grown on 1 kPa PDMS substrata yielded the highest survival with significantly higher survival curves than MSCs grown on 100 kPa PDMS and unsorted MSCs grown on TCPS ($p = 0.0027$ and 0.0001, respectively, as calculated from Mantel-Cox or Log-Rank test). Also consistent with the PLSR predictions, the end-point survival proportion of mice injected with MSCs grown on 1 kPa PDMS was greater than for D^{hi} MSCs (83.2% vs. 55.6%); this survival percentage for MSCs on 1 kPa PDMS exceeded our PLSR model prediction. However, the difference between these mechanoprimed and sorted D^{hi} MSCs was not statistically significant ($p > 0.05$). Additionally, the mouse cohort injected with MSCs grown on 100 kPa declined below that of the 1 kPa cohort at ~40 days post-irradiation. Finally, in the cohort injected with the D^{hi} cells, we observed a near 50% drop in survival within the first 15 days, which then plateaued (Fig. 5-6 B).

Several findings were not predicted precisely by the PLSR model. For example, for the first 40 days of the study, unsorted MSCs cultured on both PDMS substrata (100 kPa and 1 kPa) yielded higher survival proportions than the D^{hi} cells. The PLSR model predicted cohorts administered the unsorted MSCs on TCPS to fare worse (i.e., lower survival percentages by day 40) than observed. In fact, the mouse cohort injected with unsorted MSCs on TCPS fared similarly to the D^{hi} cells up to day 37 post-treatment, and only later proceeded to decline rapidly. Pairwise comparisons across survival curves showed that all treatments with MSCs yielded statistically significant ($p<0.05$, calculated from Mantel-Cox or Log-Rank test) higher survival when compared to no-treatment (saline injection) controls. All cohorts injected with MSCs also had much higher median survival times, suggesting improved support of hematopoietic recovery. (Mice with no treatment exhibited a median survival time of 13 days, comparable to median survival times in previous studies of radiation rescue [202], but not predicted quantitatively by the PLSR model because there are no expression data corresponding to the no-treatment

condition.) When comparing among MSC-injected cohorts, the cohorts injected with unsorted MSCs grown on 1 kPa PDMS and D^{hi} MSCs both exhibited median survival times of >50 days, but the survival proportion for mice injected with MSCs grown on 1 kPa PDMS exhibited a much higher survival proportion (>80%) at this experiment endpoint of 50 days. Moreover, mice injected with D^{hi} MSCs had a much higher hazard ratio (calculated from Mantel-Haenszel method, for projecting difference in outcomes when survival curves are statistically indistinguishable) of 4.4 when compared to MSCs expanded on 1 kPa PDMS. That is, mouse survival was more than four times more likely for injection of mechanoprimed vs. sorted MSCs. Both the unsorted MSCs grown on TCPS and 100 kPa PDMS exhibited lower median survival times of 39 days and 49 days, respectively. This suggests that MSCs mechanoprimed on 100 kPa PDMS still yielded an improvement in survival when compared to standard MSC expansion on TCPS. Concurrent with improved survival, we also recorded the weight recovery of the mice (see Appendix B Fig. B-2), which was indicative of overall animal health and recovery after induced hematopoietic failure.

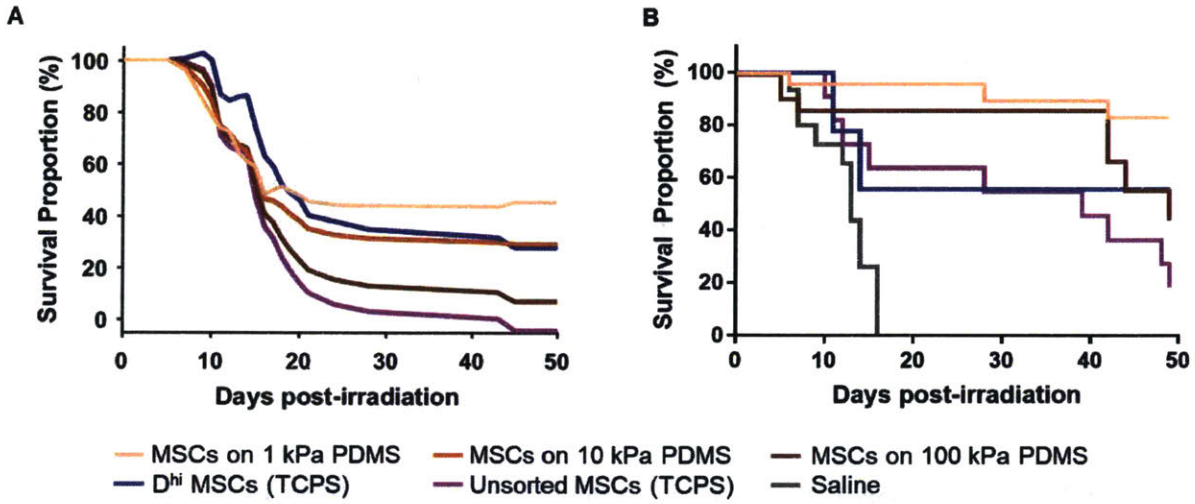

Figure 5-6. *In Vivo* Hematopoietic Recovery: Mouse Survival. A) Survival curves were predicted using the PLSR model for mice injected with unsorted MSCs grown on PDMS (three orange lines), D^{hi} MSCs (blue line) on TCPS, and unsorted MSCs (purple line) on TCPS. PDMS substrata of varying stiffness (1, 10 and 100 kPa PDMS) are represented by light, medium, and dark orange colors, respectively. B) Mice were irradiated with 4.0 Gy gamma irradiation at day 0 and injected with MSCs from four experimental groups at day 1. These four experimental groups included unsorted MSCs grown on 1 kPa PDMS (light orange), 100 kPa (dark orange) PDMS, TCPS (purple) and D^{hi} MSCs grown on TCPS (blue). A no treatment or saline control is also included in gray. Mouse survival for each group was tracked over the course of 50-days after irradiation and N≥9 for all conditions.

5.4.6 Complete blood count

In addition to mice weight and survival, we also analyzed the complete blood counts (CBCs) of mice from the no-treatment control group, and the two groups injected with unsorted MSCs grown on PDMS of lower and higher stiffness (Fig 5-7). We drew blood from mice prior to the experiment and prior to irradiation (drawn multiple weeks before, but graphed at day 0) to determine the basal concentrations of white blood cells (WBCs), red blood cells (RBCs), and platelets (PLTs). At early time points of 1-week post-irradiation, we observed no differences in CBCs, as none of the mice had begun to recover. At 2 weeks post-irradiation, we observed that the WBC and PLT concentrations began to recover, indicated by upwards trends, for mice injected with MSCs grown on the more compliant (1 kPa) PDMS (Fig. 5-7 A, C). Interestingly, at this same time point, the RBC concentration began to recover for mice injected with MSCs grown on the stiffer (100 kPa) PDMS (Fig. 5-7 B). At 4 weeks, mice injected with MSCs grown on both PDMS of either stiffness recovered or exceeded the baseline minimum CBC for that cohort. At the last time point (5 weeks) at which we analyzed CBC, we observed that all blood and platelet counts were closest to basal levels for mice injected with MSCs grown on the more compliant (1 kPa) PDMS.

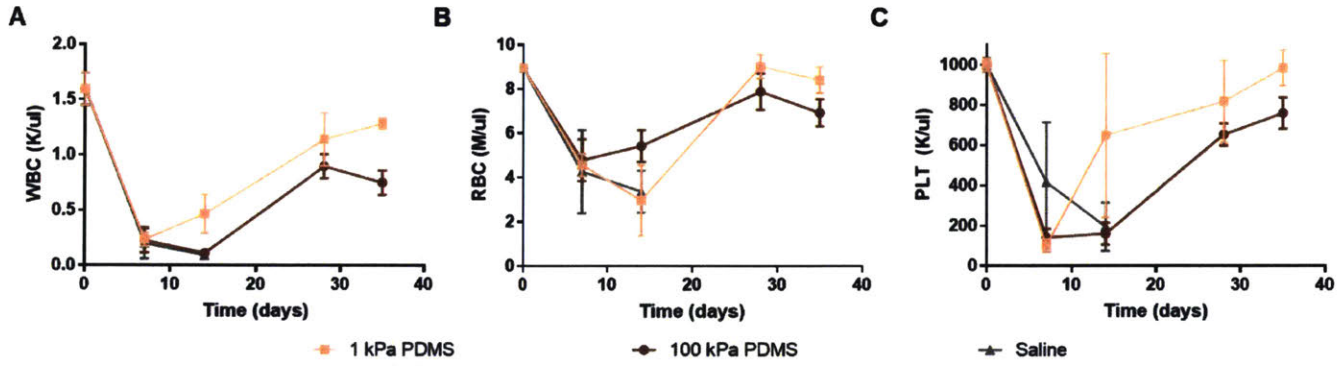

Figure 5-7. *In Vivo* Hematopoietic Recovery: Complete Blood Count (CBC). A-C) CBC analysis was performed at 7, 14, 28, and 35 days post-irradiation. Blood was collected from two experimental mouse groups: mice injected with MSCs grown on 1 kPa PDMS (light orange) and 100 kPa PDMS (dark orange). At early times of 7 and 14 days, the no treatment saline control group (gray) was also included. Mean A) white blood cell concentration, B) red blood concentration, and C) platelet concentrations are plotted with SEM. Blood was drawn from at least three mice per time point (N≥3).

5.5 Discussion

Regression techniques such as linear Pearson correlations and PLSR are useful in identifying proteins that are highly correlated with improved survival or hematopoietic recovery (Table 5-1 and Fig. 5-2 A-B). From both of these techniques, we identified eight proteins that were significantly correlated with mouse survival after irradiation injury indicative of improved hematopoietic recovery. We deem these proteins or cytokines as those secreted factors that may play a direct role in supporting hematopoietic recovery, or at least convey strong correlations with that clinical endpoint. To validate the importance of these identified proteins, we also computationally removed or incorporated expression data of each protein individually (see Appendix B, section B.4). Moreover, using PLSR, we generated a predictive model (Fig. 5-2 C-D) to predict survival trends of recovery from new sets of secretome expression data.

After creating a regression model to predict mouse survival, we applied the model to data obtained from a set of MSCs modulated with cell-material interactions. In a previous published study, we demonstrated that we could mechanically modulate the MSC secretome by growing the MSCs on PDMS substrata of varying stiffness [113]. Here, we used these same material mechanics to tune the MSC secretome for use as test data in our regression model of animal survival (Fig. 5-3 A). To determine if these changes in expression could be physiologically relevant in supporting hematopoietic recovery, we then compared the expression of MSCs cultured on PDMS to that of D^{hi} MSCs and unsorted MSCs grown on TCPS and obtained from the same donor cell source (Fig. 5-3 B). From our secretome characterization, we found that mechanically modulated MSCs can attain secretome expression levels similar to or higher than the D^{hi} cells (Fig. 5-3 B) of the proteins correlated with survival (Table 1). Together, these data suggest that we can use material mechanics to modulate the unsorted MSCs secretome to approximate that of the therapeutically effective sorted MSCs, or D^{hi} phenotype.

Such mechanical priming of the MSC secretome *in vitro* could plausibly support HSPC production *in vitro* and hematopoietic recovery in bone marrow upon *in vivo* administration. Thus, we next validated *in vitro* that our mechanically modulated MSCs could have a direct effect on HSPC behavior. Figures 5-4 and 5-5 summarizes the effect of PDMS substratum stiffness on co-cultured HSPCs. Note that in Figure 5-4 cells were co-cultured in non-contact conditions between the MSCs and HSPCs to explore the effects of the secretome independently of heterotypic cell-cell interactions and to decouple HSPC-substrata interactions [142]. MSCs [264,265] and extracellular vesicles from MSCs [287] have been shown to promote *in vitro* proliferation of HSPCs in co-culture and prime the HSPCs for myeloid and erythroid commitment. In agreement with prior studies, we demonstrated that presence of MSCs (+MSC condition) to typical HSPC expansion conditions (-MSC condition, on PS in monoculture) can significantly increase HSPC proliferation (Fig. 5-4) [270,274,283,288,289]. Moreover, we found that HSPC proliferation increased even further over current materials and protocols when co-cultured with MSCs adhered to PDMS substrata. When expressed as a percentage increase in the fold-change of HSPC proliferation, this capacity to produce HSPCs increased by 57% and 23%

on PDMS of lowest (1 kPa) and highest (100 kPa) stiffness, respectively, with respect to HSPCs expanded on PS in the absence of MSCs (Fig. 5-4 A).

This increase in HSPC proliferation with decreasing PDMS stiffness persisted for HSPCs in direct contact with the MSCs (see Fig. 5-5 A-B and Appendix Fig. A-10), indicating that MSC secretome-stimulated proliferation is not abrogated by heterotypic cell-cell contact. We observed an overall increase in HSPC proliferation when HSPCs were grown in co-culture with MSCs on our most compliant PDMS substrata. However, these trends in proliferation were highly variable and time dependent (Fig 5-5 A-B). For example, there were proportionally larger increases in proliferation at day 4 (~300-400% increase) than at day 7 (~50-100% increase). Additionally, for some replicate experiments, we noted the maximum increase in proliferation on the 10 kPa PDMS substrata instead of the more compliant 1 kPa substrata (Fig 5-5 A). We attributed this high variance due to the fact that we used a different HSPC human donor for each independent experiment, with the potential for significantly different initial genetic profiles among HSPC donors. In the *in vivo* experiments, we were not subject to these same limitations because we used a single strain of mice that were all genetically identical, and we obtained our MSCs from a single donor source and subjected them to varied culture conditions.

To explore whether lineage commitment of the HSPCs was also modulated by the MSC mechanical secretome, we compared HSPC expression of CD123+ (also known as IL3 receptor) as a marker of common myeloid progenitor commitment [290,291], and CD10+ as a marker of common lymphoid progenitor commitment [292]. For all conditions in non-contact co-culture, percentages of lymphoid and myeloid progenitor commitment were statistically indistinguishable when compared to HSPCs expanded alone in monoculture on polystyrene. This suggests that non-contact co-culture with the mechanically modulated MSCs does not shift the differentiation potential of the HSPCs detectably. However, a significantly larger number of both CD123+ and CD10+ expressing HSPC subpopulations was obtained when in non-contact co-culture with MSCs adhered to the most compliant PDMS. Proliferation of all progenitor phenotypes can thus be enhanced *in vitro*, without altering the potential for subsequent terminal differentiation induction (Appendix Fig. A-11). One can maximize proliferative capacity of HSPCs while maintaining the differentiation potential across all lineages. After non-contact co-culture, we then transplanted the human HSPCs into mouse models of radiation injury and assayed chimerism within the mouse peripheral blood (see Appendix B, section B.3). We found that the HSPCs grown in non-contact co-culture with mechanoprimed MSCs (1 kPa) exhibited the highest degree of chimerism at week 12 (see Appendix B, Fig. B-3). These data suggest that the non-contact co-culture condition with mechanoprimed MSCs best promotes *ex vivo* expansion of HSPCs that also retain their ability to differentiate and engraft *in vivo*.

On the other hand, contact co-culture promoted PDMS stiffness-dependent expression of a myeloid progenitor marker (CD123+), so HSPC naïveté was not maintained upon direct contact with MSCs adhered to PDMS of varying stiffness (Figure 5-5 and Appendix Fig. A10).

We observed higher CD123+ expression on HSPCs grown in contact co-culture with MSCs on the stiffest 100 kPa PDMS substrata (Fig 5-5 E). This suggests that at a co-culture time of 1 week, our MSCs grown on the stiffest PDMS substrata could prime the HSPCs towards myeloid lineages [293,294]. Additionally, we observed a decrease in CD34+ expression concurrent with this increases in CD123+ (Fig. 5-5 D). This suggests that while MSCs grown on the 100 kPa PDMS substrata may be useful for myeloid priming of the HSPCs, the MSCs grown on the 1 kPa PDMS may be better for maintaining the naivety of the HSPCs. Nevertheless, these HSPCs grown with MSCs on 1 kPa PDMS express lower CD34+ than those grown on TCPS. These concurrent changes in CD123+ and CD34+ expression suggest that our mechanically-modulated MSCs may play a direct role in regulating the proliferation and differentiation of HSPCs. In both co-culture cases, modulation of MSC mechanical environment via the adherent substratum was sufficient to then modulate proliferation and differentiation of HSPCs.

We then explored how our mechanically modulated MSCs could affect hematopoietic recovery *in vivo*. We first used our PLSR model to predict the survival curves of the mice injected with MSCs grown on our three different PDMS substrata. For these *in vivo* experiments, we chose to deliver and compare outcomes for MSCs grown on the stiffest (100 kPa) and most compliant (1 kPa) substrata, because those two cell populations yielded statistically significant differences in HSPC surface marker expression when grown in co-culture (Fig. 5-5 D-E). Although our model predicted some relative trends in survival across experimental groups correctly, the predicted survival proportions were uniformly lower than the experimental data (Fig 5-6 A-B). We attribute this discrepancy in our PLSR model to the limited expression data used to construct the model. We used targeted, antibody-based techniques (Luminex & ELISAs) or targeted assays to characterize the concentration of only 35 proteins. However, there are likely other proteins that could play a role in supporting hematopoietic recovery, and these were not included in our regression model because the initial data set was constrained by a prudently targeted profiling approach. For example, we found that osteopontin is highly upregulated in our MSCs grown on PDMS substrata [90]. Osteopontin is also a marker for osteoprogenitors and of the D^{hi} MSC phenotype in our previous studies on hematopoietic recovery [202]. In the literature, osteopontin has been demonstrated to play a role in regulating the self-renewal capacity of HSPCs [91,266,268]. However, we were unable to incorporate osteopontin in our initial regression model, as it was not known at the time of those *in vivo* experiments to be correlative with survival outcomes. Thus, we did not acquire osteopontin expression across all experimental groups used to construct our predictive model. A non-targeted approach to more wholly characterize the MSC secretome can identify additional proteins including osteopontin, which also may be correlative and crucial in supporting hematopoietic recovery and would then also improve the accuracy of the animal survival model.

In addition to observing mouse survival over the course of the experiment, we also tracked weight at multiple time points. Weight recovery was concurrent with improved survival, with surviving mice recovering approximately $\geq$ 90% of their original weight by day 35 (see

Appendix B, Fig. B-2 and Table B-1). Mice with induced hematopoietic failure and then injected with MSCs grown on the most compliant (1 kPa) PDMS exhibited the highest survival proportion of 83.2% at the end of the experiment (Fig. 5-6 B). This suggests that of all conditions tested, MSCs grown on compliant substrata, with stiffness comparable to bone marrow [81,295], were most efficient at supporting radiation rescue *in vivo*. Together, these findings demonstrate that by growing the unsorted MSCs on PDMS, therapeutic potential to support hematopoietic recovery is realized even more effectively than by sorting D^{hi} MSC subpopulations. The animal cohorts injected with D^{hi} MSCs and the unsorted MSCs on TCPS exhibited similar survival and weight recovery in the first five weeks of the experiment (see Fig. 5-6 B and Appendix B, Fig. B-2 B-C). Note that the D^{hi} MSCs in Fig. 5-6 B (used in the present *in vivo* experiments used to validate the model) and D^{hi} MSCs in Fig. 5-2 C (used in previously published *in vivo* experiments used to construct the model) were obtained from different human donors. Thus, the differing survival responses can also be attributed in part to this donor cell source variation, with corresponding biological variation in secretome profile. It is plausible that the therapeutic efficacy of the D^{hi} MSCs is donor dependent, and thus that biophysically sorting of donor cells maybe insufficient as a sole method to improve therapeutic efficacy in supporting hematopoietic recovery. However, our results demonstrate that mechanically modulated MSCs can robustly improve the secretory profile and improve radiation rescue, as compared to both sorted D^{hi} MSC subpopulations and unsorted MSCs grown on TCPS and obtained from the same donor (Fig 5-6 B). In the present experiments, mechanoprimed MSCs resulted in a fourfold decrease in risk hazard (likeliness of survival) and circumvented the fivefold reduction in cell yield by obviating the biophysical sorting of a subpopulation.

After mice nearly recovered initial weights at day 35, we obtained blood samples from multiple mice within cohorts injected with MSCs grown on 100 kPa or 1 kPa PDMS; we conducted cheek bleeds to obtain minimally sufficient blood volumes for CBC results that still facilitated continued recovery beyond day 35. Nevertheless, that procedure induced a minor injury to the recovering mouse (~10-20% blood volume loss) and resulted in subsequent weight loss. The mice injected with MSCs grown on 100 kPa PDMS continued to lose weight after this procedure, and did not recover initial weight at the end of the experiment (see Appendix B Fig. B-2 A and Table B-1). Interestingly, however, mice injected with MSCs expanded on the more compliant (1 kPa) PDMS ceased weight loss after day 42 (see Appendix B Fig B-2 A). At 49 days, or two weeks after re-injury, mice injected with MSCs expanded on 100 kPa PDMS exhibited significantly lower weight recovery (adjusted $p<0.05$) than mice injected with MSCs expanded on 1 kPa PDMS (see Appendix B, Fig. B-2 A and Table B-2). This comparison suggests that mechanoprimed MSCs (expanded on 1 kPa PDMS) could support long term hematopoiesis including recovery from re-injury after initial radiation-induced hematopoietic failure.

From the complete blood count analysis (Figs. 5-7 A-C), we observed that mice injected with MSCs grown on PDMS recovered white blood cell, red blood cell, and platelet levels by

day 35. At that time point, all three blood count components were highest for mice injected with the MSCS grown on more compliant PDMS (Fig. 5-7 A-C). At 35 days, WBC concentrations were significantly higher ($p=0.001$, calculated from one-tailed student's t-test with unequal variance), but RBC and platelet levels were insignificantly higher ($p=0.057$ and $p=0.086$, respectively) due to low sample size ($n = 5$ or 6) and large variance. Nevertheless, this suggests that such mechanoprimed MSC populations can support more efficient recovery of the hematopoietic lineages. Interestingly, at day 14 we observed a slightly higher concentration of RBCs ($p = 0.13$, $n = 3$) in the cohort injected with MSCs grown on the stiffer (100 kPa) PDMS (Fig. 5-7 B). Additionally, when comparing across experimental conditions only, we observed a significant weight increase (adjusted p-values <0.05, see Appendix B Table B-2) at days 7 and 14 when comparing mice injected with MSCs grown on 100 kPa and D^{hi} MSCs (see Appendix B Fig B-2 C and Table B-1). This suggest that this second type of mechanoprimed MSCs could potentially support faster short-term recovery of RBCs and mouse weight than any other experimental condition, though this increased recovery was not sustained beyond day 30. This faster increase in RBC recovery may be analogous to the myeloid priming we observed in *in vitro* co-culture. Thus, the *in vitro* co-culture may serve as a useful model to determine the short term effects of how mechanoprimed MSCs can influence hematopoietic recovery.

5.6 Conclusion

In this study, we mined previous *in vitro* and *in vivo* data to identify key factors in the MSC secretome that were correlated highly with improved radiation rescue in an *in vivo* mouse model of hematopoietic failure. Our regression model generally predicted survival post-irradiation accurately, including the improved survival outcomes for MSCs cultured on materials that were orders of magnitude more compliant that the typical polystyrene materials (10^9 Pa) used for MSC expansion in preclinical studies. Despite these clear correlations between these MSC secretome elements and animal recovery, it remains an open question whether and how these identified factors play a role in directly supporting hematopoiesis. Nevertheless, we chose to explore how these identified secretome components could be used as predictive markers of an MSC phenotype that is therapeutically effective in promoting hematopoietic recovery.

We modulated the MSC secretome by tuning the extracellular mechanical properties of the cell culture substrata, engineering the cell culture-compatible material PDMS to range in stiffness from 10^3 to 10^5 Pa. By using these mechanical cues, we could obtain concentrations of the aforementioned key secretome components that were comparable to concentrations secreted by D^{hi} MSCs, a phenotype we previously showed to be effective in supporting hematopoietic recovery. This suggested that mechanical modulation of the MSC secretome could be tuned to physiologically relevant levels that could improve hematopoietic recovery, without the need to isolate minor subpopulations of cells expressing that secretome.

Thus, we went on to test whether these mechanically-modulated MSCs could support hematopoiesis *in vitro* and *in vivo*. Using co-culture models with HSPCs, we showed that our

mechanically-modulated MSCs could increase HSPC expansion. This MSC mechanopriming can be used to improve production of other cell types *in vitro* that can be subsequently used for *in vivo* applications such as hematopoietic recovery. For example, here HSPC proliferation was maximized in non-contact co-culture with MSCs adhered to the most compliant PDMS, without altering the multipotency of HSPCs for either myeloid (blood cell) or lymphoid (immune cell) lineages. Such increased production efficiency of HSPC-derived progenitors suggests promising clinical implications in simultaneously maximizing proliferation and differentiation of multiple hematopoietic lineages *in vitro*. Mechanoprimed MSCs also increased HSPC expansion in contact co-culture, and those MSCs mechanoprimed on stiffer PDMS (100 kPa) also exhibited increased myeloid priming (increase in CD123 and decrease in CD34) of HSPCs. This finding demonstrated that mechanically modulated MSCs could differentially modulate the expansion and differentiation of HSPCs *in vitro.* Mechanoprimed MSCs also resulted in markedly improved mouse survival, for a hematopoietic failure model induced by sub-lethal irradiation. Mice injected with MSCs grown on the most compliant PDMS had an overall survival proportion of 83%, which was higher than any other condition including state-of-art MSC expansion or size-sorted MSC subpopulations on TCPS. Moreover, for that same experimental group we also observed nearly complete weight recovery and recovery of all hematopoietic lineages (red and white blood cells and platelets). This suggests that we could improve the MSC capacity to indirectly support hematopoietic recovery by simply culturing MSCs on compliant PDMS substrata that elicit the desired secretome profile.

The partial least squares regression (PLSR) model developed herein successfully predicted *in vivo* hematopoietic recovery from MSC secretion data. This approach should be applicable generally to prediction of the therapeutic efficacy of other MSC populations. We additionally predicted and validated the ability of mechanically modulated MSC populations to facilitate bone marrow recovery in a mouse model of radiation-induced hematopoietic failure. This method of mechanopriming MSCs through modification of the material substratum stiffness is more scalable than previously reported sorting methods that isolated 20% of the cells as phenotypically desirable. In contrast, mechanopriming via the substratum mechanical cues affords that the full culture-expanded cell population will exhibit the predictably therapeutic phenotype. This validated modeling approach enables more efficient production of therapeutically viable MSCs for cell therapy applications *in vivo*, as well as new routes to more efficient HSPC production *in vitro*.

Chapter 6

Conclusions

This thesis explored two cell-based processes that are known to indirectly support hematopoietic repair and recovery *in vivo*: angiogenesis and mesenchymal stem cell (MSC) paracrine signaling. We specifically explored how biophysical and mechanical cues regulate these pathways *in vitro*, as well as how these cues can modulate vascular endothelial cell (VEC) or MSC phenotypes. These engineered VEC and MSC phenotypes can in turn be used to develop improved therapeutics for hematopoietic recovery. We divided the contributions of this thesis into three broad categories: angiogenesis *in vitro* (Section 6.1.1), characterization and modulation of the MSC secretome (Section 6.1.2), and improving hematopoiesis *in vitro* and *in vivo* (Section 6.1.3).

With reference to the discussion and concluding sections of Chapters 2-5, we summarize here the key results and scientific questions addressed throughout this thesis. Chapters 2-3 address key cues necessary to developing accurate models of angiogenesis *in vitro*. Chapters 4-5 span identification of the therapeutically effective MSC secretome and how we engineer the MSC secretome using mechanical cues. Lastly, Chapter 5 uses both *in vitro* and *in vivo* models to validate that these engineered MSCs improve HSPC expansion *in vitro* as well as promote hematopoietic recovery *in vivo*.

6.1 Contributions

6.1.1 Angiogenesis *in vitro*

Accurate *in vitro* models of angiogenesis are crucial to understanding how hematopoietic recovery is regulated by interactions with VECs. Whether this recovery proceeds chiefly through paracrine signaling or whether direct cell-cell interactions are required for VECs to support hematopoiesis still remains to be understood. Prior to asking these questions, *in vitro* models of angiogenesis must first be created to replicate and probe these interactions. This thesis contributes insight into how biophysical cues and mechanical cues regulate angiogenesis. We first explored how macromolecular crowding affects ECM formation and organization in the basement membrane of VECs (Chapter 2). We then determined whether or not static, mechanical strain analogous to the hoop strain exerted by contractile pericytes could promote angiogenic

sprouting (Chapter 3). Below, we list and answer the key questions addressed in the chapters of this thesis that pertain to generating improved *in vitro* models of angiogenesis.

How does MMC affect the formation of VEC-derived ECM?

Interactions between biological cells and surrounding extracellular matrix (ECM) materials modulate many cell behaviors including adhesion and migration. One key example of this cell-matrix reciprocity is in the context of angiogenesis, the sprouting of new blood vessels from pre-existing vasculature. Vascular endothelial cells (VECs) create and remodel the ECM during this process. *In vivo*, the surrounding fluid environment includes high concentrations of macromolecules, and is considered "crowded" in comparison to *in vitro* environments. In Chapter 2, we quantified the amount and organization of collagen IV, a prominent ECM component of VECs, that was produced by these cells over four weeks *in vitro* in the presence or absence of macromolecular crowder (MMC) nanoparticles that approximated *in vivo* crowding. In the presence of MMCs, cells secreted more collagen IV and those collagen fibrils appeared more aligned in terms of a local order parameter. This ECM difference emerged within one week and was sustained for over four weeks. We explored the effect of initial cell density (cells/μm^2) on this matrix production, to consider potential differences at a wound site versus an intact vessel. Moreover, we found the biophysical effect of MMCs to be unmodulated by secretions from an adjacent cell type in microvessels, pericytes. These results suggest that macromolecular crowding plays a direct role in remodeling the basement membrane, and that such crowding can be induced *in vitro* to more closely approximate the cell microenvironment.

Is static, uniaxial strain sufficient to induce angiogenic sprouting?

Vascular endothelial cells are known to respond to a range of biochemical and time-varying mechanical cues that can promote angiogenesis. It is less understood how these cells respond to sustained (i.e., static) mechanical cues such as the deformation generated by other contractile perivascular cells. In our work, we created an in-house tissue culture-compatible PDMS-based strain device to apply static, uniaxial strain to a confluent monolayer of VECs. In Chapter 3, we demonstrated that static tensile strain of 10%, consistent with that exerted by contractile microvascular pericytes, can directly and rapidly induce cell cycle re-entry in growth-arrested microvascular endothelial cell monolayers. In addition to inducing cell-cycle re-entry in this 2D strain case, we also explored if we could induce angiogenesis-like sprouting in the presence of strain by developing a quasi-3D model. We determined that this modest 10% strain promotes sprouting of endothelial cells, suggesting a novel mechanical "angiogenic switch." These findings suggest that static tensile strain can directly stimulate angiogenesis.

6.1.2. Characterization and modulation of the MSC secretome

In addition to angiogenesis and angiocrine signaling, MSCs have been established to be a crucial hematopoietic niche component necessary in promoting recovery and maintaining hematopoiesis after hematopoietic failure. MSCs primarily participate in indirect repair of the hematopoietic compartment through paracrine signaling. Thus, in this thesis, we first set out to characterize and identify the MSC secretome components that may be key players in supporting hematopoietic recovery (Chapter 5). We also demonstrated that we could use mechanical cues such as substratum stiffness to modulate and engineer the MSC secretome (Chapter 4). In this section, we summarize the primary questions asked and answers that we have developed in the course of this thesis.

What components of the MSC secretome are correlated with improved hematopoietic recovery?

Previously, our group studied populations of MSCs at various passages and size-sorted MSC subpopulations. We had also characterized the secretome expression of these MSC populations. We had then injected five of these MSC populations or subpopulations into sublethally-irradiated mouse models of hematopoietic failure and observed their survival. Taking these data together, in Chapter 5 of this thesis, we used those prior data in a new way, to create a predictive model of hematopoietic recovery. Using Pearson's linear regression and partial least squares regression, we were able to identify the proteins that were highly, positively correlated with improved mouse survival. From these analyses, we identified eight key proteins including IL-6, IL-8, BMP2, EGF, FGF1, RANTES, VEGF-A, and ANG-1. In addition to identifying these key proteins, we were also able to generate the regression parameters necessary for a predictive model. These models should, in theory, be able to predict the therapeutic efficacy of any population of MSCs for which we have the secretome expression. This provides an *in vitro* method to perform quality assurance checks on any population of MSCs being used as a therapeutic, specifically for hematopoietic recovery.

Can we leverage substrata mechanical properties to modulate the MSC Secretome?

To test and validate our predictive model, we also needed to develop a means to engineer the MSC secretome. Human MSCs exhibit morphological and phenotypic changes that correlate with mechanical cues presented by the substratum material to which those cells adhere. Such mechanosensitivity has been explored *in vitro* to promote differentiation of MSCs along tissue cell lineages for direct tissue repair. However, MSCs are increasingly understood to facilitate indirect tissue repair *in vivo* through paracrine signaling via secreted biomolecules. In Chapter 4, we leveraged cell-material interactions *in vitro* to induce human bone marrow-derived MSCs to preferentially secrete factors that are beneficial to hematopoietic cell proliferation. First, using

our knowledge from Chapter 3 of treating PDMS substrata to become tissue-culture compatible, we also developed PDMS substrata of tunable stiffness that were compatible for MSC culture. We characterized these bulk and surface properties of these PDMS substrata to verify that were controlling the mechanical properties of the substrata independent of changes from biochemical surface properties such as surface wettability and protein adsorption. We varied the viscoelastic properties of cell culture-compatible polydimethylsiloxane (PDMS) substrata to demonstrate modulated MSC expression of biomolecules including osteopontin, a secreted phosphoprotein implicated in tissue repair and regeneration. We observed an approximate three-fold increase in expression of osteopontin for MSCs on PDMS substrata of lowest stiffness (elastic moduli < 1 kPa) and highest ratio of loss to storage elastic moduli ($\tan \delta > 1$). A specific subpopulation of these cells that were of higher diameter (D^{hi} MSCs), shown previously to express increased osteopontin *in vitro* and to promote bone marrow recovery *in vivo*, also exhibited up to a five-fold increase in osteopontin expression when culture-expanded on compliant PDMS relative to expression by heterogeneous MSC populations on polystyrene (i.e., standard culture-expanded and unsorted cell populations).

In addition to osteopontin, we also observed the upregulation of a dozen different secreted proteins that were significantly correlated with decreasing substratum stiffness. Moreover, MSCs grown on compliant substrata (elastic moduli < 1 kPa) had equal or higher expression of the key secretome factors identified from statistical analysis than the D^{hi} MSCs grown on polystyrene. These data suggest that a mechanical cue, such as substratum stiffness, was sufficient to modulate the MSC secretome and increase the expression of the key secretome components to similar expression levels as the MSC phenotype therapeutically effective in supporting hematopoietic recvoery. Importantly, this mechanically modulated – or mechanoprimed – increase in protein expression preceded detectable changes in terminal differentiation capacity of MSCs. Cytokine and protein expression by human MSCs can thus be manipulated directly by mechanical cues conferred by the material substrata, prior to and instead of tissue lineage differentiation. This approach enables enhanced *in vitro* production of MSCs with tunable secretory profiles that can aid regenerative clinical applications.

6.1.3. Improving hematopoiesis *in vitro* and hematopoietic recovery *in vivo*

After identifying the key secretome components correlated with improved hematopoietic recovery, we needed to validate whether those factors could be biomarkers for identifying therapeutically effective MSC phenotypes. Using substratum mechanics, we could modulate the MSC secretome to express high levels of those important cytokines and growth factors. We subsequently went on to test how these mechanically-modulated MSCs could regulate hematopoiesis *in vitro* and promote hematopoietic recovery *in vivo* (Chapter 5).

How do the mechanically-modulated MSCs and their secretome regulate hematopoiesis *in vitro?*

MSCs are not known to differentiate into or re-populate the hematopoietic cell lineages of the bone marrow. Recovery of the bone marrow is generally attributed instead to proliferation and differentiation of hematopoietic stem and progenitor cells (HSPCs). In Chapter 5, we utilized *in vitro* co-culture of MSCs and HSPCs to test whether our mechanically modulated MSCs may have a therapeutic effect on hematopoiesis *in vitro*. We grew the MSCs and HSPCs in both contact co-culture and non-contact co-culture conditions. Non-contact co-culture conditions allowed us decouple the effects of the MSC secretome from heterotypic cell-cell contacts. Nevertheless, contact co-culture may be more representative of the *in vivo* environment, as MSCs and HSPCs have been demonstrated to directly interact via cell-cell contacts. For both non-contact and contact co-culture, we observed a marked increase in proliferation of HSPCs when grown in co-culture with MSCs that were adhered to PDMS of stiffness ~1 kPa. In contact co-culture, we observed a significant increase in CD123+ expression of the HSPCs when grown in co-culture with MSCs that were adhered to PDMS of stiffness ~100 kPa, which is indicative of myeloid differentiation. Concurrent with this increases in CD123+ expression was a decrease in CD34+ expression, suggesting a decrease in HSPC naiveté. However, in non-contact co-culture we observed no significant changes in HSPC expression of surfaces markers for differentiation across our substrata of varying stiffness. Together, these data suggest that increases in HSPC proliferation appear to be MSC secretome mediated, but changes in HSPC expression and differentiation capacity require heterotypic cell-cell contacts. Nevertheless, these results demonstrate that mechanoprimed MSCs have the potential to regulate both expansion and differentiation of HSPCs *in vitro.*

Can the mechanically-modulated MSCs promote hematopoietic recovery *in vivo?*

To validate the predictive regression model and determine if our mechanically-modulated MSCs had improved therapeutic efficacy, we then move towards administering our MSCs in our mouse model for hematopoietic failure. Systemic administration of these mechanoprimed MSCs resulted in improved mouse survival and weight recovery after bone marrow ablation, as compared with both standard MSC expansion on stiffer materials (polystyrene) and with biophysically sorted MSC subpopulations (D^{hi} MSCs). Additionally, we observed recovery of white blood cells, platelets, and red blood cells, indicative of complete recovery of all hematopoietic lineages. MSCs that had been expanded on stiffer PDMS (~100 kPa) resulted in faster short-term recovery of red blood cells, which was analogous to the myeloid priming that we observed in contact co-culture conditions. This suggests that the aforementioned *in vitro* co-culture models may be informative in understanding how MSCs support hematopoietic differentiation *in vivo*. Ultimately, these results demonstrate that computational techniques to identify MSC biomarkers – specifically secreted proteins correlative with *in vivo* outcomes – can

be leveraged to predict and engineer therapeutically effective MSC phenotypes, for translational applications including hematopoietic recovery.

6.2 Outlook and Perspectives

6.2.1. Outstanding Questions

Despite important contributions to the topics and questions listed above, there still remain many outstanding questions regarding the physical and mechanical cues that guide cell function in complex repair processes. Below is a list of potential areas of future research that expand upon the current findings of this thesis.

Angiogenesis *in vitro*

- How does the re-organized ECM under MMC affect VEC paracrine signaling? VECs have been shown to indirectly support hematopoiesis through angiocrine signaling. Does the increased amount, increased alignment, and increased areal spreading of ECM affect VEC paracrine signaling? Does it sequester or help store signaling proteins?
- How do changes in vascular basement membrane formation under MMC affect HSPC behavior? MMC has been shown to stiffen the ECM secreted by MSCs, in part through greater alignment and larger-diameter of ECM fibers. These changes in MSC-derived ECM architecture have been demonstrated to support expansion of HSPCs. Does the same hold true for VECs?
- How do cues like strain affect HSPC interaction with VECs? Is VEC paracrine signaling changed in the presence of strain?

The MSC Secretome

- How else is the MSC secretome affected by mechanical cues? We took a targeted, antibody-based approach in characterizing the MSC secretome grown on our PDMS susbtrata. However, the expression of hundreds or thousands of proteins could also be modulated by these same mechanical cues. Taking a non-targeted approach to characterize the MSC secretome could reveal more about how we changed the MSC phenotype.
- What other mechanical or biophysical cues (e.g., MMC, topography, dimensionality, porosity, geometry and etc.) modulate the MSC secretome? Many studies have explored how biochemical cues (i.e., induction media, hypoxia, addition of growth factors and cytokines) affect the MSC secretome, but most studies to date exploring mechanical or biophysical have focused on the differentiation capacity of MSCs. As MSCs play a predominant role in indirect repair via paracrine signaling, knowing how these different

cues regulate the MSC secretome may be more important in advancing MSCs as a clinically relevant therapy.

- Could these mechanoprimed MSCs and the resulting secretome be useful for other indications? In this study, we have focused on hematopoietic recovery as our translational application, a specific and narrow indication that allowed us to compare *in vitro* and *in vivo* data, so the generality of this approach is unestablished. For example, we also found that MSCs on compliant substrata also increased their expression of BDNF and bNGF, which are both neurogenic factors. When we evaluated MSC expression of chondrogenic factors on compliant substrata, we also observed the overexpression of osteoprotegerin. We also observed the upregulation of immune modulatory factors such as IFNγ, IL-2, IL-7, IL-6, IL-8, IL-21, MCP-1 when MSCs are cultured on compliant PDMS substrata. These data suggest that these mechanically-modulated MSCs could potentially be used for applications in neural regeneration, bone formation, or immune regulation.

Hematopoietic Recovery

- How do identified key factors interact with and affect hematopoiesis? We did not explore extensively how these isolated secreted proteins (IL-6, IL-8, BMP2, FGF1, RANTES, VEGF-A, and ANG-1) may support hematopoiesis. Are all of these factors necessary to support hematopoiesis? Is administration of a single isolated protein sufficient to support hematopoietic recovery? Is the inhibition of or loss of one of these proteins sufficient to abrogate hematopoietic support? We demonstrated *correlation* between these factors and improved hematopoietic recovery, but we did not demonstrate *causation.*
- Are there additional MSC secreted factors important to supporting hematopoietic recovery? Our predictive model did not match perfectly with experimental survival curves, which suggests that we do not have a complete set of predictive biomarkers. In Chapter 4, we identified osteopontin as a key marker of the D^{hi} MSC phenotype, but we were unable to incorporate it in the regression model as we did not fully characterize its expression when we initially conducted the survival experiments. Because we used antibody-based techniques to characterize the MSC secretome, our predictive model is limited to the expression of 35 proteins. Full characterization of the MSC secretome using untargeted approaches such as mass spectrometry may help to identify novel factors that are important in supporting hematopoietic recovery. While we considered this approach, we were limited by low signal to noise ratio due to masking from serum components. Thus, further development of experimental design and sample preparation would need to be pursued in order to fully characterize the MSC secretome.
- Can the accuracy of the predictive model be improved? The regression model was developed based on five experimental groups. From the newest expression and survival data acquired in Chapter 5, we can develop a more robust model with four new experimental conditions. With further characterization of the MSC secretome as mentioned in the previous point, we could also expand the repertoire of potential

biomarkers or predictors. Expanding both the response and predictor variables incorporated into the model would increase the robustness of the model. Using an expanded model, can we then predict the therapeutic efficacy of any new MSC population?

6.2.2. Outlook

This thesis focused primarily on understanding how biophysical and mechanical cues such as macromolecular crowding, static strain, and substratum stiffness can modulate biological processes such as basement membrane formation, angiogenic sprouting, and paracrine signaling. We explored these processes in the context of developing therapies for improving hematopoietic recovery.

As stated in Chapter 1, angiogenesis and angiocrine signaling from VECs are known to regulate the self-renewal capacity and migration of HSCs *in vivo* after hematopoietic injury. However, mechanistic understanding of how HSCs and VECs interact to promote hematopoietic recovery is unknown. Thus, there is a need for accurate *in vitro* model of angiogenesis to discover the heterotypic cell-cell interactions between HSCs and VECs. In Chapter 3, we demonstrated that the biophysical cue of MMC increased the deposition, the areal density and alignment of basement membrane protein fibers. Using synthetic MMC, we were able to re-capitulate the endogeneous vessel basement membrane *in vitro.* In Chapter 4, we applied mechanical strain analogous to pericyte contraction to induce angiogenic-like sprouting from VECs. This demonstrated that mechanical cues, de-coupled from chemical cues, was sufficient to induce angiogenesis. These biophysical and mechanical cues demonstrated that biophysical and mechanical cues are crucial to replicating angiogenesis *in vitro.* By including biophysical and mechanical cues, this thesis has contributed in improving the comprehensiveness of *in vitro* models of angiogenesis. This expanded *in vitro* model of angiogenesis provides a new tool to understand how VECs participate in supporting hematopoietic recovery and serves as a platform to address the outstanding questions listed in the section above.

In Chapter 4, we demonstrated mechanical modulation of the MSC secretome using the viscoelastic properties of the cell culture substratum material. This mechanical modulation of the MSC secretome can be applied to developing improved therapies for hematopoietic recovery in two ways. First, the mechanically-modulated MSCs can be used to improve or regulate hematopoiesis *in vitro*. Secondly, the MSCs themselves can be directly administered as an adjuvant therapy to support hematopoietic recovery *in vivo*.

The mechanopriming of the MSCs can be used to promote HSPC expansion or regulate HSPC differentiation *ex vivo*. In Chapter 5, we observed that mechanopriming of the MSCs on ~1 kPa PDMS yielded a significant increase in expansion of HSPCs in non-contact co-culture without altering HSPC surface marker expression. This suggests that we can use mechanoprimed

MSCs to maximize HSPC expansion without altering the HSPC differentiation capacity. Alternatively, in Chapter 5, we also observed increased CD123+ expression when HSPCs were grown in contact co-culture with MSCs grown on ~100 kPa PDMS. This increased CD123+ expression is indicative of myeloid differentiation, which suggests that we can myeloid prime HSPCs by modifying their co-culture conditions with MSCs. These are two examples in which mechanoprimed MSCs grown on either ~1 kPa or ~100 kPa substrata can be used to either maximize expansion of naive HSPCs or to prime the HSPCs towards myeloid differentiation. These HSPCs expanded with mechanoprimed MSCs can then be subsequently transplanted as a therapy.

Alternatively, MSCs can be administered separately as a supportive or adjuvant therapy to promote hematopoietic recovery *in vivo*. Our group had previously identified a specific cell size-sorted subpopulation of MSCs (D^{hi} MSCs) that were therapeutically effective in supporting hematopoietic recovery *in vivo*. Using a computational regression model, we identified the MSC secretome components correlative with improving hematopoietic recovery in mouse models. This regression model, in principle, is predictive of the therapeutic efficacy of any population of MSCs for this specific indication. Using this information, we then engineered or mechanically modulated the MSCs towards higher expression of these key secretome components. Using an *in vivo* model of hematopoietic failure, we then validated that these engineered MSCs could support hematopoietic recovery *in vivo*. Together, these thesis results suggest that we can now predict MSC therapeutic efficacy and can use mechanical cues to engineer MSC phenotype to become more therapeutically effective. However, we note that this approach has been demonstrated in this thesis only at the preclinical (mouse model) level, and this model and findings would need to be repeated for human clinical trial data to be validated fully for MSC critical quality attributes appropriate for clinical trials and commercialized cell therapy. Although MSCs have been used in hundreds of clinical trials, there is still no U.S. FDA approved MSC-based therapy. Our aim and aspiration are that these results predicting MSC therapeutic efficacy and ability to engineer MSC phenotype will help enable well characterized MSCs to become a translational, clinically relevant therapy in indications such as hematopoietic recovery.

Appendix A

Supplemental data

A.1 Viscoelastic characterization of polydimethyl siloxanes (PDMS) substrata (Chapter 4)

We used shear rheology to characterize the mechanical properties of polydimethyl siloxane (PDMS) substrata because these materials deform in a time- and rate-dependent manner (viscoelastically), with the viscous component or loss modulus dominating for the most compliant formulations of PDMS considered herein. For such materials, the storage or elastic moduli vary appreciably with strain rate or deformation frequency. However, methods such as instrumented indentation load-depth hystereses to determine Young's modulus assume a linear elastic response. Thus, for materials such as these which do not behave as linear elastic solids across a wide range of conditions, viscoelastic characterization methods such as shear rheology can more completely characterize the material deformation and potential correlations with cell response.

To determine the linear viscoelastic range of these substrata, we conducted amplitude sweeps at 1.6 Hz (or 10 rad/s) from 0.01% to 10% strain on all PDMS compositions noted. We observed that the shear storage and loss moduli G' and G'', respectively, remained approximately constant for all PDMS compositions from 0.5% strain to 10% strain (Fig. A-1). This informed our decision to conduct all frequency sweeps at 1% strain (Fig. 4-1). At this particular frequency, our three compositions of PDMS exhibited constant shear storage modulus, from 0.5% strain to 10% strain, of ~0.8 kPa (Fig. A-1 A), ~3 kPa (Fig. A-1 B), and ~50 kPa (Fig. A-1 C). These shear storage moduli decreased with decreasing frequency (Fig. 4-1). Because these storage moduli are frequency dependent, we refer to these by order of magnitude within Chapters 4 and 5 (i.e., as ~1 kPa, ~10 kPa, and ~ 100 kPa). Shear storage modulus can also be related to Young's elastic modulus if we approximate these materials to be homogeneous and elastically isotropic and further approximate $E' = 2G'(1+\nu)$ or $E' \sim 3G'$, where G' is the shear storage modulus and ν is the Poisson's ratio taken as 0.5. This approximation of E' remains on the same order for the three sample types: ~1 kPa, ~10 kPa and ~100 kPa, respectively.

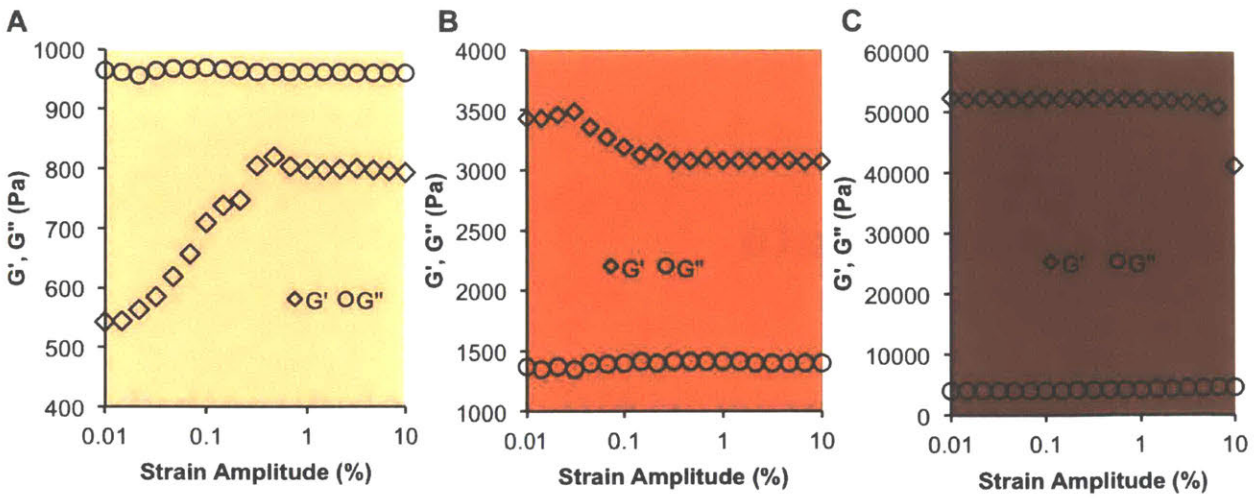

Figure A-1| Determining Linear Viscoelastic Range. Amplitude sweeps correspond with PDMS substrata that have shear storage modulus *G'* (1 Hz) on the order of (A) ~1 kPa, (B) ~10 kPa, and (C) ~100 kPa. Amplitude sweeps measuring loss and storage moduli were conducted at an angular frequency of 10 rad/s.

These mechanical properties of these viscoelastic substrata were all frequency dependent. Another parameter that we measured from shear rheology is the damping factor, $\tan(\delta) = G''/G'$, a ratio of the viscous to elastic portion of the material. We observed that tan(δ) was distinct at all frequencies measured for each PDMS composition (Fig. A-2). Other than the storage modulus (*G'*) being distinct on each PDMS composition, the damping factor (tan(δ)) and loss modulus (*G"*) were also distinct across each PDMS compositions. Thus, it is incorrect to say that these changes in cell behavior are correlated with elastic or storage moduli alone. The viscous properties of these PDMS substrata are also coupled with the adhesive properties of the material [296]. For these particular formulations of PDMS it is difficult to de-couple the viscous and elastic properties of the material [296]. However, the changes in gene expression, such as in osteopontin can also be correlated with viscoelastic properties such as damping factor and loss moduli. We found that osteopontin expression increased with increasing damping factor (Fig A-2 B) with decreasing loss moduli (Fig. A-2 C). Together, these data suggest that the expression changes we observed may be correlated with viscous or dissipative properties of the substrata, not elastic properties alone.

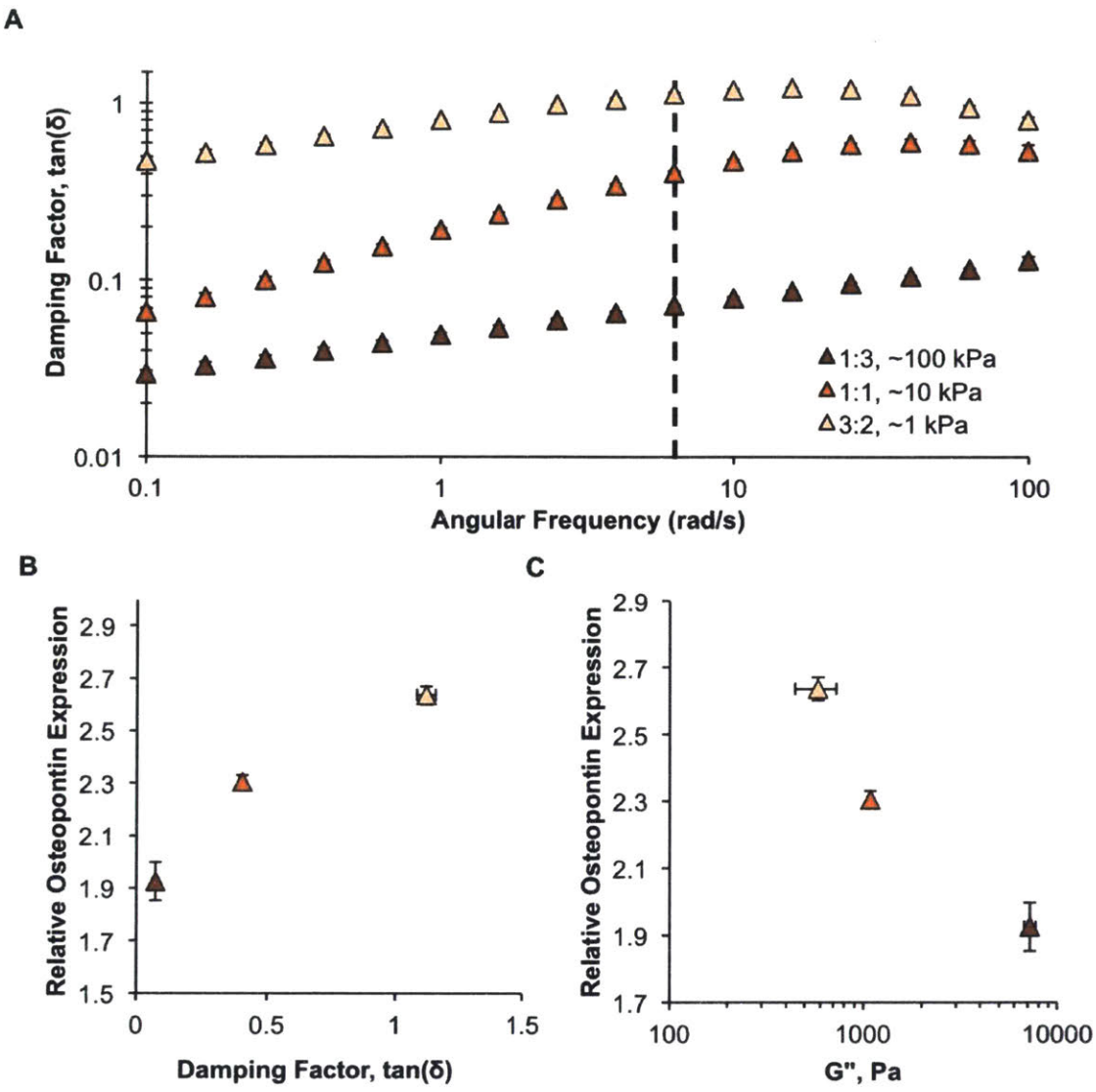

Figure A-2 | Additional Viscoelastic Characterization of PDMS Substrata. (A) Frequency sweep of damping factor (tan(δ) = G"/G') from 0.1 rad/s to 100 rad/s. The equivalent of 1 Hz is marked with a dashed line. Osteopontin expression as a function of PDMS (B) damping factor and (C) loss modulus at 1 Hz show opposite trends in expression with both viscoelastic parameters. Note that Fig. A-2 B-C appear as Fig. 4-3 C-D in Chapter 4, and are reproduced here for comparison with the rheology frequency sweep. Vertical and horizontal error bars represent standard deviations across technical replicates for expression, and viscoelastic parameter measurements, respectively.

A.2 Further Characterization of PDMS Surfaces (Chapter 4)

In Figure 4-1 D of Chapter 4, we determined the total amount of protein was approximately equal across all substrata. However, even if the total protein concentrations were equivalent, the composition of proteins adsorbed to the surfaces could be different. To determine if serum proteins were differentially adsorbed on PDMS surfaces, we conducted 1D SDS-PAGE analysis. PDMS wells of each composition were prepared in triplicate following the procedure as stated in the materials and methods of the Chapter 4 for determining total protein content. However, instead of adding trypsin to the wells, loading buffer (NuPage LDS Sample Buffer 4x, Thermo Fisher) was added directly to the wells to help elute protein from PDMS surfaces. Samples and protein standard (Precision Plus Dual Color Standard, Bio-Rad) were then loaded onto a Novex NuPAGE 4-12% Bis-Tris protein gel (Life technologies) for SDS-PAGE analysis. Gels were developed by silver staining using the Pierce Silver Stain Kit (Thermo Fisher).

We observed that the samples eluted from polystyrene (TCPS) surfaces appeared to have thicker bands than PDMS samples. We attributed this difference to the fact that TCPS exhibits a different surface chemistry and the proteins may elute more easily in loading buffer from TCPS than from the PDMS substrata. On the other hand, for total protein content in Chapter 4 (Fig. 4-1 D), we used enzymatic cleavage instead of chemical elution. When analyzing the protein gel for the PDMS substrata only, we observed no distinct differences in the banding patterns of lanes loaded with samples from the three different PDMS substrata (Fig. A-3). These data suggest that the composition of proteins on these PDMS substrata were indistinguishable via SDS-PAGE analysis. Thus, we assert that the viscoelastic properties of these PDMS substrata differed without altering the total amount nor composition of serum proteins adsorbed. However, we do note that SDS-PAGE is not the most sensitive analysis availabe for adsorbed protein analysis (so proteins of low abundance may differ but not be detected readily), and that protein conformation could differ among substrata for which the type and amount of protein is indistinguishable. Further targeted analysis would be required to explore differential conformations of surface adsorbed proteins.

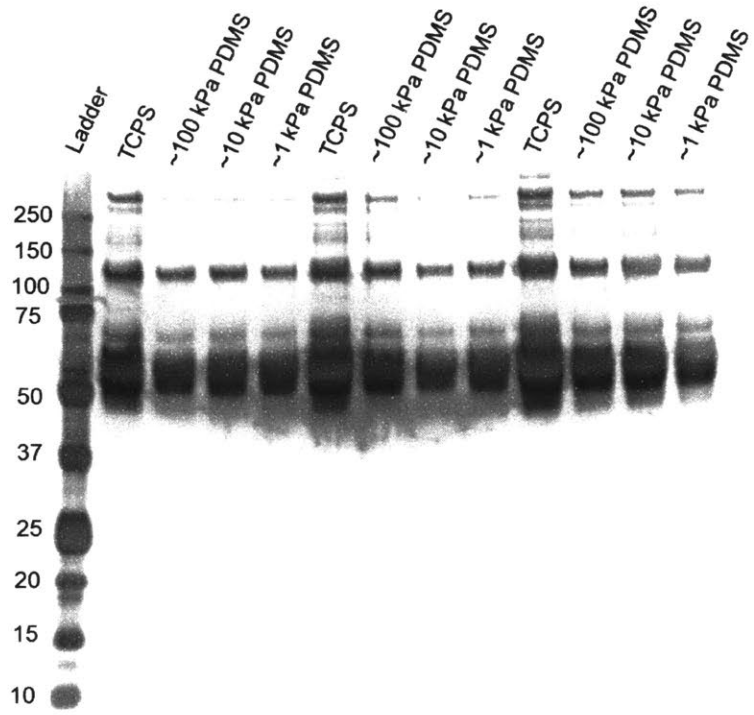

Figure A-3 | Protein Gel of Non-Specifically Adsorbed Protein. Serum proteins non-specifically adsorbed to polydimethylsiloxane (PDMS) substrata of varying stiffness (~ 1 kPa, ~ 10 kPa, ~ 100 kPa) and tissue culture polystyrene (TCPS) were visualized using SDS-PAGE in triplicate.

A.3 PDMS Wrinkling (Chapter 4)

In addition to assaying the non-specifically adsorbed protein content and composition, we also characterized the surface topography of the PDMS substrata. Prior to the attachment of cells, we imaged the PDMS surface under phase contrast to verify that the cells were actively wrinkling the surface. We saw no perturbations in any of the PDMS surfaces before plasma treatment (Fig. A-4 A, D, G), after plasma treatment (Fig. A-4 B, E, H), nor after the addition of media (Fig. A-3 C, F, I). These were the exact steps taken to prepare the PDMS surfaces prior to the addition of cells. To ensure that we were imaging the PDMS surfaces, we focused on debris on the surface (white specks in images). In the absence of cells, we observed no features on any of the PDMS substrata surfaces. The lack of PDMS surface changes in the images suggest that the cells are actively wrinkling the surface and that the cells are not preferentially attaching to areas of varying surface topography. Images were taken at lower magnification to verify that no wrinkling was present anywhere on the surface (Fig. A-4). To focus on the local vicinity of the cell-enabled PDMS surface wrinkling, images were acquired at higher magnification with the addition of cells (Figure A-5).

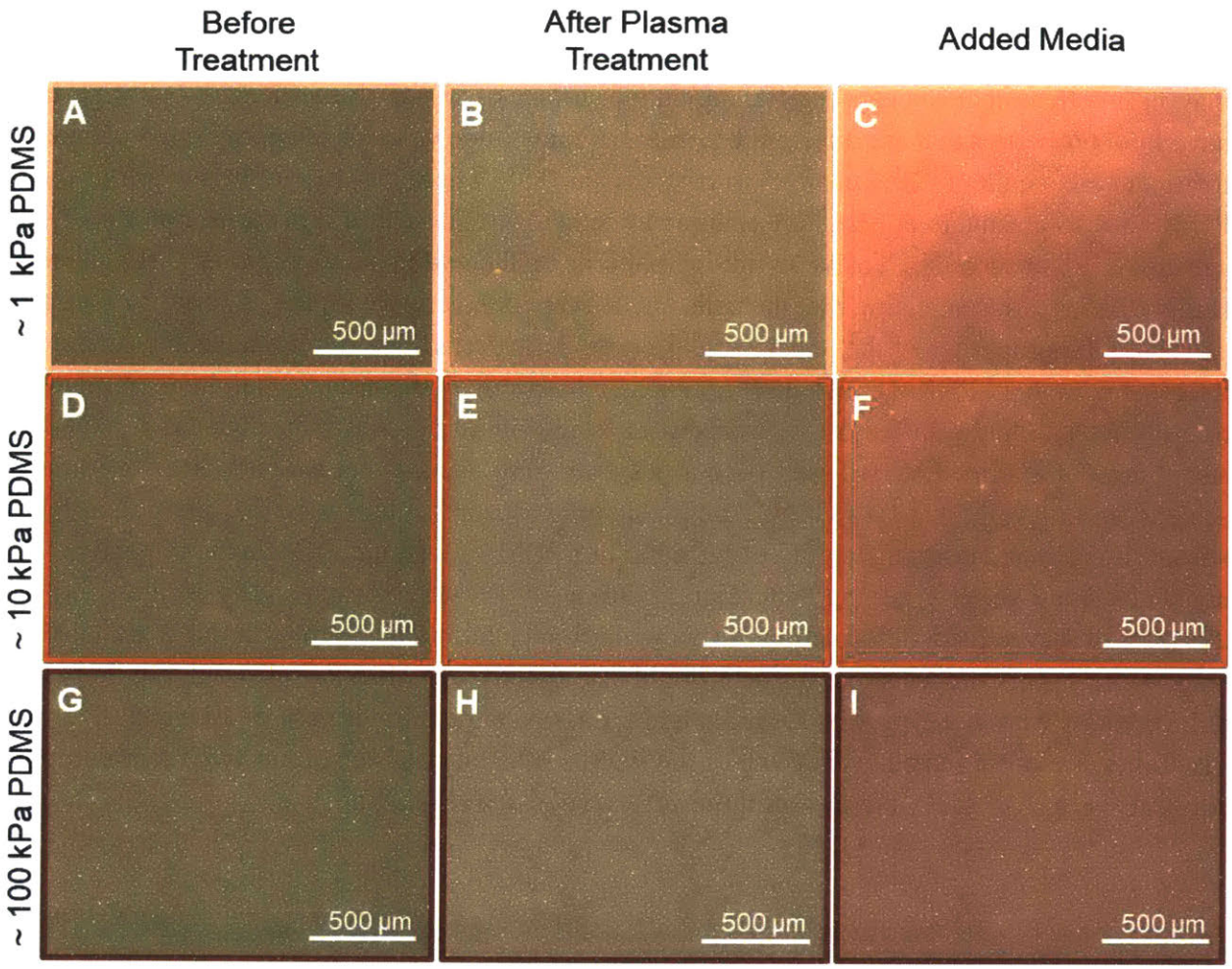

Figure A-4 | Phase Contrast Images of PDMS Substrata. Phase contrast images of PDMS of varying viscoelastic properties corresponding to (A-C) ~1 kPa, (D-F) ~10 kPa, and (G-I) ~100 kPa prior to the addition of cells. Substrata were imaged (A, D, G) prior to plasma oxidation, (B, E, H) after plasma treatment, and (C, F, I) after the addition of cell culture media. Images are focused on debris at the substrata surface (small white specks) and no other features were noted on substrata surfaces in the absence of cells.

Previous researchers have suggested that PDMS formulations are too stiff and that the surface treatments may increase the material's stiffness.[79,255] Bartalena et al. have suggested that plasma treatment can cause stiffening on the surface of PDMS. Nevertheless, our materials have bulk properties that are different by orders of magnitude whereas changes due to plasma treatment are smaller (<20% change) in comparison.[255] These changes in the surface of the PDMS due to plasma treatment may enable our cells to wrinkle a thin film surface of our PDMS substrata. We observed extensive wrinkling patterns on the two more compliant PDMS substrata (Figure A-5 A-B), suggesting that the cells are actively interacting with the material surface and can sense the properties of the underlying viscoelastic material. We observed large wrinkles on the most compliant PDMS substrata (Fig. A-5 A) that were on the order of hundreds of microns to millimeters. On the stiffest PDMS we saw no wrinkling of the substrata (Fig. A-5 C). On the substratum of intermediate stiffness (~10 kPa substratum), we saw occasionally see very small scale wrinkling (Fig. A-5 B). We were only able to consistently observe wrinkling in the ~10 kPa substrata when an elastic instability occurred in our PDMS substrata. This elastic instability enabled a small-scale wrinkling pattern in the surface of PDMS that was highly regular.[297–299] We observed local deformation of this wrinkling pattern in the vicinity around each cell (Fig. A-5 B). This suggests that the cells could also deform our ~10 kPa substrata, but these deformations were not typically observed under phase contrast. In the case of an elastic instability, we observed cell wrinkling of the PDMS substrata on both of our two more compliant substrata (Fig. A-5 A-B), but never on the stiffest substrata (Fig. A-5 C).

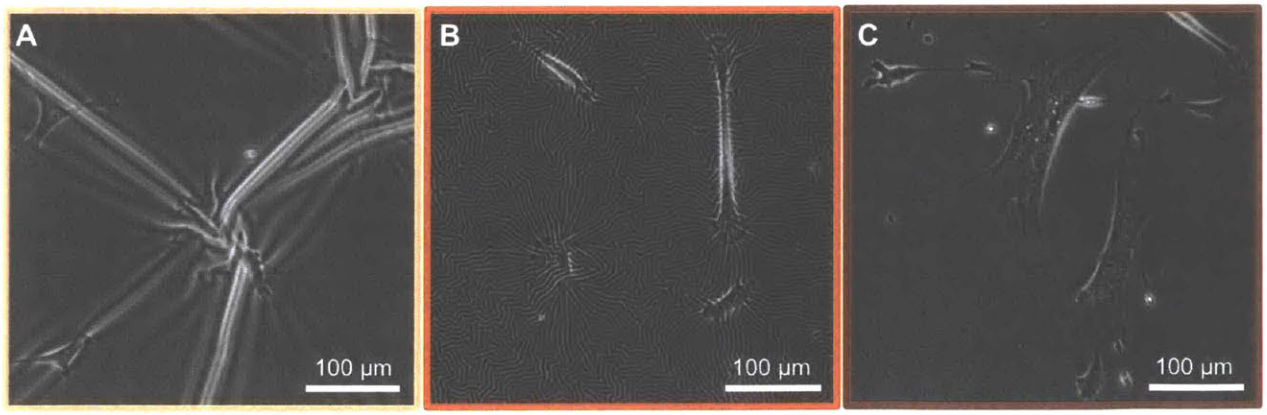

Figure A-5 | Phase Contrast Images of Cells on All PDMS Substrata. (A-C) Phase contrast images of MSCs grown on PDMS of varying viscoelastic properties corresponding to increasing shear storage modulus (~1 kPa, ~10 kPa, and ~100 kPa, respectively).

A.4 Changes in Cell Diameter on PDMS (Chapter 4)

After five days in culture, mean suspended cell diameter exhibited significant differences, as presented and discussed in the main text of Chapter 4. The magnitude of this diameter difference (~0.5 μm between PDMS nominal stiffness of 1 kPa and 10 kPa, and between 10 kPa and 100 kPa), as measured by geometric mean of the cell population, was an order of magnitude less than the difference in cell diameter between size-sorted subpopulations when compared to the difference in diameter of sorted cells (~5 μm difference). However, as described below, those mean diameter changes were significantly different (Fig. 4-2 C in Chapter 4) according to statistical analysis, as discerned from the large sample size per condition.

Distribution of suspended cell diameters varied greatly for a given condition, ranging from ~10-50 μm, with correspondingly appreciable standard deviations (Fig. A-6 A). This variation is in fact typical of culture-expanded MSCs. Despite these large standard deviations, statistical differences in the means were still detectable due to the large sample size. For data collected at 9 hours, we imaged and analyzed approximately 2000 cells per condition (1754, 2308, 2203 cells for ~ 1, 10, 100 kPa conditions, respectively). For data collected at 5 days, we measured diameters from ~3000 cells (3091, 2127, 3020 cells for ~ 1, 10, 100 kPa conditions, respectively). These large numbers of cells analyzed resulted in low standard error of the mean (SEM) and significant differences across different PDMS conditions (Fig. 4-2 C in Chapter 4). Figures A-6 B-C also show the distribution of cell diameters as histograms, including bootstrapped confidence intervals. Bootstrapped confidence intervals were calculated using MATLAB (Appendix I, Section I.2). At the initial time point of 9 hours, the histograms of cell-size distribution overlapped almost perfectly for all three PDMS conditions (Fig. A-6 B). After 5 days of culture on PDMS, the distributions still overlapped significantly, though slight differences are visually apparent. In the range of diameters >~30 μm, the histogram for cells on ~100 kPa PDMS slightly raised (Fig. A-6 C). At the lower range of diameters, between ~14-20 μm, the histogram for cells on ~1 kPa PDMS is slightly raised (Fig A-6 C). These results were consistent with the fact that the projected area of attached cells (a coarse measure of cell size for in the attached state) also tends to increase on stiffer PDMS substrata. The considerable overlap in the histograms at day 5 is also consistent with the fact that the magnitude of changes in cell size was <1 μm. Importantly, we detected no differences in cell diameter at 9 hours, indicating that larger cells did not adhere preferentially to stiffer substrata.

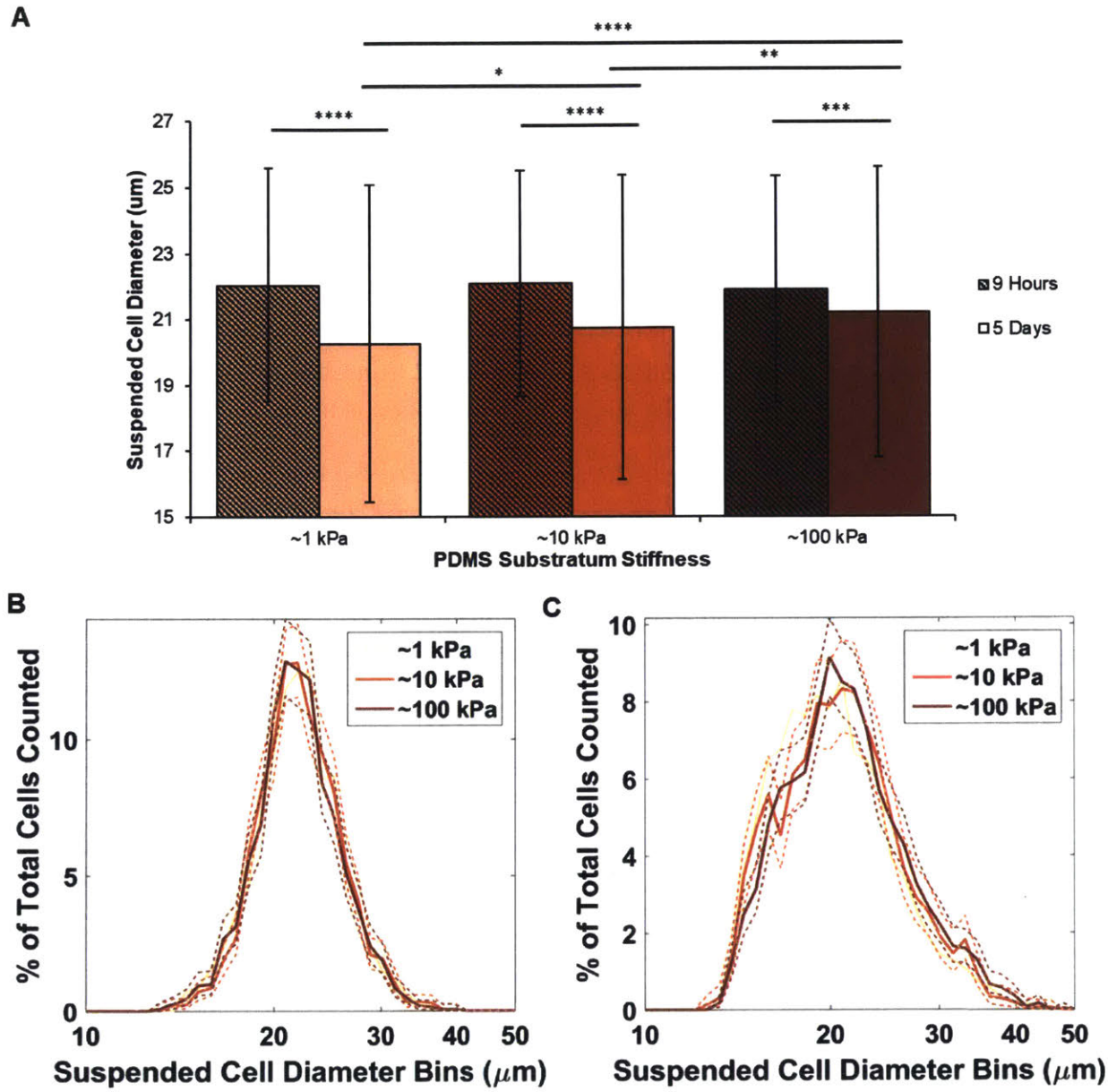

Figure A-6 | Distribution of Cell Diameters on PDMS Substrata. A) Geometric means +/- geometric standard deviations of suspended cell diameter was determined on substrata of varying stiffness (striped bars) nine hours and (solid bars) five days after seeding cells on substrata. Statistical differences in expression were determined using unpaired, two-tailed student's t-test with unequal variance (*$p<0.0005$, **$p<0.0001$, ***$p<1e\text{-}9$, ****$p<5e\text{-}15$). Histograms of cell size distributions at (B) 9 hours and (C) 5 days after culture on PDMS substrata. Dotted lines represent 95% boot-strapped confidence intervals.

A.5 Determining Relative Expression Using the $\Delta\Delta C_T$ Method (Chapters 4 & 5)

We calculated all relative expression using the double delta C_T ($\Delta\Delta C_T$) method. A detailed derivation and application of the $\Delta\Delta C_T$ method is described by Livak et al [300]. Here, we briefly described this method.

From qRT-PCR, we obtained C_T values for each gene and sample analyzed. These C_T values were the thermal cycle number corresponding to a pre-specified fluorescence threshold that represents a cut off concentration. These C_T values were lower for genes that have higher abundance and were higher for genes of low abundance as amplification is faster for higher starting concentrations (lower C_T for genes of higher concentrations). In theory, PCR doubles the concentration of DNA polymerized during every thermal cycle. Thus, the final amplified concentration (C_{final}) for a PCR reaction should be as follows. We can then use this same equation to determine the original concentration (C_o) of a particular amplicon in the sample before the reaction.

$$C_{final} = C_o * 2^{C_T} \qquad \therefore\ C_o = C_{final} * 2^{-C_T}$$

The final concentration is the same across all samples because the fluorescence threshold at which the C_T is determined is the same. Thus, the value of the final concentration (C_{final}) cancels out and is not important in determining the original relative concentrations. Assuming that starting total cDNA concentrations are the same, the following is true if we are determining relative expression of the same gene across two samples.

$$\frac{C_{o,sample\ 1}}{C_{o,sample\ 2}} = \frac{2^{-C_{T,sample\ 1}}}{2^{-C_{T,sample\ 2}}} = 2^{C_{T,sample\ 2} - C_{T,sample\ 1}}$$

We first take the difference in C_T values between our target or gene of interest ($C_{T,target}$) and our reference gene ($C_{T,reference}$), this allows us to normalize all concentrations by our reference gene. We perform this first normalization for each well because each experimental sample may have different starting concentrations of cDNA. For all expression data, we used GAPDH as our reference gene to allow us to normalize approximately by cell number.

$$\Delta C_T = C_{T,target} - C_{T,GAPDH}$$

To then determine relative expression across multiple experimental samples, we then take the differences of those differences.

$$\Delta\Delta C_T = \Delta C_{T,target\ 1} - \Delta C_{T,target\ 2}$$

We then used this double difference as our exponent to determine the relative concentrations for a particular target gene across our two samples that have been normalized by their sample concentrations.

$$\frac{[gene\ 1,\ sample\ 1]}{[gene\ 1,\ sample\ 2]} = 2^{-\Delta\Delta C_T} = 2^{\Delta C_{T,target\ 2} - \Delta C_{T,target\ 1}} = \frac{2^{\Delta C_{T,target\ 2}}}{2^{\Delta C_{T,target\ 1}}}$$

A brief derivation of how the above equation determined the relative starting concentrations, normalized to starting GAPDH concentration, is shown below.

$$\frac{2^{\Delta C_{T,target\ 2}}}{2^{\Delta C_{T,target\ 1}}} = \frac{2^{C_{T,target\ 2} - C_{T,GAPDH\ 2}}}{2^{C_{T,target\ 1} - C_{T,GAPDH\ 1}}} = \frac{\frac{2^{C_{T,target\ 2}}}{2^{C_{T,gapdh\ 2}}}}{\frac{2^{C_{T,target\ 1}}}{2^{C_{T,gapdh\ 1}}}} = \frac{\frac{\frac{C_{final}}{C_{o\ sample\ 2}^{target}}}{\frac{C_{final}}{C_{o\ sample\ 2}^{gapdh}}}}{\frac{\frac{C_{final}}{C_{o\ sample\ 1}^{target}}}{\frac{C_{final}}{C_{o\ sample\ 1}^{gapdh}}}} = \frac{\frac{C_{o\ sample\ 1}^{target}}{C_{o\ sample\ 1}^{gapdh}}}{\frac{C_{o\ sample\ 2}^{target}}{C_{o\ sample\ 2}^{gapdh}}}$$

In summary, this $\Delta\Delta C_T$ method allowed us to determine relative expression of a given gene across multiple samples. This first "difference" ΔC_T allowed us to normalize to a reference gene, which accounted for differences in starting concentration or cell numbers. The second "difference" $\Delta\Delta C_T$ determined the relative concentrations across two samples. All relative expression data presented were calculated using this method. As a standard of comparison, we typically used a single control or reference sample to determine all relative concentrations across multiple samples. For our experiments, this control sample was unsorted cells expanded on tissue culture polystyrene.

A.6 Expression Regulation Across Multiple Donors (Chapter 4)

Donor to donor variation in primary cells makes it difficult to draw statistically significant conclusions in biological research. However, we tested five different lots or donors from three commercially available MSC sources (ReachBio, RoosterBio, and Lonza). We sorted cells using 2 outlet spiral microfluidic device and then grew them on our different PDMS substrata for 7 days. Across all 5 donors and subpopulations, we observed similar trends in osteopontin expression (Fig. A-7 A-E). Table A-1 lists which vendors and donors correspond with the data presented in Fig. A-7 and also includes where the cells can be found in the Van Vliet Laboratory. Within the same donor, we also saw repeatable results (Fig. A-7 B and Fig. 4-4 F in Chapter 4). These data suggest that our mechano-priming of MSCs is robust across different donors and replicate experiments.

Table A-1. List of Human MSC Donors and Vendors Used

Corresponding Figure Panel	Vendor	Catalog #	Internal Donor #	Abbreviation	Received From	LN2 Dewar Rack #/Box Location (of earliest passage)
A-7 A	Rooster Bio	MSC-001	1	RoostBio1	Dr. John Maloney	3C (p2)
A-7 B	Reach Bio	N/A	1	RB1	Dr. John Maloney	1A (p1)
A-7 C	Lonza	PT-2501	13	PL13	Dr. Zhiyong Poon	2D (p3)
A-7 D	Lonza	PT-2501	7	PL7	Dr. Zhiyong Poon	2D (p4)
A-7 E	Lonza	PT-2501	11	PL11	Dr. Zhiyong Poon	2D (p4)

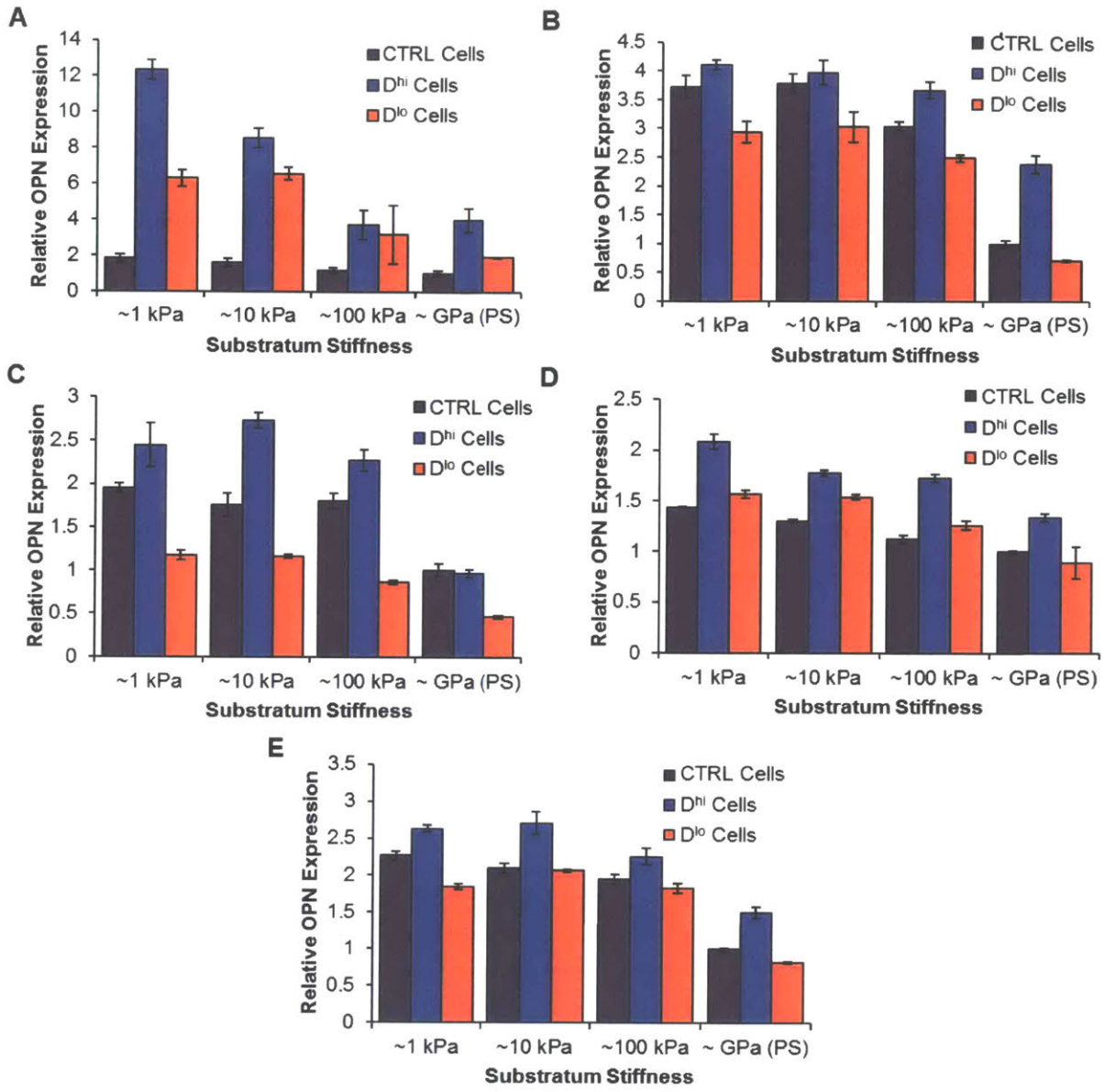

Figure A-7 | Expression Data Across Five Additional Donors. (A-E) Expression data from unsorted (CTRL) and sorted cells (D^{hi} and D^{lo}) were collected from five donors. Donor's cells came from the following vendors: (A) RoosterBio Inc., (B) ReachBio LLC, and (C-E) Lonza Biologics Inc. Osteopontin expression was determined for all subpopulations of cells grown on all three PDMS substrata in addition to polystyrene.

A.7 Collagen Functionalization (Chapter 4)

Results of MSCs cultured on 2D substrata of varying stiffness vary widely among published reports, depending in part on the types of materials and degree of characterization of the mechanical and other properties of those substrata [77–79]. Due to the importance of extracellular matrix ligands (such as fibronectin and collagen) in transducing the mechanical signal, it is important that ligands are uniformly displayed on these varying substrata. Ligand density, presentation or patterning can drastically change cell behavior [239,250]. It has also been shown that the tethering of these ligand molecules to the substratum can drastically alter cell function [78]. Moreover, the tethering can be altered by the surface properties, such as porosity, of the hydrogel material. This effect of ligand tethering may be conflated with the stiffness of the substratum [78]. To overcome these effects, one study used elastomeric micropillars of varying heights to alter the effective rigidity of the substrata instead of changing the material's adhesive and surface properties [77]. The study showed that MSCs grown on rigid pillars exhibited higher traction forces and were more osteogenic and that the cells grown on less rigid pillars were more adipogenic [77]. These studies caution researchers to be careful in choosing a substratum and characterizing its surface and bulk properties.

We chose to use an elastomeric material (PDMS) because it is non-porous and does not lead to differential ligand tethering [78]. We used a hetero-bifunctional cross-linker, Sulfo-SANPAH, to attempt to covalently bind type 1 collagen to PDMS with UV light following a previously published protocol [78]. With the addition of type I collagen to the material surface, we saw no changes in expression with substratum stiffness that is observed without covalently bound ligands (Appendix A, Fig. A-8). This suggests that MSC expression is either being dominated biochemically by the ligand or that the cells may not be able to sense the underlying substrata because it is binding to the collagen layer that is self cross-linked instead of covalently binding to the substratum [79]. The same study that pointed out the inefficiency of sulfo-SANPAH as a covalent crosslinker proposed further surface modification of the PDMS with (3-aminopropyl)triethoxysilane (APTES) to covalently bind biotin [79]. In another study within our own group, we have used a similar surface modification to covalently bind matrix ligands to PDMS for culture of a different cell type [301]. Nevertheless, collagen functionalization using Sulfo-SANPAH as the covalent crosslinker is masking the effects of the substratum. Thus, we chose to use non-specific protein adsorption to the material surface as opposed to covalent crosslinking of the proteins to the material. By assuring that all surface properties are similar, such as surface hydrophobicity and protein adsorption concentration, we expect that there should be no differences in ligand attachment. Thus, all changes in cell behavior observed should be related to the material's viscoelastic and not biochemical properties (See also Appendix A.2).

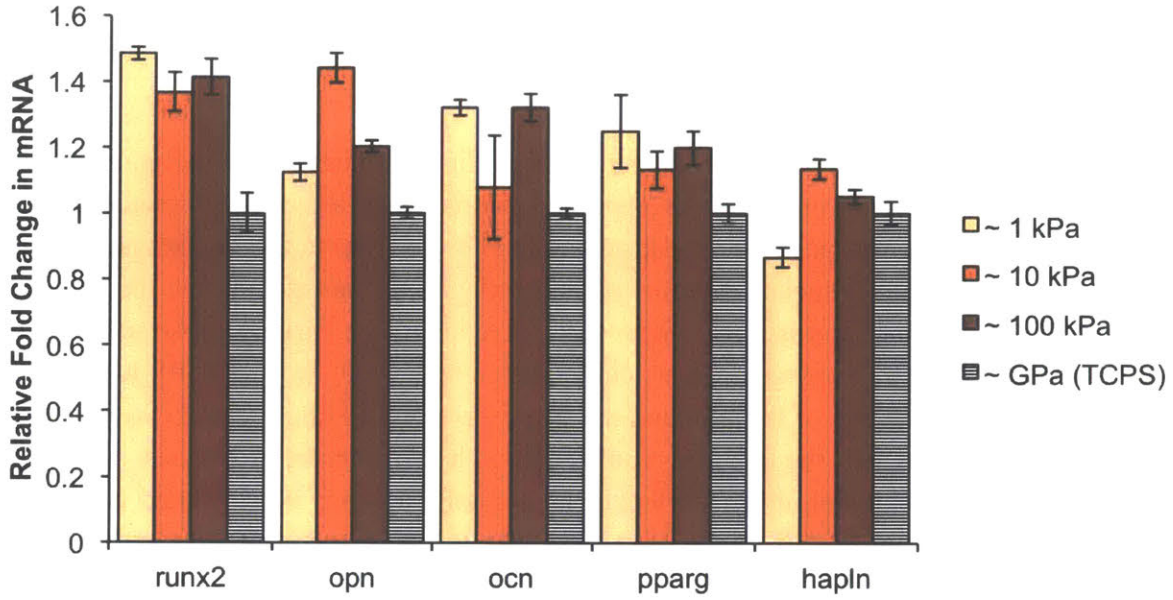

Figure A-8 | Expression Data with Collagen Functionalization on PDMS Substrata. Cells were lysed and RNA was extracted and analyzed after one week in culture on top of PDMS substrata (orange bars) and polystyrene (black-striped bars) that were covalently functionalized with Sulfo-SANPAH and type I collagen. First three genes are osteogenic markers (runx2, opn, ocn), fourth gene is a chondrogenic marker (hapln), and last gene is an adipogenic marker (pparg). $\Delta\Delta C_T$ method was used for relative quantification of expression levels from qRT-PCR with normalization to expression levels of MSCs grown on polystyrene (black-striped bars) with error bars represent standard deviation.

A.8 Expression of Chondrogenic Genes (Chapter 4)

The D^{hi} MSCs that supported hematopoiesis *in vivo* were also bipotent osteochondral progenitors. Thus, we also explored if chondrogenic differentiation potential was also altered by growing the MSCs on PDMS. In a separate experiment, we also assayed the mRNA expression of various chondrogenic markers (Figure A-9). In addition to hyaluronan and proteoglycan link protein 1 (hapln1), a cartilage oligomatrix protein, we also explored early and late stage chondrogenic markers. These markers include bone morphogenetic protein 2 (bmp2) as an early marker; Sox9 as a mid-stage marker; and Aggrecan (agg) and alpha-1 type II collagen (col2a1) as late-stage markers [302].

In this separate experiment, we also included opn and hapln1 to verify that the expression profile of the cells on PDMS was consistent with previous experiments. For all chondrogenic markers assayed, there were no significant trends correlated with PDMS stiffness. We observed a greater than 2-fold increased expression of bmp2 on all PDMS susbtrata, but these increases were not stiffness dependent. Note that although bmp2 is considered an early chondrogenic marker here, it is also an osteogenic marker, which may be why it was up-regulated along with osteopontin [303]. Sox9 was most highly expressed on the stiffest PDMS substrata, but the changes in expression were <2-fold on all substrata, suggesting that changes in expression were small. Both aggrecan and hapln1 were down-regulated on PDMS, suggesting that growth on PDMS does not promote chondrogenic differentiation. Type II collagen (col2a1) is also a late-stage chondrogenic marker similar to aggrecan. Although col2a1 appeared up-regulated by 4-fold on the ~10 kPa PDMS substrata, the absolute expression levels were very low. During qPCR, the exponential amplification phase for col2a1 was very late (thermal cycle number, Cp ~30-35) and noisy within samples, suggesting very little to no col2a1 expression for all samples. Thus, this apparent up-regulation of col2a1 may not be accurate. In summary, we did not see consistent up-regulation of chondrogenic markers in the MSCs grown on PDMS substrata. Additionally, any changes in chondrogenic marker expression did not appear to be mechanosensitive.

These data suggest that we mechanically modulated the MSC secretome without altering the chondrogenic differentiation capacity of the MSCs when growing them on PDMS substrata. Moreover, these results exploring chondrogenic differentiation were consistent with our results exploring osteogenic differentiation in Chapter 4 (Figs. 4-3 A, E-F).

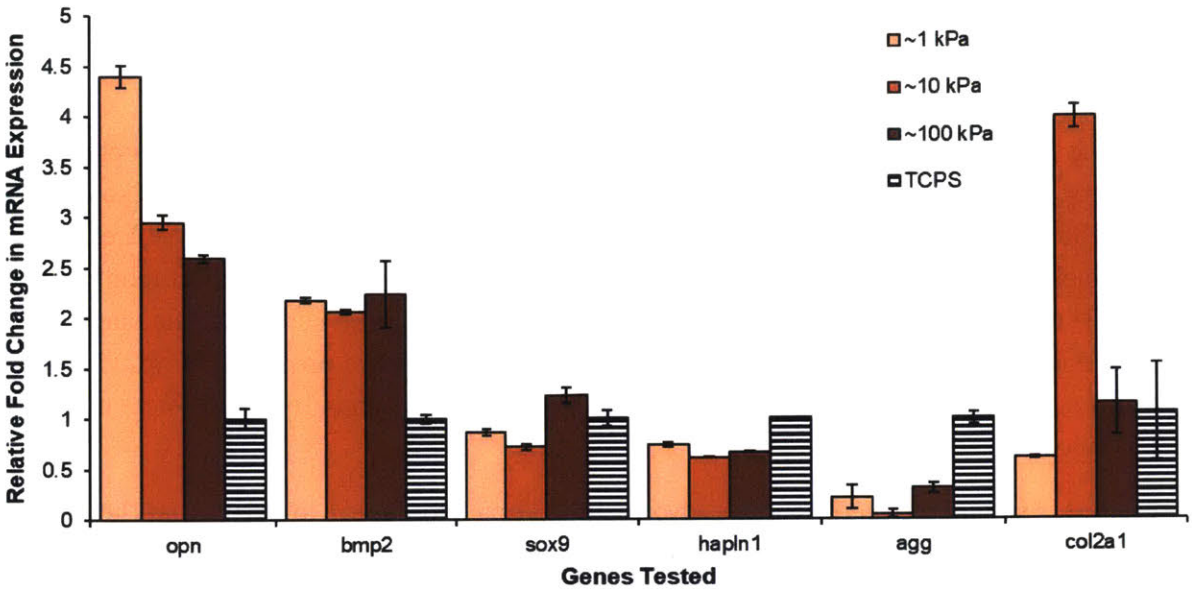

Figure A-9 | Expression of Chondrogenic Genes on Elastomeric Substrata. $\Delta\Delta C_T$ method was used for relative quantification of expression levels from qRT-PCR with normalization to expression levels of MSCs grown on polystyrene (black striped bars) with error bars representing standard deviation. Osteopontin (opn) was assayed to verify that the cells maintained consistent expression across experiments. Bone morphogenetic protein 2 (bmp2) was assayed as an early chondrogenic marker. Sox9 and cartilage oligomatrix protein (hapln1) were assayed as mid-stage chondrogenic differentiation markers. Aggrecan (agg) and alpha-1 type II collagen (col2a1) were assayed as late-stage chondrogenic differentiation markers.

A.9 Contact co-culture of MSCs and HSPCs (Chapter 5)

In addition to non-contact co-culture, we also explored contact co-culture conditions. In the *in vivo* bone marrow compartment, there is nothing to physically separate the HSPCs from MSCs. Thus, it is also plausible that the two different cell types may interact other than through their secretomes via cell-cell contacts. Because both cells types are in direct contact in this assay, a few measures were taken to distinguish the MSCs from HSPCs. During counting, the cells were distinguished by size and morphology: HSPCs have a rounded morphology with mean diameter of ~10 μm whereas MSCs have a mean diameter of ~20 μm. For flow cytometry analysis, the much larger MSCs have much higher forward scatter and were gated out using a MSC-specific surface marker, CD73.

Similar to non-contact co-culture, Fig. A-10 A shows that HSPC proliferation depended strongly on the substratum material to which MSCs were adhered, and was maximized for the most compliant PDMS substratum (1 kPa). Additionally, Fig. A-10 B shows that specific HSPC surface markers (CD123+ and CD34+) associated with hematopoietic lineage commitment varied monotonically with increasing PDMS substratum stiffness. Production of CD123+ HSPCs increased with increasing PDMS stiffness, whereas production of CD34+ HSPCs decreased with increasing PDMS stiffness over the substratum range considered. As expected from other differences in PDMS and polystyrene (PS) substrata properties, these trends did not extend to HSPC cultured in tissue culture-treated PS wells, either with or without adherent MSCs present.

Figure A-10 summarizes the effect of PDMS substratum stiffness on co-cultured HSPCs, with the orange shaded region distinguishing this mechanical modulation from standard control conditions on tissue culture-treated PS. In agreement with other studies, we demonstrated that adding MSCs (+MSC condition) to typical HSPC expansion (-MSC condition, on PS in monoculture) can increase proliferation expressed as fold change by 46%.[270,274,283,288,289] Moreover, we found that HSPC proliferation further increased over current materials and protocols when co-cultured with MSCs adhered to PDMS substrata: Proliferation expressed as fold change increased by 67% and 53% on PDMS of lowest (1 kPa) and highest (100 kPa) stiffness, respectively, with respect to HSPCs grown on PS with no MSCs.

The percentage of CD34+ or naïve, uncommitted HSPCs also increased significantly with decreasing PDMS substratum stiffness, attaining up to ~25% of the HSPC population on PDMS of 1 kPa stiffness. Thus, if one's goal is to increase production of uncommitted HSPCs, co-culture with MSC on PDMS of this stiffness will increase both proliferation rate and population fraction of these CD34+ HSPCs, as compared with stiffer PDMS substrata or with PS (Fig. A-10 B). In contrast, the percentage of CD123+ HSPCs increased with increasing PDMS substratum stiffness, and also exceeded the percentages attainable in co-cultures or monocultures on PS. This increased yield of myeloid progenitor cells compared to state-of-the-art HSPC expansion

protocol (both monoculture HSPCs[304] and co-culture with MSCs on tissue culture PS[283,289]) provides a potential means to produce myeloid lineages such as erythrocytes or platelets. In a recent study, MSCs have also been reported to elicit an immune modulatory effect on HSPCs *in vitro*, maintaining HSPC myeloid progenitor state in a contact-dependent manner [305]. In fact, this opposite trend in CD34+ and CD123+ HSPCs is expected, in that an increase in CD123+ or myeloid lineage committed cells is concomitant with a decrease in the naïve HSPC population fraction. As CD123+ (also known as IL3 receptor) is a marker of myeloid lineage commitment (as distinct from lymphoid commitment),[290,291] this finding shows that production of myeloid progenitors can be maximized by expanding HSPCs in co-culture with MSCs on PDMS of 100 kPa stiffness. In this approach, HSPC proliferation would be similar to that attained for co-culture on PS (Fig. A-10 A), but the conversion of those HSPCs to myeloid progenitors would be increased by 12% (Fig. A-10 B).

Additionally, Fig. A-10 B shows that specific HSPC surface markers (CD123+ and CD34+) associated with hematopoietic lineage commitment varied monotonically with increasing PDMS substratum stiffness. Production of CD123+ HSPCs increased with increasing PDMS stiffness, whereas production of CD34+ HSPCs decreased with increasing PDMS stiffness over the substratum range considered. As expected from other differences in PDMS and PS substrata properties, these trends did not extend to HSPC cultured in tissue culture-treated PS wells, either with or without adherent MSCs present.

These application examples underscore the key finding: mechanical priming of MSCs via the substratum material mechanics is sufficient to augment HSPC response in co-culture. Given that the MSC secretome components known to affect HSPC behavior are also correlative with substratum stiffness, these findings suggest that HSPC response is mediated by secreted MSC signals modulated by mechanical cues.

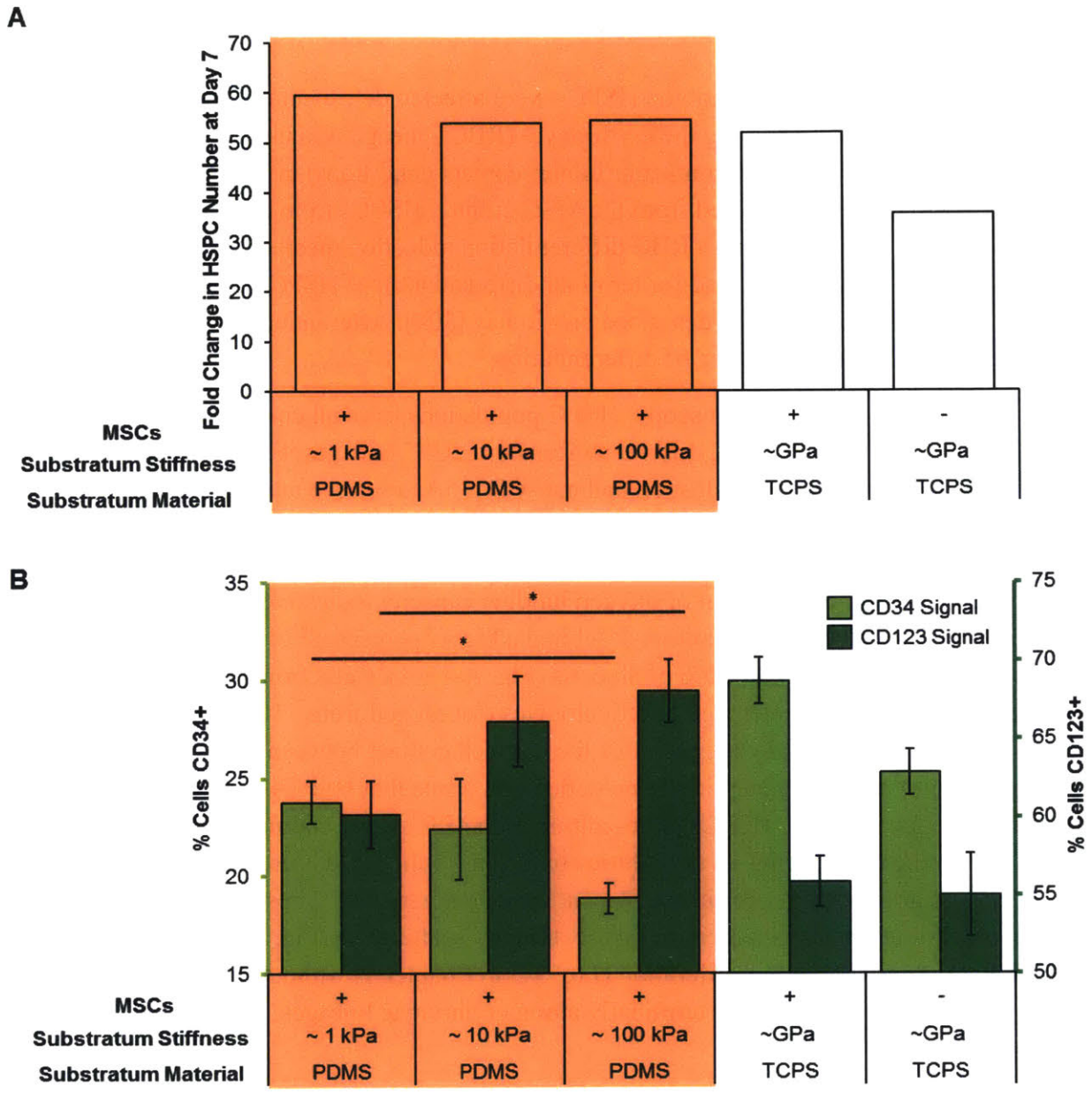

Figure A-10 | Effects of the Mechanically Modulated MSCs on Hematopoietic Stem & Progenitor Cells. (A) HSPCs were counted 7 days after being in co-culture with MSCs on various substrata. Far right bars represent typical HSPC growth conditions with no MSCs on tissue culture polystyrene. Conditions where cells were grown on PDMS substrata are highlighted in orange. (B) Surface marker expression of CD34 (light green) and CD123 (dark green) were assayed using flow cytometry. Conditions where cells were grown on PDMS substrata are highlighted in orange. Percentage of positive CD34 expression is on the left, primary axis, percentage of positive CD123 expression is displayed on the right, secondary axis. Statistical differences in expression were determined using unpaired, two-tailed Student's t-test with unequal variance (*$p < 0.05$).

A.10 Differentiation of HSPCs after co-culture (Chapter 5)

To determine whether or not the HSPCs were affected detrimentally by co-culture with MSCs, HSPC differentiation along the erythrocyte (RBC) lineage was induced and analyzed. After one week of co-culture (in contact or in non-contact conditions) in HSPC expansion media, HSPCs were isolated and harvested from the MSC culture. HSPCs from every condition were then transferred to a new plate with RBC differentiation induction media. The protocol, materials, and induction media used for terminal differentiation of HSPCs into reticulocytes, or immature RBCs, was followed as described previously [304]. After induction for 21 days, the cells were then evaluated for extent of differentiation.

Under phase contrast microscopy, HSPC populations from all co-culture conditions were red in color, suggesting successful differentiation along RBC lineages. HSPCs were then stained with Hoechst to demonstrate enucleation and anti-CD235A, a surface marker of reticulocytes. Note that this induction protocol only induces differentiation of the HSPCs into reticulocytes, and not mature red blood cells with oval biconcave disk morphology. Moreover, we did not measure the amount of hemoglobin or oxygen binding capacity indicative of fully functional RBCs. The cells from contact co-culture exhibited a higher percentage of reticulocytes (CD235+, Hoechst-) that ranged from ~15-30% of all cells (Fig. A-11 A). Cells from non-contact co-culture exhibited a lower percentage of reticulocytes that ranged from ~10-20% of the total population (Fig. A-11 B). This suggests that the cell-cell contact between HSPCs and MSCs in contact co-culture before differentiation induction can prime that HSPCs for erythrocyte differentiation. As a control, HSPCs in co-culture with MSCs were compared to HSPCs in monoculture. When comparing all co-culture conditions to the HSPCs grown in monoculture, there were no marked differences in the percentage of reticulocytes. These similarities in population distributions are apparent in flow cytometry scatterplots (Fig. A-11 C). This finding suggests that we can increase proliferation (Fig. 5-5 in Chapter 5) without diminishing the capacity of HSPCs to differentiate terminally along erythrocyte lineages.

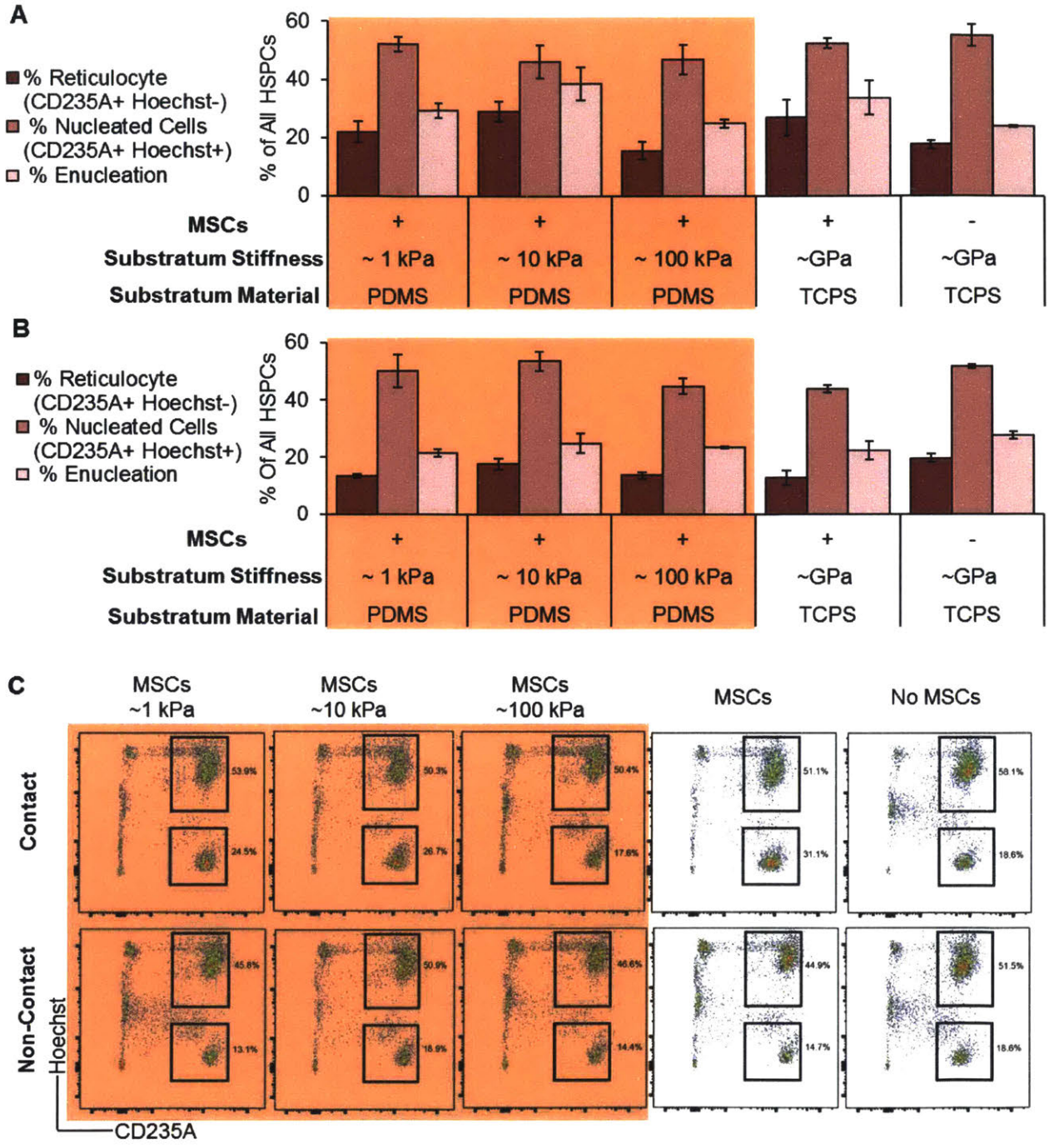

Figure A-11 | Chemical Induction into Erythrocyte Lineage. (A-B) After RBC differentiation induction, HSPCs were stained to determine percentages of HSPCs that have differentiated into reticulocytes and enucleated cells after being isolated from (A) contact co-culture and (B) non-contact co-culture conditions. (C) Representative flow cytometry scatterplots of differentiated HSPCs isolated from (top) contact and non-contact (bottom) co-culture conditions. Horizontal axis represents CD235A fluorescence, a reticulocyte marker, and vertical axis represents Hoechst fluorescence, a nuclear stain. CD235A+ signal and Hoechst- signal are indicative of enucleated reticulocytes. HSPCs that were grown in co-culture on PDMS prior to RBC induction are highlighted in orange. Boxes inside dot plots represent gates used to identify CD235A+ cells with (top) and without nuclei (bottom).

Appendix B

Further predictive modeling and *in vivo* results (Chapter 5)

B.1 Variance Explained in PLSR Components (Chapter 5)

To determine the number of principal components necessary to build our PLSR space, we plotted the cumulative variance in both the predictor variable (X) and the response variable (Y) against the number of PLS components (Fig B-1). In Fig. B-1, over 90% of the variance is captured with a 2-component PLS model for both the predictor (Fig. B-1 A) and the response (Fig. B-1 A) variables, which represent the expression and survival data, respectively. Although a third component increases the variance explained in X and Y by 2.5% and 6.6%, respectively, these increases are small compared to the increases of the second component (26.4% and 44.6% for X and Y, respectively). Thus, to avoid overfitting the regression model with such limited model data, we chose to use a 2-component or 2-dimensional PLSR model.

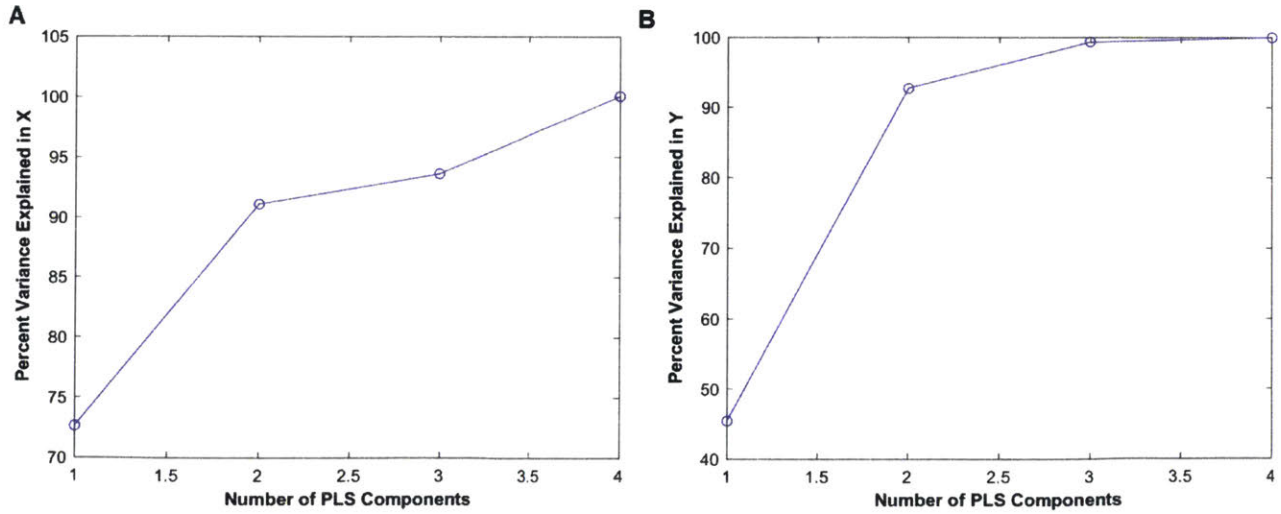

Figure B-1. PLSR Components and Variance. A) Percent variance explained in predictor variable, X, captured by 1 to 4 number of PLS components. B) Percent variance explained in response variable, Y, captured by 1 to 4 number of PLS components.

B.2 Weight Recovery (Chapter 5)

Along with mouse survival (Fig. 5-6 in Chapter 5), we also tracked the weight recovery of each mouse in all experimental groups (Fig. B-2). Weight recovery was indicative of the overall health of the mice in each experimental group. Nevertheless, we could only track the weights of surviving mice, so differences in experimental groups are abrogated towards the end of the experiment when surviving mice are the ones that have recovered. To more easily compare trends in weight recovery, we calculated the mean % weight recovery for all experimental cohorts at each week post-irradiation (Table B-1). Although not statistically significant, we observed that the mice injected with unsorted MSCs grown on PDMS showed faster and greater weight recovery at around day 28 post-irradiation, when compared to the MSCs grown on TCPS. This higher mean weight recovery is recorded in Table B-1 at day 28 post-irradiation.

We also observed a slight separation between the weight recovery curves of unsorted MSCs grown on PDMS (orange curves, Fig. B-2 A) and unsorted MSCs expanded on TCPS (Fig. B-2 B). The mean weight recovery for mice injected with unsorted MSCs expanded on TCPS does not recover above 80% at the end of the experiment (Table B-1). This suggests that mechanopriming unsorted MSCs by expanding them on PDMS can help support the weight recovery of the mice over standard culture conditions. For the D^{hi} MSCs expanded on TCPS, the weight recovery is more comparable to that of MSCs expanded on PDMS (Fig. B-2 B), but also appears to decline in the last weeks of the experiment. Moreover, early on in the experiment (day 7 and day 14), mice injected with mechanoprimed MSCs grown on ~100 kPa PDMS appear to have the highest weight recovery that is statistically significantly higher than mice injected with D^{hi} MSCs (Fig. B-2 C and Table B-2). This suggests that the mechanoprimed MSCs grown on ~100 kPa PDMS supports faster, short-term recovery in the overall health of the mice that D^{hi} MSCs. Towards the end of the experiment (beyond day 40), we also observed a separation between D^{hi} MSCs and MSCs mechanoprimed on ~1 kPa PDMS (Fig. B-2 C). However, the difference in weight recovery between these two groups were not statistically significantly different due to high variance. Moreover, as the experiment proceeds towards later times fewer mice survive, so we could not observe statistically significant differences across all experimental groups.

When comparing between the two groups injected with mechanoprimed MSCs (Fig. B-2 A, 100 kPa and 1 kPa conditions), we observed differences in their weight recovery towards the end of the experiment. After re-injury (day 35) due to cheek bleeding, the mice injected with mechanoprimed MSCs expanded on ~100 kPa PDMS decline in their weight and do not recover their original weight (~75% at day 49-50, Table B-1). At the experiment conclusion (day 50), mice injected with MSCs expanded on ~1 kPa PDMS exhibited the highest overall weight recovery that was statistically significantly higher than MSCs expanded on ~100 kPa PDMS (Table B-2). This suggests that the mechanoprimed MSCs expanded on ~1 kPa PDMS can better support recovery and maintenance of mice weight even after re-injury.

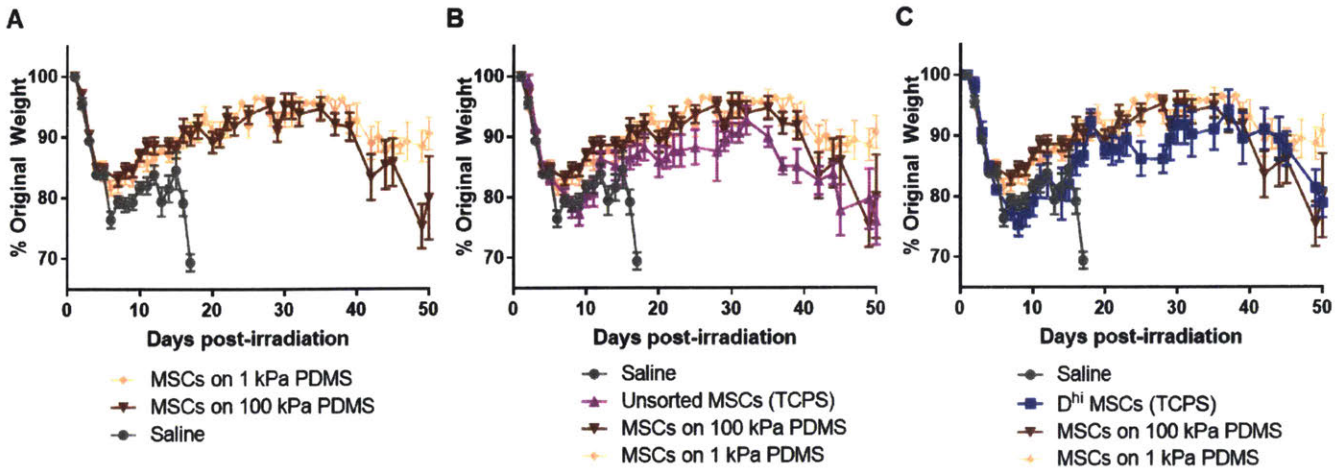

Figure B-2. Weight Recovery of Sub-lethally Irradiated Mice. Mouse models of hematopoietic failure were injected with MSCs from four experimental groups including unsorted MSCs grown on ~1 kPa PDMS (light orange), ~100 kPa (dark orange) PDMS, TCPS (purple) and D^{hi} MSCs grown on TCPS (blue). A no treatment or saline control is also included in gray. A-C) Mice weights corresponding to each experimental group in Fig. 5-6 of Chapter 5 were tracked over the course of 50-days after irradiation. Mean percentage of original weight values are plotted with ±SEM (N≥9 for all conditions). For easier visual comparison, mice weight recovery is plotted separately A) for MSCs grown on PDMS conditions only, B) all unsorted MSCs on PDMS and TCPS, and C) sorted D^{hi} MSCs with MSCs expanded on PDMS.

Table B-1. Mean Weight Recovery at Each Week.

	Mean % Original Weight				
	Saline	D^{hi} MSCs on TCPS	Unsorted on TCPS	Unsorted on 100 kPa PDMS	Unsorted on 1 kPa PDMS
Day 7	79.37	76.83	80.40	83.07	82.19
Day 14	81.56	80.42	85.20	88.61	87.13
Day 21		87.52	86.46	89.81	90.75
Day 28		86.05	87.48	95.21	93.72
Day 35		90.93	89.89	94.72	95.44
Day 42		90.93	82.65	83.47	89.14
Day 49		81.29	79.61	75.36	88.57

Mean weight recovery was calculated each week post-irradiation.

Table B-2. Statistical Comparisons of Weight Recovery Across Experimental Groups

	Tukey's multiple comparisons test						
	Adjusted p value						
	Day 7	Day 14	Day 21	Day 28	Day 35	Day 42	Day 49
D^{hi} MSCs vs. Unsorted	0.5132	0.5091	0.9896	0.9887	0.9952	0.5377	0.9928
D^{hi} MSCs vs. 100 kPa	0.0439	0.043	0.8801	0.1245	0.778	0.5200	0.691
D^{hi} MSCs vs. 1 kPa	0.0917	0.1145	0.7143	0.2315	0.6381	0.9843	0.3951
Unsorted vs. 100 kPa	0.5738	0.6368	0.6202	0.1569	0.578	0.9987	0.9015
Unsorted vs. 1 kPa	0.8078	0.8992	0.3949	0.3003	0.4129	0.5780	0.3823
100 kPa vs. 1 kPa	0.9505	0.9128	0.9748	0.9555	0.9951	0.5268	0.0378

Entries highlighted in green are statistically significant, with adjusted p-values < 0.05. P-values were adjusted to account for family-wise error due to the multiple pair-wise comparisons made across experimental groups at every time point.

B.3 Engraftment after non-contact co-culture (Chapter 5)

To determine if co-culture negatively impacted HSPC ability to differentiate and engraft, we transplanted HSPCs into mouse models of irradiation injury. We collected HSPCs after growing them in non-contact co-culture (Chapter 5, Section 5.4.3) with unsorted MSCs grown on TCPS, 100 kPa PDMS, and 1 kPa PDMS for ~1 week. We chose to only include the 1 kPa and 100 kPa co-culture conditions, omitting the 10 kPa condition, as those two PDMS conditions represent the mechanical extremes tested and were statistically distinct in terms of HSPC proliferation (Chapter 5, Fig. 5-4 C). As a comparison to standard HSPC transplants, we also grew HSPCs in monoculture with no MSCs. Instead of normalizing cells to equal concentrations for administration, we pooled HSPCs from four wells of the same experimental condition and divided them equally among four recipient mice. Doing so allowed us to maintain the differences in improved *ex vivo* expansion across experimental conditions. We irradiated NSG mice with 240 cGy of gamma irradiation to induce slight hematopoietic injury and administered HSPCs via tail vein injection. We collected peripheral blood from the mice every 2 weeks after HSPC transplantation to assay human versus mouse CD45 cell counts. Higher % CD45 chimerism is indicative of differentiation and engraftment of the transplanted human HSPCs.

At week 8, we observed that HSPCs isolated from mechanoprimed MSCs (1 kPa PDMS) were the only experimental group with statistically significantly higher chimerism than HSPCs expanded in monoculture (Fig B-3). By week 12, this same experimental group of HSPCs has statistically higher chimerism than all other experimental groups (Fig. B-3). This suggests that the increased expansion observed *in vitro* co-culture (Fig. 5-4, Chapter 5) is maintained *in vivo* after transplantation. Moreover, these results also demonstrate that *in vitro* HSPC co-culture with mechanoprimed MSCs can support long-term engraftment and differentiation of HSPCs *in vivo* up to week 12.

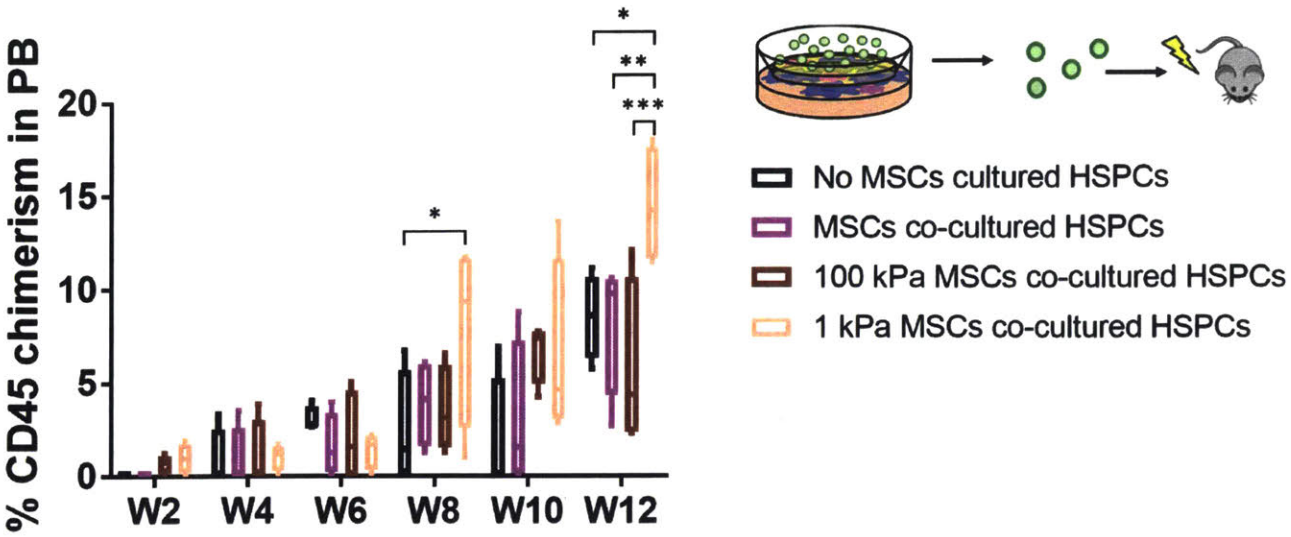

Figure B-3. Engraftment of HSPCs after Non-Contact Co-Culture. Human HSPCs (green) were expanded for one week in monoculture (black) and non-contact co-culture with unsorted MSCs on top of tissue-culture polystyrene (purple), 100 kPa PDMS (dark orange), and 1 kPa PDMS (light orange). Human HSPCs were then isolated from co-culture and administered via tail-vein injection into mice after irradiation injury. CD45 chimerism in the peripheral blood, indicative of engraftment and differentiation of human HSPCs, was tracked every 2 weeks after HSPC transplantation. To account for multiple hypothesis testing, Tukey's multiple comparison test was used with adjusted p-values to determine statistical differences (* $p< 0.05$, ** $p<0.01$, *** $p<0.005$).

B.4 Evaluating Individual Secretome Components of the PLSR Model (Chapter 5)

To ascertain the importance of each protein identified as highly correlative with improved mouse survival and hematopoietic recovery in Table 5-1 (Chapter 5), we explored modifying their expression in our PLSR model. To do so, we removed or incorporated expression of those proteins one at a time from our PLSR model predictions (Figure 5-6 A, Chapter 5).

To remove expression of a given protein, we set its concentration to 0 across all experimental conditions. In other words, we "knocked out" (KO) the expression of each of those proteins deemed to be significantly correlated to survival and most highly-weighted in our predictive model. We then re-plotted the predicted survival curves with the expression of each protein abrogated (Figure B-4). We plotted these new predicted survival curves for ANG-1 (Fig. B-4 B), EGF (Fig. B-4 C), FGF1 (Fig. B-4 D), IL6 (Fig. B-4 E), IL8 (Fig. B-4 F), RANTES (Fig. B-4 G), and VEGFA (Fig B-4 H). Note that we could not conduct this analysis for BMP2 as we could not detect BMP2 when we quantified secretome expression. For ease of comparison, we also plotted the original predicted survival curves (Fig. B-4 A), which are the same curves as predicted in Chapter 5 (Figure 5-6 A). When comparing the individual KOs with the original survival curves, there are not large changes in survival proportions. However, we do see some slight changes in the relative differences across experimental groups in terms of survival proportion when comparing to the original survival predictions. For example, when ANG-1 expression was removed (Fig B-4 B), the survival predicted for mice injected with D^{hi} MSCs is shifted to values higher than those injected with the MSCs grown on 10 kPa PDMS. However, we observed an opposite shift for RANTES at the time points beyond 45 days (Fig. B-4 G). Knocking out protein expression independently did not seem to strongly affect survival predictions, but did change relative trends across experimental groups.

To further understand why this may be the case, we also predicted changes in survival due to expression of each factor identified to be significantly correlated with survival. In this case, we removed expression for all proteins (setting all concentrations to 0), except for the concentrations of the protein of interest. We set concentrations of the protein of interest to 1, 2, 3, 4, or 5. As concentrations were z-score normalized in our PLSR predictions, these values would correspond to linear changes in concentration (1x, 2x, 3x, 4x, 5x concentrations) across experimental groups. We chose to use linear changes in concentration as most differences in secretome expression across experimental groups did not exceed an order of magnitude. We conducted predictions for all proteins deemed to be significantly correlated with improved survival (Fig B-5). At first glance, these predicted survival curves appear to almost overlapping across conditions, which suggests very minor differences in predicted survival. For all proteins, the 5x concentration led to an endpoint survival proportion that ranged from 24.1% to 25.6%. On the other hand, the 1x concentration led to an endpoint survival proportion that ranged from 16.2 to 17.7%. Overall, these survival proportions ranged in the middle of the original predicted

survival curves. We chose to calculate the differences in endpoint survival proportions, as this time point is where the differences are maximized across experimental conditions. The difference in endpoint survival proportions between the best (5x) and worst (1x) ranged from 6.8% to 9.4% across the different proteins. This suggests that the changes in expression from a single protein leads to a <10% change in predicted survival proportion.

From Figs. B-4 and B-5, we found that the KO or addition of individual proteins led to very small changes in predicted survival. When each factor was expressed independently (Fig B-5), a 5-fold change in expression led to a <10% change in predicted survival. These minimal changes predicted may also be why we observed minimal changes in predicted survival when we KOed expression of these factors (Fig B-4). However, we also explored how the survival predictions would change when we KO'ed expression of all the highly correlative factors, but not the expression of the remaining factors. In Fig. B-6, we predicted survival with expression of all correlative factors set to 0 (ANG1, BMP2, EGF, FGF1, IL6, IL8, RANTES, VEGFA). When all these factors are computational knocked out at the same time, the predicted survival curves appeared to collapse on top of each other (Fig B-6 B). In our original predictions, the "best" condition (MSCs on 1 kPa PDMS) have a higher endpoint survival proportion that the "worst" condition (unsorted MSCs on TCPS) by ~50% (Fig B-6 A). When expression of all correlative factors are knocked out, this difference in endpoint survival was reduced to ~12% (Fig B-6 B). This suggested that all factors together contributed to large changes in predicted survival, as opposed to a single factor alone. Biologically, this may suggest that a combination of these identified secreted factors is necessary to support radiation rescue. In other words, improved recovery cannot be attributed to a single factor.

In addition to knocking out all factors, we also explored how the expression of BMP2 could change predicted survival when added to the original expression data (with no KOs). For the secretome samples we acquired, BMP2 was below the detection limit of our assay. Thus, we had no expression data for BMP2 to implement in our model predictions. To explore how BMP2 could affect the survival predictions, we also computed the survival proportions by including arbitrary concentrations of BMP2 (Fig. B-6 C) along with the expressions of all proteins used for the original survival predictions (Fig. B-6 A, no KOs). We used concentration values of 1x, 2x, 3x, 4x, 5x for the unsorted MSCs expanded on TCPS, D^{hi} MSCs previously expanded on TCPS, and unsorted MSCs expanded on 100 kPa, 10 kPa, 1 kPa PDMS, respectively. The addition of these BMP2 concentrations for these experimental conditions led to visible changes in predicted survival. For the "best" condition where predicted survival proportion is highest (1 kPa PDMS), the endpoint survival proportion was shifted from 45.2% without BMP2 (Fig B-6 A) to 52% with BMP2 (Fig B-6 C). Additionally, the predicted difference between the "best" and "worst" conditions at the end point or plateau would then be ~63% (Fig. B-6 C) instead of ~50% in our original prediction (Fig. B-6 A). This difference was even larger than the shift we observed when exploring BMP2 alone (Fig B-5 B). Although the concentrations of BMP2 added to the model were chosen arbitrarily, its inclusion in the survival predictions can lead to large changes in

predicted survival. Thus, the lack of inclusion of a single correlative factor, such as BMP2, illustrates potential reasons for discrepancy between our model prediction and our experimental results (Fig 5-6 A-B in Chapter 5).

Together, these results suggest that many secreted factors together are required to support hematopoietic recovery. A single factor alone leads to small changes in predicted survival. We attribute the discrepancy between model predictions and experimental results due to missing expression of other proteins, such as for BMP2. This suggests that incorporation of more factors into the predictive model can aid in increasing the predictive accuracy of animal survival.

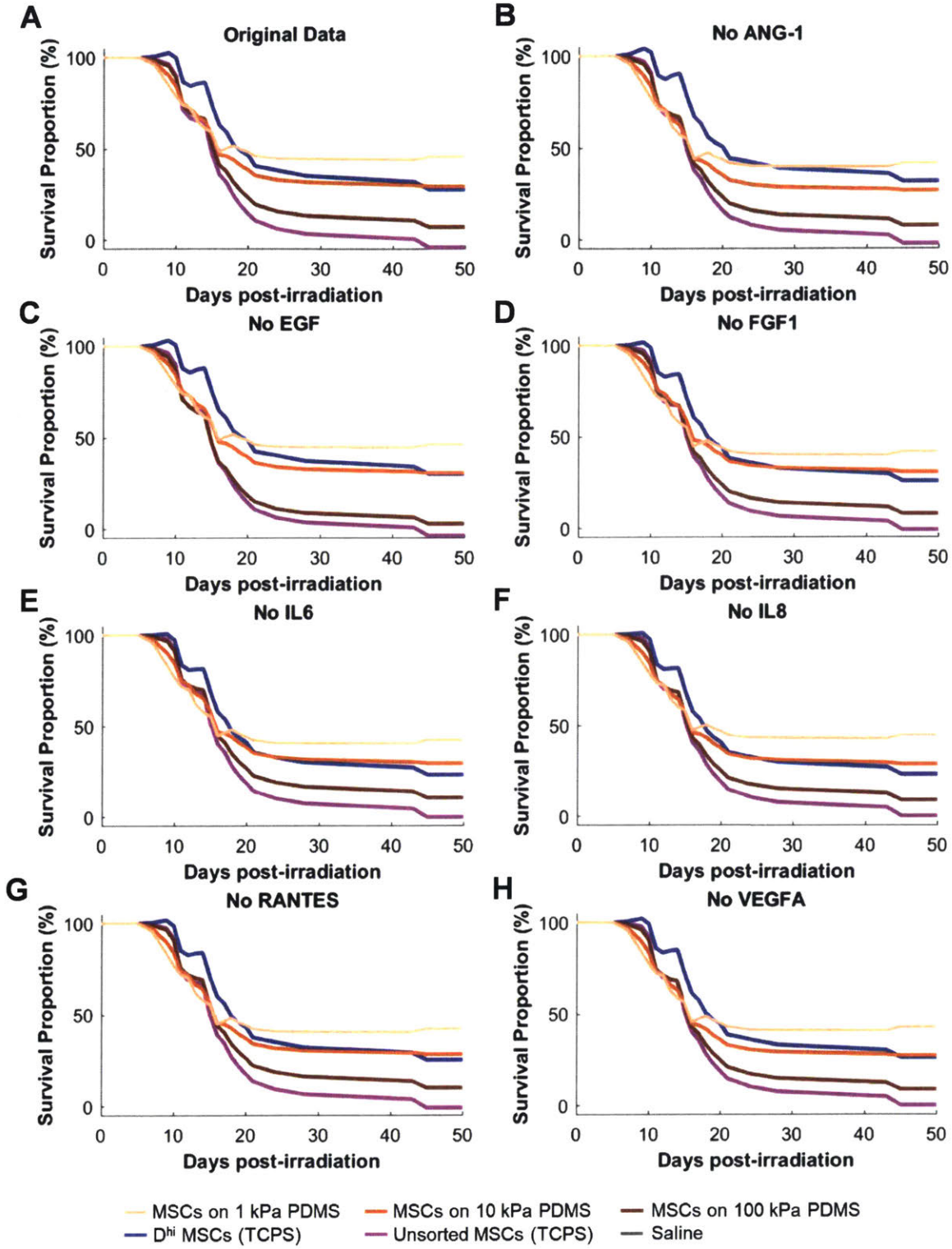

Figure B-4. Knocking out expression of correlative proteins independently in our PLSR model predictions. A) The original predicted survival curves. Predicted survival with no expression of B) ANG-1, C) EGF, D) FGF-1, E) IL6, F) IL8, G) RANTES, and H) VEGFA. Experimental groups predicted included unsorted MSCs grown on PDMS (three orange lines), D^{hi} MSCs (blue line) on TCPS, and unsorted MSCs (purple line) on TCPS. PDMS substrata of varying stiffness (1, 10 and 100 kPa PDMS) are represented by light, medium, and dark orange colors, respectively.

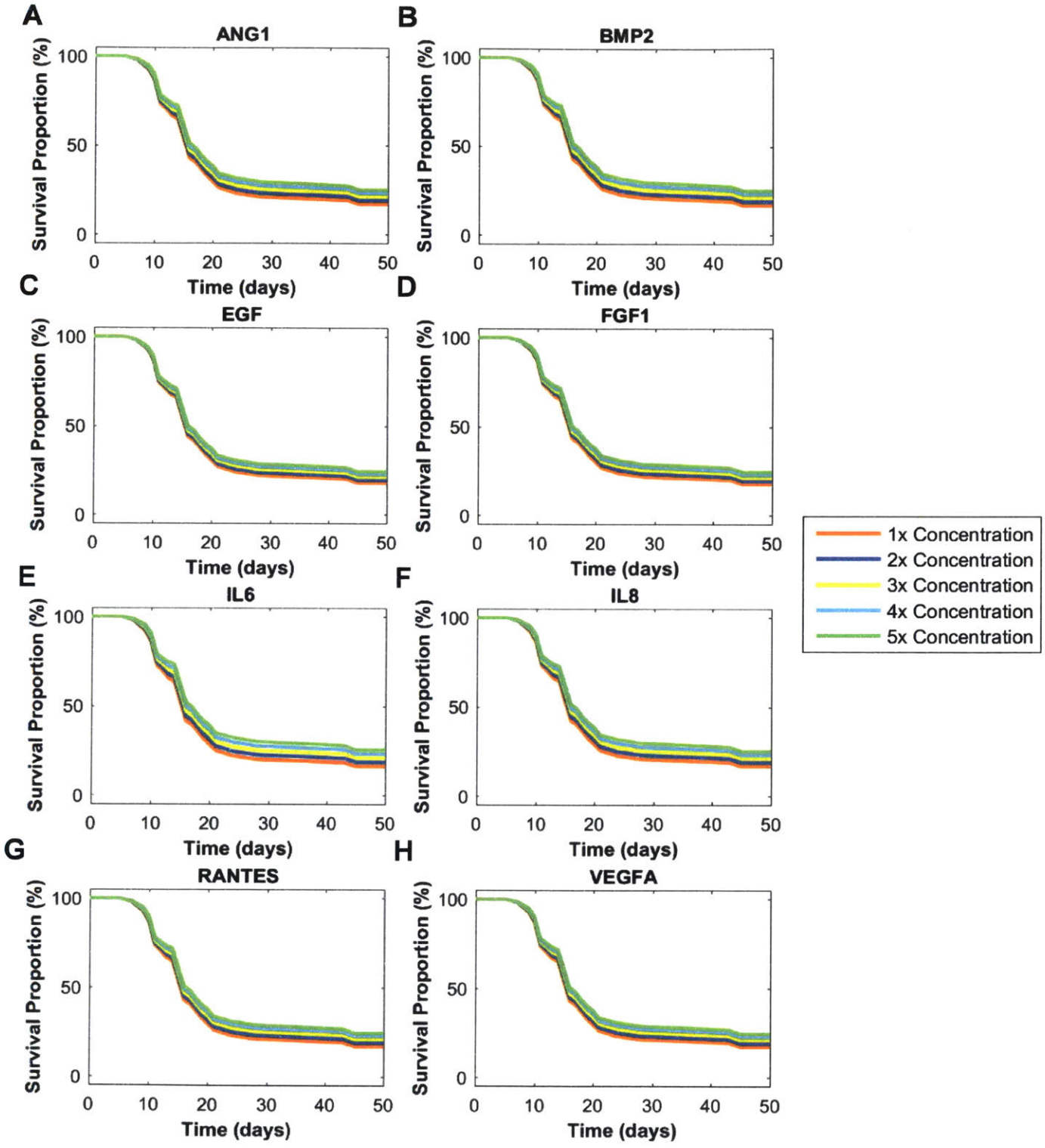

Figure B-5. Survival due to expression of correlative proteins independently in our PLSR model predictions. Predicted survival curves with only expression of A) ANG1, B) BMP2, C) EGF, D) FGF1, E) IL6, F) IL8, G) RANTES, or H) VEGFA. Expression values were input as 1, 2, 3, 4, 5 to represent linear changes in concentration (orange, blue, yellow, cyan, and green curves, respectively).

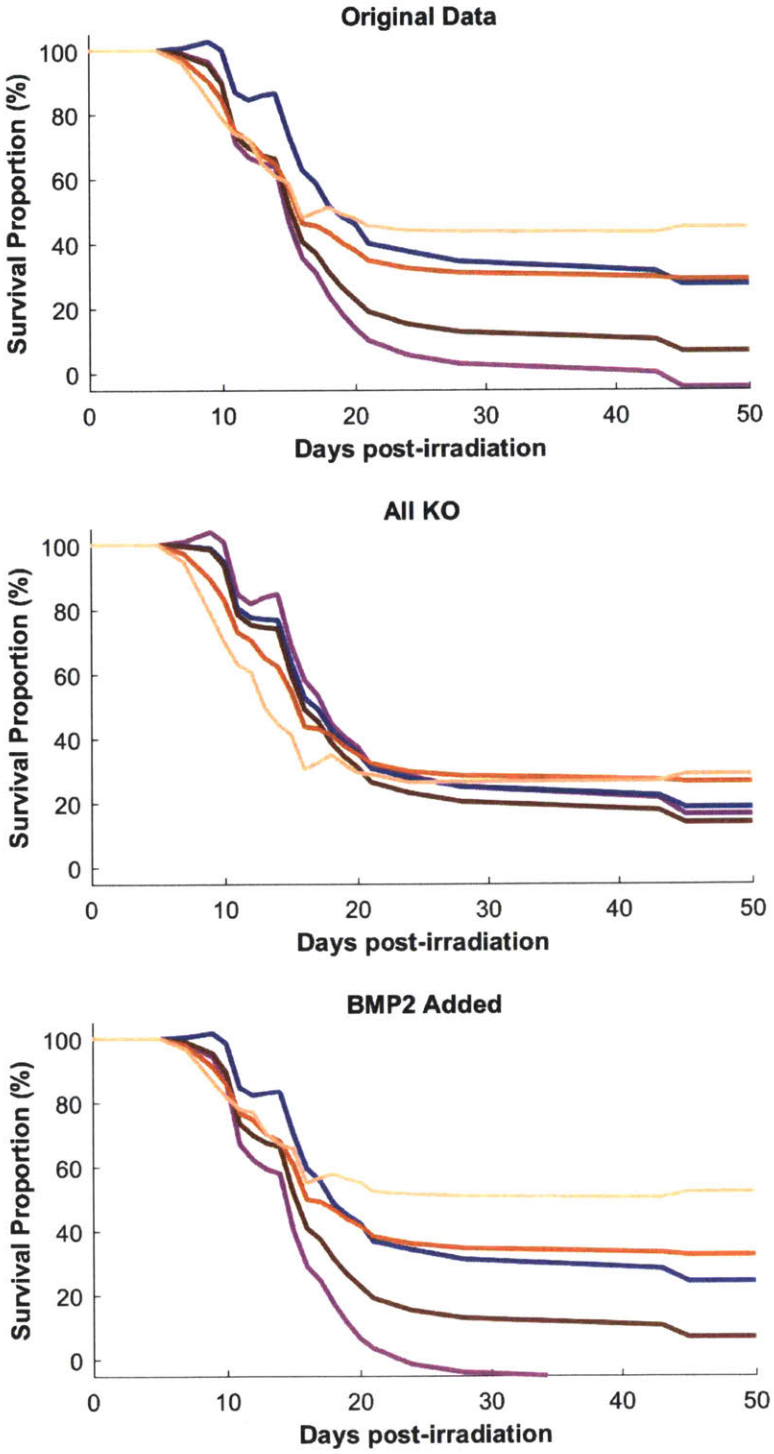

Figure B-6. Knocking out expression of all correlative proteins and incorporating BMP2 in our PLSR model predictions. A) The original predicted survival curves. B) Predicted survival curves with expression of all correlative proteins removed or knocked out (KO). C) Predicted survival curves with BMP2 expression incorporated.

Appendix C

Analyzing and Segmenting Images with and without Macromolecular Crowder (Chapter 2)

C.1 Acknowledgements

The original MATLAB code was obtained from Dr. Adam Zeiger and subsequently modified for the particular set of experiments outlined in Chapter 2 of this thesis.

C.2 Identifying ECM Fiber Orientation in VEC Images

In this Appendix, we detail how the images of vascular endothelial cells (VECs) were analyzed in the absence and presence of macromolecular crowder (MMC). We grew VECs in glass-bottomed well plates to confluent monolayers (Chapter 2). We added synthetic MMC to VEC monolayers after 24 hrs of culture and imaged the VECs at various time points thereafter. To explore basement membrane formation, we stained for and imaged type IV collagen. For the following figures presented in this appendix, data and images corresponding to VECs grown in the absence and presence of MMC correspond to the left (A) and right (B) subpanels, respectively. We present and analyze representative images from each of these experimental group.

Initially, when looking at the raw images (Fig. C-1), we observed distinct fibers formed in the absence of MMC (Fig. C-1 A). In the presence of MMC, the collagen IV looks relatively uniform with almost complete coverage of the field of view (Fig. C-1 A). When acquiring these images, we used low-powered objectives with low magnification (10x) to cover a wide field of view. Due to this low magnification, we modified the local neighborhood size and filtering parameter by changing the "block size" in order to better segment the images. In addition to filtering, we also re-sized the images and removed out the background (low fluorescence intensity) in order improve image segmentation. The re-sized, thresholded, and filtered images are presented in Fig. C-2. From these modified images, we could then better visualize the differences in fibers in both experimental conditions (Fig C-2). The fibers appeared to be

visually thinner and more dispersed in the presence of MMC (Fig C-2 B). After these initial steps, we then used the same code as previously published to further process the images and segment the fibers to identify their orientations [68].

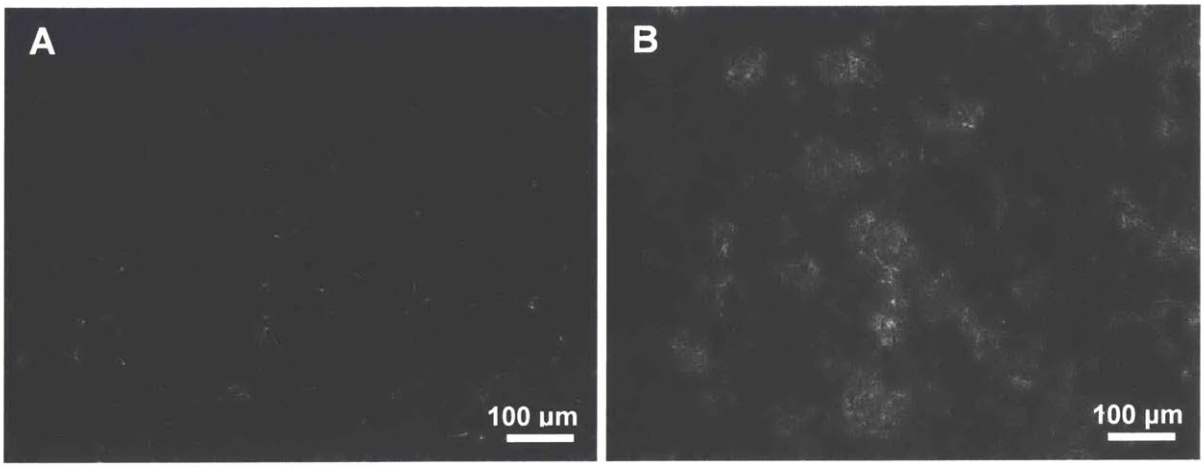

Figure C-1. Raw Images Stained for Analysis. Type IV Collagen was antibody-stained and image for vascular endothelial cells grown A) without crowder and B) with macromolecular crowder (MMC).

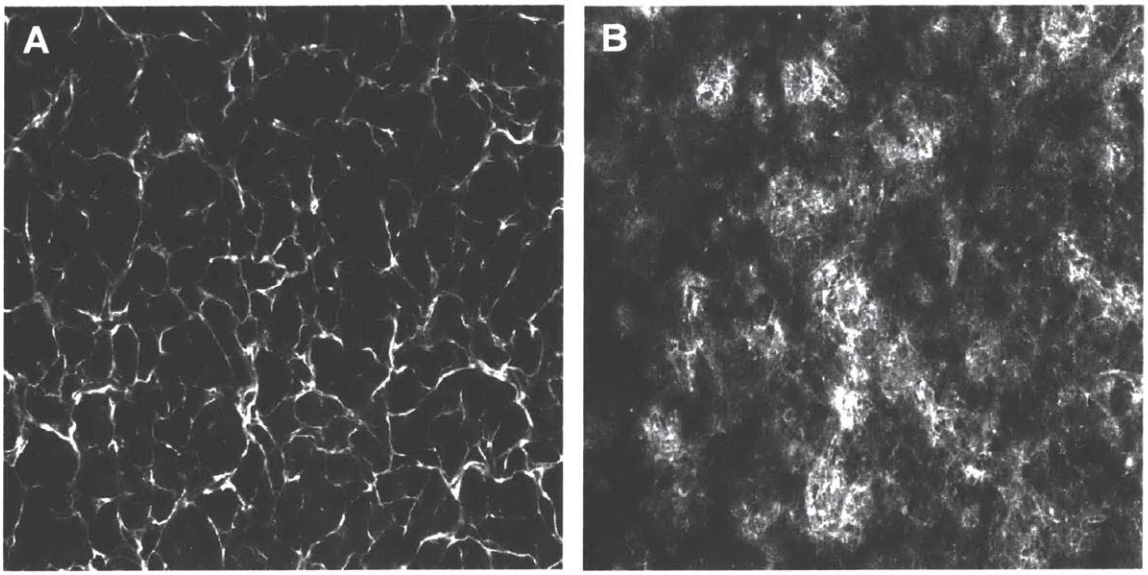

Figure C-2. Re-sized and Filtered Images. For simplifying analysis, images were re-sized and filtered to better segment collagen fibers in images taken A) without crowder and B) with macromolecular crowder (MMC). Note that scale bars were not included in these images because images were re-scaled differently in the X and Y directions for ease of image processing and analysis.

In Fig. C-3, we present the segmented images corresponding to the same two representative images displayed in Fig. C-1 and Fig C-2. Each color in the segmented image represents a distinct fiber identified from the image. We can see that the fibers in the absence of MMC seem to be longer (Fig C-3 A). The collagen IV fibers in the presence of MMC appear to be more punctate and have shorter persistence lengths (Fig. C-3 B). Along with the larger areal coverage, the shorter fibers results in many more fibers being identified in a single image with the presence of MMC. The increase in the number of fibers per image with MMC leads to a smoother histogram of the orientation angles of the ECM fibers (Fig. C-4 B). This results in a gaussian-like distribution of orientation angles. On the other hand, the distribution of orientation angles in the absence of crowder appears to have multiple distinct peaks (Fig. C-4 A). These histograms are centered around the maximum orientation angle of the local neighborhood as defined by the block size.

From these histograms, we then quantified the standard deviation of that distribution of orientation angles. We then reported that standard deviation as our local order parameter, α_{SD}. A higher α_{SD} suggests that the fibers are more randomly oriented, and less aligned. On the other hand, a lower α_{SD} is indicative of increased alignment.

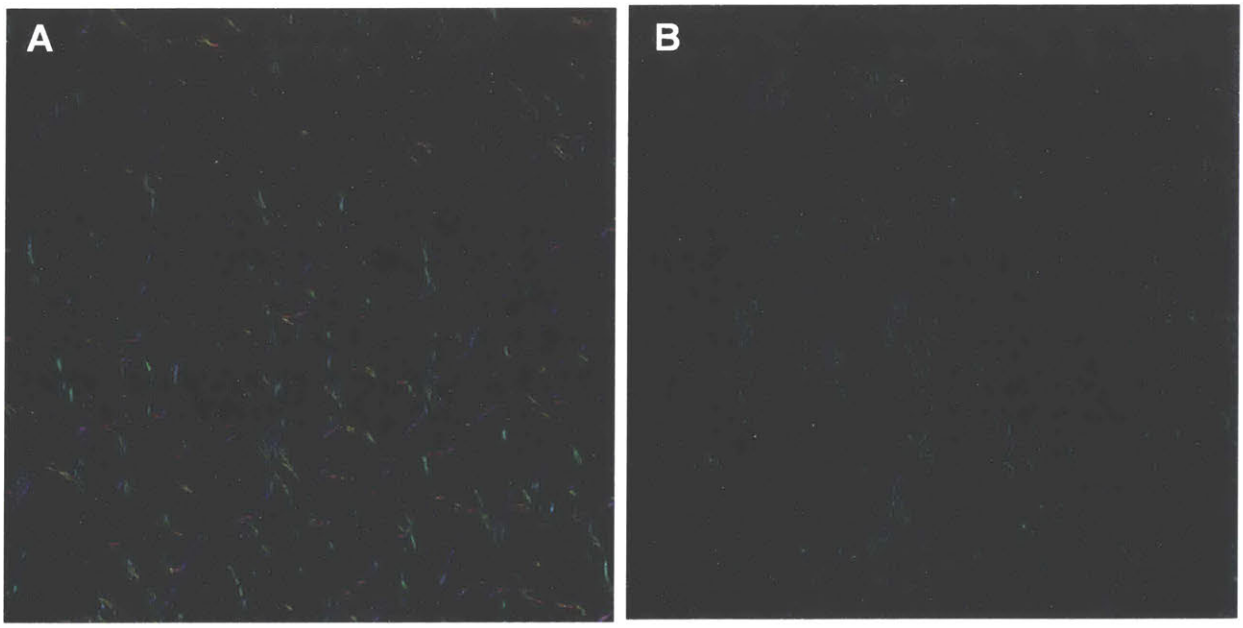

Figure C-3. Segmented images identifying ECM fibers. Images were analyzed A) without crowder and B) with macromolecular crowder (MMC). Individually identified ECM fibers are colored differently. Note that scale bars were not included in these images because images were re-scaled differently in the X and Y directions for ease of image processing and analysis.

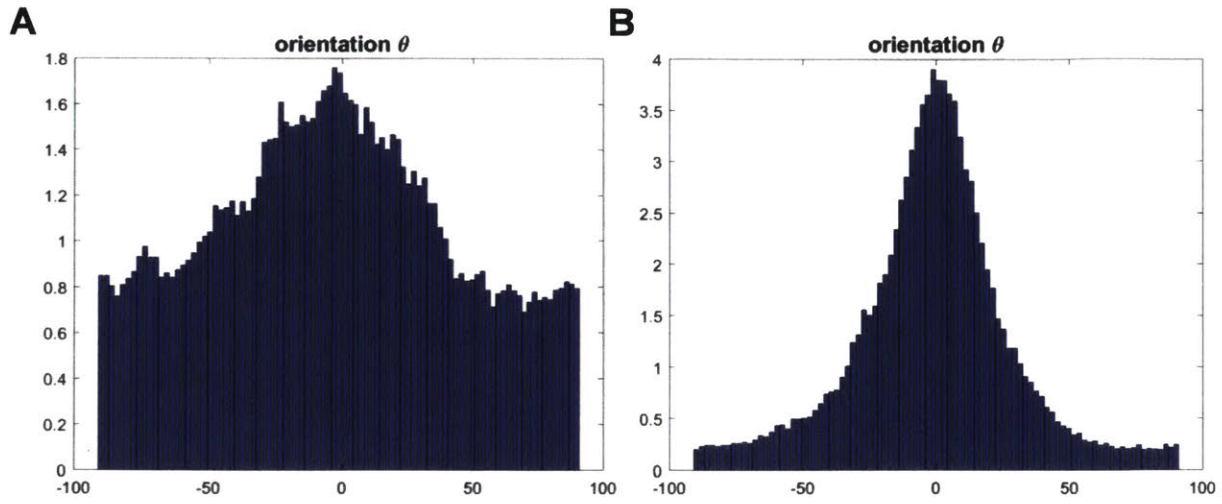

Figure C-4. Representative histograms of local fiber orientation. Histograms of orientation angles and ECM fibers identified from segmented images A) without crowder and B) with macromolecular crowder (MMC). The standard deviations of these histograms were calculated to be A) $\alpha_{SD} = 52.1°$ and B) $\alpha_{SD} = 28.15°$.

C.3 MATLAB Code used to analyze fiber orientation

The following MATLAB code was used for image analysis. Note that the following code contains analysis for all images in a specified folder. For this particular set of code, the only images analyzed are shown above. Additionally, this code also contains the option to vary the block size (currently commented out in line 50, as variable "LPBlockSize = varyBlockSize(j)"), a filtering parameter, to better optimize the segmentation of the images with and without MMC.

```
% CollagenOrient_20140715_fdl

% m-file for the detection of local orientation in image neighbourhoods
% The algorithm is described on Jaehne B., Digital Image Processing, 6th
% Edition, Springer, 2005
%
% Dimitrios Tzeranis, December 2007

% Modified orginally by Sezen Beull 2007

% Modified for hMSCs by Adam Zeiger 2009. Special thanks to Ran Li for
% insight and assistance


% Modified for BRECs by Frances Liu 2014. Modified to "vary" block size
```

```
% (filtering parameter)through a for loop.
% Also modified to run ALL files from a single folder through entire code
% in nested for loop.


clc;
clear all;
close all;

tic

% Use following line to specify folder path
myFolder = 'C:\Users\franc\Dropbox (MIT)\Mac Files Jan 2017\MATLAB\MMCFilesforThesis';
filePattern = fullfile(myFolder, '*A488*.tiff'); % File Name Pattern - the
% asterisk in the line above represents variable string in file name
tiffFiles = dir(filePattern);

%varyBlockSize = [1,2,3,5,8,10]; % Uncomment to vary block size

% Pre-Allocating Matrices
outputNames = cell(length(tiffFiles),1);
output=zeros(length(tiffFiles));
% output=zeros(length(tiffFiles),length(varyBlockSize)); % Replace
% preceding line with this to vary block size

%for j = 1:length(varyBlockSize) % Uncomment to vary block size

    for k = 1:length(tiffFiles)


baseFileName{k,:}=tiffFiles(k).name;

% % % algorithm parameters
LPBlockSize = 5; % Change filter size manually HERE
% LPBlockSize = varyBlockSize(j); % Replace preceding line with this to
% vary block size automatically with for loop
gammac = 0.1;

% read image
RawFrame = imread(tiffFiles(k).name);
figure
imshow(RawFrame,[]);
RawFrameLength=length(RawFrame);
RawFrame = imresize(RawFrame,[RawFrameLength,RawFrameLength]);
RawFrame = RawFrame(:,:);RawFrame = imresize(RawFrame,[RawFrameLength,RawFrameLength]);
RawFrame = imadjust(RawFrame);
RawFrame = double(RawFrame)';
figure
imshow(RawFrame,[]);

PhotonC = double(RawFrame)/double(max(max(RawFrame)));
PhotonC2 = reshape(PhotonC,1,RawFrameLength^2);
```

```
% % % ========================= local orientation analysis
Hx = [3,0,-3;10,0,-10;3,0,-3]/32;
Ax = imfilter(RawFrame,Hx,'replicate');
Ay = imfilter(RawFrame,Hx',replicate');
% Ax = imfilter(RawFrame,fspecial('sobel'),'replicate');
% Ay = imfilter(RawFrame,fspecial('sobel')',replicate');


Axx = Ax.*Ax;
Ayy = Ay.*Ay;
Axy = Ax.*Ay;

Jxx = imfilter(Axx,fspecial('average',LPBlockSize),'replicate');
Jyy = imfilter(Ayy,fspecial('average',LPBlockSize),'replicate');
Jxy = imfilter(Axy,fspecial('average',LPBlockSize),'replicate');

PhotonC = imfilter(RawFrame,fspecial('average',LPBlockSize),'replicate');

% coherence values
c = sqrt((Jyy - Jxx).^2 + 4*Jxy.^2)./(Jxx + Jyy);
c2 = reshape(c,1,RawFrameLength^2);
chist = hist(c2,linspace(0,1,20));
%figure,bar(linspace(0,1,20),chist)
%title('cohesion','FontSize',14)

% theta values
BandNum = 90;
theta = atan2(2*Jxy,Jyy-Jxx )/2;
theta2 = reshape(theta,1,RawFrameLength^2);

% magnitude of orientation vector
BandNum = 90;
mag = sqrt(double((2*Jxy).^2) + double((Jyy-Jxx).^2));
mag2 = reshape(mag,1,RawFrameLength^2);
MaxMag = max(mag2);
mag2 = mag2/MaxMag;
maghist = hist(mag2,linspace(1/BandNum/2,1-1/BandNum/2,BandNum));
%figure,bar(linspace(1/BandNum/2,1-1/BandNum/2,BandNum),maghist)
%title('orientation vector magnitude','FontSize',14)

HsvImage = ones(RawFrameLength,RawFrameLength,3);
HsvImage(:,:,1) = (theta + pi/2)/pi;
HsvImage(:,:,3) = double(PhotonC)/double(max(max(PhotonC))).*mag/max(max(mag));
RgbImage = hsv2rgb(HsvImage);

%figure,imshow(PhotonC);
figure,imshow(RgbImage); % If you want to display the "colored" fiber
%image,uncomment this line (line 101)!

Mask1 = PhotonC2>0.1;
Mask2 = mag2>0.1;
theta2(~(Mask1&Mask2)) = [];
theta3=2*theta2';
```

```
% The standard deviation "sdev" of fiber orientation distribution is calculated here
avgsin=mean(sin(theta3));
avgcos=mean(cos(theta3));
rvector=sqrt(avgsin^2+avgcos^2);
sdev(k,:)=sqrt(log(1/rvector^2))/2; % The standard deviation or alpha_SD
Size=size(theta2);
thetahist = hist(theta2,linspace(-pi/2+pi/BandNum/2,pi/2-pi/BandNum/2,BandNum));
export=thetahist/Size(2)*100;
figure,bar(linspace(-pi/2,pi/2,BandNum)/pi*180,thetahist/Size(2)*100)
title('orientation \theta','FontSize',14)
%^^ These two lines display the histogram



output = 180*sdev/pi(); % The alpha_SD is converted to degrees and output as angle values

    end
% end % Uncomment to use nested for loop to analyze changing block size

baseFileName
output

toc
```

```
displaying at 67%

baseFileName =

    'BRECs_Col_Act_2wk_A - 1_A488.tiff'
    'BRECs_MMC_Col_Act_2wk_A - 3_A488.tiff'


output =

   52.0945
   28.1455

Elapsed time is 4.464679 seconds.
```

Published with MATLAB® R2015b

Appendix D

Detailed Protocol for Preparation of Cell Stretcher PDMS Molds and VEC Sprouting Assay (Chapter 3)

D.1 Acknowledgements

Dr. Adam Zeiger developed and assembled the following protocol. Frances Liu was responsible for further editing and optimizing this protocol. The original recipe for the 3D-gel was developed by Dr. Jennifer Durham. Additional details for the cell-stretcher protocol are included Chapter 3 and the supporting information of the article published in Physical Biology [120].

D.2 Materials

For PDMS Molds

- Sylgard 184 Silicone Elastomer Kit
- KitKraft 1/2" circle mirrors (http://www.kitkraft.biz/product.php?productid=5184)
- Lids of 48-well TCPS plates (e.g., Greiner Bio-One #677180)
- Cyanacrylate-based "super glue" (e.g., Pacer Technology Super Glue #SGP3)
- Parafilm

For Cell Culture

- Bovine retinal endothelial cells (BRECs) at passage 12-15 (Located in LN2 Dewar in the boxes 1B, 2C, 3C, 8C, 8D, 8E)
- DMEM (low glucose 1g/L)
- Bovine Calf Serum (5% by volume)
- Pen/Strep (1% by volume)

For 3D Gel

- Collagen Type I (Rat Tail BD Biosciences #354236)
- Growth Factor Reduced Matrigel Matrix (BD Biosciences #354230)

- AnaSpec FITC-conjugated Collagen Type I (AnaSpec #85111)

For Fixation/Staining
- 36% Formaldyhde for Cell Biology (Sigma #F8775)
- Glutaraldehyde (Sigma #G6257)
- 3% BSA (Sigma #A7906) in 1X PBS
- Triton X-100
- Hoechst (Invitrogen #33342)
- Alexa Fluor 594 Phalloidin (Invitrogen #A12381)
- Approximately 1 L of unfiltered PBS (from 10X stock)
- 2-4L Wash Tray – wide enough to hold two PDMS molds side-by-side, but deep enough to fully submerge the molds

D.3 Preparation of PDMS Molds

Day 1 - Preparation of Stretchable PDMS Molds
1) Line lids of TCPS plates with parafilm. Lining with parafilm ensures that the PDMS molds (or stretchable wells) can be easily removed after curing.
2) Adhere kitkraft mirrors to parafilm with "super glue" using lid template as a guide. We typically create a 4x4 grid of 16 wells in the center of the lid. Make sure mirror surfaces are reflective face-up and have clean surface. If not, clean mirror surfaces with
3) While glue cures, prepare 1:20 mixture (curing agent:base) of Sylgard 184 PDMS
4) Mix well for 3 minutes
5) Pour approximately 25 mL of PDMS per lid. This is the maximum volume that fits in the lid. Estimate 25 mL by using lines on cup used to mix PDMS that typically have volume markings. If not, use a graduated cylinder and water to measure volumes in cup and draw your own volume markings.
6) Place lids in vacuum oven and apply vacuum for approximately 1 hour (to remove air bubbles)
7) Release vacuum and bake at 45°C for >24 hours. Do not use higher temperatures as parafilm will melt.

Day 2 - Acetone treatment of PDMS:
1) Remove molds from oven and allow to cool to room temperature
2) Carefully remove parafilm and mirrors
3) Trim molds to proper size for mounting in strain devices (7.5-8 cm x 10.5-11.5 cm)
4) Soak molds in 100% acetone for >24 hours

Day 3 - Removal of acetone-:
1) Remove PDMS from acetone
2) Bake at 45C in vacuum oven (no vacuum) for >24 hrs
3) Molds can be stored up to a week in advance of experiments

D.4 VEC Culture on PDMS Molds

Day 4 – Experiment Start (Seeding of cells):

1) Prepare PDMS molds by vacuum corona treatment for 30-60 seconds per well (molds should be used immediately after treatment). Alternatively, treat with vacuum plasma chamber for ~10-15 minutes.
2) Add 100uL of 5% BCS in DMEM + 1:100 Pen/Strep to each well. Confirm that media spreads quickly and completely over well bottom (indicative of hydrophilicity).
3) Mount PDMS into strain devices. Make sure PDMS molds are "pre-strained" so that they lie taut and flat in stretcher device.
4) Prepare and seed BRECs in 5% BCS in DMEM + 1:100 Pen/Strep at 100,000 cells/cm^2 in each well (add 100uL per well)

Day 5 – Cell Cycle Synchronization (Serum starvation):

1) Carefully and gently aspirate away media from cells. Place micropipette tip over Pasteur pipette to reduce vacuum pressure. Do not touch wells with pipette tip.
2) Serum starve BRECs using 0.5% BCS in DMEM + 1:100 Pen/Strep for 24 hours. Add 150ul/well.
3) Remove matrigel aliquot from -20°C freezer and defrost in 4°C fridge, overnight

Day 6 – 3D Gel Formation and Strain Application:

1) Carefully aspirate away media from cells
2) Add 3 μg/mL Collagen Type-I in 100 uL to each well and incubate at 37°C for 30 min. This extra layer of Collagen Type-I helps to stabilize the BREC monolayer.
3) Carefully aspirate away residual media/collagen from cells
4) Add 100-150 μL of Matrigel mixture
   - 50% Matrigel, 16% Collagen Type-I, 4% FITC-Collagen, 30% 0.5% BCS in DMEM with Pen/Strep (volume percentages as volume percent). The addition of Collagen Type-1 helps to make the gel stiffer.
   - Also add 5uL/mL of 1M NaOH
   - For example: for 4 mL of gel
     - 2 mL matrigel
     - 640 uL collagen type-I
     - 160 uL FITC-collagen
     - 1.2 mL of 0.5% BCS in DMEM with P/S
     - 20uL NaOH
5) Incubate gel at 37°C for 2 hours. Matrigel cross-links at physiological temperatures and remains a liquid at room temperature and below.
   AFTER THIS STEP - NO MORE VACUUM ASPIRATION CAN BE USED
6) Do not remove gel. Carefully add 100uL of 5% BCS in DMEM + 1:100 Pen/Strep on top of each well.
7) Apply no strain (control), or 10%, uniaxial strain for 48 hours

Day 8 - Staining Cells (48 hours after strain):
DO NOT USE VACUUM ASPIRATION!!!

1) Pre-warm 1L of 1X PBS and fixation solution to 37°C. Prior to fixation, solutions need to be at physiological temperatures to avoid dissolving Matrigel.
2) Carefully remove PDMS molds from strain devices. Make sure to keep track of which one is the no strain control and which was strained.
3) Carefully invert the mold over wash tray to remove media
4) Carefully add fixation solution (2% paraformaldehyde + 1% glutaraldehyde) on to the gels in each well (100 ul/well). A mix of both aldehydes is used to limit auto fluorescence from the paraformaldehyde fixation. Wait 15-20 minutes.
5) Soak molds in >300mL warmed 1X PBS in cleaned wash tray for 1 minute (then dispose of 1X PBS). Note that repeated wash steps are avoided to minimize disturbance to the gels.
6) Remove and gently invert molds over wash tray to remove solution
7) Add 100uL of Triton X-100 to each well for permeabilization
8) Wait 15-20 minutes
5) Soak molds in fresh >300mL warmed 1X PBS in empty wash tray for 1 minute
6) Add 100uL of mixture of Phalloidin (1:500) and Hoechst (1:5000) to each well
9) Wait 20-30 minutes
10) Soak molds in fresh >300mL warmed 1X PBS in empty wash tray for 1 minute
11) Add ~100uL of 1X PBS to each well for storage

Day 9 or Later – Imaging Sprouts

1) Do not refrigerate fixed molds. They must remain at room temperature or warmer to maintain gelation.
2) Carefully and gently invert molds on to thin glass cover slide that can cover all wells.
3) Image using epifluorescence to quantify sprouts
    a. A488 or FITC channel used to visualize collagen I. According to manufacturer, proteolysis or MMP activity (degradation of collagen I) increases fluorescence. However, we did not observe distinct changes in A488 fluorescence.
    b. A594 or red channel used to visualize actin cytoskeleton
    c. DAPI or blue channel to visualize nuclei
4) Image on confocal microscope
    a. Find sprout first using low-powered objective on epifluoresecence.
    b. Then image at high resolution. Imaging at high resolution requires inverting the molds due to short working distance with high-powered objectives on confocal
    c. The PDMS mold is too thick to image through for effective confocal imaging

Appendix E

Detailed MSC Subculture (Chapters 4 and 5)

E.1 Materials

- Human MSCs – keep track of vendor (Lonza, ReachBio, RoosterBio, and etc.), lot # (or donor), and passage number
- T175 Flasks for adherent cells (175 cm^2 growth area)
- 2.0 ml Cryovials
- 15mL & 50mL conical centrifugal tubes
- 5.0 mL syringes
- Sterile Syringe filters (25mm, 0.2 um pore filter membrane)
- Certified Fetal Bovine Serum (Gibco, Cat# 16000-044)
    - Keep track of lot #
    - Typically stored in 50 ml aliquots in -20°C Freezer
- Low-glucose DMEM (Gibco, Cat# 11885-092)
- Penicillin/Streptomycin (100x)
- Trypsin-EDTA (0.25%), phenol red (Gibco, Cat #25200-114)
- 1x PBS, ph7.4 (Gibco, Cat # 10010-049) – no calcium, no magnesium, no phenol red
- Ice
- DMSO
- Mr. Frosty
- Isopropyl alcohol

E.2 Preparing Media (in 50ml aliquots)

1) Thaw FBS in 37°C heat bath – avoid leaving it for too long (no more than 30-45 min) and causing protein denaturation
2) Sterilize 5.0mL of FBS with 5.0mL syringe and syringe filter directly into 50mL tube
3) Add 45 mL DMEM
4) Add 0.5 mL Pen/Strep
5) Return completed expansion media (10% FBS, 1% P/S in LG-DMEM) to heat bath prior to use. Refrigerate if not using immediately.

E.3 Thawing Cells

1) Take cryovial from liquid nitrogen dewar. Ensure that you have marked it as used in the Liquid Nitrogen Logs.
2) Transfer directly to 37°C heat bath. Wait ~ 5min.
3) Remove from heat bath when mostly thawed (slushy pellet still visible)
4) Add 1.0 mL warm media directly to 2.0mL cryovial drop by drop and mix with cells
5) Transfer all contents of cryovial to 15mL conical tube
6) Add 10mL warm media to conical tube
7) Spin down cells into pellet
    a. Make sure to balance centrifuge
    b. Typical spin speed 1200 RPM (~300xg) for 8 min on centrifuge in 8-214. Can also use higher speeds up to 400xg for 5 min
8) After spinning down, MSC pellet should be visible. Aspirate to remove supernatant

E.4 Expansion

1) Re-suspend pellet with 1.0 mL warm media. Pipette up and down to ensure even mixing and complete suspension. Avoid forming air bubbles while mixing and/or pipetting.
2) Transfer 10 ul to small Eppendorf tube for counting
3) Add 10 ul of trypan blue to Eppendorf tube (1:1 volume ratio or 2-fold dilution)
4) Count live cells
    a. Manual counting – 10 ul per hemacytomer chamber
        i. Number of cells counted x 10^4 cells/mL – cell concentration
        ii. Multiply by 2 to account for trypan blue dilution
    b. Automatic counting – 20 ul per hemacytometer chamber slide
        i. Automatically gives you cell concentration
        ii. Make sure to account for trypan blue dilution
5) Determine number of flasks needed based on total number of cells
    a. We typically use T175 flasks (175 cm^2 of growth area)
    b. Aim to seed cells at ~1000 cells/cm^2 for expansion
    c. For example: for ~500K cells → we need to use 3 T175 flasks
6) Add media to T175 flasks (~20-25mL/flask)
    a. ~20-25 mL per flask
7) Re-suspend 1.0 ml cell suspension with small volume media and split equally into flasks
    a. For example: for 3xT175 flasks
        i. Add 23 mL media to each flask
        ii. Add 5.0 mL media to 1.0 mL cell suspension (6.0 mL total) mix thoroughly → For 500K cells, this would be ~83K cells/mL
        iii. Add 2.0 mL of new cell suspension to flasks
    b. Final volume in flask
        i. Minimum of 25 mL/flask (few cells)

ii. Up to 35 ml/flask (more cells)

c. Label flasks with hMSC vendor, donor #, passage #, initials, date

8) Exchange media during expansion
   a. Immediately after thawing – remove dead cells after 1 day
   b. During expansion (or after passaging) – every 3-4 days
   c. Two population doublings (one passage) is typically 7-10 days for cells

E.5 Passaging Cells

1) Passage when cells become ~90% confluent. View cells under phase contrast microscope. Estimate when cells have spread and covered ~90% of the culture surface area. Several areas of the culture will have cells that are tightly packed, but you should still see some space between cells in other areas. This usually takes around 7-10 days between passages. An example image (4x) of cells approaching ~90% confluent is shown below.

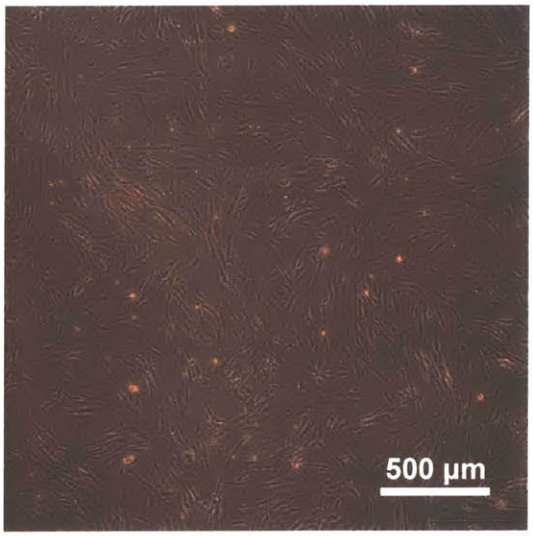

2) Aspirate to remove all media
3) Wash MSCs with 1xPBS
   a. ~15-20mL/flask to fully cover MSC layer and remove residual media
   b. Helps to remove divalent cations and serum proteins that can inhibit trypsin activity
   c. Aspirate to remove PBS. Be careful not to touch MSCs on flask bottom.
4) Add Trypsin/EDTA
   a. Make sure trypsin/EDTA is heated to 37°C
   b. Add 7mL/flask (DO NOT ASPIRATE)
5) Transfer flask with Trypsin/EDTA to 37°C incubator for ~5 min
   a. Inspect under microscope to ensure detachment of MSCs
   b. Agitate flask to ensure complete cell detachment
   c. Try not to trypsinize >10 min to avoid cell death

6) Add warm media (~18 ml/flask) directly to flasks after cells are detached to inactivate trypsin
7) Transfer media and cells from flask to 50mL conical tube
8) Spin down cells into pellete
    a. Make sure to balance centrifuge
    b. Typical spin speed 1200 RPM (~300xg) for 8 min on centrifuge in 8-214. Can also use higher speeds up to 400xg for 5 min
9) After spinning down, MSC pellet should be visible. Aspirate to remove supernatant.
    a. Repeat steps in section E.4 for continued Expansion
    b. Proceed to section E.6 for freezing down cells

E.6 Freezing Cells

1) Preparing freezing media
    a. Sterilize FBS (tube 1)
    b. Prepare tube of 20% DMSO in FBS (tube 2)
    c. Store both on ice to keep cold
2) Re-suspend pellet in 0.5-1.0 mL cold FBS (volume variable depending on how big the pellet is)
3) Count cells according to steps 2-4 of Section E.4
4) Label cryovials
    a. hMSC Donor #
    b. Passage #
    c. # of cells (typically 500K/vial, can go up to 1M/vial)
    d. Initials & date

5) Re-suspend pellet to a final concentration of $1.0x10^6$ cells/mL with cold FBS (for 500K cells/cryovial) – concentration can be scaled depending on how many cells you want to freeze down per vial
6) Add 0.5 mL cells in FBS to each cryovial (500K hMSCs/vial)
7) Add 0.5mL 20% DMSO in FBS to each cryovial – final DMSO concentration of 10% in 1.0 mL volume
8) Gently mix cells in freezing media
9) Close cryovials and place inside Mr. Frosty
    a. Do not seal cryovial too tightly – may explode when thawed
    b. Make sure there is sufficient isopropyl alcohol (IPA) in the Mr. Frosty. It should be refreshed after every 5 uses
10) Leave Mr. Frosty in -80°C for 24 hrs
11) Transfer cryovials to freezer box in liquid nitrogen dewar – take note of box & rack numbers and update in Liquid Nitrogen Logs

Appendix F

Detailed Tunable PDMS Substrata Fabrication Protocol

F.1 Materials

- Sterile Cell Culture Dishes
  - 12 or 24 well-plates (for many experimental conditions or replicates)
  - Petri dishes (for larger growth area)
- Dow Corning CY52-276 PDMS
  - Component A
  - Component B
- Plasma Chamber
- 1.0 mL syringes for transferring PDMS mixtures
- 20mL Scintillation Vials (or any small container) for mixing components
- Handheld mixer (from VWR, located on shelf under table in 8-214, pictured below)

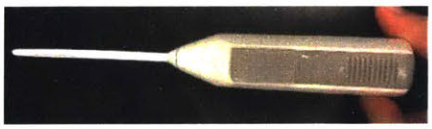

F.2 PDMS Mix Preparation

1) Label mixing containers (20 mL scintillation vials) with mass ratios: 1:3, 1:1, 3:2
2) Measure PDMS component A:B in those same mass ratios (1:3, 1:1, 3:2)
   a. Use syringe to transfer small amounts of PDMS components
   b. Measure A, then calculate amount of B needed to obtain appropriate mass ratio
   c. Try to be within 10-20mg of each mass ratio
3) Use handheld mixer to mix components for ~2-3 minutes, air bubbles will form
4) Transfer mixtures to desiccator and pull vacuum in fume hood to remove air bubbles/degas (<5 min)
5) Label dishes or well-plates while degassing
   a. Mass ratio
   b. Name, date
6) Transfer appropriate volume of each PDMS mixture to dish or well plate

a. Use volumes that will form ~500 um layer on top of the polystyrene well bottom or dish
b. 1.0 mL syringes (with 0.1 mL markings) are useful for transferring each mix
c. Do NOT re-use the same syringe for different mixes
d. For 60mm diameter petri dish ~ 1.4 mL
e. For 150 mm diameter petri dish ~ 8.8 mL
f. ~0.2mL/well for 12-well dishes, ~0.1 mL/well for 24-well dishes
g. Do not take too long to transfer PDMS mixes to wells as the 1:1 mix will begin curing at room temperature. Try to finish transfer PDMS mixes in <30 min.

7) Use syringe to remove any air bubbles that may have formed or debris that may have gotten on to the PDMS mixture
8) Place dishes or well plate on level surface. Let PDMS spread evenly and cover the bottom of the well or dish
9) After PDMS is evenly spread, transfer to oven. Cure at 80 °C for 24 hrs. Make sure surface is level.

F.3 Surface Treatment

1) Turn on air plasma chamber, run a for a few minutes to ensure that chamber is primed
2) Plasma treat well-plates or petri dishes
    a. In our group, we use the Atto (Diener electronic) plasma treatment unit located in 8-206
    b. We have no gas tanks hooked up to the plasma machine, so we are using low-pressure air plasma to treat the surface
    c. Set the power to ~90-91%
    d. Make sure pressure valves (pulling in air) reach 75-80 bars prior to plasma treatment
    e. Use treatment times as follows
        i. ~10 min for well-plates
        ii. ~ 5 min for petri dishes
    f. Treatment time may need to be optimized. Plasma treat for long enough times to render surfaces hydrophilic. Longer times may crack the surface of the 3:2 PDMS mixture.
    g. Plasma treatment is also a means to clean or sterilize the surface
    h. Cover with lid immediately after treatment
3) Immediately add media (in biosafety cabinet) after plasma treatment to retain hydrophilicity
    a. Add minimally sufficient volume of media to cover the bottom of the well or dish
    b. Media should spread quickly and completely over PDMS surface
4) Proceed to cell culture protocol
    a. As an example, preparation of MSCs on PDMS-based well plates for co-culture is detailed in Appendix G

Appendix G

Detailed MSC/HSPC Co-Culture Protocol (Chapter 5)

G.1 Acknowledgements

Co-culture for in vitro assays were designed and conducted in collaboration with Ms. Novalia Pishesha at the Whitehead Institute. Co-culture for in vivo assays were conducted by Dr. Kimbereley Tam and Dr. Zhiyong Poon at SMART BioSyM in Singapore.

G.2 Materials

- Primary Human Cells
    - MSCs – Mesenchymal stromal (stem) cells
    - HSPCs – Hematopoietic stem and progenitor cells (mobilized CD34+ cells)
- Falcon Cell Culture Inserts
    - Transparent inserts, 12 wells
    - 1.0um pores, $1.6x10^6$ pores/um
    - VWR Catalog # 62406-172 (Falcon No. 353103)
- Falcon Companion Plates for Cell Culture Inserts
    - 12-well plate format
    - VWR Catalog #62406-187 (Supplier No. 353503)
- MSC Expansion Media: LG-DMEM, 10% FBS, 1% P/S
- HSPC Source
    - Cord Blood CD34+ Cells (from PZY)
    - Bone marrow CD34+ Cells (from Nova)
- HSPC Expansion Media: StemSpan SFEMII + Cytokines
    - *Use either "set" of cytokines for a ~50mL aliquot of StemSpan*

- TPO-2ul, SCF-2ul, FLT3-1ul (PZY/Singapore)
- FLT3, SCF, IL3, Dexamethasone (Nova/MIT) – concentrations specified in Chapter 6 and published in *ACS Biomat. Sci. & Eng.* Article [90].

G.3 Co-Culture Protocol

Day 0 – PDMS Plate Preparation

- Prepare PDMS in mixtures by mass ratio (A : B)
  - 1:3 (~100 kPa), 1:1 (~10 kPa) and 3:2 (~1 kPa)
  - Only need to prepare ~1mL of each mix for each 12-well plate used (e.g. if you're preparing 4 well-plates, you only need to mix 4mL ~ 4 g total)
- Mix both PDMS mixes vigorously, de-gas to remove air bubbles
- Add ~0.2mL PDMS/well to form ~500um thick gels following the diagram below:

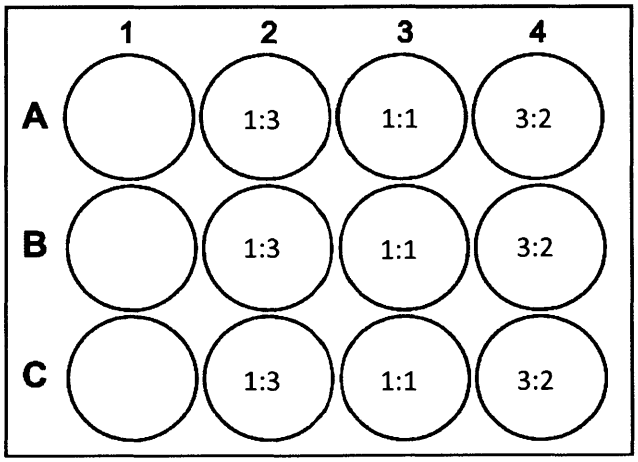

- For co-culture experiment, follow diagram above
- Let PDMS spread to cover entire well bottom
  - Make sure plate is level
  - Put into oven overnight @80°C

Day 1 – MSC Plating

- Plasma treat each plate for ~10min. Use the same equipment and settings as detailed in Appendix F.3.
  - *Plasma treatment timing may need to be optimized for maximum time without surface cracking*
  - 1:3 Mix won't crack, 3:2 mix may crack at the surface
- Immediately add 1mL MSC media/well after plasma treatment

- Thaw RB1, p6 MSCs
    - Spin down @ 300g for 8 min (or 400g for 5min)
    - Re-suspend and count cells (use live cell count)
- Plate MSCs at a density of ~10K cells/cm^2 (suspend at ~80K cells/mL prior to plating)
    - Each well is ~3.8-4.0 cm^2 => **~40K/well**
    - *Cell seeding density may need to be optimized to maximize total time of MSC culture to be 9-11 days*
    - Plate MSCs in ~0.5mL/well => Resulting in total volume of 1.5mL/well
    - Follow well-plate format below:

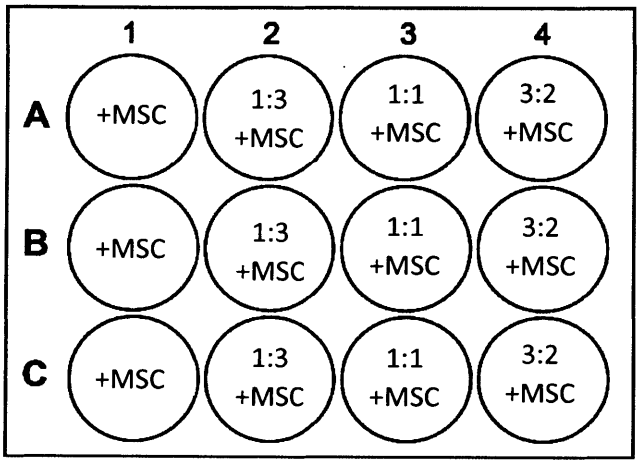

- 15-30 minutes after plating cells, gently swirl well plates (manually shake in circular motion) to assure even distribution of cells around wells

Day 2 – Feeding MSCs

- Make sure not to touch MSC layer at bottom while aspirating wells
- Use micropipette tip at end of Pasteur pipette to ensure "gentle" vacuum suction
- Aspirate off media to remove any dead or unattached cells
- Add ~1.5-2.0mL of MSC media/well

Day 4-5 – HSPC Plating

- Pick when to proceed with this step when MSCs are approximately confluent
- When plated at ~40K/well, MSCs should be confluent after ~3-4 days
- Aspirate off all MSC expansion media
- Add 1.0mL/well HSPC expansion media into ALL wells
- Subsequent steps will all be conducted with HSPC expansion media
- *Gently* place transwell inserts into ALL wells (including wells with no MSCs) making sure the inserts are in the notched positions (skip this step for contact co-culture conditions)

- Thaw HSPCs
    - Follow attached protocol for thawing (Section G.4)
    - After thawing, spin down HSPCs at 500g for 10min
    - Re-suspend HSPCs in expansion media
    - Count HSPCs
- Plate HSPCs at **~5K cells/well** on top of transwell inserts in to ALL wells; as a standard of comparison, grow HSPCs alone in a separate set of wells
- HSPCs can be added to the top of transwell inserts in a total volume of 0.5mL/well
    - Be careful not to puncture membrane
    - Pipette into transwell directly to make sure all HSPCs are in transwell and that they do not contact MSC layer
- This results in a total volume of 1.5mL/well
- After 3-4 days if HSPCs looked crowded, you can add an additional volume of 0.3mL/well of HPSC expansion media

Day 10-12 (6-7 days after HSPC Plating) – Harvesting HSPCs

- Pick endpoint *before* MSCs all come off (6 to 7 days max, but check at day 4 to 5)
    - MSCs may begin to sheet off (peel off as an entire sheet or bundle of cells)
    - MSC morphology will change with time in HSPC expansion media – this is OK
    - MSCs peeling away at the edges of the well is OK as long as MSCs remain intact underneath the transwell inserts
    - This timing may take some optimizing
- Harvest HSPCs
    - Gently use micropipette to transfer all HSPCs from each transwell insert to a conical tube => transfer 1 well to 1 tube
    - Avoid touching transwell membrane with pipette tip as membranes may get punctured
    - Wash the top of each transwell insert with 1.0mL PBS/insert, transfer PBS wash containing residual HSPC to corresponding conical tube
    - Repeat PBS wash step (2 PBS washes total + initial HSPC transfer in media)
    - Spin down HSPCs in conical tubes @ 500g for 10min
    - Discard underlying plates with MSCs
        - You can save the MSCs for further analysis
        - For example, you could lyse the MSCs directly in the well-plate for mRNA extraction & subsequent qPCR
- Re-suspend HSPCs
    - Count samples from each well
    - Stain for Flow cytometry analysis (described in Chapter 5)

G.4 HSPC Thawing Protocol (Courtesy of Novalia Pishesha)

1. Thaw cells at 37°C in water bath
2. Move cells into 50mL conical tube; add 1mL 1% FBS/PBS at room temperature
3. Slowly mix by pipetting up and down gently and let sit for 3min
4. Add 2mL 1% FBS/PBS at room temperature
5. Slowly mix and let sit for 3min
6. Add 4mL 1% FBS/PBS at room temperature
7. Slowly mix and let sit for 3min
8. Add 8mL 1% FBS/PBS at room temperature
9. Slowly mix and let sit for 3min
10. Add 16mL 1% FBS/PBS at room temperature
11. Slowly mix and let sit for 3min
12. Spin down 500g, 10min, RT
13. Get rid of supernatant and add desired volume of expansion media

Appendix H

Detailed MSC Spiral Microfluidic Sorting Protocol

H.1 Acknowledgements

Protocol adapted and inherited from Dr. Zhiyong Poon that was published previously in Stem Cells Transl. Med.[202].

H.2 Materials

- Aluminum master mold (pictured on the right, located on shelf in Chem Bay in 8-214)
- 100% Isopropyl alcohol (IPA)
- Medical grade PDMS
    - Silastic MDX4-4210 (Dow Corning)
    - 2 Components
        - Medical Grade elastomer base
        - Curing agent
- Razor blade (for cutting and trimming)
- 1.5mm biopsy punch
- Thick glass slides (2"x3")
- Scotch tape
- Capillary tubing
- Blunt end ½" 22 or 23-gauge needle
- Syringe pump
- 10 ml Syringe
- 15 mL conical tubes
- 70% Ethanol
- 1x PBS
- 150mm Petri dishes (for storage)
- Paper towels (for storage)

H.3 Device Fabrication

Cleaning Aluminum Mold

1) Clean aluminum mold by rinsing with (IPA). Use pressurized air or nitrogen (in fume hood) to blow off IPA.
2) Let residual IPA evaporate in oven at 80°C overnight
    a. Use 150 mm petri dish to hold aluminum mold while in oven and for long-term storage
    b. Fold paper towel and insert between aluminum mold and petri dish. This ensures that if the aluminum overheats, it will not melt the polystyrene dish
    c. If short on time, IPA evaporation can be minimized to 2 hours

Day 1 – Casting Spiral Microfluidic Devices

1) Prepare PDMS mixture in plastic cup
    a. ~10mL PDMS / device → ~ 40 mL for entire mold
    b. Prepare PDMS in a 10:1 ratio by mass of elastomer base to curing agent
    c. For example: weigh ~36 g elastomer base with ~3.6 g of curing agent
2) Mix PDMS vigorously for ~2-3 min
    a. Use disposable serological pipette or popsicle stick
    b. Mixture is very viscous – do not use handheld mixer
3) Degas to remove air bubbles
    a. Because of how viscous it is, the hood vacuum is not strong enough
    b. Use vacuum oven (MTI vacuum oven, 8-212, mechanical bay) at room temperature OR
    c. Use plasma chamber pump but must be SUPER careful
        i. Be VERY careful not to let PDMS overflow into plasma chamber
        ii. Watch while degassing and pulling vacuum
        iii. Switch pump off and ventilation on to "pop" air bubbles. Turn pump on and repeat this on/off process.
        iv. Do NOT turn on plasma treatment
4) Pour onto aluminum mold at room temperature (on paper towel, in petri dish)
    a. Pour from center, let spread to all four quadrants of mold
    b. Make sure the aluminum mold is level so PDMS spreads evenly and does not spill over the edge of the device
    c. Minimize introduction of air bubbles
5) Degas PDMS in aluminum mold to remove air bubbles
6) Cure in oven at 80 °C for ~1-2 hours. Fully cured PDMS not sticky to touch. Can cure overnight. Make sure aluminum mold is not in direct contact with polystyrene dish (should have folded paper towel underneath).
7) Peel PDMS devices from aluminum mold when the mold is still warm
    a. Easier to peel when warm

b. Once aluminum mold is cooled to room temp steps 4-6 can be repeated if extra PDMS mixture was prepared

8) Cut PDMS devices apart using razor blade. Only trim excess PDMS if it may interfere with bonding.
9) Use biopsy bunch to punch holes at inlet and two outlets. Make sure punched holes span across the entire inlet/outlet channel
    a. Make sure to punch on plastic (polystyrene or acrylic) surfaces to avoid dulling the biopsy punch
    b. Do NOT punch directly on bench top or steel table
    c. Make sure punched PDMS is removed – i.e. make sure there is a hole
10) Use IPA to rinse PDMS devices
    a. In particular, make sure that the bonding surface (device face where the channels are) is clean
    b. Squirt IPA through inlets/outlets to ensure cleanly punched holes
    c. Use pressurized air or nitrogen (in fume hood) to blow off excess IPA.
11) Let residual IPA evaporate in oven at 80°C overnight

Day 2 – Bonding Devices

1) Remove PDMS devices from 80°C oven
2) Clean glass slides and PDMS devices with scotch tape
    a. Use scotch tape to remove any dust or debris
    b. Make sure to thoroughly clean the bonding surfaces
3) Place cleaned glass and PDMS with bonding surfaces face-up in plasma chamber
    a. Pick one side of the glass to clean and bond
    b. Bonding surface of PDMS device is the face/surface with channels
4) Plasma treat for ~2 min
5) Immediately press the bonding surfaces of the PDMS device and glass slide together
    a. Leave glass on flat surface, flip PDMS on to it
    b. Ensure no dust gets in between the PDMS device and glass
    c. Press down firmly and evenly over PDMS device (use a large flat object)
    d. Visually inspect for good bonding
        i. No bubbles between glass/device
        ii. Make sure you do not press too hard and collapse the channels
6) Wrap bonded device in paper towel, store in 150 mm petri dish
7) Place in oven at 80°C overnight to ensure full bonding. Weigh down petri dish lid to help compress device. Paper towel helps to protect and compress the device.
8) Remove device from oven the next day. Devices can be kept wrapped in paper towel in petri dish for long-term storage at room temperature

H.4. Sorting Cells

Device set-up

1) Cut capillary tubing into 3 segments
    a. 1 segment that is ~5-6 inches
    b. 2 equally segments that are ~4 inches each
2) Perform all following steps in biosafety cabinet to ensure stirility
3) Insert longer capillary tubing into inlet. Capillary tubing can be more easily manipulated/maneuvered with tweezers
4) Insert remaining two capillary tube segments into outlets
    a. Larger diameter cells come from "inner" outlet. This outlet is on the bottom (closer to you) if inlet → outlet is arranged from left → right
    b. Smaller diameter cells come from "outer" outlet. This outlet is on the top (further from you) if inlet → outlet is arranged from left → right
    c. Set up conical tubes to collect liquid from outlets
5) Insert blunt ended needle into the input tubing
6) Fill syringe with ~10mL of 70% ethanol and connect to needle.
7) Invert syringe vertically and tap to collate air bubbles. Push air bubbles out of syringe.
8) Set up syringe pump with a flow rate of 3.5 ml/min (make sure syringe size/settings are set correctly)
9) Push all liquid through device for ~2-3 min without introducing air bubbles
10) Set up syringe/device again with 1xPBS instead. Repeat Steps 7-9 twice to ensure all ethanol is flushed from device. Push ~20mL PBS through spiral device. Tap on device gently to dislodge any air bubbles that may be introduced from re-filling or switching the syringe.
11) With syringe (containing PBS) still attached to PDMS device, let sit under UV light for ~30 min – 1 hr to sterilize setup

Cell Preparation

1) While device setup is being sterilized prepare cells
2) Re-suspend cell pellet (from passaging) at a concentration of 500K cells/mL up to a maximum concentration of 1M cells/mL
    a. Ensure that cells are fully separated and dispersed when re-suspending
    b. Lower concentrations ensure fewer cell clumps that may clog the device
    c. Higher concentrations may be used for higher throughput
3) Transfer cells to a new 10mL syringe
    a. May choose to use a 5 mL syringe if dealing with very few cells – just ensure you have input the right settings on the syringe pump when sorting
    b. Use micropipette to transfer remaining amount of cells to syringe
    c. Vertically invert syringe and tap to collate and remove air bubbles
4) Turn off UV light
5) Connect syringe with cells to device.

6) Transfer outlet tubing to new, clean, conical tubes. Label collection tubes.
7) Sort cells with a flow rate of 3.5 mL/min until all cells have been sorted
    a. Note this is a higher flow rate than previously published
    b. Increasing the flow rate biases flow towards the "outer" outlet thereby giving a more "pure" or enriched population of D^{hi} cells, but smaller in number. Using this flow rate, I typically get ~15-25% of the total population as D^{hi} cells.
    c. On the other hand, reducing the flow rate biases the flow towards the "inner" outlet thereby giving a more "pure" or enriched population of D^{lo} cells
8) Optional: Re-fill syringe with media and sort to ensure all cells have been pushed through device
9) Cover collection tubes and spin down.
    a. Count cells
    b. Image/analyze cells to ensure differences in cell size across the two outlets
        i. Manually
            1. Add 10ul suspended cells to each chamber of disposable hemacytometer slide (INCYTO C-Chip, Neubauer improved)
            2. Take multiple images at 10x (at least 5 per chamber)
            3. Export images and use MATLAB code (Appendix I.1) to determine suspended cell diameters
        ii. Automatically
            1. Add 20ul suspended cells to automatic counter slides (Nexcelom, SD100 slides)
            2. Count cells on Cellometer Auto T4 (Nexcelom) – use "Large Cells" setting for MSCs
            3. Export data as excel spreadsheet – includes all diameter measurements and corresponding histogram

Appendix I

MATLAB Codes

I.1 MATLAB Code for Determining Suspended Cell Diameters

Finding circles using Hough transform

```
close all
clear all
clc

tic

myFolder = '\Users\franc\OneDrive\Documents\MATLAB\Manual Counting';
filePattern = fullfile(myFolder, '*.jpg');
jpgFiles = dir(filePattern);

AllRadii = [];

for i=1:length(jpgFiles)

im = imread(jpgFiles(i).name);
imgray = rgb2gray(im);

figure(i)

subplot(1,2,1)
imshow(imgray)

%[centers1, radii1, metric1] = imfindcircles(imgray,[6 16]);
%[centers2, radii2, metric2] = imfindcircles(imgray,[15 40]);

%centers = [centers1;centers2];
%radii = [radii1;radii2];

[centers, radii, metric] = imfindcircles(imgray,[8 32]);

subplot(1,2,2)
imshow(imgray)
viscircles(centers, radii,'EdgeColor','b');
```

```
AllRadii = [AllRadii;radii];

end

AllRadii_mic = AllRadii*0.68775791;

figure
hist(AllRadii_mic,sqrt(length(AllRadii)))

toc
```

```
Warning: You just called IMFINDCIRCLES with a large radius range. Large
radius ranges reduce algorithm accuracy and increase computational time.
For high accuracy, relatively small radius range should be used. A good
rule of thumb is to choose the radius range such that Rmax < 3*Rmin and
(Rmax - Rmin) < 100. If you have a large radius range, say [20 100],
consider breaking it up into multiple sets and call IMFINDCIRCLES for each
set separately, like this:

       [CENTERS1, RADII1, METRIC1] = IMFINDCIRCLES(A, [20 60]);
       [CENTERS2, RADII2, METRIC2] = IMFINDCIRCLES(A, [61 100]);

Elapsed time is 38.733976 seconds.
```

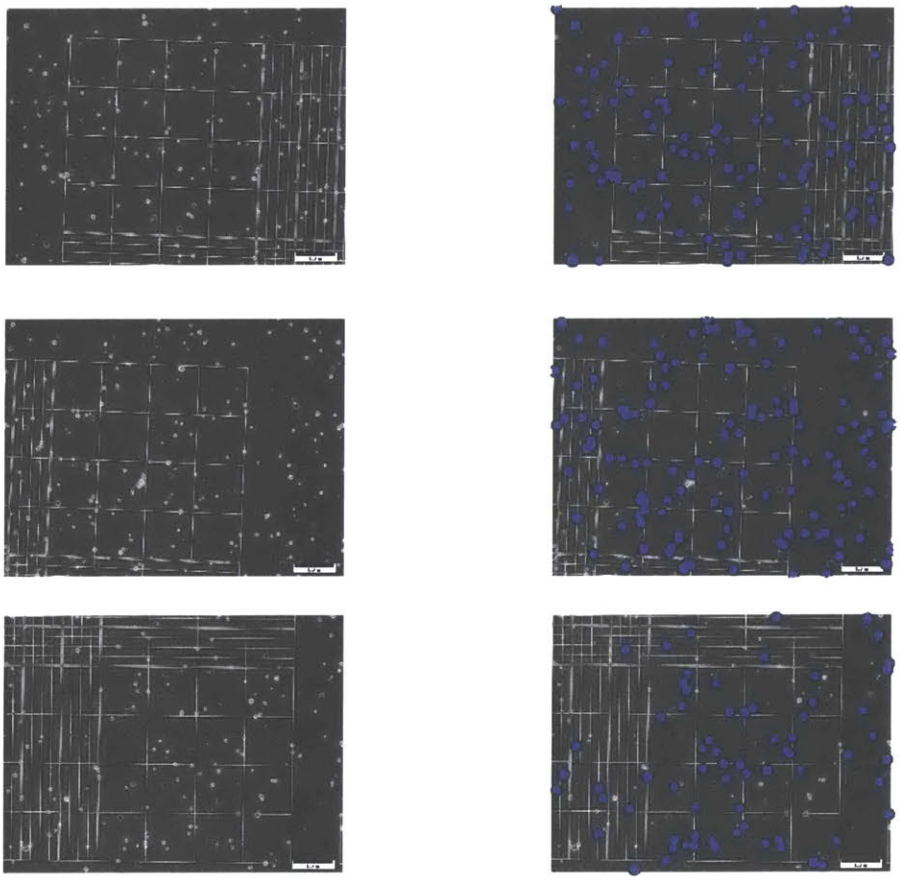

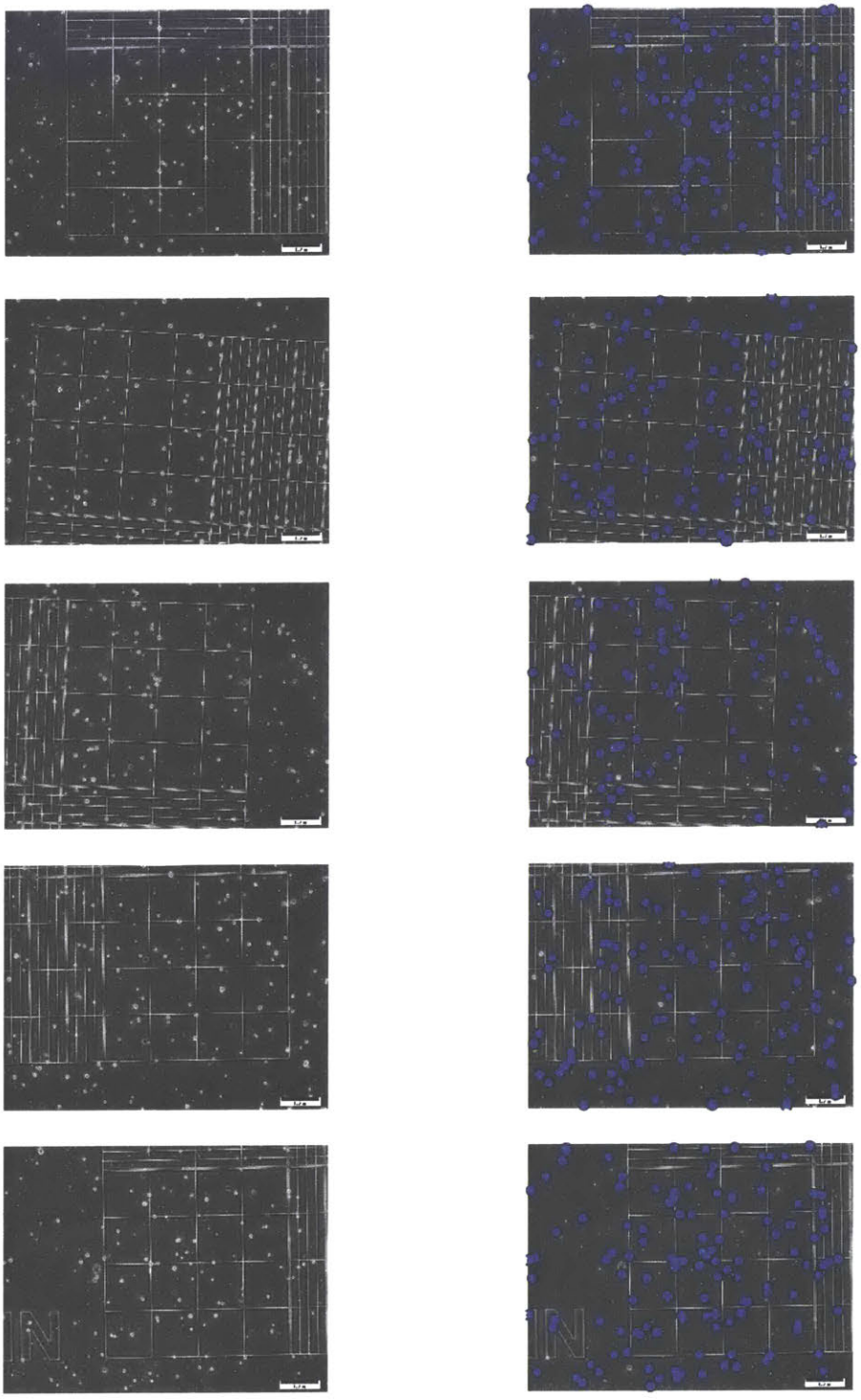

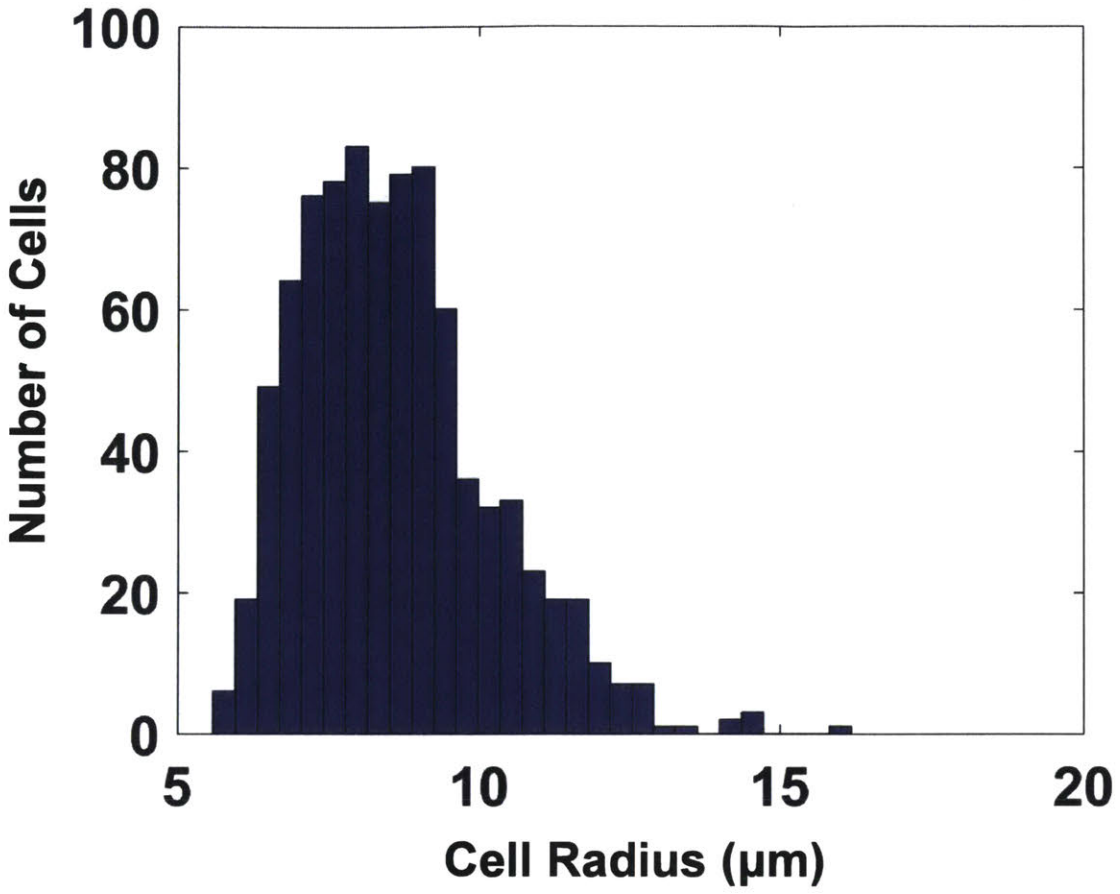

Published with MATLAB® R2015b

I.2 MATLAB Code for Analyzing Suspended Cell Diameter Distributions

Loading Data

```
close all
clear all
clc

A = xlsread('1.19.17 - hMSC PL17 Sorting.xlsx');

AllRadiipix = A(:,1);
AllRadiipix = 2*AllRadiipix(isfinite(AllRadiipix));
cells1 = length(AllRadiipix);

AllRadii2pix = A(:,2);
AllRadii2pix = 2*AllRadii2pix(isfinite(AllRadii2pix));
```

```
cells2 = length(AllRadii2pix);

AllRadii3pix = A(:,3);
AllRadii3pix = 2*AllRadii3pix(isfinite(AllRadii3pix));
cells3 = length(AllRadii3pix);
```

```
figure
set(0,'DefaultAxesFontSize',14,'DefaultAxesFontWeight','bold')
hold on
[nelements,center]=hist(AllRadiipix,sqrt(cells1));
plot(center,100*nelements./cells1,'b','LineWidth',2)
[nelements2,center2]=hist(AllRadii2pix,sqrt(cells2));
plot(center2,100*nelements2./cells2,'r','LineWidth',2)
[nelements3,center3]=hist(AllRadii3pix,sqrt(cells3));
plot(center3,100*nelements3./cells3,'g','LineWidth',2)
legend('CTRL','LCF','SCF') % LCF = Dhi cells, SCF = Dlo cells
%axis ([10 50 -In 15])
ylabel('% of Total Cells Counted')
xlabel('Suspended Cell Diameter Bins (\mum)')
```

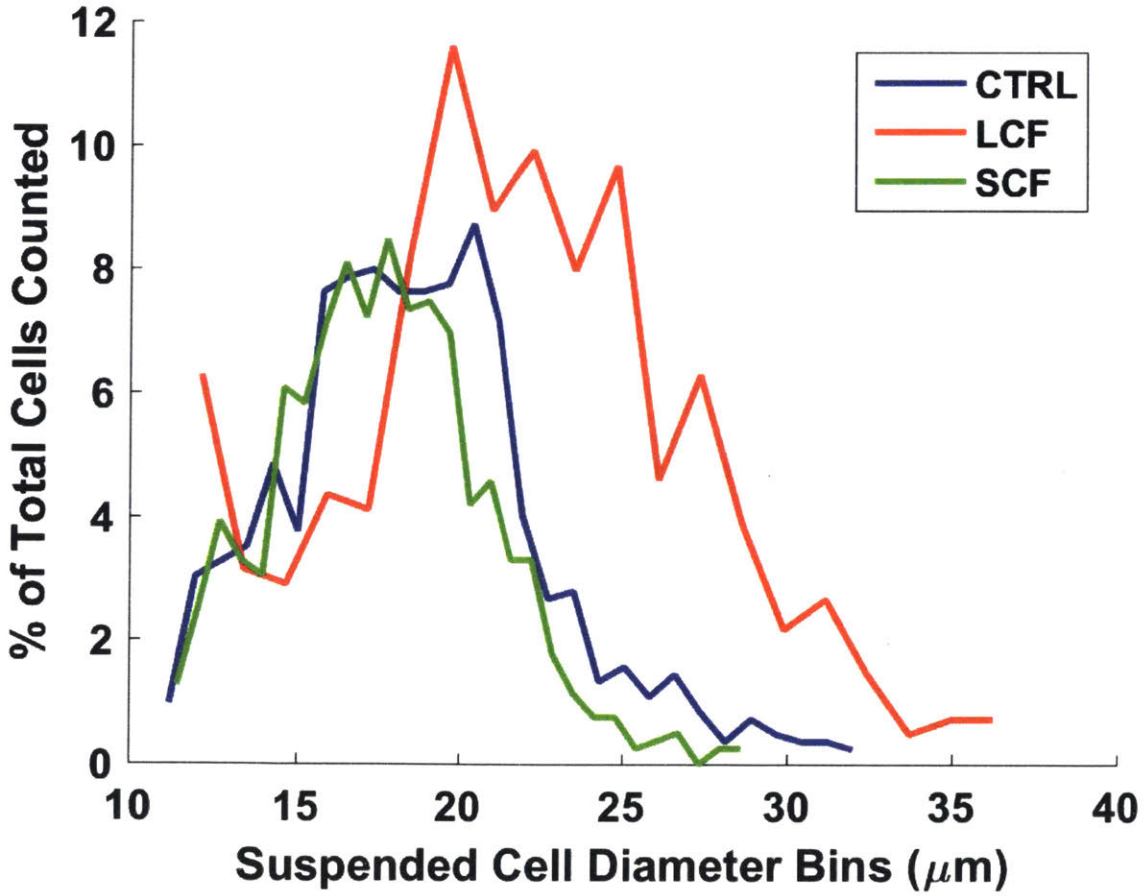

Calculating Arithmetic /SEM

```
arithmetic1 = mean(AllRadiipix);

arithmetic2 = mean(AllRadii2pix);

arithmetic3 = mean(AllRadii3pix);

sem1 = std(AllRadiipix)/sqrt(length(AllRadiipix));
sem2 = std(AllRadii2pix)/sqrt(length(AllRadii2pix));
sem3 = std(AllRadii3pix)/sqrt(length(AllRadii3pix));

means = [arithmetic1,arithmetic2, arithmetic3];
sems = [sem1,sem2,sem3];
```

Calculating Geometric Means/GeoSEM

```
geometric1 = geomean(AllRadiipix);
geometric2 = geomean(AllRadii2pix);
geometric3 = geomean(AllRadii3pix);

%Calculating positive geometric SEM

geoSEMPOS1 = geometric1*(exp(std(log(AllRadiipix))/sqrt(length(AllRadiipix)))-1);
geoSEMPOS2 = geometric2*(exp(std(log(AllRadii2pix))/sqrt(length(AllRadii2pix)))-1);
geoSEMPOS3 = geometric3*(exp(std(log(AllRadii3pix))/sqrt(length(AllRadii3pix)))-1);

%Calculating negative geometric SEM

geoSEMNEG1 = geometric1*(1-1/exp(std(log(AllRadiipix))/sqrt(length(AllRadiipix))));
geoSEMNEG2 = geometric2*(1-1/exp(std(log(AllRadii2pix))/sqrt(length(AllRadii2pix))));
geoSEMNEG3 = geometric3*(1-1/exp(std(log(AllRadii3pix))/sqrt(length(AllRadii3pix))));

geomeans = [geometric1,geometric2,geometric3];
geoSEM_Positive = [geoSEMPOS1,geoSEMPOS2,geoSEMPOS3];
geoSEM_Negative = [geoSEMNEG1,geoSEMNEG2,geoSEMNEG3];
```

TTESTs

```
[h_arith,p_arith] = ttest2(AllRadii3pix,AllRadii2pix,'Vartype','unequal','Tail','left')
[h_geo1,p_geo1] = ttest2(log(AllRadiipix),log(AllRadii2pix),'Vartype','unequal','Tail','both')
[h_geo2,p_geo2] = ttest2(log(AllRadiipix),log(AllRadii3pix),'Vartype','unequal','Tail','both')
[h_geo3,p_geo3] = ttest2(log(AllRadii2pix),log(AllRadii3pix),'Vartype','unequal','Tail','both')
```

```
h_arith =

     1


p_arith =
```

```
   1.3190e-41

h_geo1 =

     1

p_geo1 =

   1.5231e-22

h_geo2 =

     1

p_geo2 =

   4.5178e-07

h_geo3 =

     1

p_geo3 =

   1.7541e-38
```

Bootstrapping

```
n=1000;

[nelements,center] = hist(AllRadiipix, sqrt(cells1));

%[bootstat,bootsam] = bootstrp(n,@(AllRadiipix) [hist(AllRadiipix,binsize)],AllRadiipix);
ci = bootci(n,@(AllRadiipix) [hist(AllRadiipix,sqrt(cells1))],AllRadiipix);
ci_norm = 100*ci/cells1;


plot(center,ci_norm,'b--')

[nelements2,center2] = hist(AllRadii2pix, sqrt(cells2));

ci2 = bootci(n,@(AllRadii2pix) [hist(AllRadii2pix, sqrt(cells2))],AllRadii2pix);
ci_norm2 = 100*ci2/cells2;

plot(center2,ci_norm2,'r--')
```

```
[nelements3,center3] = hist(AllRadii3pix, sqrt(cells3));

ci3 = bootci(n,@(AllRadii3pix) [hist(AllRadii3pix, sqrt(cells3))],AllRadii3pix);
ci_norm3 = 100*ci3/cells3;

plot(center3,ci_norm3,'g--')


hold off
```

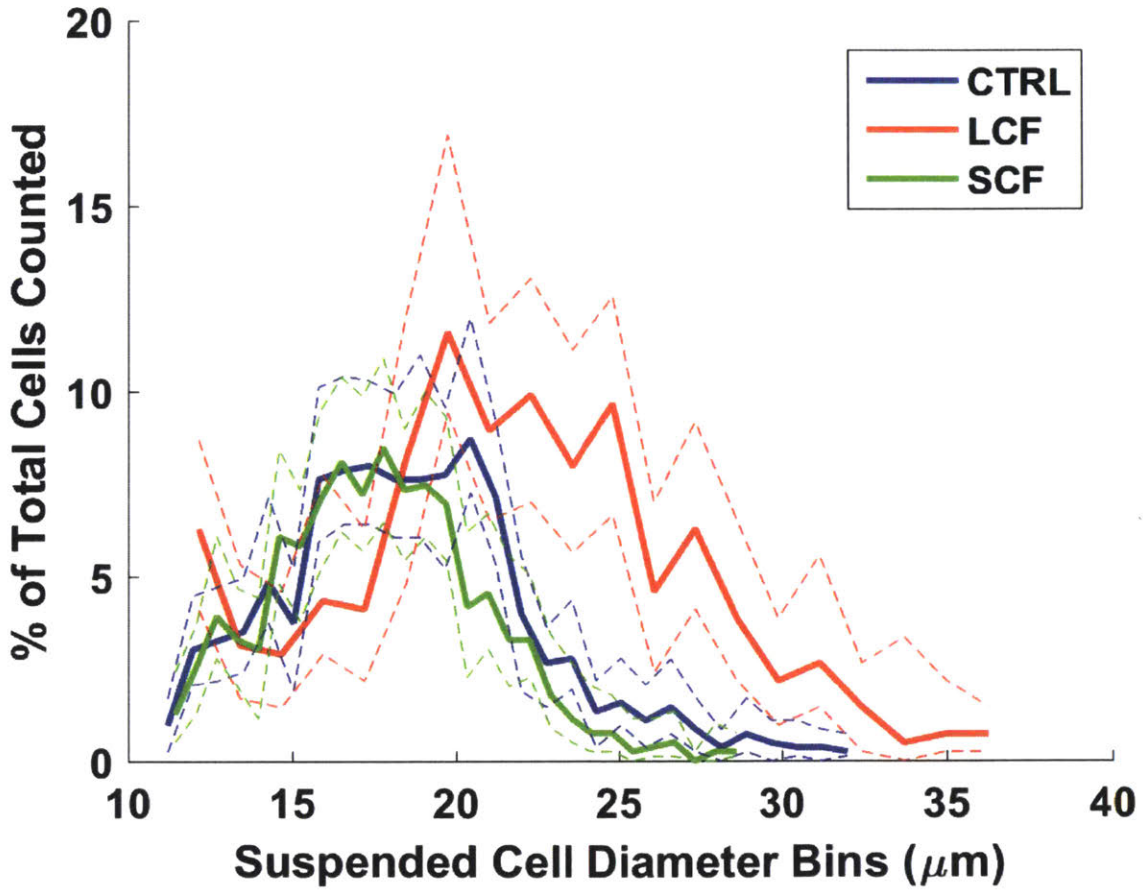

Log Transforming data and plotting

```
logbins = 100;

for i = 1:logbins

    logbinsize(i) = 10^(2*i/logbins);
end

% figure
% semilogx(center,100*nelements./cells1,center2,100*nelements2./cells2)
```

```
set(0,'DefaultAxesFontSize',20,'DefaultAxesFontWeight','bold')

[nelementslog,centerlog]=hist(AllRadiipix,logbinsize);
[nelements2log,center2log]=hist(AllRadii2pix,logbinsize);
[nelements3log,center3log]=hist(AllRadii3pix,logbinsize);
```

Bootstrapping Log Transformed data

```
figure
n=1000;
%[bootstat,bootsam] = bootstrp(n,@(AllRadiipix) [hist(AllRadiipix,binsize)],AllRadiipix);
ci = bootci(n,@(AllRadiipix) [hist(AllRadiipix,logbinsize)],AllRadiipix);
ci_norm = 100*ci/cells1;

%semilogx(centerlog,ci_norm,'b--')

ci2 = bootci(n,@(AllRadii2pix) [hist(AllRadii2pix,logbinsize)],AllRadii2pix);
ci_norm2 = 100*ci2/cells2;

%semilogx(center2log,ci_norm2,'r--')

ci3 = bootci(n,@(AllRadii3pix) [hist(AllRadii3pix,logbinsize)],AllRadii3pix);
ci_norm3 = 100*ci3/cells3;

loghandle = semilogx(centerlog,100*nelementslog./cells1,...
    center2log,100*nelements2log./cells2,...
    center3log,100*nelements3log./cells3,...
    centerlog,ci_norm,'--',...
    center2log,ci_norm2,'--',...
    center3log,ci_norm3,'--');

set(loghandle(1:3),'LineWidth',2);
set(loghandle(4:9),'LineWidth',1);

set(loghandle(1),'Color',[0.5 0 0.5])
set(loghandle(2),'Color',[0 0 1])
set(loghandle(3),'Color',[1 0 0])
set(loghandle(4:5),'Color',[0.5 0 0.5])
set(loghandle(6:7),'Color',[0 0 1])
set(loghandle(8:9),'Color',[1 0 0])

legend('CTRL','LCF','SCF')

axis ([10 50 -Inf Inf])
ylabel('% of Total Cells Counted')
xlabel('Suspended Cell Diameter Bins (\mum)')
set(gca,'XTick',[10 20 30 40 50])
set(gca,'XTickLabel',{'10','20','30','40','50'})

figure
loghandle = semilogx(center2log,100*nelements2log./cells2,'b',
center3log,100*nelements3log./cells3,'r',center2log,ci_norm2,'b--',center3log,ci_norm3,'r--');
```

```
set(loghandle(1:3),'LineWidth',2);
set(loghandle(3:6),'LineWidth',1);

legend('LCF','SCF')

axis ([10 50 -Inf Inf])
ylabel('% of Total Cells Counted')
xlabel('Suspended Cell Diameter Bins (\mum)')
set(gca,'XTick',[10 20 30 40 50])
```

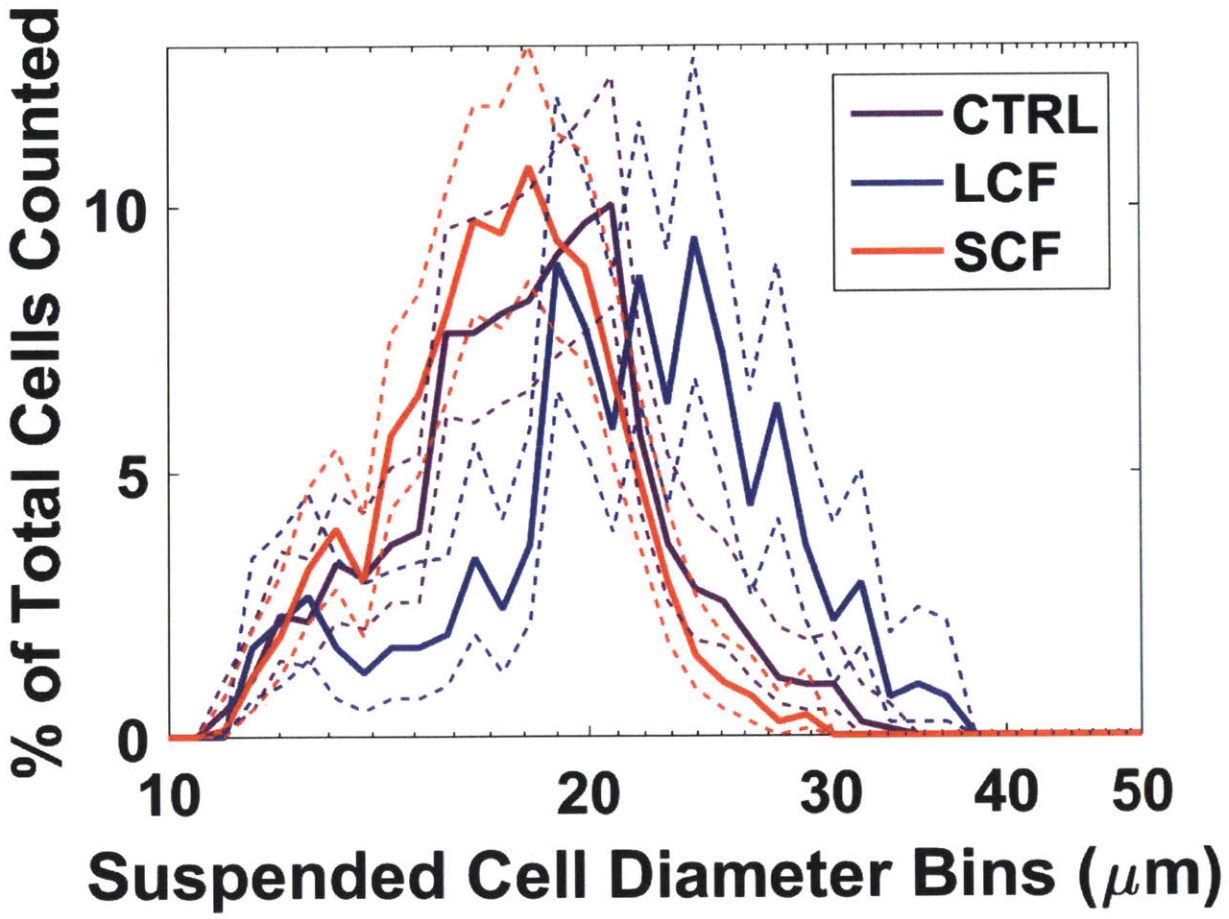

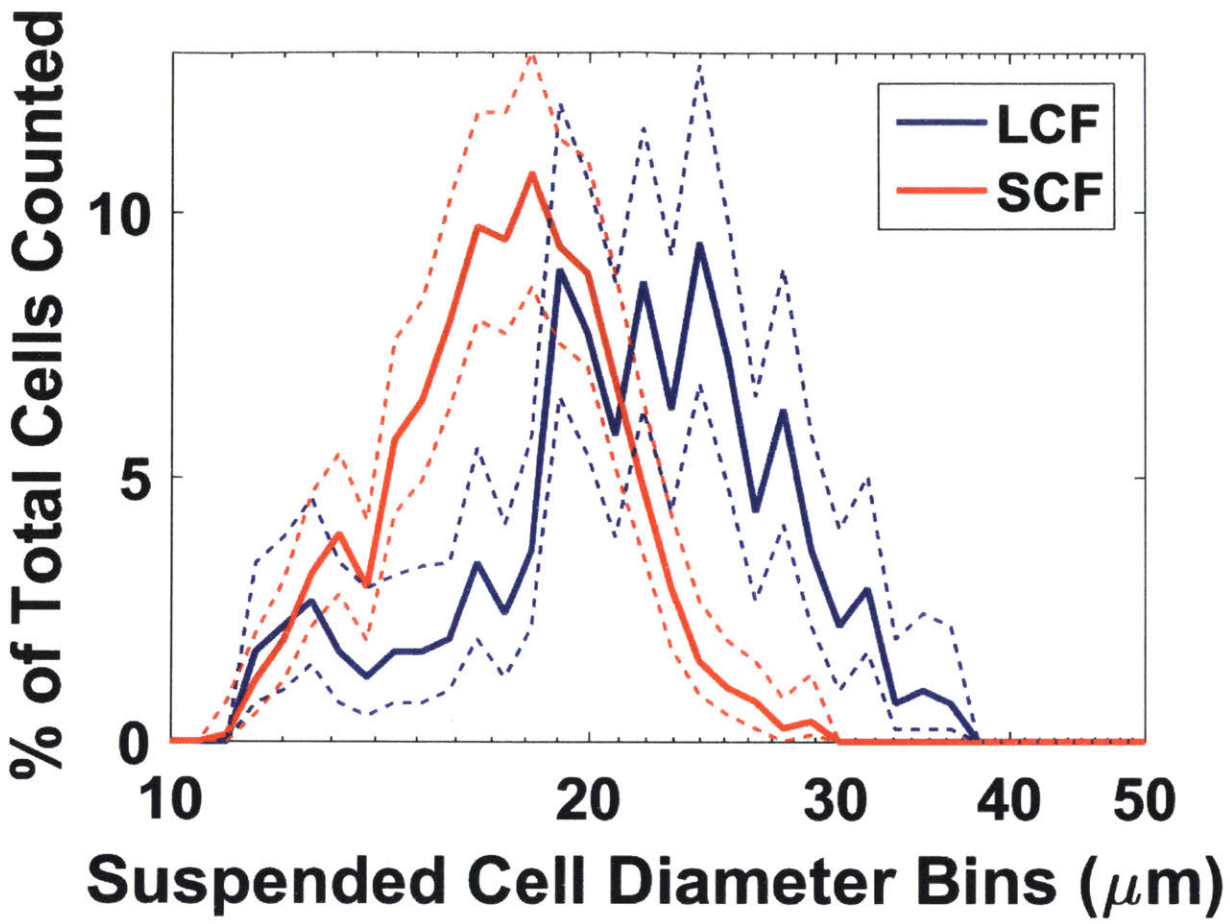

Determining Size Groupings

```
% For Four Groups

FourGroups = [];
FourGroups(1,1) = sum(AllRadiipix<16);
FourGroups(2,1) = sum(AllRadiipix>=16 & AllRadiipix<20);
FourGroups(3,1) = sum(AllRadiipix>=20 & AllRadiipix<24);
FourGroups(4,1) = sum(AllRadiipix>=24);

FourGroups(1,2) = sum(AllRadii2pix<16);
FourGroups(2,2) = sum(AllRadii2pix>=16 & AllRadii2pix<20);
FourGroups(3,2) = sum(AllRadii2pix>=20 & AllRadii2pix<24);
FourGroups(4,2) = sum(AllRadii2pix>=24);

FourGroups(1,3) = sum(AllRadii3pix<16);
FourGroups(2,3) = sum(AllRadii3pix>=16 & AllRadii3pix<20);
FourGroups(3,3) = sum(AllRadii3pix>=20 & AllRadii3pix<24);
FourGroups(4,3) = sum(AllRadii3pix>=24);

% For Two Groups with 18um Cutoff
TwoGroups18 = [];
TwoGroups18(1,1) = sum(AllRadiipix<18);
```

```
TwoGroups18(2,1) = sum(AllRadiipix>=18);
TwoGroups18(1,2) = sum(AllRadii2pix<18);
TwoGroups18(2,2) = sum(AllRadii2pix>=18);
TwoGroups18(1,3) = sum(AllRadii3pix<18);
TwoGroups18(2,3) = sum(AllRadii3pix>=18);

% For Two Groups with 19 um Cutoff
TwoGroups19 = [];
TwoGroups19(1,1) = sum(AllRadiipix<19);
TwoGroups19(2,1) = sum(AllRadiipix>=19);
TwoGroups19(1,2) = sum(AllRadii2pix<19);
TwoGroups19(2,2) = sum(AllRadii2pix>=19);
TwoGroups19(1,3) = sum(AllRadii3pix<19);
TwoGroups19(2,3) = sum(AllRadii3pix>=19);
```

Published with MATLAB® R2015b

I.3 MATLAB Code for Analyzing ELISA Data

```
clear all;
close all;
clc;
```

Loading Data

```
[A] = xlsread('10.19.17 - ANG1 ELISA Results.xlsx', 'Sheet1');

x = []; % Std Concentration vector
y = []; % Std Fluorescence matrix


for i = 1:8
    x(i,1) = A(11+i,1);

    y(i,1) = A(i+1,1);
    y(i,2) = A(i+1,2);
end

[cf, G] = L5P(x,y);
```

Determining Fit for Standard Curve

Evaluating fitted curve

```
xf = [0:x(1)];
yf = feval(cf,xf);
```

```
figure
semilogx(x,y(:,1),'bo',x,y(:,2),'bo',xf,yf,'r')

fluor = [];
for i = 1:10
fluor(:,i) = A(:,i+2);
end
```

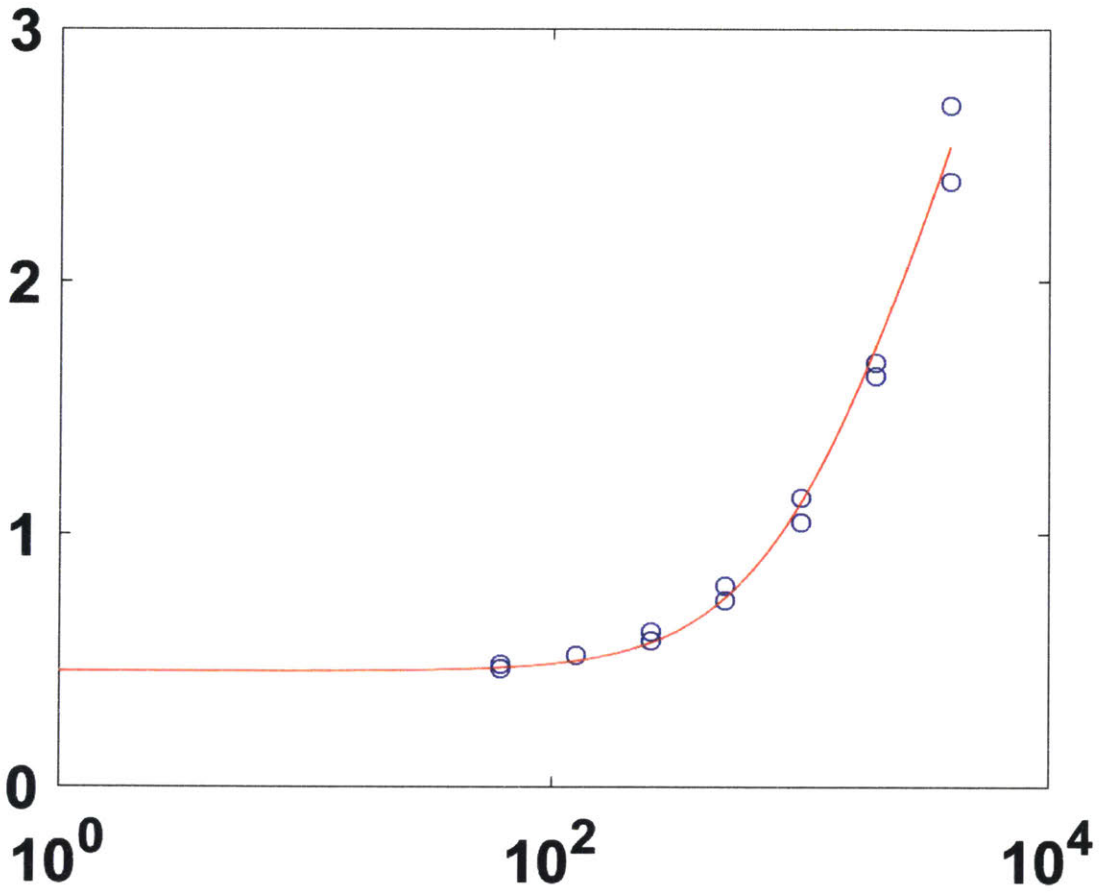

Calculating Concentration Values

```
fluor(1,:) = [];
fluor(9:18,:) = [];

conc = [];
for i = 1:10
conc(:,i) = L5Pinv(cf,fluor(:,i));
end
```

Normalizing to Cell Count

```
[B] = xlsread('10.19.17 - FGF1 ELISA Results.xlsx', 'CellNorm');
```

```
C=min(min(B));

conc_norm=C*conc./B;

% Grouping Replicates

RB1_Group23 = [];
RB1_GroupBC = [];
PL18_Group23 = [];
PL18_GroupBC = [];

for i = 1:5
    RB1_Group23(1,i) = conc_norm(1,2*i-1);
    RB1_Group23(2,i) = conc_norm(2,2*i-1);
    RB1_Group23(3,i) = conc_norm(1,2*i);
    RB1_Group23(4,i) = conc_norm(2,2*i);

    RB1_GroupBC(1,i) = conc_norm(3,2*i-1);
    RB1_GroupBC(2,i) = conc_norm(4,2*i-1);
    RB1_GroupBC(3,i) = conc_norm(3,2*i);
    RB1_GroupBC(4,i) = conc_norm(4,2*i);

    PL18_Group23(1,i) = conc_norm(5,2*i-1);
    PL18_Group23(2,i) = conc_norm(6,2*i-1);
    PL18_Group23(3,i) = conc_norm(5,2*i);
    PL18_Group23(4,i) = conc_norm(6,2*i);

    PL18_GroupBC(1,i) = conc_norm(7,2*i-1);
    PL18_GroupBC(2,i) = conc_norm(8,2*i-1);
    PL18_GroupBC(3,i) = conc_norm(7,2*i);
    PL18_GroupBC(4,i) = conc_norm(8,2*i);
end

Averages = [mean(RB1_Group23);mean(RB1_GroupBC);mean(PL18_Group23);mean(PL18_GroupBC)];
StDevs = [std(RB1_Group23);std(RB1_GroupBC);std(PL18_Group23);std(PL18_GroupBC)];
```

Determining Spearman Correlation Between PDMS Stiffness and Expression

```
% Removing LCF Data Point
RB1_Group23_NoLCF = reshape([RB1_Group23(:,1),RB1_Group23(:,3:5)],[],1);
RB1_GroupBC_NoLCF = reshape([RB1_GroupBC(:,1),RB1_GroupBC(:,3:5)],[],1);
PL18_Group23_NoLCF = reshape([PL18_Group23(:,1),PL18_Group23(:,3:5)],[],1);
PL18_GroupBC_NoLCF = reshape([PL18_GroupBC(:,1),PL18_GroupBC(:,3:5)],[],1);

AllGroups_NoLCF = [RB1_Group23_NoLCF,RB1_GroupBC_NoLCF,PL18_Group23_NoLCF,PL18_GroupBC_NoLCF];

% Removing PS Data Point
RB1_Group23_NoPS = reshape(RB1_Group23(:,3:5),[],1);
RB1_GroupBC_NoPS = reshape(RB1_GroupBC(:,3:5),[],1);
PL18_Group23_NoPS = reshape(PL18_Group23(:,3:5),[],1);
PL18_GroupBC_NoPS = reshape(PL18_GroupBC(:,3:5),[],1);

AllGroups_NoPS = [RB1_Group23_NoPS,RB1_GroupBC_NoPS,PL18_Group23_NoPS,PL18_GroupBC_NoPS];
```

```
% Defining independent variable, substratum stiffness
X_Stiff = [1000000 1000000 1000000 1000000 ...
    95.03333 95.03333 95.03333 95.03333 ...
    2.086666 2.086666 2.086666 2.086666 ...
    0.2436667 0.2436667 0.2436667 0.2436667]';

[rho_NoLCF,pval_NoLCF]=corr(X_Stiff,AllGroups_NoLCF,'type','Spearman');

% Defining independent variable, substratum stiffness
X_Stiff_NoPS = [95.03333 95.03333 95.03333 95.03333 ...
    2.086666 2.086666 2.086666 2.086666 ...
    0.2436667 0.2436667 0.2436667 0.2436667]';

[rho_NoPS,pval_NoPS]=corr(X_Stiff_NoPS,AllGroups_NoPS,'type','Spearman');

Stats4xls = [rho_NoLCF;pval_NoLCF;rho_NoPS;pval_NoPS]';
```

Published with MATLAB® R2015b

I.4 MATLAB Code for Analyzing Luminex-Based Data

Luminex-based assays were used to determine concentrations of MSC-derived secretome components (Chapters 4 and 5). Depending upon the vendor from which these Luminex-based assays were purchased, the kits had different names (BioPlex or Procartaplex). Thus, the names BioPlex, Procartaplex, and Luminex were used interchangeably. Because of different kits, equipment, and analysis programs that were used across our different labs (at MIT and in Singapore), we developed our own code to determine concentrations from the raw fluorescence values.

```
%Procartaplex 45-plex Data
clear all;
close all;
clc;
```

Reading raw data

```
[A,text] = xlsread('4.26.17 - BioPlex Results.xlsx', 'MFI');

for i = 1:136
    MFI(i,:) = A(i,:);
end
```

Generating MFI matrices for Standards

```
% Average across both MFI values for Standards

Std_Ave = [];
for i = 1:8
    Std_Ave(i,:) = (MFI(i,:)+MFI(i+8,:))/2;
end

% Constructing a 3D matrix of MFI values for Standards

Std_MFI_3D = zeros(8,46,2); %46 proteins now because of the addition of OPN

for i = 1:8
    Std_MFI_3D(i,:,1) = MFI(i,:);
    Std_MFI_3D(i,:,2) = MFI(i+8,:);
end
```

Generating MFI matrix for Unknown Samples only (excluding stds)

```
for i = 1:120
    Sample_MFI(i,:) = MFI(i+16,:);
end
```

Generating Matrix of Standard Concentration Values based of CoA

Getting Standard 1 concentrations from excel sheet

```
B = xlsread('4.26.17 - BioPlex Results.xlsx','Std Conc');

Std1_conc = B(:,3)';

Std_Mtrx = zeros(8,46);
for i = 1:7
    Std_Mtrx(i,:) = Std1_conc(1,:)/4^(i-1);
end
```

Fitting based off of both MFIs & StDev

```
Conc = [];

for i = 1:46
    x = Std_Mtrx(:,i); %Concentration values
    y = squeeze(Std_MFI_3D(:,i,:));%Fluorescence Values
    y_Ave = Std_Ave(:,i);

    [cf, G] = L5P(x,y_Ave); % Fit looks better with average MFI
    %[cf, G] = L5P(x,y);

    Conc(:,i) = L5Pinv(cf,Sample_MFI(:,i));
```

```
    % Evaluating fitted curve
    xf = [0:x(1)];
    yf = feval(cf,xf);

    % Following three lines plot the fitted curves for standards using the
    % same analysis conducted for ELISAs
    %figure(i)
    %hold on; plot(x,y,'bo'); plot(cf,'r'); hold off
    %semilogx(x,y(:,1),'bo',x,y(:,2),'bo',xf,yf,'r')

%
end

% Setting all complex numbers to 0
Conc(logical(imag(Conc)))=0;

Conc_Ave = [];
Conc_Std = [];
% Average & Standard Deviation across 4 wells (2 technical replicates, 2
% well replicates)
for i = 1:length(Conc)/4
    Conc_Ave(i,:) = (Conc(4*i-3,:)+Conc(4*i-2,:)+Conc(4*i-1,:)+Conc(4*i,:))/4;
    Conc_Std(i,:) = std([Conc(4*i-3,:);Conc(4*i-2,:);Conc(4*i-1,:);Conc(4*i,:)]);
end


% Fitting with average MFIs gave VERY poor fits
```

Re-Arranging into Experimental Groups (Fit with Discrete MFI)

```
RB1_Grp12 = [];
RB1_Grp12_Std = [];
for i = 1:6
RB1_Grp12(i,:) = Conc_Ave(2*i-1,:);
RB1_Grp12_Std(i,:) = Conc_Std(2*i-1,:);
end

RB1_GrpAB = [];
RB1_GrpAB_Std = [];
for i = 1:6
RB1_GrpAB(i,:) = Conc_Ave(2*i,:);
RB1_GrpAB_Std(i,:) = Conc_Std(2*i,:);
end

RB1_Grp34 = [];
RB1_Grp34_Std = [];
for i = 1:6
RB1_Grp34(i,:) = Conc_Ave(2*i+11,:);
RB1_Grp34_Std(i,:) = Conc_Std(2*i+11,:);
end

RB1_GrpCD = [];
RB1_GrpCD_Std = [];
```

```
for i = 1:6
RB1_GrpCD(i,:) = Conc_Ave(2*i+12,:);
RB1_GrpCD_Std(i,:) = Conc_Std(2*i+12,:);
end

RB1_Grp56= [Conc_Ave(25,:); Conc_Ave(26,:);
Conc_Ave(27,:);Conc_Ave(28,:);Conc_Ave(29,:);Conc_Ave(30,:)];
RB1_Grp56_Std = [Conc_Std(25,:);
Conc_Std(26,:);Conc_Std(27,:);Conc_Std(28,:);Conc_Std(29,:);Conc_Std(30,:)];
```

Evaluating Spearman Rho/p-values based off of discrete concentration points

```
% Defining independent variable, substratum stiffness
X_Stiff = [1000000 1000000 1000000 1000000 95.03333 95.03333 95.03333 95.03333 ...
    2.086666 2.086666 2.086666 2.086666 0.2436667 0.2436667 0.2436667 0.2436667]';

% Defining dependent variable, Y

Group1 = []; % Group 1 as RB1 Grp 12
Group2 = []; % Group 2 as RB1 GrpAB
Group3 = []; % Group 3 as RB1 Grp34
Group4 = []; % Group 4 as RB1 Grp CD
Group5 = []; % Group 5 as RB1 Grp 56

% Defining Conc. Values for PS Condition
for i = 1:4
Group1(i,:) = Conc(i,:); % Group 1 as RB1 Grp12
Group2(i,:) = Conc(i+4,:); % Group 2 as RB1 GrpAB
Group3(i,:) = Conc(i+48,:); % Group 3 as RB1 Grp34
Group4(i,:) = Conc(i+52,:); % Group 4 as RB1 Grp CD
Group5(i,:) = Conc(i+96,:); % Group 5 as RB1 Grp 56
end

% Defining Conc. Values for 1:3 Condition
for i = 5:8
Group1(i,:) = Conc(i+20,:);
Group2(i,:) = Conc(i+24,:);
Group3(i,:) = Conc(i+68,:);
Group4(i,:) = Conc(i+72,:);
Group5(i,:) = Conc(i+104,:);
end

% Defining Conc. Values for 1:1 Condition
for i = 9:12
Group1(i,:) = Conc(i+24,:);
Group2(i,:) = Conc(i+28,:);
Group3(i,:) = Conc(i+72,:);
Group4(i,:) = Conc(i+76,:);
Group5(i,:) = Conc(i+104,:);
end

% Defining Conc. Values for 3:2 Condition
for i = 13:16
```

```
Group1(i,:) = Conc(i+28,:);
Group2(i,:) = Conc(i+32,:);
Group3(i,:) = Conc(i+76,:);
Group4(i,:) = Conc(i+80,:);
Group5(i,:) = Conc(i+104,:);
end

% Finding Spearman rho & p-value for all groups

[rho1,pval1] = corr(X_Stiff,Group1,'type','Spearman');
[rho2,pval2] = corr(X_Stiff,Group2,'type','Spearman');
[rho3,pval3] = corr(X_Stiff,Group3,'type','Spearman');
[rho4,pval4] = corr(X_Stiff,Group4,'type','Spearman');
[rho5,pval5] = corr(X_Stiff,Group5,'type','Spearman');

% Combining all Rho/P-values

rho = [rho1;rho2;rho3;rho4;rho5];
pval = [pval1;pval2;pval3;pval4;pval5];
```

Looking at Correlation of PDMS ONLY (no TCPS condition)

These correlation analyses were performed to determine if we could mechanically modulate the MSC secretome. We excluded expression of cells expanded on tissue culture polystyrene (TCPS) from this correlation analysis because it is a substratum material with distinct surface chemistry and topography. Thus, there are additional variables, other than substratum stiffness, that we cannot decouple and could be causing changes in expression.

```
% Defining independent variable, substratum stiffness (no TCPS)
X_Stiff_NoPS = [95.03333 95.03333 95.03333 95.03333 ...
    2.086666 2.086666 2.086666 2.086666 0.2436667 0.2436667 0.2436667 0.2436667]';

for i = 1:12
    Group1_NoPS(i,:) = Group1(i+4,:);
    Group2_NoPS(i,:) = Group2(i+4,:);
    Group3_NoPS(i,:) = Group3(i+4,:);
    Group4_NoPS(i,:) = Group4(i+4,:);
    Group5_NoPS(i,:) = Group5(i+4,:);
end

% Finding Spearman rho & p-value for all groups

[rho1_NoPS,pval1_NoPS] = corr(X_Stiff_NoPS,Group1_NoPS,'type','Spearman');
[rho2_NoPS,pval2_NoPS] = corr(X_Stiff_NoPS,Group2_NoPS,'type','Spearman');
[rho3_NoPS,pval3_NoPS] = corr(X_Stiff_NoPS,Group3_NoPS,'type','Spearman');
[rho4_NoPS,pval4_NoPS] = corr(X_Stiff_NoPS,Group4_NoPS,'type','Spearman');
[rho5_NoPS,pval5_NoPS] = corr(X_Stiff_NoPS,Group5_NoPS,'type','Spearman');

% Combining all Rho/P-values
```

```
rho_NoPS = [rho1_NoPS;rho2_NoPS;rho3_NoPS;rho4_NoPS;rho5_NoPS];
pval_NoPS = [pval1_NoPS;pval2_NoPS;pval3_NoPS;pval4_NoPS;pval5_NoPS];
```

Published with MATLAB® R2015b

I.5 MATLAB Code for Modeling Luminex-Based Data and Survival

We used MATLAB to model the Luminex-based data in order to predict survival after radiation injury (Chapter 5). The Luminex-based data was the expression of the MSC secretome from various MSC populations that had varied therapeutic efficacy in supporting hematopoietic recovery *in vivo* [202]. These two data sets allowed us to develop a regression model using PLSR. We then used the same PLSR model parameters to predict survival with new "test" data from our mechanoprimed MSCs. Additional details on this implementation process are included in Chapter 5.

```
clear all; close all;
clc
```

Reading Data

Reading gene expression data

```
Data_Dia = xlsread('1.22.15 - BioPlex Data.xlsx','Bioplex Large and Small','Z2:AA36');
Data_Pas = xlsread('1.22.15 - BioPlex Data.xlsx','Bioplex Passages','T2:V36');
% Reading "response" data
% Data_Surv is the "response" data (survival) as a VECTOR at 18days,
Data_Surv = xlsread('1.22.15 - BioPlex Data.xlsx','Median Survival','K2:K7');
% Data_Prop is the "response" data (survival)  as a MATRIX at all days,
Data_Prop = xlsread('1.22.15 - BioPlex Data.xlsx','Survival Proportions','B2:F22')';
Times = xlsread('1.22.15 - BioPlex Data.xlsx','Survival Proportions','A2:A22')';
% Reading all the gene names a vector of strings
[~,~,GeneNames] = xlsread('1.22.15 - BioPlex Data.xlsx','Bioplex Large and Small','A2:A36');

% Concatenating ALL expression data as single matrix and then transposing
Dhi_exp = Data_Dia(:,1);
Dlo_exp = Data_Dia(:,2);
P3_exp = Data_Pas(:,1);
P6_exp = Data_Pas(:,2);
P9_exp = Data_Pas(:,3);

All_exp = [Dhi_exp, Dlo_exp, P6_exp, P3_exp, P9_exp]';
% Removing all "zero" columns => Resulting matrix is 5x35
%All_exp = All_exp(:,any(All_exp));
```

```
% Order of Survival is Dhi, Dlo, P6, P3, P9 (re-wrote the expression matrix
% in this same order
```

Plotting Expression Data vs. Survival @18 Days

```
% Sorting the vector response in "order" to assign colors
[dummy,h] = sort(Data_Surv);
oldorder= get(gcf,'DefaultAxesColorOrder');
set(gcf,'DefaultAxesColorOrder',jet(5));
plot3(repmat(1:length(All_exp), 5,1)',
repmat(Data_Surv(h),1,length(All_exp))',All_exp(h,:)','LineWidth',2);
set(gcf,'DefaultAxesColorOrder',oldorder);
xlabel('Genes'); ylabel('Survival Proportion @t=18 days');
set(gca,'XTick',1:length(All_exp),'XTickLabel',GeneNames);
axis('tight')
grid on
```

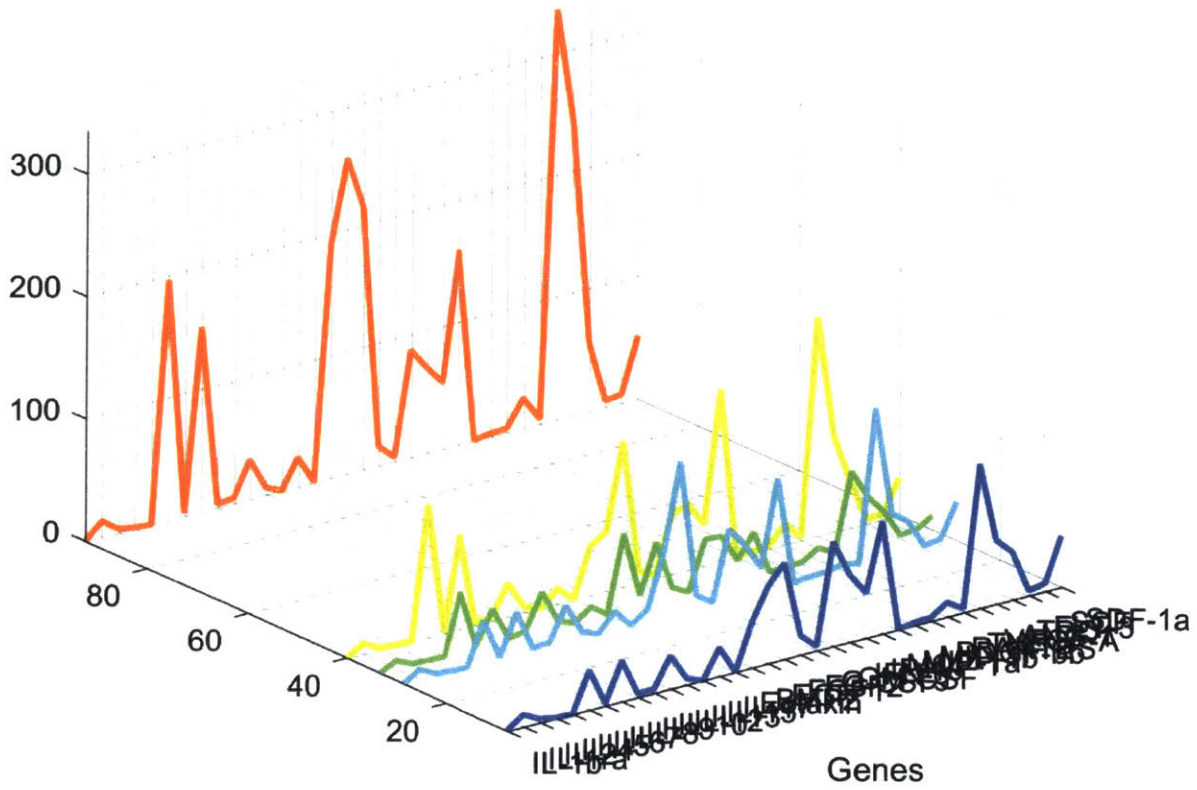

Survival Proportion @t=18 days

Correlation

```
% Calculating r => Pearson's LINEAR correlation coefficient
% Calculating p => two-tailed, null hypothesis as "no-correlation" (i.e.
% r=0) vs. non-zero correlation
```

```
% Finding linear correlation against response vector data
[r,p] = corr(All_exp,Data_Surv); % Linear Correlations at Day 18

%Threshold via either p-value or r-value
%[row, col] = find(r>0.8 | r<-0.8);
[row, col] = find(p<0.05);

empty = [];
for i=1:length(row);
    r_found(i) = r(row(i));
    genes_found(i) = GeneNames(row(i));
    p_found(i) = p(row(i));
end

Found = [genes_found;num2cell(r_found);num2cell(p_found)]';

% Finding linear correlation against response matrix data
[r2,p2] = corr(All_exp,Data_Prop); % Linear Correlations at ALL times

%[row2, col2] = find(r2>0.8 | r2<-0.8);
[row2, col2] = find(p2<0.05);

empty = [];
for i=1:length(row2);
    r_found2(i) = r2(row2(i),col2(i));
    genes_found2(i) = GeneNames(row2(i));
    times_found2(i) = Times(col2(i));
    p_found2(i) = p2(row2(i),col2(i));
end

Found2 = [genes_found2;num2cell(times_found2);num2cell(r_found2);num2cell(p_found2)]';
```

2-Component PLSR/PCA with Single Time Point

```
% Mean-center and univariate scale X and Y.  Note that this reduces the
% fundamental dimensionality of the dataset by 1, since you can predict any
% missing data point from the others knowing mean = 0.
Z_exp = zscore(All_exp);
%Z_resp = zscore(Data_Prop);
Z_resp = zscore(Data_Surv);

[n,p] = size(Z_exp);

% Build a 3D PLS model (which is the maximum possible: 5 observations, -1
% for mean centering).
[XL,YL,XS,YS,beta,PCTVAR, MSE, STATS]=plsregress(Z_exp,Z_resp,4);

figure(2)
plot(1:4,cumsum(100*PCTVAR(1,:)),'-bo');
xlabel('Number of PLS Components');
ylabel('Percent Variance Explained in X')
```

```
figure(3)
plot(1:4,cumsum(100*PCTVAR(2,:)),'-bo');
xlabel('Number of PLS Components');
ylabel('Percent Variance Explained in Y');

% The 2-PC approximation is:
Xapprox = XS(:,1:2) * XL(:,1:2)';
Yapprox = XS(:,1:2) * YL(:,1:2)';

% Plot scores and loadings:
% Set up axes.
figure(4);
axis([-2 2 -2 2])
plot([-2 2], [0, 0], 'k-')
hold on;
plot([0 0], [-2, 2], 'k-')
xlabel('PC1')
ylabel('PC2')
title('Scores and Loadings Plot in the 2D Approx.')

% XS tells us where in PC space each observation resides in the 2D approx.
scatter(XS(:,1),XS(:,2), 'r*')
text(XS(:,1)-.2,XS(:,2),['O1'; 'O2'; 'O3'; 'O4';'O5'], 'EdgeColor', 'red');

% XL tells us where in PC space each signal resides in the 2D approx.
scatter(XL(:,1),XL(:,2), 'g*')

% YL tells us where in PC space the response resides in the 2D approx.
scatter(YL(:,1),YL(:,2), 'b*')
text(YL(:,1)-.2,YL(:,2),['y'], 'Edgecolor', 'blue');

hold off

index = find(XL(:,1)>1 & XL(:,2)>0);

empty = [];
for i=1:length(index);
    PC1_PLSR(i) = XL(index(i),1);
    PC2_PLSR(i) = XL(index(i),2);
    genes_foundPLSR(i) = GeneNames(index(i));
end

FoundPLSR = [genes_foundPLSR;num2cell(PC1_PLSR);num2cell(PC2_PLSR)]';

% PLSR With 2-Components
[Xloadings,Yloadings,Xscores,Yscores,betaPLS]=plsregress(Z_exp,Z_resp,2);
yfitPLS = [ones(n,1) Z_exp]*betaPLS;


% PCA Regression with 2-Components
[PCALoadings, PCAScores, PCAVar] = pca(Z_exp, 'Economy',false);
[n,m] = size(Z_resp);
betaPCR = regress(Z_resp-mean(Z_resp), PCAScores(:,1:2));
```

```
betaPCR = PCALoadings(:,1:2)*betaPCR;
betaPCR = [mean(Z_resp) - mean(Z_exp)*betaPCR; betaPCR];
yfitPCR = [ones(n,1) Z_exp]*betaPCR;

figure(5)
plot(Z_resp,yfitPLS,'bo',Z_resp,yfitPCR,'r^');
xlabel('Observed Response');
ylabel('Fitted Response');
legend({'PLSR with 2 Components' 'PCR with 2 Components'},  ...
       'location','NW');
```

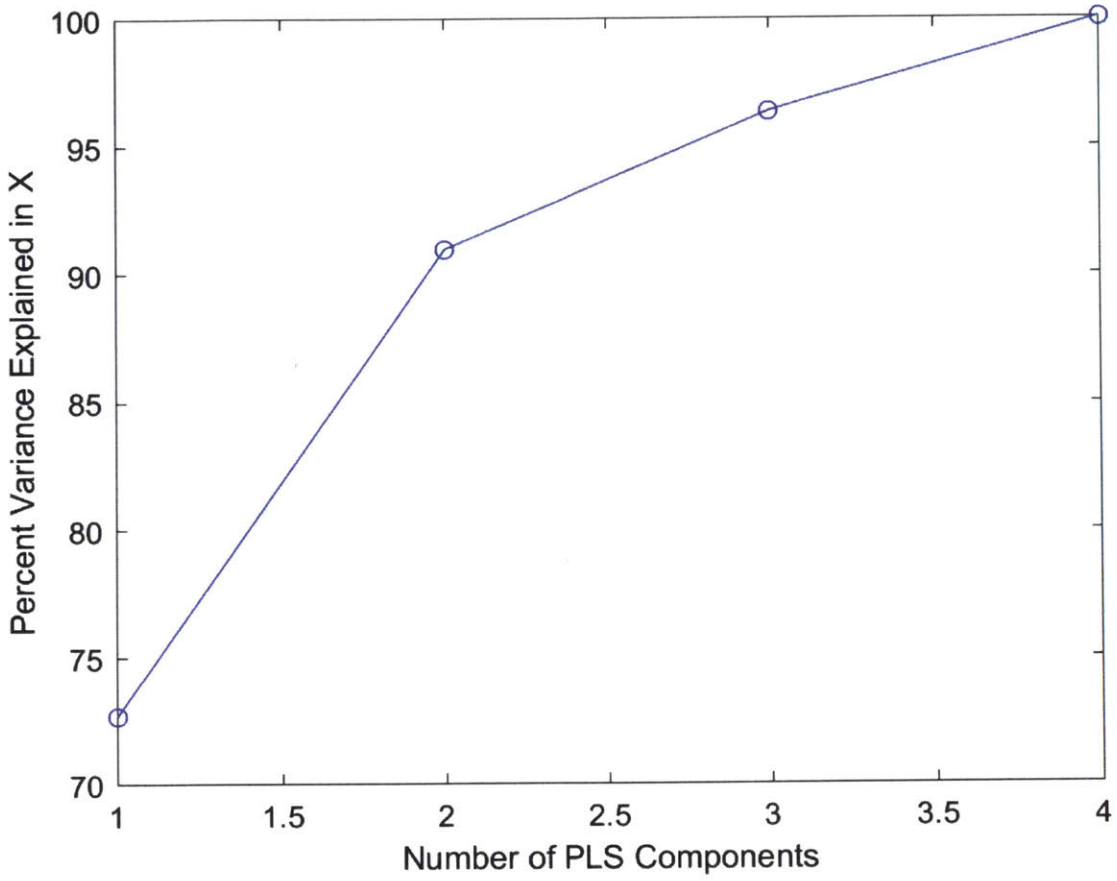

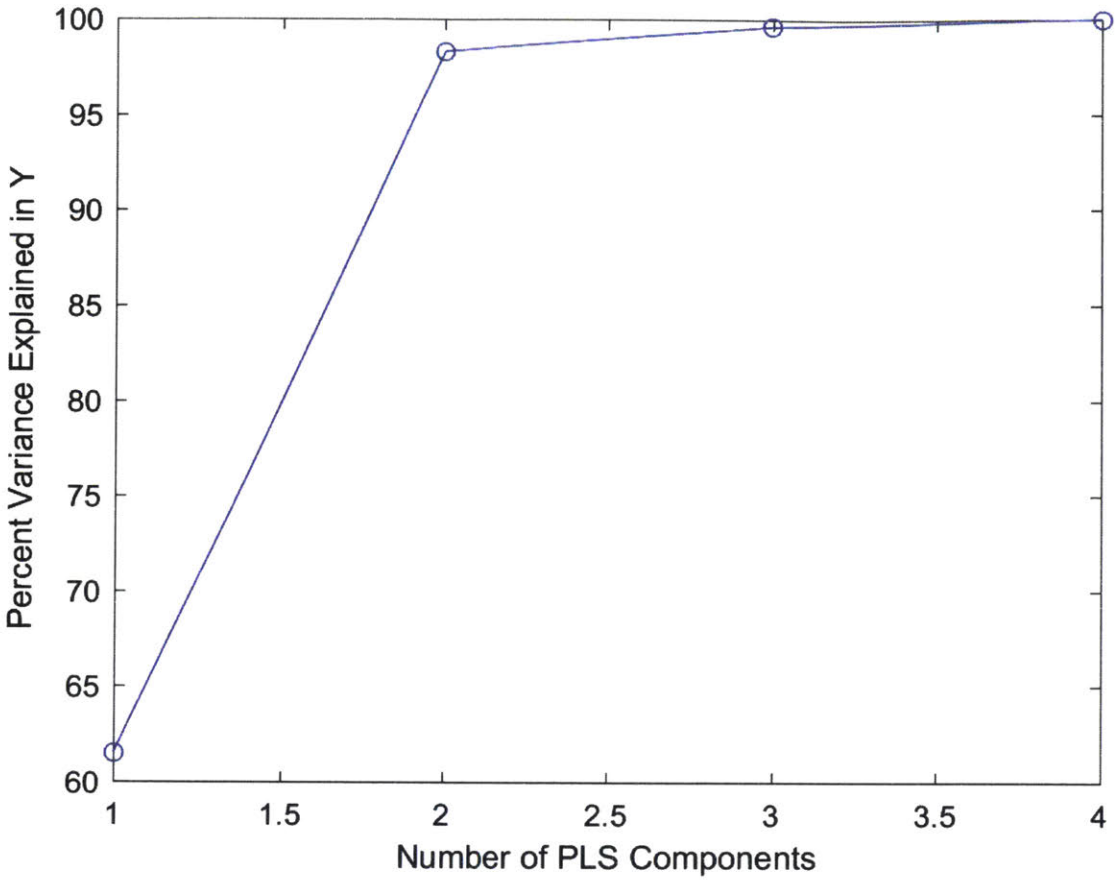
Percent Variance Explained in Y
100
95
90
85
80
75
70
65
60
1
1.5
2
2.5
3
3.5
4
Number of PLS Components

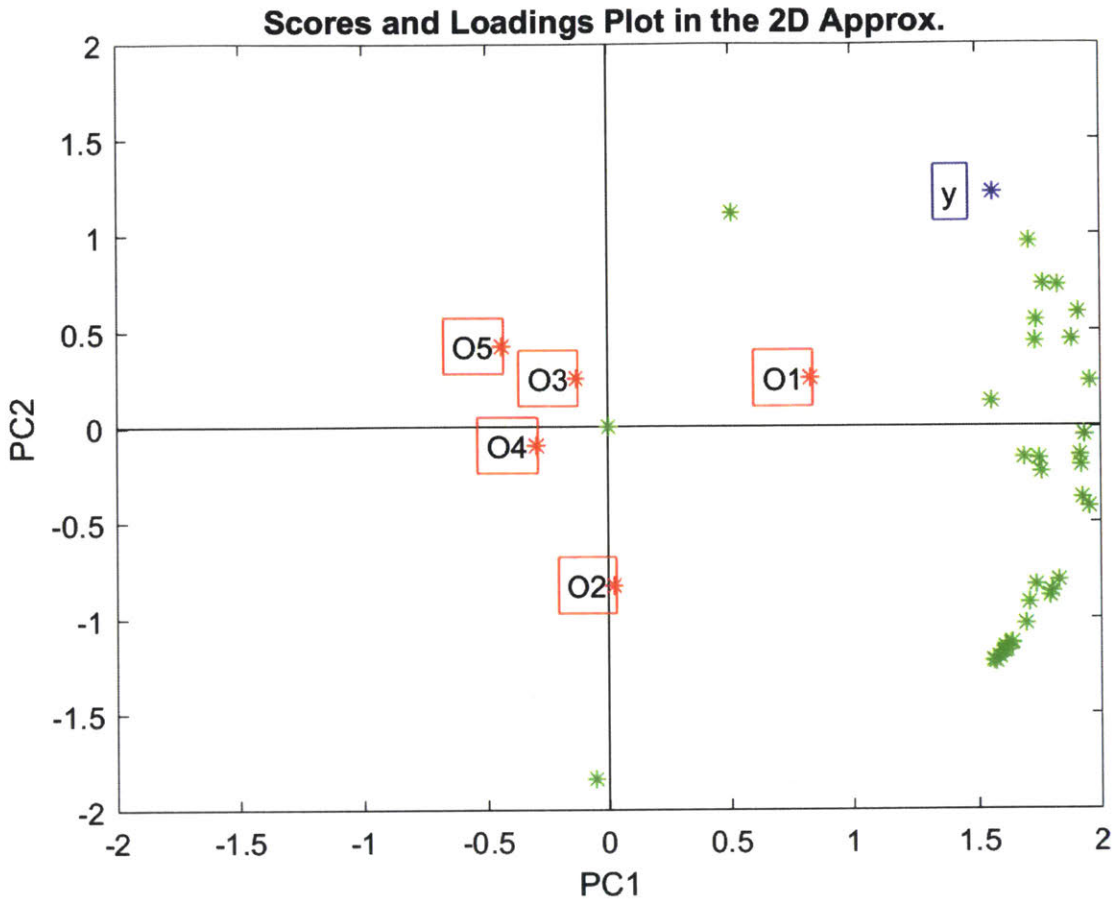
Scores and Loadings Plot in the 2D Approx.
PC2
PC1
y
O1
O2
O3
O4
O5
2
1.5
1
0.5
0
-0.5
-1
-1.5
-2
-2
-1.5
-1
-0.5
0
0.5
1
1.5
2

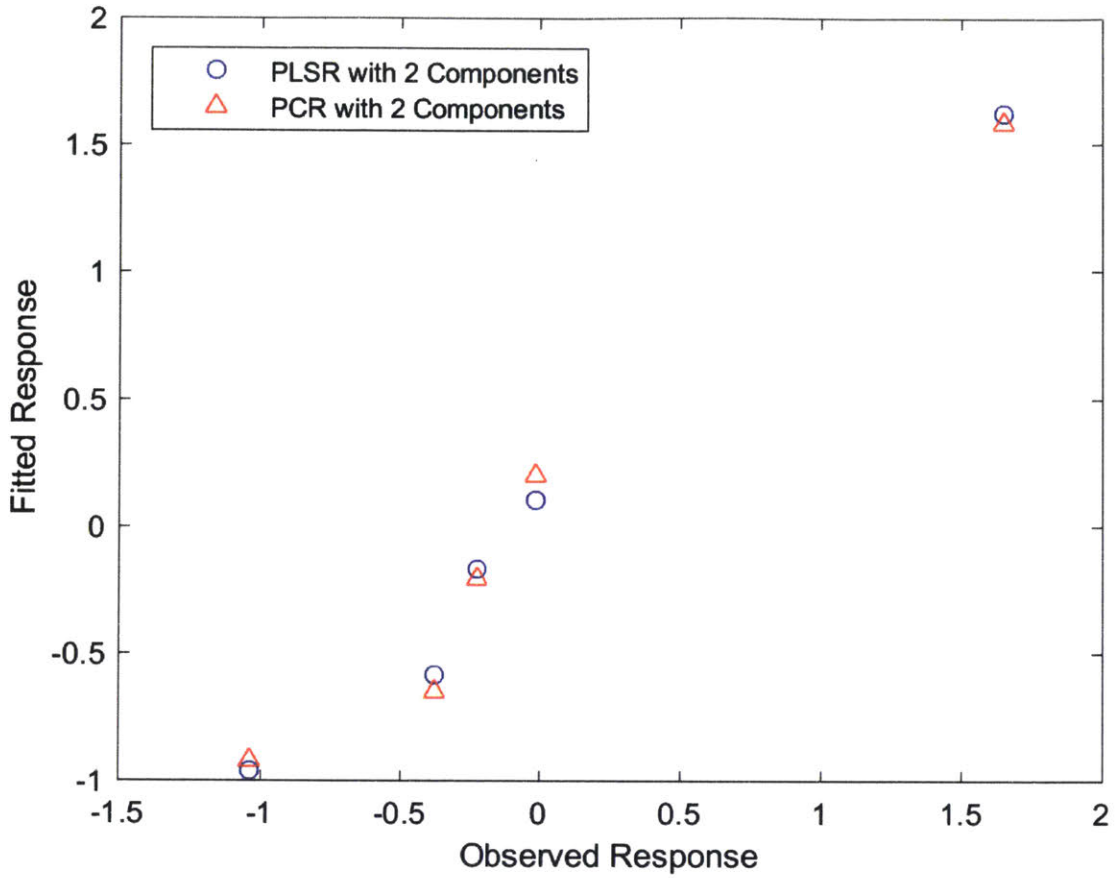

2-Component PLSR with All Time Points

```
% Mean-center and univariate scale X and Y.  Note that this reduces the
% fundamental dimensionality of the dataset by 1, since you can predict any
% missing data point from the others knowing mean = 0.
Z_exp = zscore(All_exp);
[Z_resp,mu,sigma] = zscore(Data_Prop);

[n,p] = size(Z_exp);

% Build a 3D PLS model (which is the maximum possible: 5 observations, -1
% for mean centering).
[XL,YL,XS,YS,beta,PCTVAR, MSE, STATS]=plsregress(Z_exp,Z_resp,4, 'CV',4);

figure(6)
plot(1:4,cumsum(100*PCTVAR(1,:)),'-bo');
xlabel('Number of PLS Components','FontWeight','bold');
ylabel('Percent Variance Explained in X','FontWeight','bold')
figure(7)
plot(1:4,cumsum(100*PCTVAR(2,:)),'-bo');
xlabel('Number of PLS Components','FontWeight','bold');
ylabel('Percent Variance Explained in Y','FontWeight','bold');
```

```
% The 2-PC approximation is:
Xapprox = XS(:,1:2) * XL(:,1:2)';
Yapprox = XS(:,1:2) * YL(:,1:2)';

% Plot scores and loadings:
% Set up axes.
figure(8);
axis([-2 2 -2 2])
plot([-2 2], [0, 0], 'k-')
hold on;
plot([0 0], [-2, 2], 'k-')
xlabel('PC1')
ylabel('PC2')
%title('Scores and Loadings Plot in the 2D Approx.')

% XS tells us where in PC space each observation resides in the 2D approx.
%scatter(XS(:,1),XS(:,2), 'r*')
%text(XS(:,1)-.2,XS(:,2),['O1'; 'O2'; 'O3'; 'O4';'O5'], 'EdgeColor', 'red');

% XL tells us where in PC space each signal resides in the 2D approx.
scatter(XL(:,1),XL(:,2), 'm*')

% YL tells us where in PC space the response resides in the 2D approx.
scatter(YL(:,1),YL(:,2), 'b*')
%text(YL(:,1)-.2,YL(:,2),['y'], 'Edgecolor', 'blue');

hold off
legend('','','Predictor Loadings','Response Loadings')

% PLSR With 2-Components
[Xloadings,Yloadings,Xscores,Yscores,betaPLS]=plsregress(Z_exp,Z_resp,2);
yfitPLS = [ones(n,1) Z_exp]*betaPLS;


figure(9)
plot(Z_resp,yfitPLS,'ko');
xlabel('Observed Response');
ylabel('Fitted Response');
```

```
Warning: Cannot cross-validate more than 2 components.
```

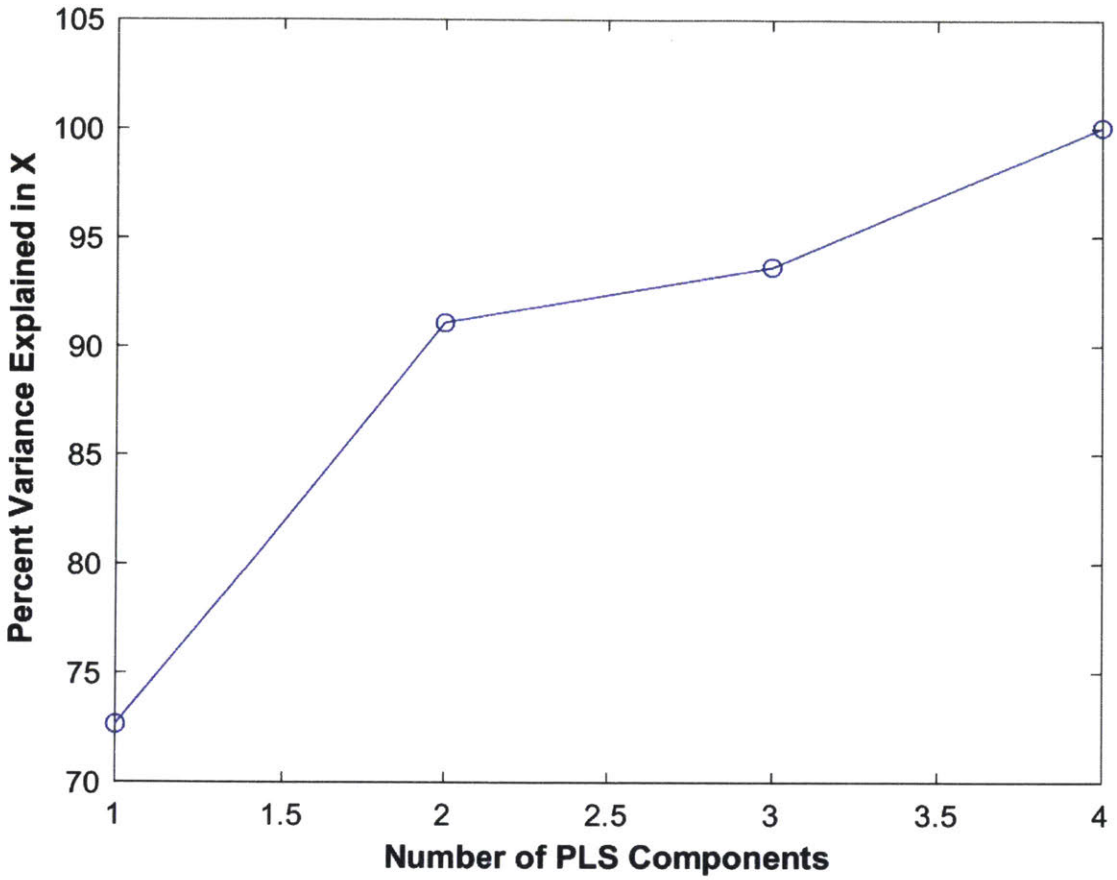
105
100
95
90
85
80
75
70
Percent Variance Explained in X
1
1.5
2
2.5
3
3.5
4
Number of PLS Components

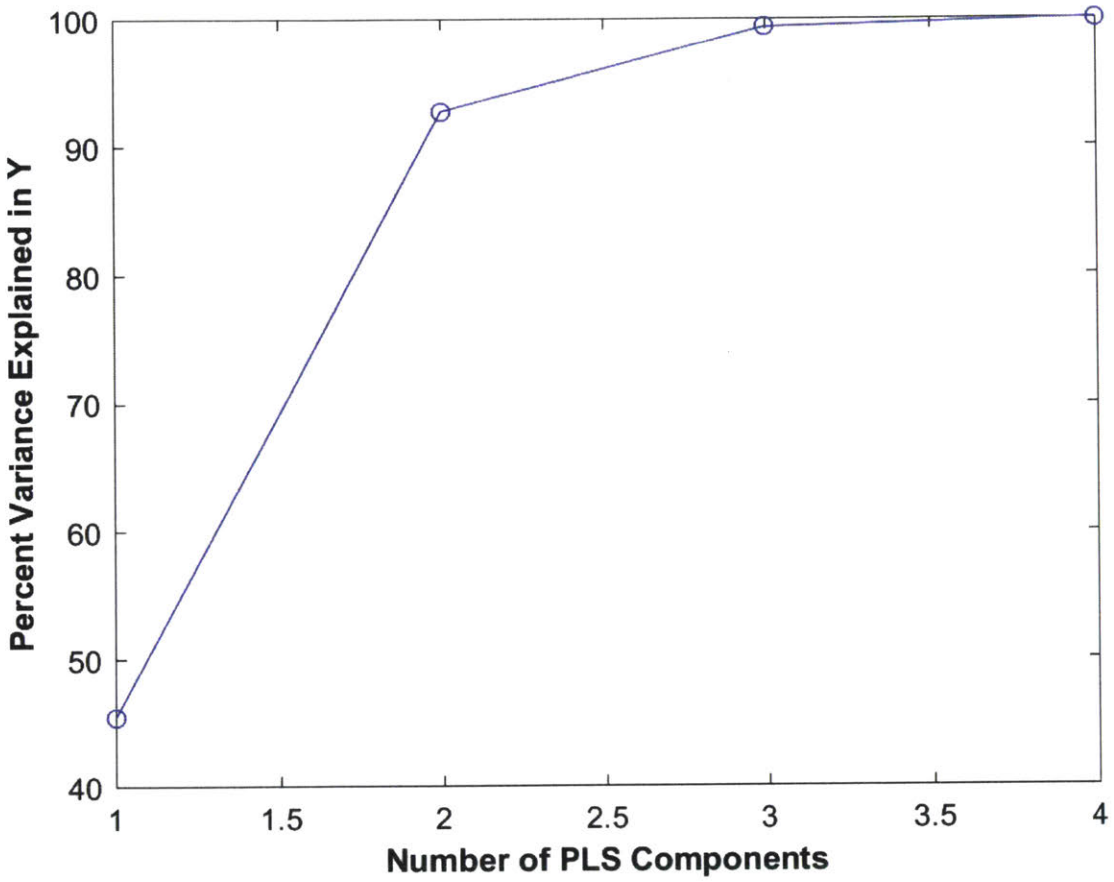
Percent Variance Explained in Y
100
90
80
70
60
50
40
1
1.5
2
2.5
3
3.5
4
Number of PLS Components

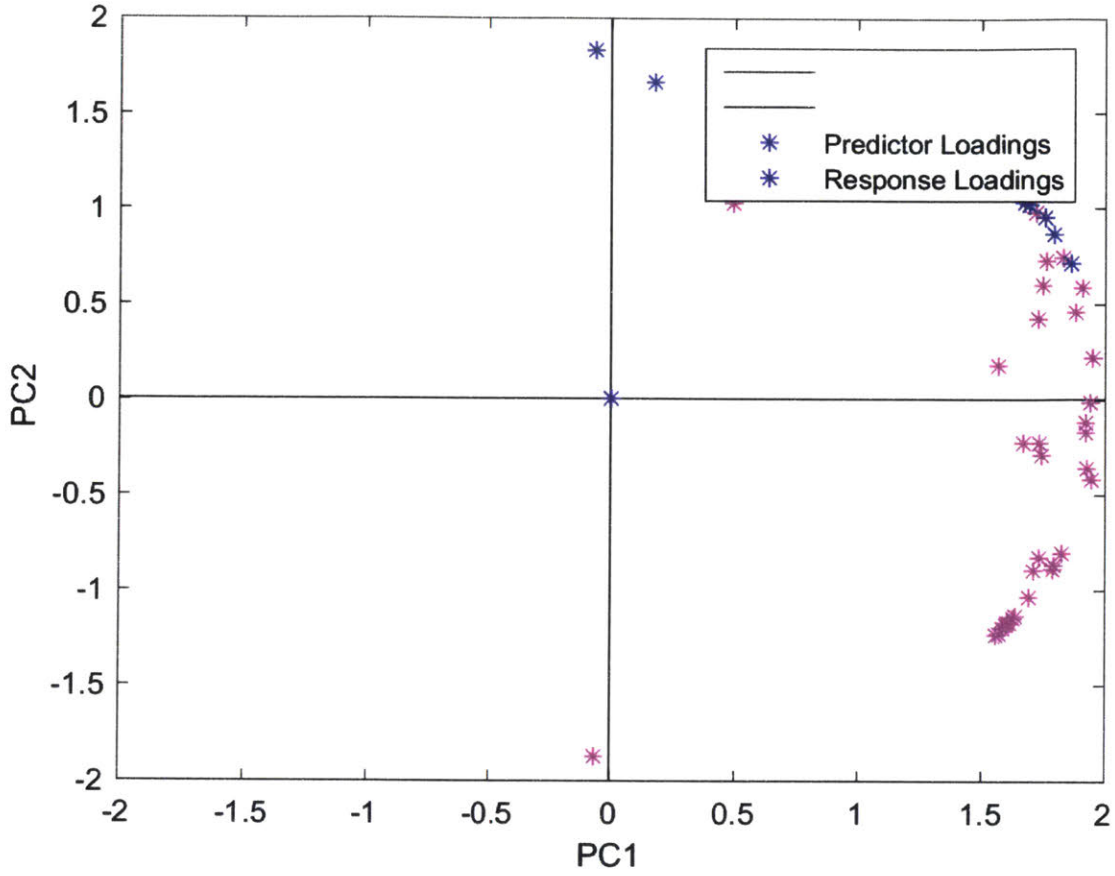
Predictor Loadings
Response Loadings
PC1
PC2
2
1.5
1
0.5
0
-0.5
-1
-1.5
-2
-2
-1.5
-1
-0.5
0
0.5
1
1.5
2

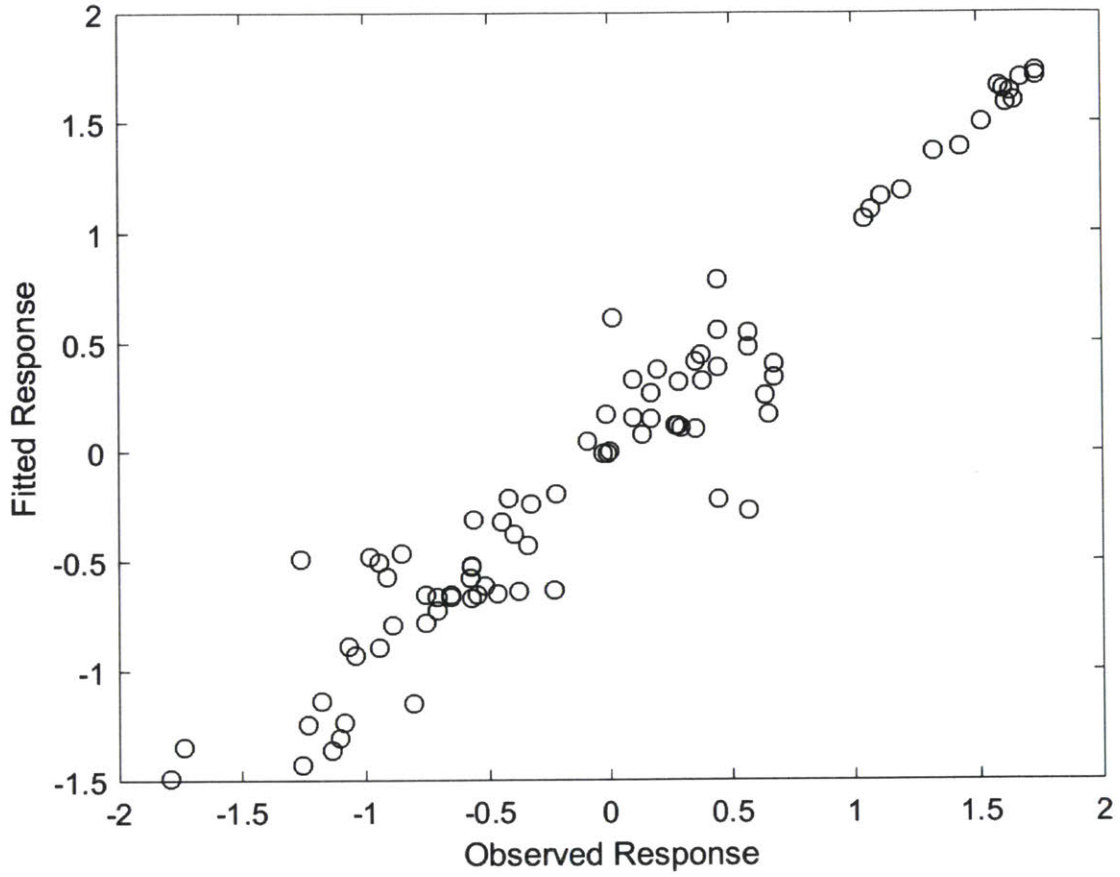

Reversing Z-Score Normalization to determine predicted values

```
Z_resp_Rev = zeros(size(Z_resp));
yfitPLS_val = zeros(size(Z_resp));

for i = 1:5
   Z_resp_Rev(i,:) = Z_resp(i,:).*sigma+mu;
   yfitPLS_val(i,:) = yfitPLS(i,:).*sigma+mu;
end

% figure(10)
% plot(Z_resp_Rev,yfitPLS_val,'bo');
% xlabel('Observed Response');
% ylabel('Fitted Response');
```

Plotting Survival Curves

```
SurvivalDays = xlsread('1.22.15 - BioPlex Data.xlsx', 'Survival Proportions','A2:A22')';

co = [1 0.5 0; 0 0.5 1; 1 1 0; 0 1 1; 0.5 1 0.5];
set(groot, 'defaultAxesColorOrder', co)
figure(11)
```

```
axis([0 50 -10 110])
hold on
plot(SurvivalDays,Z_resp_Rev, 'LineWidth',2)
%legend('P6 LCF', 'P6 SCF','P6 CTRL','P3 CTRL','P9 CTRL')
plot(SurvivalDays,yfitPLS_val,'--','LineWidth',2)
% legend('P6 LCF', 'P6 SCF','P6 CTRL','P3 CTRL','P9 CTRL',...
%     'P6 LCF Model', 'P6 SCF Model','P6 CTRL Model','P3 CTRL Model','P9 CTRL Model')
xlabel('Time (days)')
ylabel('Survival Proportion (%)')
hold off
```

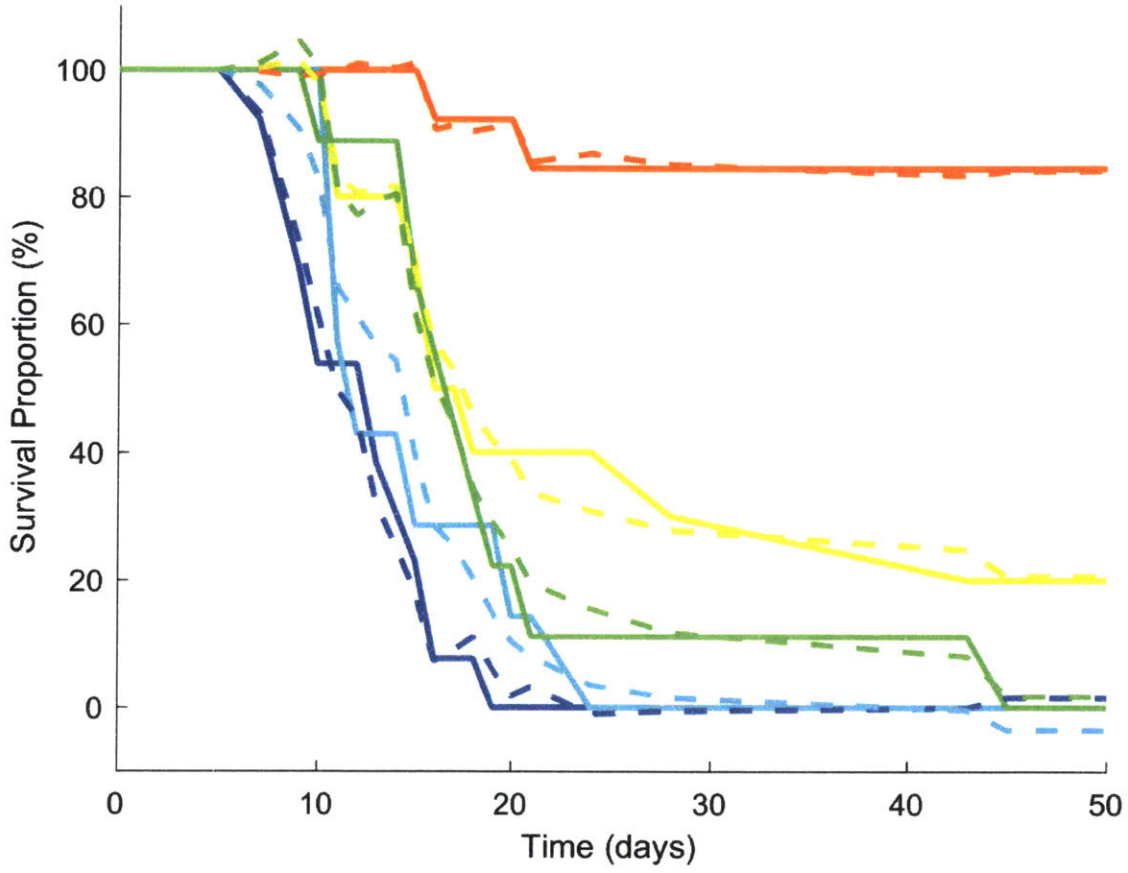

Fitting the new "test" data -- PL7 Grp AB + PL18 Grp ABC

Note that in the loaded excel file name we refer to the data as "BioPlex" and that the data is "Re-Arranged." As stated at the beginning of Section I.4, the terms BioPlex, Luminex, and Procartaplex are used interchangeably. The original data used to develop the PLSR model was generated on the equipment in our Singapore-based lab. The later Luminex-based data was generated on a separate Luminex reader (FlexMap 3D) in our MIT-based lab. The orders in which these Luminex readers output the fluorescence data for each protein varies. However, the expression data used as the "test" data input into the regression model must have the same order as the "model" data in order to accurately make model predictions. Each data column in the

excel spreadsheets represents the expression of a single protein. Thus, we had to ensure that the proteins expressed in the "test" data were in the same column number as the "model" data. We did this by manually re-arranging the columns of data in our excel spreadsheets.

```
All_exp_test = xlsread('10.23.17 - BioPlex Test Data Re-Arranged.xlsx','PL7 GrpAB','B2:AJ7');
Z_exp_test = zscore(All_exp_test);

[n,p] = size(Z_exp_test);

yfitPLS_test = [ones(n,1) Z_exp_test]*betaPLS;

yfitPLS_testval = [];

for i = 1:6
   yfitPLS_testval(i,:) = yfitPLS_test(i,:).*sigma+mu;
end
figure(16)
plot(SurvivalDays, yfitPLS_testval, 'LineWidth',2)
legend('CTRL','LCF','SCF','100 kPa','10 kPa','1 kPa')
xlabel('Time (days)')
ylabel('Survival Proportion (%)')
title('PL7 Group AB + PL18 Group ABC')
```

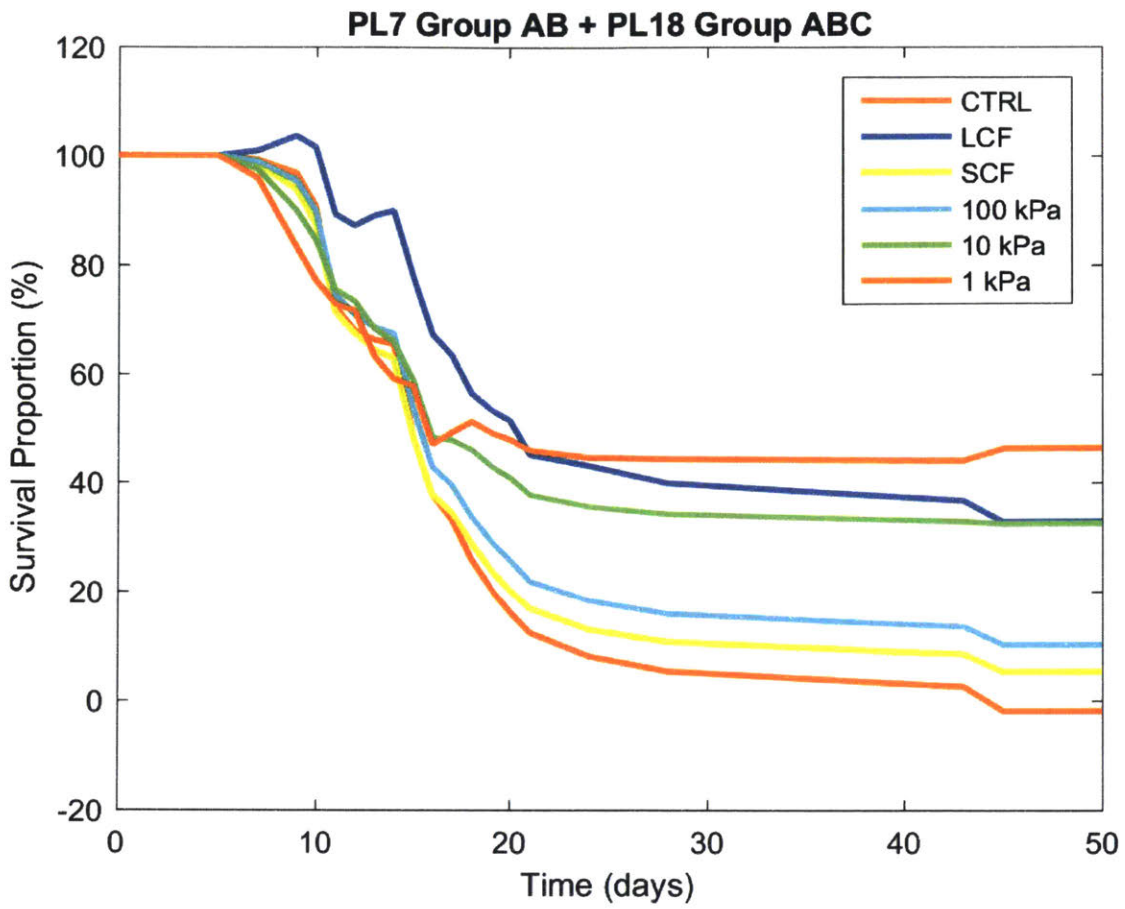

Fitting the new "test" data -- PL7 Grp AB + PL18 Grp ABC; Sorted Cells Only

```
All_exp_test = xlsread('10.23.17 - BioPlex Test Data Re-Arranged.xlsx','PL7 GrpAB','B2:AJ4');
Z_exp_test = zscore(All_exp_test);

[n,p] = size(Z_exp_test);

yfitPLS_test = [ones(n,1) Z_exp_test]*betaPLS;

yfitPLS_testval = [];

for i = 1:3
   yfitPLS_testval(i,:) = yfitPLS_test(i,:).*sigma+mu;
end
figure(17)
plot(SurvivalDays, yfitPLS_testval, 'LineWidth',2)
legend('CTRL','LCF','SCF')
xlabel('Time (days)')
ylabel('Survival Proportion (%)')
title('PL7 Group AB + PL18 Group ABC')
```

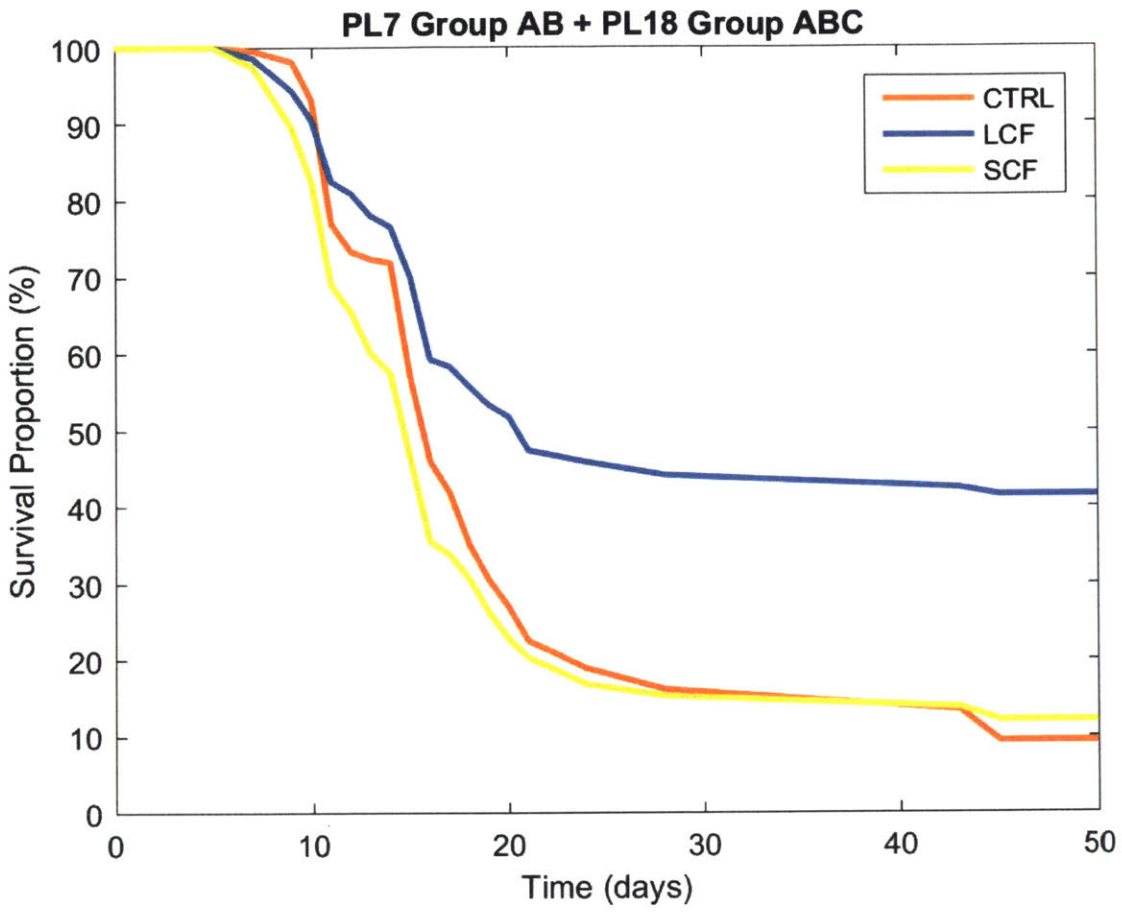

Fitting the new "test" data -- PL7 Grp AB + PL18 Grp ABC; PDMS Cells Only

```
All_exp_test = xlsread('10.23.17 - BioPlex Test Data Re-Arranged.xlsx','PL7 GrpAB','B5:AJ7');
Z_exp_test = zscore(All_exp_test);

[n,p] = size(Z_exp_test);

yfitPLS_test = [ones(n,1) Z_exp_test]*betaPLS;

yfitPLS_testval = [];

for i = 1:3
   yfitPLS_testval(i,:) = yfitPLS_test(i,:).*sigma+mu;
end
figure(18)
plot(SurvivalDays, yfitPLS_testval, 'LineWidth',2)
legend('100 kPa','10 kPa','1 kPa')
xlabel('Time (days)')
ylabel('Survival Proportion (%)')
title('PL7 Group AB + PL18 Group ABC')
```

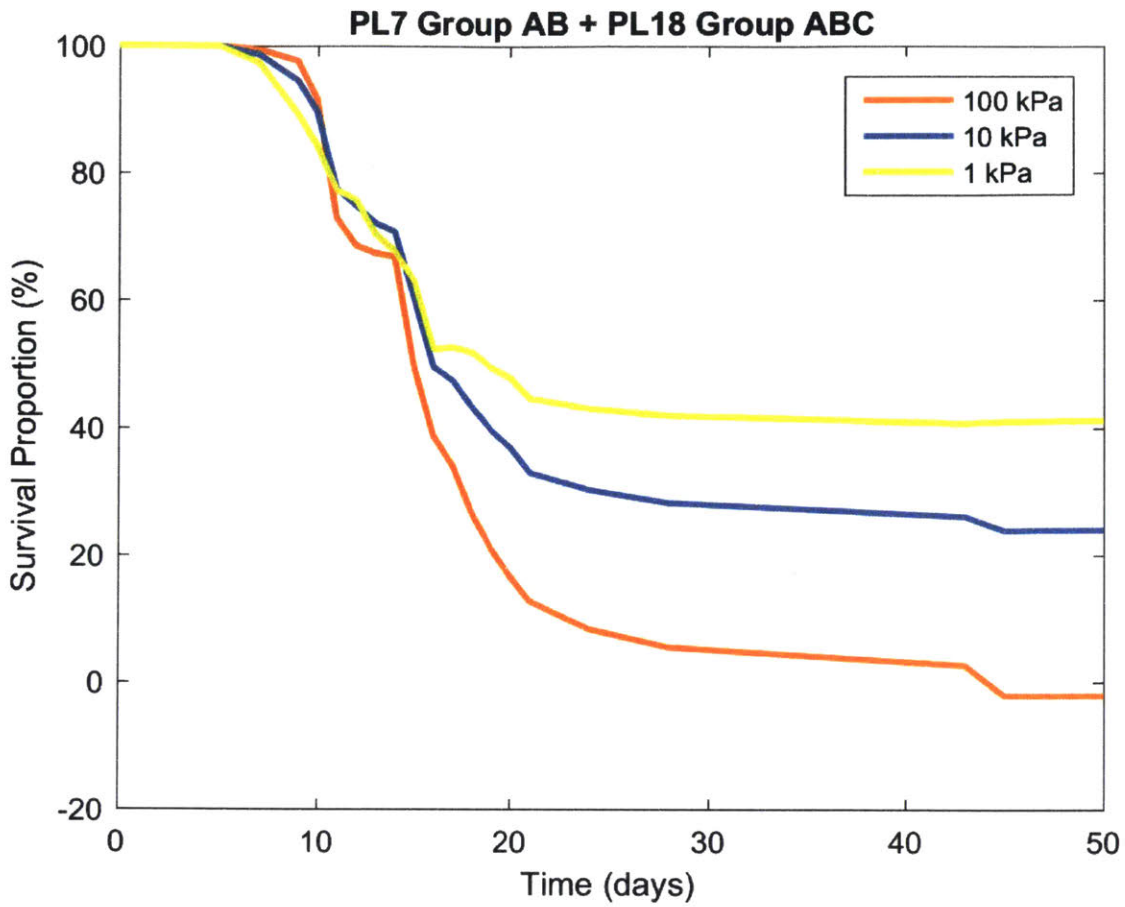

Fitting the new "test" data -- PL7 Grp AB + PL18 Grp ABC; no SCF

```
All_exp_test = xlsread('10.23.17 - BioPlex Test Data Re-Arranged.xlsx','PL7 GrpAB no
SCF','B2:AJ6');
Z_exp_test = zscore(All_exp_test);

[n,p] = size(Z_exp_test);

yfitPLS_test = [ones(n,1) Z_exp_test]*betaPLS;

yfitPLS_testval = [];

for i = 1:5
   yfitPLS_testval(i,:) = yfitPLS_test(i,:).*sigma+mu;
end
figure(19)
plot(SurvivalDays, yfitPLS_testval, 'LineWidth',2)
axis([0 50 -5 105])
legend('CTRL','LCF','100 kPa', '10 kPa', '1 kPa')
xlabel('Time (days)')
ylabel('Survival Proportion (%)')
title('PL7 Group AB + PL18 Group ABC')
```

```
figure(20)
hold on
axis([0 50 -5 105])
plot(SurvivalDays,yfitPLS_testval(1,:), 'Color', [0.80078125 0 0.80078125], 'LineWidth', 2)
plot(SurvivalDays,yfitPLS_testval(2,:), 'Color', [0 0 1], 'LineWidth', 2)
plot(SurvivalDays,yfitPLS_testval(3,:), 'Color', [0.59765625 0.28515625 0.03125], 'LineWidth', 2)
% Dark Orange
plot(SurvivalDays,yfitPLS_testval(4,:), 'Color', [0.89453125 0.42578125 0.04296875], 'LineWidth',
2) % Medium Orange
plot(SurvivalDays,yfitPLS_testval(5,:), 'Color', [0.98828125 0.8359375 0.7109375], 'LineWidth',
2) % Light Orange
legend('CTRL','LCF','100 kPa', '10 kPa', '1 kPa')
xlabel('Days post-irradiation','FontWeight','bold')
ylabel('Survival Proportion (%)','FontWeight','bold')
hold off
```

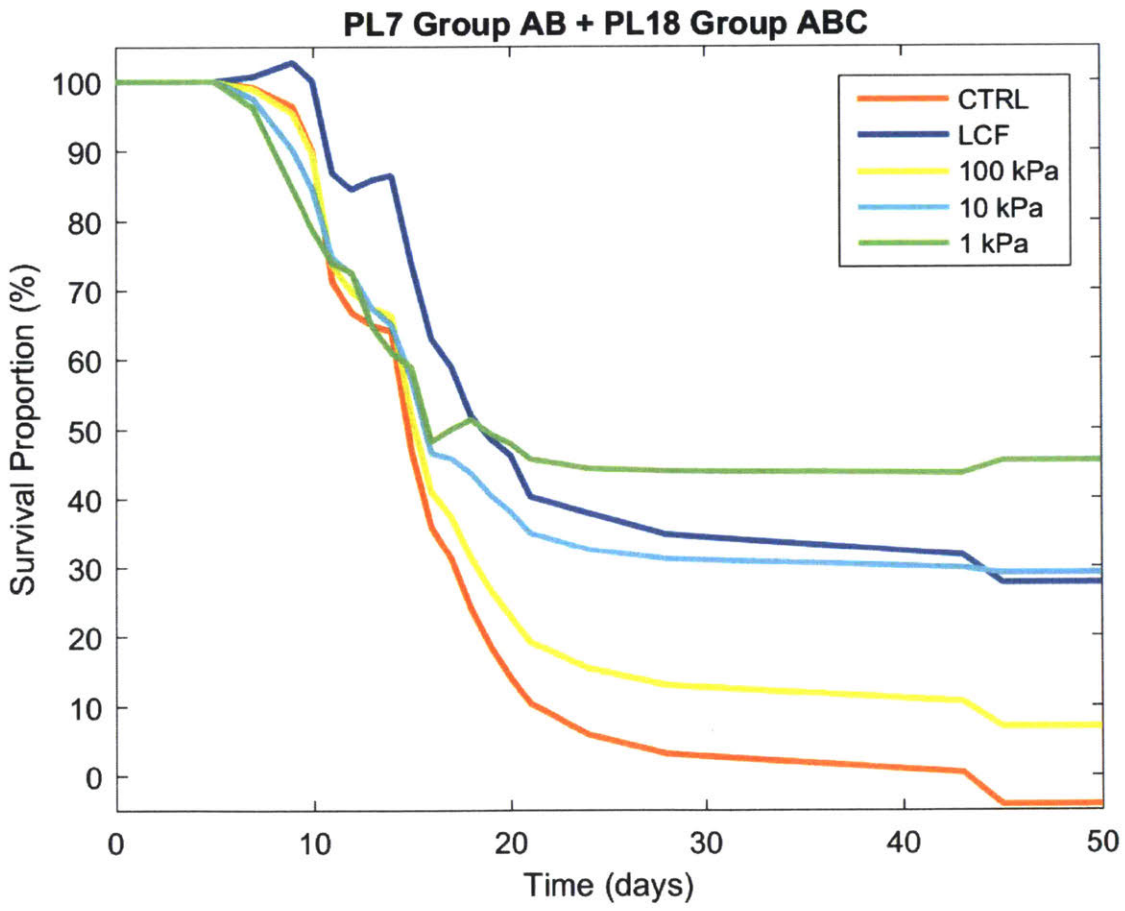

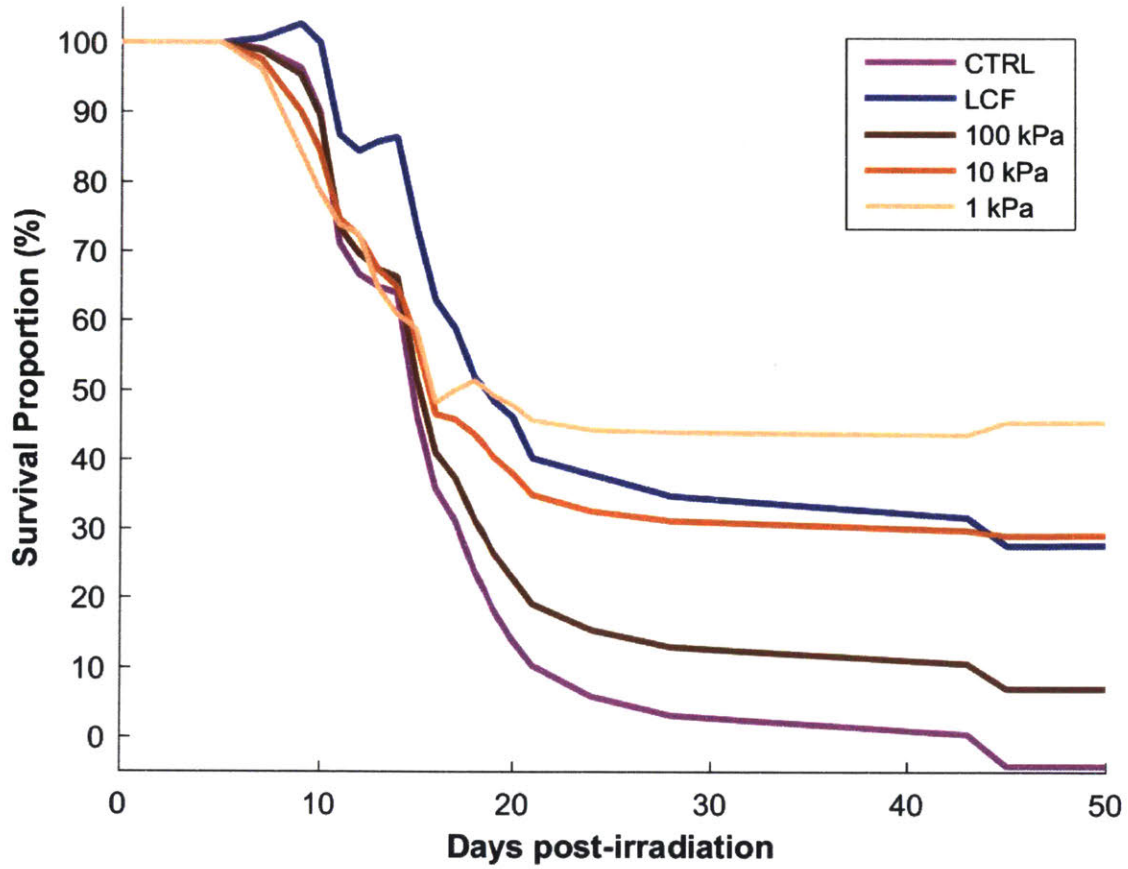

Re-Evaluating PLSR with Key Secretome Components "knocked" out one at a time

```
All_exp_test = xlsread('2.25.18 - Evaluating PLSR.xlsx','PL7 GrpAB no SCF','B2:AJ6');
Z_exp_test = zscore(All_exp_test);

[n,p] = size(Z_exp_test);

yfitPLS_test = [ones(n,1) Z_exp_test]*betaPLS;

yfitPLS_testval = [];

for i = 1:5
   yfitPLS_testval(i,:) = yfitPLS_test(i,:).*sigma+mu;
end

figure(21)

% Original Expression

subplot(4,2,1)
hold on
axis([0 50 -5 105])
plot(SurvivalDays,yfitPLS_testval(1,:), 'Color', [0.80078125 0 0.80078125], 'LineWidth', 2)
```

```
plot(SurvivalDays,yfitPLS_testval(2,:), 'Color', [0 0 1], 'LineWidth', 2)
plot(SurvivalDays,yfitPLS_testval(3,:), 'Color', [0.59765625 0.28515625 0.03125], 'LineWidth', 2)
% Dark Orange
plot(SurvivalDays,yfitPLS_testval(4,:), 'Color', [0.89453125 0.42578125 0.04296875], 'LineWidth',
2) % Medium Orange
plot(SurvivalDays,yfitPLS_testval(5,:), 'Color', [0.98828125 0.8359375 0.7109375], 'LineWidth',
2) % Light Orange
%legend('CTRL','LCF','100 kPa', '10 kPa', '1 kPa')
title('Original Data')
xlabel('Days post-irradiation','FontWeight','bold')
ylabel('Survival Proportion (%)','FontWeight','bold')
hold off

% No Expression of ANG1

All_exp_test = xlsread('2.25.18 - Evaluating PLSR.xlsx','No ANG1','B2:AJ6');
Z_exp_test = zscore(All_exp_test);

[n,p] = size(Z_exp_test);

yfitPLS_test = [ones(n,1) Z_exp_test]*betaPLS;

yfitPLS_testval = [];

for i = 1:5
   yfitPLS_testval(i,:) = yfitPLS_test(i,:).*sigma+mu;
end


subplot(4,2,2)
hold on
axis([0 50 -5 105])
plot(SurvivalDays,yfitPLS_testval(1,:), 'Color', [0.80078125 0 0.80078125], 'LineWidth', 2)
plot(SurvivalDays,yfitPLS_testval(2,:), 'Color', [0 0 1], 'LineWidth', 2)
plot(SurvivalDays,yfitPLS_testval(3,:), 'Color', [0.59765625 0.28515625 0.03125], 'LineWidth', 2)
% Dark Orange
plot(SurvivalDays,yfitPLS_testval(4,:), 'Color', [0.89453125 0.42578125 0.04296875], 'LineWidth',
2) % Medium Orange
plot(SurvivalDays,yfitPLS_testval(5,:), 'Color', [0.98828125 0.8359375 0.7109375], 'LineWidth',
2) % Light Orange
%legend('CTRL','LCF','100 kPa', '10 kPa', '1 kPa')
title('No ANG-1')
xlabel('Days post-irradiation','FontWeight','bold')
ylabel('Survival Proportion (%)','FontWeight','bold')
hold off

% No Expression of EGF

All_exp_test = xlsread('2.25.18 - Evaluating PLSR.xlsx','No EGF','B2:AJ6');
Z_exp_test = zscore(All_exp_test);

[n,p] = size(Z_exp_test);

yfitPLS_test = [ones(n,1) Z_exp_test]*betaPLS;
```

```
yfitPLS_testval = [];

for i = 1:5
   yfitPLS_testval(i,:) = yfitPLS_test(i,:).*sigma+mu;
end


subplot(4,2,3)
hold on
axis([0 50 -5 105])
plot(SurvivalDays,yfitPLS_testval(1,:), 'Color', [0.80078125 0 0.80078125], 'LineWidth', 2)
plot(SurvivalDays,yfitPLS_testval(2,:), 'Color', [0 0 1], 'LineWidth', 2)
plot(SurvivalDays,yfitPLS_testval(3,:), 'Color', [0.59765625 0.28515625 0.03125], 'LineWidth', 2)
% Dark Orange
plot(SurvivalDays,yfitPLS_testval(4,:), 'Color', [0.89453125 0.42578125 0.04296875], 'LineWidth',
2) % Medium Orange
plot(SurvivalDays,yfitPLS_testval(5,:), 'Color', [0.98828125 0.8359375 0.7109375], 'LineWidth',
2) % Light Orange
title('No EGF')
%legend('CTRL','LCF','100 kPa', '10 kPa', '1 kPa')
xlabel('Days post-irradiation','FontWeight','bold')
ylabel('Survival Proportion (%)','FontWeight','bold')
hold off

% No Expression of FGF1

All_exp_test = xlsread('2.25.18 - Evaluating PLSR.xlsx','No FGF1','B2:AJ6');
Z_exp_test = zscore(All_exp_test);

[n,p] = size(Z_exp_test);

yfitPLS_test = [ones(n,1) Z_exp_test]*betaPLS;

yfitPLS_testval = [];

for i = 1:5
   yfitPLS_testval(i,:) = yfitPLS_test(i,:).*sigma+mu;
end


subplot(4,2,4)
hold on
axis([0 50 -5 105])
plot(SurvivalDays,yfitPLS_testval(1,:), 'Color', [0.80078125 0 0.80078125], 'LineWidth', 2)
plot(SurvivalDays,yfitPLS_testval(2,:), 'Color', [0 0 1], 'LineWidth', 2)
plot(SurvivalDays,yfitPLS_testval(3,:), 'Color', [0.59765625 0.28515625 0.03125], 'LineWidth', 2)
% Dark Orange
plot(SurvivalDays,yfitPLS_testval(4,:), 'Color', [0.89453125 0.42578125 0.04296875], 'LineWidth',
2) % Medium Orange
plot(SurvivalDays,yfitPLS_testval(5,:), 'Color', [0.98828125 0.8359375 0.7109375], 'LineWidth',
2) % Light Orange
%legend('CTRL','LCF','100 kPa', '10 kPa', '1 kPa')
title('No FGF1')
```

```
xlabel('Days post-irradiation','FontWeight','bold')
ylabel('Survival Proportion (%)','FontWeight','bold')
hold off

% No Expression of IL6

All_exp_test = xlsread('2.25.18 - Evaluating PLSR.xlsx','No IL6','B2:AJ6');
Z_exp_test = zscore(All_exp_test);

[n,p] = size(Z_exp_test);

yfitPLS_test = [ones(n,1) Z_exp_test]*betaPLS;

yfitPLS_testval = [];

for i = 1:5
   yfitPLS_testval(i,:) = yfitPLS_test(i,:).*sigma+mu;
end


subplot(4,2,5)
hold on
axis([0 50 -5 105])
plot(SurvivalDays,yfitPLS_testval(1,:), 'Color', [0.80078125 0 0.80078125], 'LineWidth', 2)
plot(SurvivalDays,yfitPLS_testval(2,:), 'Color', [0 0 1], 'LineWidth', 2)
plot(SurvivalDays,yfitPLS_testval(3,:), 'Color', [0.59765625 0.28515625 0.03125], 'LineWidth', 2)
% Dark Orange
plot(SurvivalDays,yfitPLS_testval(4,:), 'Color', [0.89453125 0.42578125 0.04296875], 'LineWidth',
2) % Medium Orange
plot(SurvivalDays,yfitPLS_testval(5,:), 'Color', [0.98828125 0.8359375 0.7109375], 'LineWidth',
2) % Light Orange
title('No IL6')
%legend('CTRL','LCF','100 kPa', '10 kPa', '1 kPa')
xlabel('Days post-irradiation','FontWeight','bold')
ylabel('Survival Proportion (%)','FontWeight','bold')
hold off

% No Expression of IL8

All_exp_test = xlsread('2.25.18 - Evaluating PLSR.xlsx','No IL8','B2:AJ6');
Z_exp_test = zscore(All_exp_test);

[n,p] = size(Z_exp_test);

yfitPLS_test = [ones(n,1) Z_exp_test]*betaPLS;

yfitPLS_testval = [];

for i = 1:5
   yfitPLS_testval(i,:) = yfitPLS_test(i,:).*sigma+mu;
end


subplot(4,2,6)
```

```
hold on
axis([0 50 -5 105])
plot(SurvivalDays,yfitPLS_testval(1,:), 'Color', [0.80078125 0 0.80078125], 'LineWidth', 2)
plot(SurvivalDays,yfitPLS_testval(2,:), 'Color', [0 0 1], 'LineWidth', 2)
plot(SurvivalDays,yfitPLS_testval(3,:), 'Color', [0.59765625 0.28515625 0.03125], 'LineWidth', 2)
% Dark Orange
plot(SurvivalDays,yfitPLS_testval(4,:), 'Color', [0.89453125 0.42578125 0.04296875], 'LineWidth',
2) % Medium Orange
plot(SurvivalDays,yfitPLS_testval(5,:), 'Color', [0.98828125 0.8359375 0.7109375], 'LineWidth',
2) % Light Orange
%legend('CTRL','LCF','100 kPa', '10 kPa', '1 kPa')
title('No IL8')
xlabel('Days post-irradiation','FontWeight','bold')
ylabel('Survival Proportion (%)','FontWeight','bold')
hold off

% No Expression of RANTES

All_exp_test = xlsread('2.25.18 - Evaluating PLSR.xlsx','No RANTES','B2:AJ6');
Z_exp_test = zscore(All_exp_test);

[n,p] = size(Z_exp_test);

yfitPLS_test = [ones(n,1) Z_exp_test]*betaPLS;

yfitPLS_testval = [];

for i = 1:5
   yfitPLS_testval(i,:) = yfitPLS_test(i,:).*sigma+mu;
end


subplot(4,2,7)
hold on
axis([0 50 -5 105])
plot(SurvivalDays,yfitPLS_testval(1,:), 'Color', [0.80078125 0 0.80078125], 'LineWidth', 2)
plot(SurvivalDays,yfitPLS_testval(2,:), 'Color', [0 0 1], 'LineWidth', 2)
plot(SurvivalDays,yfitPLS_testval(3,:), 'Color', [0.59765625 0.28515625 0.03125], 'LineWidth', 2)
% Dark Orange
plot(SurvivalDays,yfitPLS_testval(4,:), 'Color', [0.89453125 0.42578125 0.04296875], 'LineWidth',
2) % Medium Orange
plot(SurvivalDays,yfitPLS_testval(5,:), 'Color', [0.98828125 0.8359375 0.7109375], 'LineWidth',
2) % Light Orange
%legend('CTRL','LCF','100 kPa', '10 kPa', '1 kPa')
title('No RANTES')
xlabel('Days post-irradiation','FontWeight','bold')
ylabel('Survival Proportion (%)','FontWeight','bold')
hold off

% No Expression of VEGFA

All_exp_test = xlsread('2.25.18 - Evaluating PLSR.xlsx','No VEGFA','B2:AJ6');
Z_exp_test = zscore(All_exp_test);
```

```
[n,p] = size(Z_exp_test);

yfitPLS_test = [ones(n,1) Z_exp_test]*betaPLS;

yfitPLS_testval = [];

for i = 1:5
   yfitPLS_testval(i,:) = yfitPLS_test(i,:).*sigma+mu;
end


subplot(4,2,8)
hold on
axis([0 50 -5 105])
plot(SurvivalDays,yfitPLS_testval(1,:), 'Color', [0.80078125 0 0.80078125], 'LineWidth', 2)
plot(SurvivalDays,yfitPLS_testval(2,:), 'Color', [0 0 1], 'LineWidth', 2)
plot(SurvivalDays,yfitPLS_testval(3,:), 'Color', [0.59765625 0.28515625 0.03125], 'LineWidth', 2)
% Dark Orange
plot(SurvivalDays,yfitPLS_testval(4,:), 'Color', [0.89453125 0.42578125 0.04296875], 'LineWidth',
2) % Medium Orange
plot(SurvivalDays,yfitPLS_testval(5,:), 'Color', [0.98828125 0.8359375 0.7109375], 'LineWidth',
2) % Light Orange
title('No VEGFA')
%legend('CTRL','LCF','100 kPa', '10 kPa', '1 kPa')
xlabel('Days post-irradiation','FontWeight','bold')
ylabel('Survival Proportion (%)','FontWeight','bold')
hold off
```

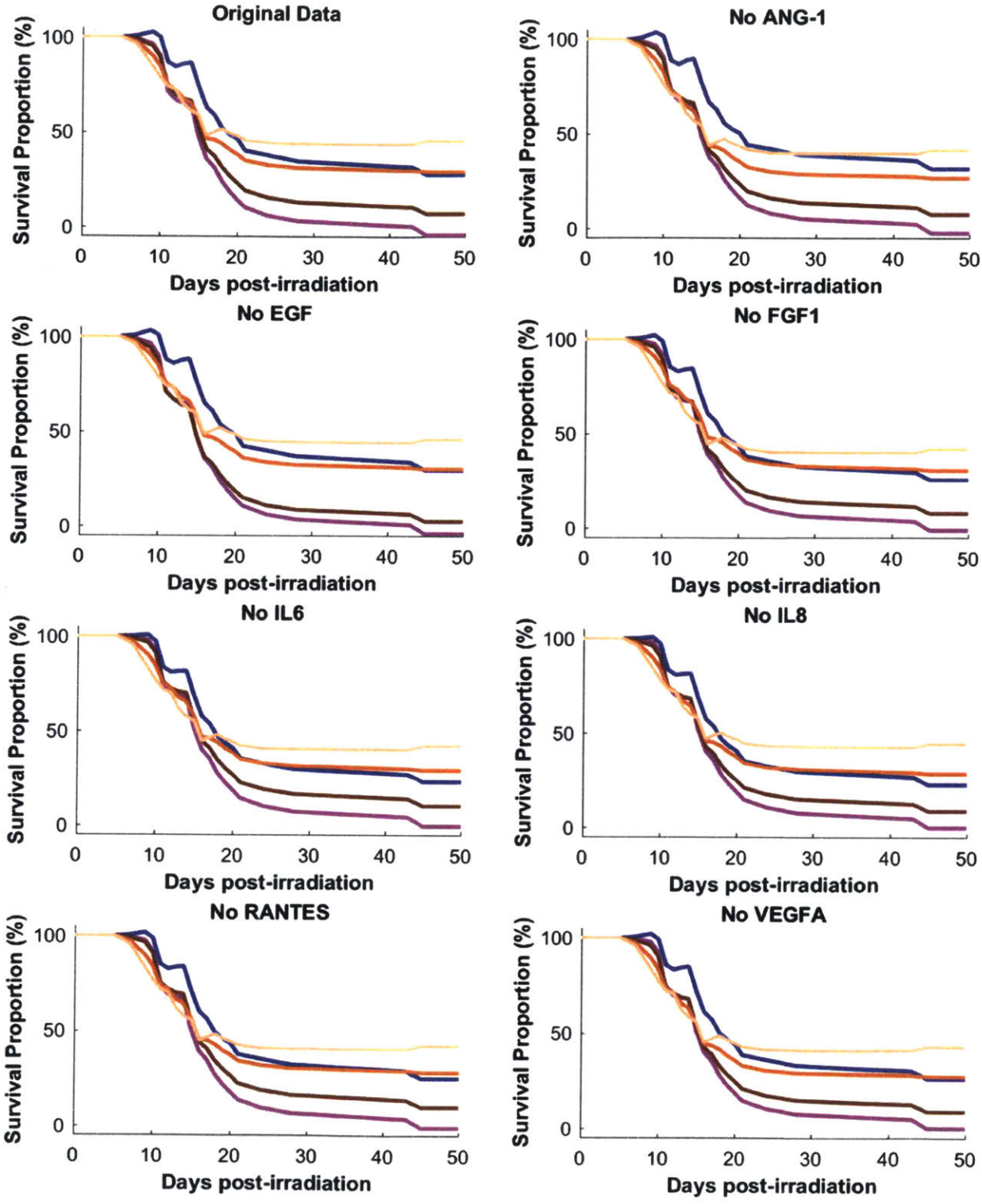
Original Data
No ANG-1
No EGF
No FGF1
No IL6
No IL8
No RANTES
No VEGFA
Survival Proportion (%)
Days post-irradiation
0
50
100
0
10
20
30
40
50

Re-Evaluating PLSR with ALL Key Secretome Components "knocked" out and BMP2

```
All_exp_test = xlsread('2.25.18 - Evaluating PLSR.xlsx','PL7 GrpAB no SCF','B2:AJ6');
Z_exp_test = zscore(All_exp_test);

[n,p] = size(Z_exp_test);

yfitPLS_test = [ones(n,1) Z_exp_test]*betaPLS;

yfitPLS_testval = [];

for i = 1:5
   yfitPLS_testval(i,:) = yfitPLS_test(i,:).*sigma+mu;
end

figure(22)

% Original Expression

subplot(3,1,1)
hold on
axis([0 50 -5 105])
plot(SurvivalDays,yfitPLS_testval(1,:), 'Color', [0.80078125 0 0.80078125], 'LineWidth', 2)
plot(SurvivalDays,yfitPLS_testval(2,:), 'Color', [0 0 1], 'LineWidth', 2)
plot(SurvivalDays,yfitPLS_testval(3,:), 'Color', [0.59765625 0.28515625 0.03125], 'LineWidth', 2)
% Dark Orange
plot(SurvivalDays,yfitPLS_testval(4,:), 'Color', [0.89453125 0.42578125 0.04296875], 'LineWidth',
2) % Medium Orange
plot(SurvivalDays,yfitPLS_testval(5,:), 'Color', [0.98828125 0.8359375 0.7109375], 'LineWidth',
2) % Light Orange
%legend('CTRL','LCF','100 kPa', '10 kPa', '1 kPa')
title('Original Data')
xlabel('Days post-irradiation','FontWeight','bold')
ylabel('Survival Proportion (%)','FontWeight','bold')
hold off

% No Expression of Key Components

All_exp_test = xlsread('2.25.18 - Evaluating PLSR.xlsx','KO All','B2:AJ6');
Z_exp_test = zscore(All_exp_test);

[n,p] = size(Z_exp_test);

yfitPLS_test = [ones(n,1) Z_exp_test]*betaPLS;

yfitPLS_testval = [];

for i = 1:5
   yfitPLS_testval(i,:) = yfitPLS_test(i,:).*sigma+mu;
end


subplot(3,1,2)
```

```
hold on
axis([0 50 -5 105])
plot(SurvivalDays,yfitPLS_testval(1,:), 'Color', [0.80078125 0 0.80078125], 'LineWidth', 2)
plot(SurvivalDays,yfitPLS_testval(2,:), 'Color', [0 0 1], 'LineWidth', 2)
plot(SurvivalDays,yfitPLS_testval(3,:), 'Color', [0.59765625 0.28515625 0.03125], 'LineWidth', 2)
% Dark Orange
plot(SurvivalDays,yfitPLS_testval(4,:), 'Color', [0.89453125 0.42578125 0.04296875], 'LineWidth',
2) % Medium Orange
plot(SurvivalDays,yfitPLS_testval(5,:), 'Color', [0.98828125 0.8359375 0.7109375], 'LineWidth',
2) % Light Orange
%legend('CTRL','LCF','100 kPa', '10 kPa', '1 kPa')
title('All KO')
xlabel('Days post-irradiation','FontWeight','bold')
ylabel('Survival Proportion (%)','FontWeight','bold')
hold off

% Added Expression of BMP2

All_exp_test = xlsread('2.25.18 - Evaluating PLSR.xlsx','BMP2','B2:AJ6');
Z_exp_test = zscore(All_exp_test);

[n,p] = size(Z_exp_test);

yfitPLS_test = [ones(n,1) Z_exp_test]*betaPLS;

yfitPLS_testval = [];

for i = 1:5
   yfitPLS_testval(i,:) = yfitPLS_test(i,:).*sigma+mu;
end


subplot(3,1,3)
hold on
axis([0 50 -5 105])
plot(SurvivalDays,yfitPLS_testval(1,:), 'Color', [0.80078125 0 0.80078125], 'LineWidth', 2)
plot(SurvivalDays,yfitPLS_testval(2,:), 'Color', [0 0 1], 'LineWidth', 2)
plot(SurvivalDays,yfitPLS_testval(3,:), 'Color', [0.59765625 0.28515625 0.03125], 'LineWidth', 2)
% Dark Orange
plot(SurvivalDays,yfitPLS_testval(4,:), 'Color', [0.89453125 0.42578125 0.04296875], 'LineWidth',
2) % Medium Orange
plot(SurvivalDays,yfitPLS_testval(5,:), 'Color', [0.98828125 0.8359375 0.7109375], 'LineWidth',
2) % Light Orange
title('BMP2 Added')
%legend('CTRL','LCF','100 kPa', '10 kPa', '1 kPa')
xlabel('Days post-irradiation','FontWeight','bold')
ylabel('Survival Proportion (%)','FontWeight','bold')
hold off
```

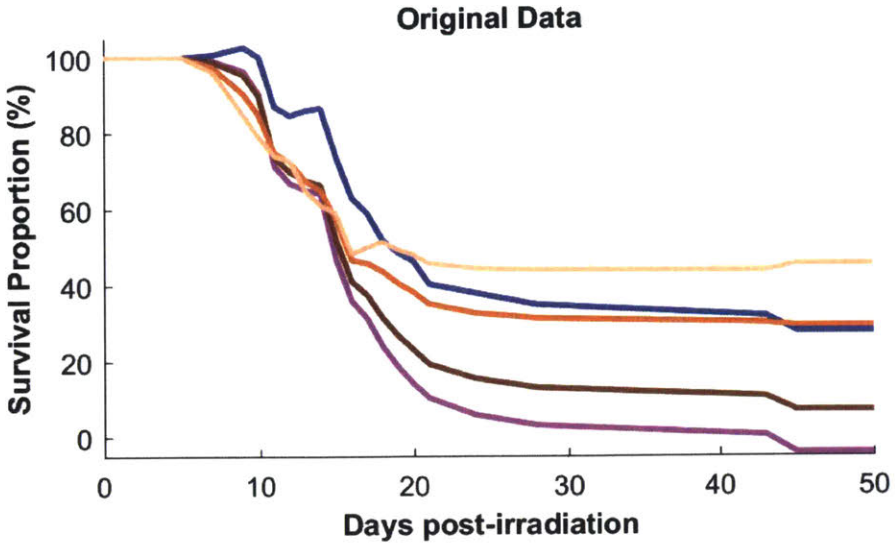
Original Data
Survival Proportion (%)
100
80
60
40
20
0
0
10
20
30
40
50
Days post-irradiation

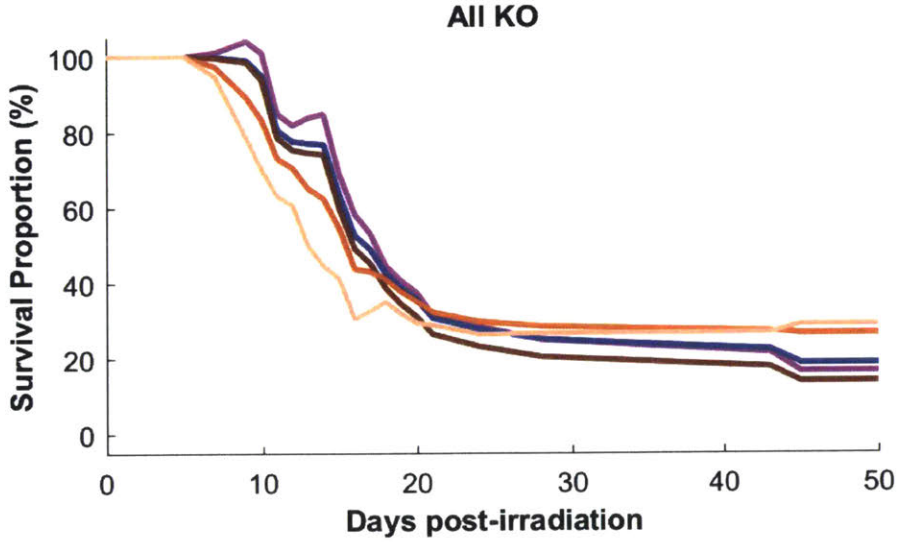
All KO
Survival Proportion (%)
100
80
60
40
20
0
0
10
20
30
40
50
Days post-irradiation

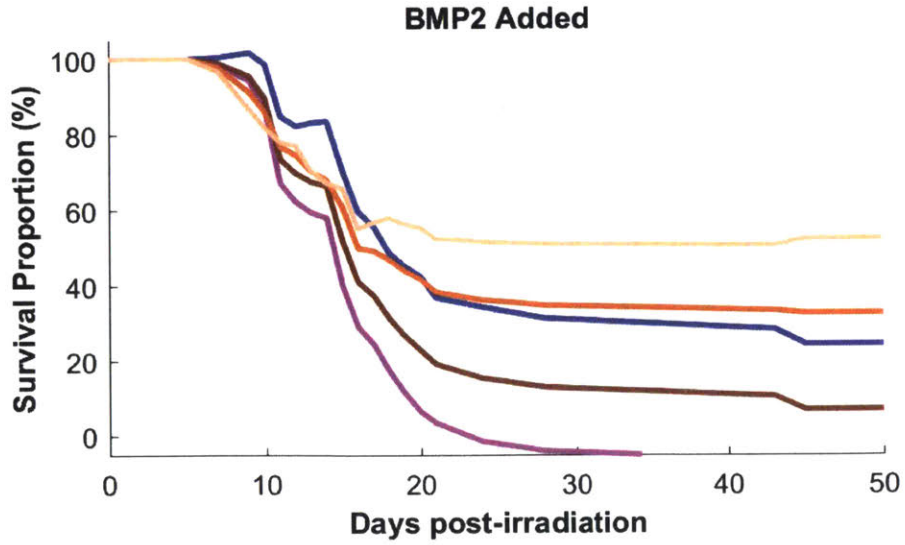
BMP2 Added
Survival Proportion (%)
100
80
60
40
20
0
0
10
20
30
40
50
Days post-irradiation

Re-Evaluating PLSR with Key Secretome Components Added one at a time

```
% Subplot 1 contains data for ANG1 expression ONLY
All_exp_test = xlsread('2.25.18 - Evaluating PLSR 2.xlsx','ANG1','B2:AJ6');
Z_exp_test = zscore(All_exp_test);

[n,p] = size(Z_exp_test);

yfitPLS_test = [ones(n,1) Z_exp_test]*betaPLS;

yfitPLS_testval = [];

for i = 1:5
   yfitPLS_testval(i,:) = yfitPLS_test(i,:).*sigma+mu;
end
figure(23)

subplot(4,2,1)

plot(SurvivalDays, yfitPLS_testval, 'LineWidth',2)
axis([0 50 -5 105])
%legend('1x Concentration','2x Concentration','3x Concentration', '4x Concentration', '5x
Concentration')
xlabel('Time (days)','FontWeight','bold')
ylabel('Survival Proportion (%)','FontWeight','bold')
title('ANG1')

% Subplot 2 contains data for BMP2 expression ONLY
All_exp_test = xlsread('2.25.18 - Evaluating PLSR 2.xlsx','BMP2','B2:AJ6');
Z_exp_test = zscore(All_exp_test);

[n,p] = size(Z_exp_test);

yfitPLS_test = [ones(n,1) Z_exp_test]*betaPLS;

yfitPLS_testval = [];

for i = 1:5
   yfitPLS_testval(i,:) = yfitPLS_test(i,:).*sigma+mu;
end
figure(23)

subplot(4,2,2)

plot(SurvivalDays, yfitPLS_testval, 'LineWidth',2)
axis([0 50 -5 105])
%legend('1x Concentration','2x Concentration','3x Concentration', '4x Concentration', '5x
Concentration')
xlabel('Time (days)','FontWeight','bold')
ylabel('Survival Proportion (%)','FontWeight','bold')
title('BMP2')
```

```
% Subplot 3 contains data for EGF expression ONLY
All_exp_test = xlsread('2.25.18 - Evaluating PLSR 2.xlsx','EGF','B2:AJ6');
Z_exp_test = zscore(All_exp_test);

[n,p] = size(Z_exp_test);

yfitPLS_test = [ones(n,1) Z_exp_test]*betaPLS;

yfitPLS_testval = [];

for i = 1:5
   yfitPLS_testval(i,:) = yfitPLS_test(i,:).*sigma+mu;
end
figure(23)

subplot(4,2,3)

plot(SurvivalDays, yfitPLS_testval, 'LineWidth',2)
axis([0 50 -5 105])
%legend('1x Concentration','2x Concentration','3x Concentration', '4x Concentration', '5x
Concentration')
xlabel('Time (days)','FontWeight','bold')
ylabel('Survival Proportion (%)','FontWeight','bold')
title('EGF')

% Subplot 4 contains data for FGF1 expression ONLY
All_exp_test = xlsread('2.25.18 - Evaluating PLSR 2.xlsx','FGF1','B2:AJ6');
Z_exp_test = zscore(All_exp_test);

[n,p] = size(Z_exp_test);

yfitPLS_test = [ones(n,1) Z_exp_test]*betaPLS;

yfitPLS_testval = [];

for i = 1:5
   yfitPLS_testval(i,:) = yfitPLS_test(i,:).*sigma+mu;
end
figure(23)

subplot(4,2,4)

plot(SurvivalDays, yfitPLS_testval, 'LineWidth',2)
axis([0 50 -5 105])
%legend('1x Concentration','2x Concentration','3x Concentration', '4x Concentration', '5x
Concentration')
xlabel('Time (days)','FontWeight','bold')
ylabel('Survival Proportion (%)','FontWeight','bold')
title('FGF1')

% Subplot 5 contains data for IL6 expression ONLY
All_exp_test = xlsread('2.25.18 - Evaluating PLSR 2.xlsx','IL6','B2:AJ6');
Z_exp_test = zscore(All_exp_test);
```

```
[n,p] = size(Z_exp_test);

yfitPLS_test = [ones(n,1) Z_exp_test]*betaPLS;

yfitPLS_testval = [];

for i = 1:5
   yfitPLS_testval(i,:) = yfitPLS_test(i,:).*sigma+mu;
end
figure(23)

subplot(4,2,5)

plot(SurvivalDays, yfitPLS_testval, 'LineWidth',2)
axis([0 50 -5 105])
%legend('1x Concentration','2x Concentration','3x Concentration', '4x Concentration', '5x
Concentration')
xlabel('Time (days)','FontWeight','bold')
ylabel('Survival Proportion (%)','FontWeight','bold')
title('IL6')

% Subplot 6 contains data for IL8 expression ONLY
All_exp_test = xlsread('2.25.18 - Evaluating PLSR 2.xlsx','IL8','B2:AJ6');
Z_exp_test = zscore(All_exp_test);

[n,p] = size(Z_exp_test);

yfitPLS_test = [ones(n,1) Z_exp_test]*betaPLS;

yfitPLS_testval = [];

for i = 1:5
   yfitPLS_testval(i,:) = yfitPLS_test(i,:).*sigma+mu;
end
figure(23)

subplot(4,2,6)

plot(SurvivalDays, yfitPLS_testval, 'LineWidth',2)
axis([0 50 -5 105])
%legend('1x Concentration','2x Concentration','3x Concentration', '4x Concentration', '5x
Concentration')
xlabel('Time (days)','FontWeight','bold')
ylabel('Survival Proportion (%)','FontWeight','bold')
title('IL8')

% Subplot 7 contains data for RANTES expression ONLY
All_exp_test = xlsread('2.25.18 - Evaluating PLSR 2.xlsx','RANTES','B2:AJ6');
Z_exp_test = zscore(All_exp_test);

[n,p] = size(Z_exp_test);

yfitPLS_test = [ones(n,1) Z_exp_test]*betaPLS;
```

```
yfitPLS_testval = [];

for i = 1:5
   yfitPLS_testval(i,:) = yfitPLS_test(i,:).*sigma+mu;
end
figure(23)

subplot(4,2,7)

plot(SurvivalDays, yfitPLS_testval, 'LineWidth',2)
axis([0 50 -5 105])
%legend('1x Concentration','2x Concentration','3x Concentration', '4x Concentration', '5x
Concentration')
xlabel('Time (days)','FontWeight','bold')
ylabel('Survival Proportion (%)','FontWeight','bold')
title('RANTES')

% Subplot 8 contains data for VEGFA expression ONLY
All_exp_test = xlsread('2.25.18 - Evaluating PLSR 2.xlsx','VEGFA','B2:AJ6');
Z_exp_test = zscore(All_exp_test);

[n,p] = size(Z_exp_test);

yfitPLS_test = [ones(n,1) Z_exp_test]*betaPLS;

yfitPLS_testval = [];

for i = 1:5
   yfitPLS_testval(i,:) = yfitPLS_test(i,:).*sigma+mu;
end
figure(23)

subplot(4,2,8)

plot(SurvivalDays, yfitPLS_testval, 'LineWidth',2)
axis([0 50 -5 105])
%legend('1x Concentration','2x Concentration','3x Concentration', '4x Concentration', '5x
Concentration') % un-comment to show legend
xlabel('Time (days)','FontWeight','bold')
ylabel('Survival Proportion (%)','FontWeight','bold')
title('VEGFA')
```

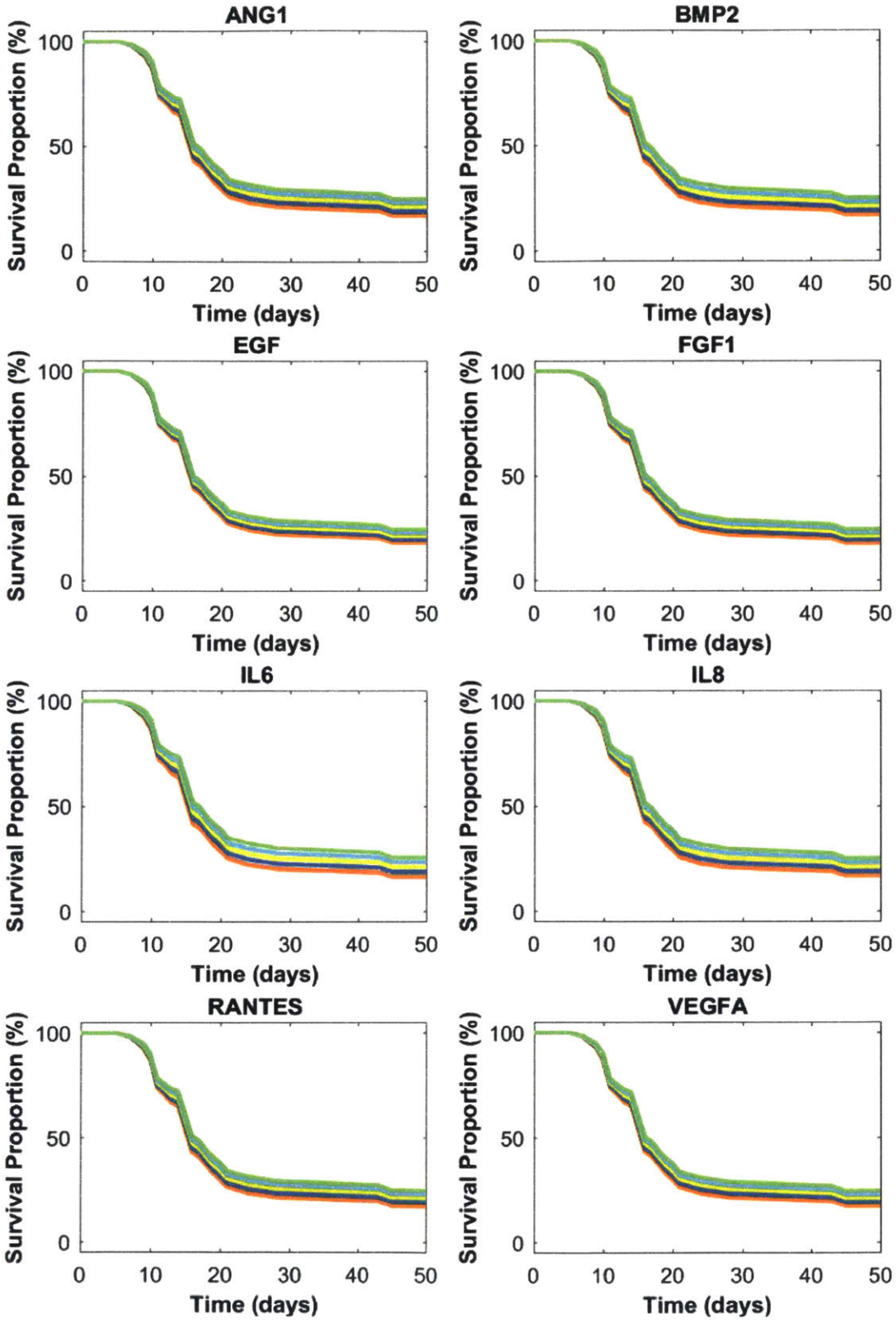

Published with MATLAB® R2015b

Bibliography

[1] Majhail N S, Rizzo J D, Lee S J, Aljurf M, Atsuta Y, Burns L J, Chaudhri N, Davies S, Okamoto S and Seber A 2012 Recommended Screening and Preventive Practices for Long-Term Survivors after Hematopoietic Cell Transplantation *Hematol. Oncol. Stem Cell Ther.* **5**

[2] Hatzimichael E and Tuthill M 2010 Hematopoietic stem cell transplantation *Stem Cells Cloning Adv. Appl.* **3** 105–17

[3] Copelan E A 2006 Hematopoietic Stem-Cell Transplantation *N Engl J Med* 354:1813-1826

[4] Shizuru J A, Negrin R S and Weissman I L 2005 Hematopoietic Stem and Progenitor Cells: Clinical and Preclinical Regeneration of the Hematolymphoid System *Annu. Rev. Med.* **56** 509–38

[5] Fruchtman S 2003 Stem Cell Transplantation *Mt. Sinai J. Med.* **70** 166–70

[6] Anon 2017 FDA Warns About Stem Cell Therapies 1–4

[7] Podestà M 2001 Transplantation hematopoiesis *Curr. Opin. Hematol.* **8** 331–6

[8] Alcorn M J, Holyoake T L, Richmond L, Pearson C, Farrell E, Kyle B, Dunlop D J, Fitzsimons E, Steward W P, Pragnell I B and Franklin I M 1996 CD34-Positive Cells Isolated from Cryopreserved Peripheral-Blood Progenitor Cells Can Be Expanded Ex Vivo and Used for Transplantation with Little or No Toxicity *J. Clin. Oncol.* **14** 1839–47

[9] Gupta V, Lazarus H M and Keating A 2003 Myeloablative conditioning regimens for AML allografts: 30 years later. *Bone Marrow Transplant.* **32** 969–78

[10] Bacigalupo A, Ballen K, Rizzo D, Giralt S, Lazarus H, Apperley J, Slavin S, Pasquini M and Sandmaier B M 2010 Defining the Intensity of Conditioning Regimens: working definitions *Biol. Blood Marrow Transplant.* **15** 1628–33

[11] Gyurkocza B and Sandmaier B M 2017 Conditioning regimens for hematopoietic cell transplantation : one size does not fi t all *Blood* **124** 344–54

[12] Oliansky D M, Larson R A, Weisdorf D, Dillon H, Ratko T A, Wall D, McCarthy P L and Hahn T 2012 The Role of Cytotoxic Therapy with Hematopoietic Stem Cell Transplantation in the Treatment of Adult Acute Lymphoblastic Leukemia: Update of the 2006 Evidence-Based Review *Biol. Blood Marrow Transplant.* **18**

[13] Awaya N, Rupert K, Bryant E and Torok-storb B 2002 Failure of adult marrow-derived stem cells to generate marrow stroma after successful hematopoietic stem cell transplantation *Exp. Hematol.* **30** 937–42

[14] Abrahamsen I W, Sømme S, Heldal D, Egeland T, Kvale D and Tjønnfjord G E 2005 Immune reconstitution after allogeneic stem cell transplantation: the impact of stem cell source and graft-versus-host disease *Haematologica* **90** 86–93

[15] van den Brink M R M and Burakoff S J 2002 Cytolytic pathways in haematopoietic stem-cell transplantation. *Nat. Rev. Immunol.* **2** 273–81

[16] Slavin S, Nagler A, Naparstek E, Kapelushnik Y, Aker M, Cividalli G, Varadi G, Kirschbaum M, Ackerstein A, Samuel S, Amar A, Brautbar C, Ben-tal O, Eldor A and Or R 1998 Nonmyeloablative Stem Cell Transplantation and Cell Therapy as an Alternative to Conventional Bone Marrow Transplantation With Lethal Cytoreduction for the Treatment of Malignant and Nonmalignant Hematologic Diseases *Blood* **91** 756–63

[17] Mattsson J, Ringdén O and Storb R 2008 Graft Failure after Allogeneic Hematopoietic Cell Transplantation. *Biol. blood marrow Transplant.* **14** 165–70

[18] Corre E, Carmagnat M, Busson M, Latour R P De, Robin M, Ribaud P, Toubert A, Rabian C and Socié G 2010 Long-term immune deficiency after allogeneic stem cell transplantation : B-cell deficiency is associated with late infections *Haematologica* **95** 1025–9

[19] Kong Y, Chang Y-J, Wang Y-Z, Chen Y-H, Han W, Wang Y, Sun Y-Q, Yan C-H, Wang F-R, Liu Y-R, Xu L-P, Liu D-H and Huang X-J 2013 Association of an Impaired Bone Marrow Microenvironment with Secondary Poor Graft Function after Allogeneic Hematopoietic Stem Cell Transplantation *Biol. Blood Marrow Transplant.* **19** 1465–73

[20] Peled A, Kollet O, Ponomaryov T, Petit I, Franitza S, Grabovsky V, Slav M M, Nagler A, Lider O, Alon R, Zipori D and Lapidot T 2000 The chemokine SDF-1 activates the integrins LFA-1 , VLA-4 , and VLA-5 on immature human CD34+ cells : role in transendothelial / stromal migration and engraftment of NOD / SCID mice *Blood* **95** 3289–96

[21] Marubini F, Davies P S, Wilkerson F P, Kobayashi D, Muscatine L, Peled A, Petit I, Kollet O, Magid M, Ponomaryov T, Byk T, Nagler A, Ben-hur H, Many A, Shultz L and Lider O 1999 Dependence of Human Stem Cell Engraftment and Repopulation of NOD / SCID Mice on CXCR4 **283** 845–9

[22] Van Overstraeten-Schlogel N, Beguin Y and Gothot A 2006 Role of stromal-derived factor-1 in the hematopoietic-supporting activity of human mesenchymal stem cells *Eur. J. Haematol.* 488–93

[23] Liang X, Su Y, Kong P, Zeng D and Chen X 2010 Human bone marrow mesenchymal stem cells expressing SDF-1 promote hematopoietic stem cell function of human mobilised peripheral blood CD34 cells in vivo and in vitro *Int. J. Radiat. Biol.* **86** 230–7

[24] Winkler I G, Barbier V, Nowlan B, Jacobsen R N, Forristal C E, Patton J T, Magnani J L and Lévesque J 2012 Vascular niche E-selectin regulates hematopoietic stem cell dormancy , self renewal and chemoresistance *Nat. Med.* **18**

[25] Greenberg A W, Kerr W G and Hammer D A 2000 Relationship between selectin-mediated rolling of hematopoietic stem and progenitor cells and progression in

hematopoietic development *Blood* **95** 478–87

[26] Adams G B and Scadden D T 2006 The hematopoietic stem cell in its place *Nat. Immunol.* **7** 333–7

[27] Wilson A and Trumpp A 2006 Bone-marrow haematopoietic-stem-cell niches *Nat. Rev. Immunol.* **6** 93–106

[28] Morrison S J and Scadden D T 2014 The bone marrow niche for haematopoietic stem cells *Nature* **505** 327–34

[29] Nilsson S K, Johnston H M and Coverdale J A 2001 Spatial localization of transplanted hemopoietic stem cells : inferences for the localization of stem cell niches *Blood* **97** 2293–300

[30] Boulais P E and Frenette P S 2015 Making sense of hematopoietic stem cell niches *Blood* **125** 2621–30

[31] Ellis S L, Grassinger J, Jones A, Borg J, Camenisch T, Haylock D, Bertoncello I and Nilsson S K 2011 The relationship between bone , hemopoietic stem cells , and vasculature *Blood* **118** 1–3

[32] Kiel M J, Yilmaz O H, Iwashita T, Yilmaz O H, Terhorst C and Morrison S J 2005 SLAM family receptors distinguish hematopoietic stem and progenitor cells and reveal endothelial niches for stem cells *Cell* **121** 1109–21

[33] Sugiyama T, Kohara H and Noda M 2006 Maintenance of the Hematopoietic Stem Cell Pool by CXCL12-CXCR4 Chemokine Signaling in Bone Marrow Stromal Cell Niches *Immunity* **25** 977–88

[34] Taichman R S and Emerson S G 1998 The role of osteoblasts in the hematopoietic microenvironment. *Stem Cells* **16** 7–15

[35] Zhang J, Niu C, Ye L, Huang H, He X, Harris S, Wiedemann L M, Mishina Y and Li L 2003 Identification of the haematopoietic stem cell niche and control of the niche size *Nature* **425** 836–40

[36] Calvi L M, Adams G B, Weibrecht K W, Weber J M, Olson D P, Knight M C, Martin R P, Schipani E, Divieti P, Bringhurst F R, Milner L A, Kronenberg H M and Scadden D T 2003 Osteoblastic cells regulate the haematopoietic stem cell niche *Nature* **425** 841–6

[37] Li W, Johnson S A, Shelley W C and Yoder M C 2004 Hematopoietic stem cell repopulating ability can be maintained in vitro by some primary endothelial cells *Exp. Hematol.* **32** 1226–37

[38] Montfort M J, Olivares C R, Mulcahy J M and Fleming W H 2002 Adult blood vessels restore host hematopoiesis following lethal irradiation *Exp. Hematol.* **30** 950–6

[39] Li B, Bailey A S, Jiang S, Liu B, Goldman D C and Fleming W H 2010 Endothelial cells mediate the regeneration of hematopoietic stem cells *Stem Cell Res.* **4** 17–24

[40] Hooper A T, Butler J M, Nolan D J, Kranz A, Iida K, Kobayashi M, Kopp H, Shido K, Petit I, Yanger K, James D, Witte L, Zhu Z, Wu Y, Pytowski B, Rosenwaks Z, Mittal V

and Sato T N 2009 Engraftment and Reconstitution of Hematopoiesis Is Dependent on VEGFR2-Mediated Regeneration of Sinusoidal Endothelial Cells *Cell Stem Cell* **4** 263–74

[41] Butler J M, Nolan D J, Vertes E L, Varnum-finney B, Kobayashi H, Hooper A T, Seandel M, Shido K, White I A, Kobayashi M, Witte L, May C, Shawber C, Kimura Y, Kitajewski J, Rosenwaks Z, Bernstein I D and Rafii S 2010 Endothelial Cells Are Essential for the Self-Renewal and Repopulation of Notch-Dependent Hematopoietic Stem Cells *Cell Stem Cell* **6** 251–64

[42] Kobayashi H, Butler J M, Donnell R O, Kobayashi M, Ding B, Bonner B, Chiu V K, Nolan D J, Shido K, Benjamin L and Rafii S 2010 Angiocrine factors from Akt-activated endothelial cells balance self-renewal and differentiation of haematopoietic stem cells *Nat. Cell Biol.* **12**

[43] Doan P L, Himburg H A, Helms K, Russell J L, Fixsen E, Quarmyne M, Harris J R, Deoliviera D, Sullivan J M, Chao N J, Kirsch D G and Chute J P 2013 Epidermal growth factor regulates hematopoietic regeneration after radiation injury *Nat. Med.* **19** 295–304

[44] Arai F, Hirao A, Ohmura M, Sato H, Matsuoka S, Takubo K, Ito K, Koh G Y and Suda T 2004 Tie2 / Angiopoietin-1 Signaling Regulates Hematopoietic Stem Cell Quiescence in the Bone Marrow Niche *Cell* **118** 149–61

[45] Caplan A I 1991 Mesenchymal stem cells. *J. Orthop. Res.* **9** 641–50

[46] Pittenger M F, Mackay A M, Beck S C, Jaiswal R K, Douglas R, Mosca J D, Moorman M A, Simonetti D W, Craig S and Marshak D R 1999 Multilineage Potential of Adult Human Mesenchymal Stem Cells *Science (80-.).* **284** 143–7

[47] Caplan A I 2008 All MSCs Are Pericytes? *Cell Stem Cell* 229–30

[48] Cano E, Gebala V and Gerhardt H 2017 Pericytes or Mesenchymal Stem Cells : Is That the Question ? *Cell Stem Cell* 296–7

[49] Guimaraes-Camboa N, Cattaneo P, Sun Y, Moore-Morris T, Gu Y, Dalton N D, Rockenstein E, Masliah E, Peterson K L, Stallcup W B, Chen J and Evans S M 2017 Pericytes of Multiple Organs Do Not Behave as Mesenchymal Stem Cells In Vivo *Cell Stem Cell* 345–59

[50] Frenette P S, Pinho S, Lucas D and Scheiermann C 2013 Mesenchymal Stem Cell : Keystone of the Hematopoietic Stem Cell Niche and a Stepping-Stone for Regenerative Medicine *Annu. Rev. Immunol.* 285–318

[51] Sacchetti B, Funari A, Michienzi S, Di Cesare S, Piersanti S, Saggio I, Tagliafico E, Ferrari S, Robey P G, Riminucci M and Bianco P 2007 Self-Renewing Osteoprogenitors in Bone Marrow Sinusoids Can Organize a Hematopoietic Microenvironment *Cell* **131** 324–36

[52] Chan C K F, Chen C, Luppen C A, Kim J, Deboer A T, Wei K, Helms J A, Kuo C J, Kraft D L and Weissman I L 2009 Endochondral ossification is required for haematopoietic stem-cell niche formation *Nature* **457** 490–5

[53] Greenbaum A, Hsu Y S, Day R B, Schuettpelz L G, Christopher M J, Borgerding J N,

Nagasawa T and Link D C 2013 CXCL12 in early mesenchymal progenitors is required for haematopoietic stem-cell maintenance *Nature* **495** 227–30

[54] Omatsu Y, Sugiyama T, Kohara H, Kondoh G, Fujii N and Kohno K 2010 The Essential Functions of Adipo-osteogenic Progenitors as the Hematopoietic Stem and Progenitor Cell Niche *Immunity* **33** 387–99

[55] Lee-Thedieck C and Spatz J P 2014 Biophysical regulation of hematopoietic stem cells *Biomater. Sci.* **2** 1548–61

[56] Rennerfeldt D A and Vliet K J Van 2016 Concise Review : When colonies are not clones: evidence and implications of intracolony heterogeneity in mesencyhmal stem cells *Stem Cells* **34** 1135–41

[57] Whitfield M J, Lee W C J and Van Vliet K J 2013 Onset of heterogeneity in culture-expanded bone marrow stromal cells. *Stem Cell Res.* **11** 1365–77

[58] Prockop D J 2009 Repair of tissues by adult stem/progenitor cells (MSCs): controversies, myths, and changing paradigms. *Mol. Ther.* **17** 939–46

[59] Hoch A I and Leach J K 2014 Concise review: optimizing expansion of bone marrow mesenchymal stem/stromal cells for clinical applications. *Stem Cells Transl. Med.* **3** 643–52

[60] Dominici M, Le Blanc K, Mueller I, Slaper-Cortenbach I, Marini F, Krause D, Deans R, Keating a, Prockop D and Horwitz E 2006 Minimal criteria for defining multipotent mesenchymal stromal cells. The International Society for Cellular Therapy position statement. *Cytotherapy* **8** 315–7

[61] Lee W C, Shi H, Poon Z, Nyan L M, Kaushik T, Shivashankar G V., Chan J K Y, Lim C T, Han J and Van Vliet K J 2014 Multivariate biophysical markers predictive of mesenchymal stromal cell multipotency *Proc. Natl. Acad. Sci.*

[62] Morikawa S, Mabuchi Y, Kubota Y, Nagai Y, Niibe K, Hiratsu E, Suzuki S, Miyauchi-hara C, Nagoshi N, Sunabori T, Shimmura S, Miyawaki A and Nakagawa T 2009 Prospective identification , isolation , and systemic transplantation of multipotent mesenchymal stem cells in murine bone marrow **206** 2483–96

[63] Chen C, Loe F, Blocki A, Peng Y and Raghunath M 2011 Applying macromolecular crowding to enhance extracellular matrix deposition and its remodeling in vitro for tissue engineering and cell-based therapies. *Adv. Drug Deliv. Rev.* **63** 277–90

[64] Prewitz M C, Stißel A, Friedrichs J, Traber N, Vogler S, Bornhauser M and Werner C 2015 Extracellular matrix deposition of bone marrow stroma enhanced by macromolecular crowding *Biomaterials* **73** 60–9

[65] Minton A P 2001 The influence of macromolecular crowding and macromolecular confinement on biochemical reactions in physiological media. *J. Biol. Chem.* **276** 10577–80

[66] van den Berg B, Wain R, Dobson C M and Ellis R J 2000 Macromolecular crowding perturbs protein refolding kinetics: implications for folding inside the cell. *EMBO J.* **19**

3870–5

[67] Ellis R J 2001 Macromolecular crowding: an important but neglected aspect of the intracellular environment. *Curr. Opin. Struct. Biol.* **11** 114–9

[68] Zeiger A S, Loe F C, Li R, Raghunath M and Van Vliet K J 2012 Macromolecular crowding directs extracellular matrix organization and mesenchymal stem cell behavior. *PLoS One* **7** e37904

[69] Tuan R S, Boland G and Tuli R 2003 Adult mesenchymal stem cells and cell-based tissue engineering *Arthritis Res. Ther.* **5**

[70] Caplan A I 2007 Adult Mesenchymal Stem Cells for Tissue Engineering Versus Regenerative Medicine *J. Cell. Physiol.* 341–7

[71] Engler A J, Sen S, Sweeney H L and Discher D E 2006 Matrix Elasticity Directs Stem Cell Lineage Specification 677–89

[72] Uccelli A, Moretta L and Pistoia V 2008 Mesenchymal stem cells in health and disease. *Nat. Rev. Immunol.* **8** 726–36

[73] Dalby M J, Gadegaard N and Oreffo R O C 2014 Harnessing nanotopography and integrin-matrix interactions to influence stem cell fate. *Nat. Mater.* **13** 558–69

[74] Huebsch N, Arany P R, Mao A S, Shvartsman D, Ali O A, Bencherif S A, Rivera-feliciano J and Mooney D J 2010 Harnessing traction-mediated manipulation of the cell / matrix interface to control stem-cell fate *Nat. Mater.* **9** 518–26

[75] Rowlands A S, George P a and Cooper-White J J 2008 Directing osteogenic and myogenic differentiation of MSCs: interplay of stiffness and adhesive ligand presentation. *Am. J. Physiol. Cell Physiol.* **295** C1037-44

[76] Cavalcanti-Adam E A, Volberg T, Micoulet A, Kessler H, Geiger B and Spatz J P 2007 Cell Spreading and Focal Adhesion Dynamics Are Regulated by Spacing of Integrin Ligands *Biophys. J.* **92** 2964–74

[77] Fu J, Wang Y, Yang M T, Desai R A, Yu X, Liu Z and Chen C S 2011 Mechanical regulation of cell function with geometrically modulated elastomeric substrates **7**

[78] Trappmann B, Gautrot J E, Connelly J T, Strange D G T, Li Y, Oyen M L, Cohen Stuart M a, Boehm H, Li B, Vogel V, Spatz J P, Watt F M and Huck W T S 2012 Extracellular-matrix tethering regulates stem-cell fate. *Nat. Mater.* **11** 642–9

[79] Wen J H, Vincent L G, Fuhrmann A, Choi Y S, Hribar K C, Taylor-weiner H, Chen S and Engler A J 2014 Interplay of matrix stiffness and protein tethering in stem cell differentiation *Nat. Mater.* **13** 979–87

[80] Huebsch N, Lippens E, Lee K, Mehta M, Koshy S T, Darnell M C, Desai R, Madl C M, Xu M, Zhao X, Chaudhuri O, Verbeke C, Kim W S and Alim K 2015 Matrix elasticity of void-forming hydrogels controls Transplanted Stem Cell-Mediated bone **14** 1–19

[81] Jansen L E, Birch N P, Schiffman J D, Crosby A J and Peyton S R 2015 Mechanics of intact bone marrow *J. Mech. Behav. Biomed. Mater.* **50** 299–307

[82] Chaudhuri O, Gu L, Klumpers D, Darnell M, Bencherif S A, Weaver J C, Huebsch N, Lee H-P, Lippens E, Duda G N and Mooney D J 2016 Hydrogels with tunable stress relaxation regulate stem cell fate and activity. *Nat. Mater.* **15** 326–33

[83] Yang C, Tibbitt M W, Basta L and Anseth K S 2014 Mechanical memory and dosing influence stem cell fate *Nat. Mater.* **13** 645–52

[84] Overstraeten-Schlogel N Van, Beguin Y, Gothot A, Van Overstraeten-Schlogel, N Beguin Y and Gothot A 2006 Role of stromal-derived factor-1 in the hematopoietic-supporting activity of human mesenchymal stem cells *Eur. J. Haematol.* **76** 488–93

[85] El-Badri N S, Wang B Y, Cherry and Good R A 1998 Osteoblasts promote engraftment of allogeneic hematopoietic stem cells. *Exp. Hematol.* **26** 110–6

[86] Majumdar M K, Thiede M A, Haynesworth S E, Bruder S P and Gerson S L 2000 Human Marrow-Derived Mesenchymal Stem Cells (MSCs) Express Hematopoietic Cytokines and Support Long-Term Hematopoiesis When Differentiated Toward Stromal and Osteogenic Lineages *J. Hematother. Stem Cell Res.* **9** 841–8

[87] Qazi T H, Mooney D J, Duda G N and Geissler S 2017 Biomaterials that promote cell-cell interactions enhance the paracrine function of MSCs *Biomaterials* **140** 103–14

[88] KASPER G, DANKERT N, TUISCHER J, HOEFT M, GABER T, GLAESER J D, ZANDER D, TSCHIRSCHMANN M, THOMPSON M, MATZIOLIS G and DUDA G N 2007 Mesenchymal Stem Cells Regulate Angiogenesis According to Their Mechanical Environment *Stem Cells* **25**

[89] Abdeen A A, Weiss J B, Lee J and Kilian K A 2014 Matrix Composition and Mechanics Direct Proangiogenic Signaling from Mesenchymal Stem Cells *Tissue Eng. Part A* **0** 1–9

[90] Liu F D, Pishesha N, Poon Z, Kaushik T and Van Vliet K J 2017 Material Viscoelastic Properties Modulate the Mesenchymal Stem Cell Secretome for Applications in Hematopoietic Recovery *ACS Biomater. Sci. Eng.* **3** 3292–306

[91] Nilsson S and Johnston H 2005 Osteopontin, a key component of the hematopoietic stem cell niche and regulator of primitive hematopoietic progenitor cells *Blood* **106** 1232–9

[92] Seib F P, Prewitz M, Werner C and Bornhäuser M 2009 Matrix elasticity regulates the secretory profile of human bone marrow-derived multipotent mesenchymal stromal cells (MSCs) *Biochem. Biophys. Res. Commun.* **389** 663–7

[93] Califano J P and Reinhart-King C a 2010 Exogenous and endogenous force regulation of endothelial cell behavior. *J. Biomech.* **43** 79–86

[94] Dewey Jr C F, Bussolari S R, Gimbrone Jr M A and Davies P F 1981 The Dynamic Response of Vascular Endothelial Cells to Fluid *J. Biomech. Eng.* **103** 177–84

[95] Ando J and Yamamoto K 2011 Effects of shear stress and stretch on endothelial function. *Antioxid. Redox Signal.* **15** 1389–403

[96] Mendelson A and Frenette P S 2014 Hematopoietic stem cell niche maintenance during homeostasis and regeneration *Nat. Med.* **20** 833–46

[97] Sterpetti A, Cucina A, Ar M, S D D, Ls D A, Cavalarro A and Stipa S 1993 Shear stress increases the release of interleukin-1 and interleukin-6 by aortic endothelial cells . *Surgery* **114** 911–4

[98] Bernad A, Kopf M, Kulbacki R, Weich N, Koehler G and Guuerrez-ramos J C 1994 Interleukin-6 Is Required In Vivo for the Regulation of Stem Cells and Committed Progenitors of the Hematopoietic System *Immunity* **1** 725–31

[99] Kosaki K, Ando J, Korenaga R, Kurokawa T and Kamiya A 1998 Fluid Shear Stress Increases the Production of Granulocyte-Macrophage Colony-Stimulating Factor by Endothelial Cells via mRNA stabilization *Circ. Res.* **82** 794–803

[100] Kinoshita T, Yokota T, Arai K and Miyajimal A 1995 Suppression of apoptotic death in hematopoietic cells by signalling through the IL-3 / GM-CSF receptors **14** 266–75

[101] Donahue R E, Seehra J, Metzger M, Lefebvre D, Rock B, Carbone S, Nanian D G, Garnick M, Sehgal P K, Laston D, Lavallie E, Mccoy J, Schendel P F, Norton C, Turner K, Yang Y and Clark S C 1988 Human IL-3 and GM-CSF Act Synergistically in Stimulating Hematopoiesis in Primates *Science (80-.).* **241** 1820–3

[102] Morita T, Yoshizumi M, Kurihara H, Maemura K, Nagai R and Yazaki Y 1993 Shear stress increases heparin-binding epidermal growth-factor-like growth factor mRNA levels in human vascular endothelial cells *Biochem. Biophys. Res. Commun.* **197** 256–62

[103] Malek A M, Gibbons G H, Dzau V J and Izumo S 1993 Fluid shear stress differentially modulates expression of genes encoding basic fibroblast growth factor and platelet-derived growth factor B chain in vascular endothelium *J. Clin. Invest.* **92** 2013–21

[104] Ohno M, Cooke J P, Dzau V J and Gibbons G H 1995 Fluid Shear Stress Induces Endothelial Transforming Growth Factor Beta-1 Transcription and Production Modulation by Potassium Channel Blockade *J. Clin. Invest.* **95** 1363–9

[105] Faloon P, Arentson E, Kazarov A, Deng C X, Porcher C, Orkin S and Choi K 2000 Basic fibroblast growth factor positively regulates hematopoietic development *Development* **1941** 1931–41

[106] Yoon K, Son Y, Choi Y, Kim J and Cho J 2017 Fibroblast growth factor 2 supports osteoblastic niche cells during hematopoietic homeostasis recovery after bone marrow suppression *Cell Commun. Signal.* **15** 1–11

[107] Hsieh H-J, Li N-Q and Frangos J A 1991 Shear stress increases endothelial growth factor mRNA levels *Am. J. Physiol. - Hear. Circ. Physiol.* **260** 642–6

[108] Mitsumata M, Fishel R S, Nerem R M, Alexander R W, Berk C, Fishel R S, Robert M, Alexander R W and Berk B C 1993 Fluid shear stress stimulates platelet-derived factor expression in endothelial cells growth *Am. J. Physiol. - Hear. Circ. Physiol.* **265** 3–8

[109] Demoulin J and Montano-almendras C P 2012 Platelet-derived growth factors and their receptors in normal and malignant hematopoiesis *Am J Blood Res* **2** 44–56

[110] Blank U and Karlsson S 2015 TGF- b signaling in the control of hematopoietic stem cells *Blood* **4** 3542–51

[111] Davis G E and Senger D R 2005 Endothelial extracellular matrix: biosynthesis, remodeling, and functions during vascular morphogenesis and neovessel stabilization. *Circ. Res.* **97** 1093–107

[112] Sanz L and Álvarez-Vallina L 2003 The extracellular matrix: a new turn-of-the-screw for anti-angiogenic strategies *Trends Mol. Med.* **9** 256–62

[113] Liu F D, Zeiger A S and Van Vliet K J 2014 Time-Dependent Extracellular Matrix Organization and Secretion from Vascular Endothelial Cells due to Macromolecular Crowding *Mater. Res. Soc. Symp. Proc.* **1623**

[114] Zieman S J, Melenovsky V and Kass D A 2005 Mechanisms, Pathophysiology, and Therapy of Arterial Stiffness *Arterioscler. Thromb. Vasc. Biol.* **25** 932–42

[115] Huynh J, Nishimura N, Rana K, Peloquin J M, Califano J P, Montague C R, King M R, Schaffer C B and Reinhart-king C A 2011 Age-Related Intimal Stiffening Enhances Endothelial Permeability and Leukocyte Transmigration **3**

[116] Califano J P and Reinhart-King C A 2008 A Balance of Substrate Mechanics and Matrix Chemistry Regulates Endothelial Cell Network Assembly *Cell. Mol. Bioeng.* **1** 122–32

[117] Saunders R L and Hammer D A 2010 Assembly of Human Umbilical Vein Endothelial Cells on Compliant Hydrogels *Cell. Mol. Bioeng.* **3** 60–7

[118] Yeung T, Georges P C, Flanagan L A, Marg B, Ortiz M, Funaki M, Zahir N, Ming W, Weaver V and Janmey P A 2005 Effects of Substrate Stiffness on Cell Morphology , Cytoskeletal Structure , and Adhesion *Cell Motil. Cytoskeleton* **34** 24–34

[119] Lee S, Zeiger A, Maloney J M, Kotecki M, Van Vliet K J and Herman I M 2010 Pericyte actomyosin-mediated contraction at the cell-material interface can modulate the microvascular niche. *J. Phys. Condens. Matter* **22** 194115

[120] Zeiger A S, Liu F D, Durham J T, Jagielska A, Mahmoodian R, Van Vliet K J and Herman I M 2016 Static mechanical strain induces capillary endothelial cell cycle re-entry and sprouting *Phys. Biol.* **13** 46006

[121] Liu W F, Nelson C M, Tan J L and Chen C S 2007 Cadherins, RhoA, and Rac1 are differentially required for stretch-mediated proliferation in endothelial versus smooth muscle cells. *Circ. Res.* **101** e44-52

[122] Sumpio B E, Chang R, Xu W J, Wang X J and Du W 1997 Regulation of tPA in endothelial cells exposed to cyclic strain: role of CRE, AP-2, and SSRE binding sites. *Am. J. Physiol.* **273** C1441-8

[123] Heissig B, Lund L R, Akiyama H, Ohki M, Morita Y, Rømer J, Nakauchi H, Okumura K, Ogawa H, Werb Z, Danø K and Hattori K 2007 The Plasminogen Fibrinolytic Pathway Is Required for Hematopoietic Regeneration *Cell Stem Cell* 658–70

[124] Yung Y C, Chae J, Buehler M J, Hunter C P and Mooney D J 2009 Cyclic tensile strain triggers a sequence of autocrine and paracrine signaling to regulate angiogenic sprouting in human vascular cells. *Proc. Natl. Acad. Sci. U. S. A.* **106** 15279–84

[125] Xue Y, Lim S, Yang Y, Wang Z, Dahl L, Jensen E, Hedlund E, Andersson P, Sasahara M, Larsson O, Galter D, Cao R, Hosaka K and Cao Y 2011 PDGF-BB modulates hematopoiesis and tumor angiogenesis by inducing erythropoietin production in stromal cells *Nat. Med.* **18** 100–10

[126] Cummins P M, Sweeney N V O, Killeen M T, Birney Y A, Redmond E M and Cahill P A 2007 Cyclic strain-mediated matrix metalloproteinase regulation within the vascular endothelium : a force to be reckoned with *Am J Physiol Hear.* 28–42

[127] Shukla A, Dunn A R, Moses M A and Van Vliet K J 2004 Endothelial cells as mechanical transducers: enzymatic activity and network formation under cyclic strain. *Mech. Chem. Biosyst.* **1** 279–90

[128] Klein G, Schmal O and Aicher W K 2015 Matrix metalloproteinases in stem cell mobilization *Matrix Biol.* **44–46** 175–83

[129] Xiong Y, Hu Z, Han X, Jiang B, Zhang R, Zhang X, Lu Y, Geng C, Li W, He Y, Huo Y, Shibuya M and Luo J 2013 Hypertensive stretch regulates endothelial exocytosis of Weibel-Palade bodies through VEGF receptor 2 signaling pathways. *Cell Res.* **23** 1–15

[130] Welling L W, Zupka M T and Welling D J 1995 Mechanical Properties of Basement Membrane *News Physiol. Sci.* **10** 30–5

[131] Chan J Y-H and Watt S M 2001 Adhesion receptors on haematopoietic progenitor cells *Br. J. Haematol.* **112** 541–57

[132] Burk A S, Monzel C, Yoshikawa H Y, Wuchter P, Saffrich R, Eckstein V, Tanaka M and Ho A D 2015 Quantifying Adhesion Mechanisms and and Progenitor Cells *Sci. Rep.* 1–8

[133] Altrock E, Muth C A, Klein G, Spatz J P and Lee-thedieck C 2012 The significance of integrin ligand nanopatterning on lipid raft clustering in hematopoietic stem cells *Biomaterials* **33** 3107–18

[134] Nilsson S K, Debatis M E, Dooner M S, Madri J A, Quesenberry P J and Becker P S 1998 Immunofluorescence Characterization of Key Extracellular Matrix Proteins in Murine Bone Marrow In Situ *J. Histochem. Cytochem.* **46** 371–7

[135] Qian H, Tryggvason K, Jacobsen S E and Ekblom M 2006 Contribution of a6 integrins to hematopoietic stem and progenitor cell homing to bone marrow and collaboration with a4 integrins *Blood* **107** 3503–11

[136] Verfaillie C . 1998 Adhesion receptors as regulators of the hematopoietic process *Blood* **92** 2609–13

[137] Schreiber T D, Steinl C, Essl M, Abele H, Geiger K, Müller C A, Aicher W K and Klein G 2009 The integrin α9β1 on hematopoietic stem and progenitor cells : involvement in cell adhesion , proliferation and differentiation *Haematologica* **94** 1493–501

[138] Murakami J L, Xu B, Franco C B, Hu X, Galli S J, Weissman I L and Chen C 2016 Stem Cell Homing and Engraftment Through Interaction with MAdCAM-1 **25** 18–26

[139] Adamo L, Naveiras O, Wenzel P L, Mckinney-freeman S, Mack P J, Gracia-sancho J,

Suchy-dicey A, Yoshimoto M, Lensch M W, Yoder M C, Daley G Q and Garcı G 2009 Biomechanical forces promote embryonic haematopoiesis *Nature* **459** 1131–5

[140] Holst J, Watson S, Lord M S, Eamegdool S S, Bax D V, Nivison-smith L B, Kondyurin A, Ma L, Oberhauser A F, Weiss A S and Rasko J E J 2011 Substrate elasticity provides mechanical signals for the expansion of hemopoietic stem and progenitor cells *Nat. Biotechnol.* **28**

[141] Shin J, Buxboim A, Spinler K R, Swift J, Christian D A, Hunter C A, Gachet C, Dingal P C D P, Ivanovska I L, Rehfeldt F, Chasis J A and Discher D E 2014 Contractile Forces Sustain and Polarize Hematopoiesis from Stem and Progenitor Cells *Cell Stem Cell* 81–93

[142] Choi J S and Harley B A C 2012 The combined influence of substrate elasticity and ligand density on the viability and biophysical properties of hematopoietic stem and progenitor cells *Biomaterials* **33** 4460–8

[143] Lee-thedieck C, Rauch N, Fiammengo R, Klein G and Spatz J P 2012 Impact of substrate elasticity on human hematopoietic stem and progenitor cell adhesion and motility *J. Cell Sci.* **125** 3765–75

[144] Raic A, Rödling L, Kalbacher H and Lee-thedieck C 2014 Biomimetic macroporous PEG hydrogels as 3D scaffolds for the multiplication of human hematopoietic stem and progenitor cells *Biomaterials* **35** 929–40

[145] Aukland K, Kramer G C and Renkin E M 1984 Protein concentration of lymph and interstitial *Am. J. Physiol.* **247** H74–9

[146] Bates D O, Levick J R and Mortimer P S Change in macromolecular composition of interstitial fluid from swollen arms after breast cancer treatment, and its implications *Clin. Sci.* **85** 737–46

[147] Wadsworth G R and Oliveiro C J 1953 Plasma Protein Concentration Of Normal Adults Living In Singapore *Br. Med. J.* **2** 1138–9

[148] Tan C, Saurabh S, Bruchez M P, Schwartz R and Leduc P 2013 Molecular crowding shapes gene expression in synthetic cellular nanosystems. *Nat. Nanotechnol.* **8** 602–8

[149] Bergers G and Song S 2005 The role of pericytes in blood-vessel formation and maintenance. *Neuro. Oncol.* **7** 452–64

[150] Ribatti D, Nico B and Crivellato E 2011 The role of pericytes in angiogenesis. *Int. J. Dev. Biol.* **55** 261–8

[151] Kutcher M E and Herman I M 2009 The pericyte: cellular regulator of microvascular blood flow. *Microvasc. Res.* **77** 235–46

[152] Berceli S A, Borovetz S and Sheppeck R A 1991 Mechanisms of vein graft atherosclerosis: LDL metabolism and endothelial actin reorganization *J. Vasc. Surg.* **13** 336–47

[153] Wong A J, Pollard T D and Herman I M 1983 Actin filament stress fibers in vascular endothelial cells in vivo *Science (80-.).* **219** 867–9

[154] Ikeda M, Takei T, Mills I, Kito H and Sumpio B E 1999 Extracellular signal-related kinases 1 and 2 activation in endothelial cells exposed to cyclic strain *Am. J. Physiol.* **276** H614--22

[155] Krishnan L, Underwood C J, Maas S, Ellis B J, Kode T C, Hoying J B and Weiss J A 2008 Effect of mechanical boundary conditions on orientation of angiogenic microvessels *Cardiovasc. Res.* **78** 324–32

[156] Matsumoto T, Sasaki J-I, Alsberg E, Egusa H, Yatani H and Sohmura T 2007 Three-Dimensional Cell and Tissue Patterning in a Strained Fibrin Gel System ed M Isalan *PLoS One* **2** e1211

[157] Matsumoto T, Yung Y C, Fischbach C, Kong H J, Nakaoka R and Mooney D J 2007 Mechanical strain regulates endothelial cell patterning in vitro. *Tissue Eng.* **13** 207–17

[158] Korff T and Augustin H G 1999 Tensional forces in fibrillar extracellular matrices control directional capillary sprouting *J. Cell Sci.* **3258** 3249–58

[159] Boerckel J D, Uhrig B a, Willett N J, Huebsch N and Guldberg R E 2011 Mechanical regulation of vascular growth and tissue regeneration in vivo. *Proc. Natl. Acad. Sci. U. S. A.* **108** E674–80

[160] Kilarski W W, Samolov B, Petersson L and Kvanta A 2009 Biomechanical regulation of blood vessel growth during tissue vascularization **15** 657–65

[161] Udan R S, Culver J C and Dickinson M E 2013 Understanding vascular development *Wiley Interdiscip. Rev. Dev. Biol.* **2** 327–46

[162] Armulik A, Genove G and Betsholtz C 2011 Pericytes: Developmental, Physiological, and Pathological Perspectives, Problems, and Promises *Dev. Cell* **21** 193–215

[163] Kotecki M, Zeiger A S, Van Vliet K J and Herman I M 2010 Calpain- and talin-dependent control of microvascular pericyte contractility and cellular stiffness. *Microvasc. Res.* **80** 339–48

[164] Herman I M and D'Amore P A 1985 Microvascular pericytes contain muscle and nonmuscle actins *J. Cell Biol.* **101** 43–52

[165] Kutcher M E, Kolyada A Y, Surks H K and Herman I M 2007 Pericyte Rho GTPase mediates both pericyte contractile phenotype and capillary endothelial growth state. *Am. J. Pathol.* **171** 693–701

[166] De Oliveira F 1966 Pericytes in Diabetic Retinopathy *Br. J. Ophthalmol.* **50** 134–44

[167] Orlidge A and D'Amore P A 1987 Inhibition of capillary endothelial cell growth by pericytes and smooth muscle cells. *J. Cell Biol.* **105** 1455–62

[168] Cogan D G, Toussaint D and Toichiro K 1961 Retinal Vascular Patterns. IV. Diabetic Retinopathy *Arch. Ophthalmol.* **66** 366–78

[169] Cai J and Boulton M 2002 The pathogenesis of diabetic retinopathy: old concepts and new questions. *Eye (Lond).* **16** 242–60

[170] Baluk P, Hashizume H and M D M 2005 Cellular abnormalities of blood vessels as targets in cancer *Curr. Opin. Genet. Dev.* **15** 102–11

[171] Durham J T, Surks H K, Dulmovits B M and Herman I M 2014 Pericyte contractility controls endothelial cell cycle progression and sprouting: insights into angiogenic switch mechanics *AJP Cell Physiol.* **307** C878–92

[172] Vickers J A, Caulum M M and Henry C S 2006 Generation of hydrophilic poly(dimethylsiloxane) for high-performance microchip electrophoresis *Anal. Chem.* **78** 7446–52

[173] Feinberg A W, Schumacher J F and Brennan A B 2009 Engineering high-density endothelial cell monolayers on soft substrates *Acta Biomater.* **5** 2013–24

[174] Liu W F, Nelson C M, Tan J L and Chen C S 2007 Cadherins, RhoA, and Rac1 are differentially required for stretch-mediated proliferation in endothelial versus smooth muscle cells *Circ. Res.* **101**

[175] Vinals F and Pouyssegur J 1999 Confluence of vascular endothelial cells induces cell cycle exit by inhibiting p42/p44 mitogen-activated protein kinase activity *Mol Cell. Biol.* **19** 2763–72

[176] Suzuma I, Hata Y, Clermont a, Pokras F, Rook S L, Suzuma K, Feener E P and Aiello L P 2001 Cyclic stretch and hypertension induce retinal expression of vascular endothelial growth factor and vascular endothelial growth factor receptor-2: potential mechanisms for exacerbation of diabetic retinopathy by hypertension. *Diabetes* **50** 444–54

[177] Suzuma I, Suzuma K, Ueki K, Hata Y, Feener E P, King G L and Aiello L P 2002 Stretch-induced retinal vascular endothelial growth factor expression is mediated by phosphatidylinositol 3-kinase and protein kinase C (PKC)-?? but not by stretch-induced ERK1/2, Akt, Ras, or classical/novel PKC pathways *J. Biol. Chem.* **277** 1047–57

[178] Kleinman H K and Martin G R 2005 Matrigel: Basement membrane matrix with biological activity *Semin. Cancer Biol.* **15** 378–86

[179] Nakatsu M N, Sainson R C a., Aoto J N, Taylor K L, Aitkenhead M, Pérez-del-Pulgar S, Carpenter P M and Hughes C C W 2003 Angiogenic sprouting and capillary lumen formation modeled by human umbilical vein endothelial cells (HUVEC) in fibrin gels: the role of fibroblasts and Angiopoietin-1☆ *Microvasc. Res.* **66** 102–12

[180] Demidova-Rice T N, Geevarghese A and Herman I M 2011 Bioactive peptides derived from vascular endothelial cell extracellular matrices promote microvascular morphogenesis and wound healing in vitro *Wound Repair Regen.* **19** 59–70

[181] Kubota Y, Kleinman H K, Martin G R and Lawley T J 1988 Role of laminin and basement membrane in the morphological differentiation of human endothelial cells into capillary-like structures. *J. Cell Biol.* **107** 1589–98

[182] Auerbach R, Lewis R, Shinners B, Kubai L and Akhtar N 2003 Angiogenesis assays: A critical overview *Clin. Chem.* **49** 32–40

[183] Norrby K 1997 Angiogenesis: new aspects relating to its initiation and control. *APMIS*

105 417–37

[184] Rundhaug J E 2005 Matrix metalloproteinases and angiogenesis Angiogenesis Review Series *J. Cell. Mol. Med* **9** 267–85

[185] Lee Y-U, Drury-Stewart D, Vito R P and Han H-C 2008 Morphologic Adaptation of Arterial Endothelial Cells to Longitudinal Stretch in Organ Culture *J. Biomech.* **41** 3274–7

[186] Durham J T, Dulmovits B M, Cronk S M, Sheets A R and Herman I M 2015 Pericyte chemomechanics and the angiogenic switch: Insights into the pathogenesis of proliferative diabetic retinopathy? *Investig. Ophthalmol. Vis. Sci.* **56** 3441–59

[187] Hammes H P, Lin J, Renner O, Shani M, Lundqvist A, Betsholtz C, Brownlee M and Deutsch U 2002 Pericytes and the pathogenesis of diabetic retinopathy *Diabetes* **51** 3107–12

[188] Hammes H-P 2005 Pericytes and the Pathogenesis of Diabetic Retinopathy *Horm. Metab. Res.* **37** 39–43

[189] Chapel A, Bertho J M, Bensidhoum M, Fouillard L, Young R G, Frick J, Demarquay C, Cuvelier F, Mathieu E, Trompier F, Dudoignon N, Germain C, Mazurier C, Aigueperse J, Borneman J, Gorin N C, Gourmelon P and Thierry D 2003 Mesenchymal stem cells home to injured tissues when co-infused with hematopoietic cells to treat a radiation-induced multi-organ failure syndrome. *J. Gene Med.* **5** 1028–38

[190] Karp J M and Leng Teo G S 2009 Mesenchymal stem cell homing: the devil is in the details. *Cell Stem Cell* **4** 206–16

[191] Khaldoyanidi S 2008 Directing stem cell homing. *Cell Stem Cell* **2** 198–200

[192] Wei X, Yang X, Han Z, Qu F, Shao L and Shi Y 2013 Mesenchymal stem cells: a new trend for cell therapy. *Acta Pharmacol. Sin.* **34** 747–54

[193] Guilak F, Cohen D M, Estes B T, Gimble J M, Liedtke W and Chen C S 2009 Control of stem cell fate by physical interactions with the extracellular matrix. *Cell Stem Cell* **5** 17–26

[194] Chen C S, Mrksich M, Huang S, Whitesides G M and Ingber D E 1998 Micropatterned surfaces for control of cell shape, position, and function. *Biotechnol. Prog.* **14** 356–63

[195] Lee J, Abdeen A A, Zhang D and Kilian K A 2013 Directing stem cell fate on hydrogel substrates by controlling cell geometry, matrix mechanics and adhesion ligand composition. *Biomaterials* **34** 8140–8

[196] Mcbeath R, Pirone D M, Nelson C M, Bhadriraju K and Chen C S 2004 Cell Shape , Cytoskeletal Tension , and RhoA Regulate Stem Cell Lineage Commitment *Dev. Cell* **6** 483–95

[197] van Velthoven C T J, Kavelaars A, van Bel F and Heijnen C J 2010 Mesenchymal stem cell treatment after neonatal hypoxic-ischemic brain injury improves behavioral outcome and induces neuronal and oligodendrocyte regeneration. *Brain. Behav. Immun.* **24** 387–93

[198] Chen J, Li Y, Wang L, Zhang Z, Lu D, Lu M and Chopp M 2001 Therapeutic Benefit of

Intravenous Administration of Bone Marrow Stromal Cells After Cerebral Ischemia in Rats *Stroke* **32** 1005–11

[199] Chen S, Fang W, Ye F, Liu Y-H, Qian J, Shan S, Zhang J, Chunhua R Z, Liao L, Lin S and Sun J 2004 Effect on left ventricular function of intracoronary transplantation of autologous bone marrow mesenchymal stem cell in patients with acute myocardial infarction. *Am. J. Cardiol.* **94** 92–5

[200] Miyahara Y, Nagaya N, Kataoka M, Yanagawa B, Tanaka K, Hao H, Ishino K, Ishida H, Shimizu T, Kangawa K, Sano S, Okano T, Kitamura S and Mori H 2006 Monolayered mesenchymal stem cells repair scarred myocardium after myocardial infarction. *Nat. Med.* **12** 459–65

[201] Cheng Z, Ou L, Zhou X, Li F, Jia X, Zhang Y, Liu X, Li Y, Ward C a, Melo L G and Kong D 2008 Targeted migration of mesenchymal stem cells modified with CXCR4 gene to infarcted myocardium improves cardiac performance. *Mol. Ther.* **16** 571–9

[202] Poon Z, Lee W C, Guan G, Nyan L M, Lim C T, Han J and Van Vliet K J 2014 Bone Marrow Regeneration Promoted by Biophysically Sorted Osteoprogenitors from Mesenchymal Stromal Cells *Stem Cells Transl. Med.* **4** 56–65

[203] Lin P, Correa D, Kean T J, Awadallah A, Dennis J E and Caplan A I 2014 Serial transplantation and long-term engraftment of intra-arterially delivered clonally derived mesenchymal stem cells to injured bone marrow. *Mol. Ther.* **22** 160–8

[204] Ankrum J and Karp J M 2010 Mesenchymal stem cell therapy: Two steps forward, one step back. *Trends Mol. Med.* **16** 203–9

[205] Lee R H, Pulin A A, Seo M J, Kota D J, Ylostalo J, Larson B L, Semprun-prieto L, Delafontaine P and Darwin J 2014 Intravenous hMSCs Improve Myocardial Infarction in Mice because Cells Embolized in Lung Are Activated to Secrete the Anti-inflammatory Protein TSG-6 *Cell Stem Cell* **5** 54–63

[206] Zimmerlin L, Park T S, Zambidis E T, Donnenberg V S and Donnenberg A D 2013 Mesenchymal stem cell secretome and regenerative therapy after cancer. *Biochimie* **95** 2235–45

[207] Nauta A J and Fibbe W E 2007 Immunomodulatory properties of mesenchymal stromal cells. *Blood* **110** 3499–506

[208] Akiyama K, Chen C, Wang D, Xu X, Qu C, Yamaza T, Cai T, Chen W, Sun L and Shi S 2012 Mesenchymal-stem-cell-induced immunoregulation involves FAS-ligand-/FAS-mediated T cell apoptosis. *Cell Stem Cell* **10** 544–55

[209] Bai L, Lennon D P, Eaton V, Maier K, Caplan A I, Miller S D and Miller R H 2009 Human bone marrow-derived mesenchymal stem cells induce Th2-polarized immune response and promote endogenous repair in animal models of multiple sclerosis. *Glia* **57** 1192–203

[210] Ryan J M, Barry F, Murphy J M and Mahon B P 2007 Interferon-gamma does not break, but promotes the immunosuppressive capacity of adult human mesenchymal stem cells. *Clin. Exp. Immunol.* **149** 353–63

[211] Le Blanc K and Ringdén O 2006 Mesenchymal stem cells: properties and role in clinical bone marrow transplantation. *Curr. Opin. Immunol.* **18** 586–91

[212] Prockop D J and Oh J Y 2012 Mesenchymal stem/stromal cells (MSCs): role as guardians of inflammation. *Mol. Ther.* **20** 14–20

[213] Duffy G P, Ahsan T, Brien T O, Barry F and Nerem R M 2009 Bone Marrow-Derived Mesenchymal Stem Cells Promote Angiogenic Processes in a Time- and Dose-Dependent Manner In Vitro *Tissue Eng. Part A* **15**

[214] Ranganath S H, Levy O, Inamdar M S and Karp J M 2012 Harnessing the mesenchymal stem cell secretome for the treatment of cardiovascular disease. *Cell Stem Cell* **10** 244–58

[215] Paul G and Anisimov S V 2013 The secretome of mesenchymal stem cells: potential implications for neuroregeneration. *Biochimie* **95** 2246–56

[216] Parr a M, Tator C H and Keating a 2007 Bone marrow-derived mesenchymal stromal cells for the repair of central nervous system injury. *Bone Marrow Transplant.* **40** 609–19

[217] Aggarwal S and Pittenger M F 2005 Human mesenchymal stem cells modulate allogeneic immune cell responses. *Blood* **105** 1815–22

[218] Parekkadan B, van Poll D, Suganuma K, Carter E a, Berthiaume F, Tilles A W and Yarmush M L 2007 Mesenchymal stem cell-derived molecules reverse fulminant hepatic failure. *PLoS One* **2** e941

[219] van Poll D, Parekkadan B, Cho C H, Berthiaume F, Nahmias Y, Tilles A W and Yarmush M L 2008 Mesenchymal stem cell-derived molecules directly modulate hepatocellular death and regeneration in vitro and in vivo. *Hepatology* **47** 1634–43

[220] Drago D, Cossetti C, Iraci N, Gaude E, Musco G, Bachi A and Pluchino S 2013 The stem cell secretome and its role in brain repair *Biochimie* **95** 2271–85

[221] Lee W C, Bhagat A A S, Huang S, Van Vliet K J, Han J and Lim C T 2011 High-throughput cell cycle synchronization using inertial forces in spiral microchannels. *Lab Chip* **11** 1359–67

[222] Bianco P 2011 Bone and the hematopoietic niche : a tale of two stem cells **117** 5281–9

[223] Chiellini C, Cochet O, Negroni L, Samson M, Poggi M, Ailhaud G, Alessi M-C, Dani C and Amri E-Z 2008 Characterization of human mesenchymal stem cell secretome at early steps of adipocyte and osteoblast differentiation. *BMC Mol. Biol.* **9** 26

[224] Foster L J, Zeemann P a, Li C, Mann M, Jensen O N and Kassem M 2005 Differential expression profiling of membrane proteins by quantitative proteomics in a human mesenchymal stem cell line undergoing osteoblast differentiation. *Stem Cells* **23** 1367–77

[225] Kristensen L P, Chen L, Nielsen M O, Qanie D W, Kratchmarova I, Kassem M and Andersen J S 2012 Temporal Profiling and Pulsed SILAC Labeling Identify Novel Secreted Proteins During Ex Vivo Osteoblast Differentiation of Human Stromal Stem Cells * □ 989–1007

[226] Lee M J, Kim J, Kim M Y, Bae Y, Ryu S H, Lee T G and Kim J H 2010 Proteomic

Analysis of Tumor Necrosis Factor- r -Induced Secretome of Human Adipose Tissue-Derived Mesenchymal Stem Cells research articles *J. Proteome Res.* 1754–62

[227] Tasso R, Gaetani M, Molino E, Cattaneo A, Monticone M, Bachi A and Cancedda R 2012 The role of bFGF on the ability of MSC to activate endogenous regenerative mechanisms in an ectopic bone formation model. *Biomaterials* **33** 2086–96

[228] Sze S K, de Kleijn D P V, Lai R C, Khia Way Tan E, Zhao H, Yeo K S, Low T Y, Lian Q, Lee C N, Mitchell W, El Oakley R M and Lim S-K 2007 Elucidating the secretion proteome of human embryonic stem cell-derived mesenchymal stem cells. *Mol. Cell. Proteomics* **6** 1680–9

[229] Li G, Zhang X, Wang H, Wang X, Meng C and Chan C 2009 Comparative proteomic analysis of mesenchymal stem cells derived from human bone marrow , umbilical cord , and placenta : Implication in the migration 20–30

[230] Madrigal M, Rao K S and Riordan N H 2014 A review of therapeutic effects of mesenchymal stem cell secretions and induction of secretory modification by different culture methods. *J. Transl. Med.* **12** 260

[231] Grayson W L, Zhao F, Izadpanah R, Bunnell B and Ma T 2006 Effects of Hypoxia on Human Mesenchymal Stem Cell Expansion and Plasticity in 3D Constructs **339** 331–9

[232] Chaturvedi P, Gilkes D M, Takano N and Semenza G L 2014 Hypoxia-inducible factor-dependent signaling between triple-negative breast cancer cells and mesenchymal stem cells promotes macrophage recruitment. *Proc. Natl. Acad. Sci. U. S. A.* **111** E2120-9

[233] Zwezdaryk K J, Coffelt S B, Figueroa Y G, Liu J, Phinney D G, LaMarca H L, Florez L, Morris C B, Hoyle G W and Scandurro A B 2007 Erythropoietin, a hypoxia-regulated factor, elicits a pro-angiogenic program in human mesenchymal stem cells. *Exp. Hematol.* **35** 640–52

[234] Chen T S, Lai R C, Lee M M, Choo A B H, Lee C N and Lim S K 2010 Mesenchymal stem cell secretes microparticles enriched in pre-microRNAs. *Nucleic Acids Res.* **38** 215–24

[235] Kim H O, Choi S-M and Kim H-S 2013 Mesenchymal stem cell-derived secretome and microvesicles as a cell-free therapeutics for neurodegenerative disorders *Tissue Eng. Regen. Med.* **10** 93–101

[236] Lavoie J R and Rosu-Myles M 2013 Uncovering the secretes of mesenchymal stem cells. *Biochimie* **95** 2212–21

[237] Yim E K F, Darling E M, Kulangara K, Guilak F and Leong K W 2010 Nanotopography-induced changes in focal adhesions, cytoskeletal organization, and mechanical properties of human mesenchymal stem cells. *Biomaterials* **31** 1299–306

[238] Baker B A, Pine P S, Chatterjee K, Kumar G, Lin N J, Mcdaniel J H, Salit M L and Simon C G 2014 Ontology analysis of global gene expression differences of human bone marrow stromal cells cultured on 3D scaffolds or 2D films *Biomaterials* **35** 6716–26

[239] Lutolf M P, Gilbert P M and Blau H M 2009 Designing materials to direct stem-cell fate.

Nature **462** 433–41

[240] Schwartz M a and DeSimone D W 2008 Cell adhesion receptors in mechanotransduction. *Curr. Opin. Cell Biol.* **20** 551–6

[241] Li B, Moshfegh C, Lin Z, Albuschies J and Vogel V 2013 Mesenchymal stem cells exploit extracellular matrix as mechanotransducer. *Sci. Rep.* **3** 2425

[242] Iyer K V, Pulford S, Mogilner A and Shivashankar G V. 2012 Mechanical activation of cells induces chromatin remodeling preceding MKL nuclear transport *Biophys. J.* **103** 1416–28

[243] Talwar S, Kumar A, Rao M, Menon G I and Shivashankar G V. 2013 Correlated spatio-temporal fluctuations in chromatin compaction states characterize stem cells *Biophys. J.* **104** 553–64

[244] Tajik A, Zhang Y, Wei F, Sun J, Jia Q, Zhou W, Singh R, Khanna N, Belmont A S and Wang N 2016 Transcription upregulation via force-induced direct stretching of chromatin *Nat. Mater.* **1**

[245] Wang N 2014 Stem cell mechanics: auxetic nuclei. *Nat. Mater.* **13** 540–2

[246] Halder G, Dupont S and Piccolo S 2012 Transduction of mechanical and cytoskeletal cues by YAP and TAZ. *Nat. Rev. Mol. Cell Biol.* **13** 591–600

[247] Dupont S, Morsut L, Aragona M, Enzo E, Giulitti S, Cordenonsi M, Zanconato F, Le Digabel J, Forcato M, Bicciato S, Elvassore N and Piccolo S 2011 Role of YAP/TAZ in mechanotransduction. *Nature* **474** 179–83

[248] Aragona M, Panciera T, Manfrin A, Giulitti S, Michielin F, Elvassore N, Dupont S and Piccolo S 2013 A mechanical checkpoint controls multicellular growth through YAP/TAZ regulation by actin-processing factors. *Cell* **154** 1047–59

[249] Chaudhuri O, Gu L, Darnell M, Klumpers D, Bencherif S a, Weaver J C, Huebsch N and Mooney D J 2015 Substrate stress relaxation regulates cell spreading. *Nat. Commun.* **6** 6365

[250] Engler A, Bacakova L, Newman C, Hategan A, Griffin M and Discher D 2004 Substrate Compliance versus Ligand Density in Cell on Gel Responses *Biophys. J.* **86** 15–25

[251] Walton E B, Lee S and Van Vliet K J 2008 Extending Bell's model: how force transducer stiffness alters measured unbinding forces and kinetics of molecular complexes. *Biophys. J.* **94** 2621–30

[252] Maloney J M, Walton E B, Bruce C M and Van Vliet K J 2008 Influence of finite thickness and stiffness on cellular adhesion-induced deformation of compliant substrata *Phys. Rev. E - Stat. Nonlinear, Soft Matter Phys.* **78** 1–15

[253] Eyckmans J and Chen C S 2014 Stem cell differentiation: sticky mechanical memory. *Nat. Mater.* **13** 542–3

[254] Zeiger A S, Hinton B and Van Vliet K J 2013 Why the dish makes a difference: Quantitative comparison of polystyrene culture surfaces *Acta Biomater.* **9** 7354–61

[255] Bartalena G, Loosli Y, Zambelli T and Snedeker J G 2012 Biomaterial surface modifications can dominate cell–substrate mechanics: the impact of PDMS plasma treatment on a quantitative assay of cell stiffness *Soft Matter* **8** 673–81

[256] Toyjanova J, Hannen E, Bar-Kochba E, Darling E M, Henann D L and Franck C 2014 3D Viscoelastic traction force microscopy. *Soft Matter* **10** 8095–106

[257] Haylock D N and Nilsson S K 2006 Osteopontin: A bridge between bone and blood *Br. J. Haematol.* **134** 467–74

[258] Reinholt F P, Hultenby K, Oldberg A and Heinegard D 1990 Osteopontin-a possible anchor of osteoclasts to bone *Proc. Natl. Acad. Sci.* **87** 4473–5

[259] Denhardt D T and Guo X 1993 Osteopontin : a protein with diverse functions *FASEB J.* **7** 1475–82

[260] Sodek J, Ganss B and McKee M D 2000 Osteopontin *Crit. Rev. Oral Biol. Med.* **11** 279–303

[261] Wang K X and Denhardt D T 2008 Osteopontin: Role in immune regulation and stress responses *Cytokine Growth Factor Rev.* **19** 333–45

[262] Dai J, Peng L, Fan K, Wang H, Wei R, Ji G, Cai J, Lu B, Li B, Zhang D, Kang Y, Tan M, Qian W and Guo Y 2009 Osteopontin induces angiogenesis through activation of PI3K/AKT and ERK1/2 in endothelial cells. *Oncogene* **28** 3412–22

[263] Ashkar S, Weber G F, Panoutsakopoulou V, Sanchirico M E, Jansson M, Zawaideh S, Rittling S R, Denhardt D T, Glimcher M J and Cantor H 2000 Eta-1 (Osteopontin): An Early Component of Type-1 (Cell-Mediated) Immunity *Science (80-.).* **287** 860–4

[264] Carrancio S, Blanco B, Romo C, Muntion S, Lopez-holgado N, Miguel J F S, Sanchez-guijo F M, Consuelo M, Blanco J F and Brin J G 2011 Bone Marrow Mesenchymal Stem Cells for Improving Hematopoietic Function : An In Vitro and In Vivo Model . Part 2 : Effect on Bone Marrow Microenvironment *PLoS One* **6** e26241

[265] Perucca S, Palma A Di, Piccaluga P P, Gemelli C, Zoratti E, Bassi G, Giacopuzzi E, Lojacono A, Borsani G, Tagliafico E, Scupoli M T, Bernardi S, Zanaglio C, Cattina F, Cancelli V, Malagola M, Krampera M, Marini M, Almici C, Ferrari S and Russo D 2017 Mesenchymal stromal cells (MSCs) induce ex vivo proliferation and erythroid commitment of cord blood haematopoietic stem cells (CB- 1–19

[266] Guidi N, Sacma M, Ständker L, Soller K, Marka G, Eiwen K, Weiss J M, Kirchhoff F, Weil T, Cancelas J A, Florian M C and Geiger H 2017 Osteopontin attenuates aging-associated phenotypes of hematopoietic stem cells *EMBO J.* e201694969

[267] Sumitomo A, Ishino R, Urahama N, Inoue K, Yonezawa K, Hasegawa N, Horie O, Matsuoka H, Kondo T, Roeder R G and Ito M 2010 The transcriptional mediator subunit MED1/TRAP220 in stromal cells is involved in hematopoietic stem/progenitor cell support through osteopontin expression. *Mol. Cell. Biol.* **30** 4818–27

[268] Stier S, Ko Y, Forkert R, Lutz C, Neuhaus T, Grünewald E, Cheng T, Dombkowski D, Calvi L M, Rittling S R and Scadden D T 2005 Osteopontin is a hematopoietic stem cell

niche component that negatively regulates stem cell pool size *J. Exp. Med.* **201** 1781–91

[269] Huynh H, Zheng J, Umikawa M, Zhang C, Silvany R, Iizuka S, Holzenberger M, Zhang W and Zhang C C 2011 IGF binding protein 2 supports the survival and cycling of hematopoietic stem cells **118** 3236–43

[270] Khoury M, Drake A, Chen Q, Dong D, Leskov I, Fragoso M F, Li Y, Iliopoulou B P, Hwang W, Lodish H F and Chen J 2011 Mesenchymal stem cells secreting angiopoietin-like-5 support efficient expansion of human hematopoietic stem cells without compromising their repopulating potential. *Stem Cells Dev.* **20** 1371–81

[271] Laterveer L, Lindley I J, Hamilton M S, Willemze R and Fibbe W E 1995 Interleukin-8 induces rapid mobilization of hematopoietic stem cells with radioprotective capacity and long-term myelolymphoid repopulating ability. *Blood* **85** 2269–75

[272] Briquet A, Dubois S, Bekaert S, Dolhet M, Beguin Y and Gothot A 2010 Prolonged ex vivo culture of human bone marrow mesenchymal stem cells influences their supportive activity toward NOD/SCID-repopulating cells and committed progenitor cells of B lymphoid and myeloid lineages *Haematologica* **95** 47–56

[273] Sharma M B, Limaye L S and Kale V P 2012 Mimicking the functional hematopoietic stem cell niche in vitro: recapitulation of marrow physiology by hydrogel-based three-dimensional cultures of mesenchymal stromal cells *Haematologica* **97** 651–60

[274] Jing D, Fonseca A V, Alakel N, Fierro F A, Muller K, Bornhauser M, Ehninger G, Corbeil D and Ordemann R 2010 Hematopoietic stem cells in co-culture with mesenchymal stromal cells -modeling the niche compartments in vitro *Haematologica* **95** 542–50

[275] Abangan R S, Williams C R, Mehrotra M, Duncan J D and Larue A C 2010 MCP1 Directs Trafficking of Hematopoietic Stem Cell-Derived Fibroblast Precursors in Solid Tumor **176** 1914–26

[276] Si Y, Tsou C, Croft K and Charo I F 2010 CCR2 mediates hematopoietic stem and progenitor cell trafficking to sites of inflammation in mice **120**

[277] Sivori S, Cantoni C, Parolini S, Marcenaro E, Moretta L and Moretta A 2003 IL-21 induces both rapid maturation of human CD34 + cell precursors towards NK cells and acquisition of surface killer Ig-like receptors **3** 3439–47

[278] Ozaki K, Spolski R, Ettinger R, Kim H, Wang G, Qi C, Hwu P, Shaffer D J, Akilesh S, Roopenian D C, Iii H C M, Lipsky P E, Leonard W J, Ozaki K, Spolski R, Ettinger R, Kim H, Wang G, Qi C, Hwu P, Shaffer D J, Akilesh S, Roopenian D C, Iii H C M, Lipsky P E and Leonard W J 2017 Generation by IL-21 , a Novel Inducer of Blimp-1 and Bcl-6 1

[279] Crigler L, Robey R C, Asawachaicharn A, Gaupp D and Phinney D G 2006 Human mesenchymal stem cell subpopulations express a variety of neuro-regulatory molecules and promote neuronal cell survival and neuritogenesis. *Exp. Neurol.* **198** 54–64

[280] Shelton D L and Reichardt L F 1984 Expression of the fl-nerve growth factor gene correlates with the density of sympathetic innervation in effector organs **81** 7951–5

[281] Kiel M J and Morrison S J 2008 Uncertainty in the niches that maintain haematopoietic stem cells *Nat. Rev. Immunol.* **8** 290–301

[282] Da Silva C L, Gonçalves R, Crapnell K B, Cabral J M S, Zanjani E D and Almeida-Porada G 2005 A human stromal-based serum-free culture system supports the ex vivo expansion/maintenance of bone marrow and cord blood hematopoietic stem/progenitor cells *Exp. Hematol.* **33** 828–35

[283] Walenda T, Bork S, Horn P, Wein F, Saffrich R, Diehlmann A, Eckstein V, Ho A D and Wagner W 2010 Co-culture with mesenchymal stromal cells increases proliferation and maintenance of haematopoietic progenitor cells *J. Cell. Mol. Med.* **14** 337–50

[284] Dumont N, Boyer L, Émond H, Çelebi-Saltik B, Pasha R, Bazin R, Mantovani D, Roy D C and Pineault N 2014 Medium conditioned with mesenchymal stromal cell-derived osteoblasts improves the expansion and engraftment properties of cord blood progenitors *Exp. Hematol.* **42** 741–52

[285] Li N, Feugier P, Serrurrier B, Latger-Cannard V, Lesesve J F, Stoltz J F and Eljaafari A 2007 Human mesenchymal stem cells improve ex vivo expansion of adult human CD34+ peripheral blood progenitor cells and decrease their allostimulatory capacity *Exp. Hematol.* **35** 507–15

[286] Rennerfeldt D and Van Vliet K J 2016 Concise Review : When Colonies Are Not Clones : Evidence and Implications of Intracolony Heterogeneity in Mesenchymal Stem Cells *Stem Cells* **34** 1135–41

[287] Goloviznina N A, Verghese S C, Yoon Y, Taratula O, Marks D L and Kurre P 2016 Mesenchymal Stromal Cell-derived Extracellular Vesicles Promote Myeloid-biased Multipotent Hematopoietic Progenitor Expansion via Toll-Like Receptor Engagement * Edited by Dennis Voelker *J. Biol. Chem.* **291** 24607–17

[288] Mehrasa R, Vaziri H, Oodi A, Khorshidfar M, Nikogoftar M, Golpour M and Amirizadeh N 2014 Mesenchymal stem cells as a feeder layer can prevent apoptosis of expanded hematopoietic stem cells derived from cord blood. *Int. J. Mol. Cell. Med.* **3** 1–10

[289] Zhang Y, Chou C, Jiang X-S, Teoh S-H and Leong K W 2006 Co-culture of Umbilical Cord Blood CD34 *Tissue Eng.* **12**

[290] Manz M G, Miyamoto T, Akashi K and Weissman I L 2002 Prospective isolation of human clonogenic common myeloid progenitors. *Proc. Natl. Acad. Sci. U. S. A.* **99** 11872–7

[291] Testa U, Pelosi E and Frankel A 2014 CD 123 is a membrane biomarker and a therapeutic target in hematologic malignancies. *Biomark. Res.* **2** 4

[292] Galy A, Travis M, Cen D and Chen B 1995 Human T, B, Natural Killer, and Dendritic Cells Arise from a Common Bone Marrow Progenitor Cell Subset *Immunity* **3** 459–73

[293] Smith B C, Gasparetto C, Collins N, Gillio A, Muench M, Oreilly R J and Moore M A S 1991 Purification and Partial Characterization of a Human Hematopoietic Precursor Population *Blood* **77** 2122–8

[294] Taussig D C, Pearce D J, Simpson C, Rohatiner A Z, Lister T A, Kelly G and Luongo J L 2005 Hematopoietic stem cells express multiple myeloid markers : implications for the origin and targeted therapy of acute myeloid leukemia *Blood* **106** 4086–93

[295] Winer J P, Sc B, Janmey P A, Ph D, Mccormick M E and Funaki M 2009 Bone Marrow-Derived Human Mesenchymal Stem Cells Become Quiescent on Soft Substrates but Remain Responsive to Chemical or Mechanical Stimuli **15**

[296] Cai L-H, Kodger T E, Guerra R E, Pegoraro A F, Rubinstein M and Weitz D a. 2015 Soft Poly(dimethylsiloxane) Elastomers from Architecture-Driven Entanglement Free Design *Adv. Mater.* **27** 5132–40

[297] Zhang Y, Matsumoto E A, Peter A, Lin P C, Kamien R D and Yang S 2008 One-step nanoscale assembly of complex structures via harnessing of an elastic instability *Nano Lett.* **8** 1192–6

[298] Ghatak A and Chaudhury M K 2003 Adhesion-induced instability patterns in thin confined elastic film *Langmuir* **19** 2621–31

[299] Brau F, Vandeparre H, Sabbah A, Poulard C, Boudaoud A and Damman P 2010 Multiple-length-scale elastic instability mimics parametric resonance of nonlinear oscillators *Nat. Phys.* **7** 56–60

[300] Livak K J and Schmittgen T D 2001 Analysis of relative gene expression data using real-time quantitative PCR and the 2-ΔΔCT method *Methods* **25** 402–8

[301] Jagielska A, Lowe A L, Makhija E, Wroblewska L and Guck J 2017 Mechanical Strain Promotes Oligodendrocyte Differentiation by Global Changes of Gene Expression **11** 1–16

[302] Xu J, Wang W, Ludeman M, Cheng K, Hayami T, Lotz J C and Kapila S 2008 Chondrogenic Differentiation of Human Mesenchymal Stem Cells in Three-Dimensional Alginate Gels *Tissue Eng. Part A* **14** 667–80

[303] Sun J, Li J, Li C and Yu Y 2015 Role of bone morphogenetic protein-2 in osteogenic differentiation of mesenchymal stem cells *Mol. Med. Rep.* **12** 4230–7

[304] Shi J, Kundrat L, Pishesha N, Bilate A, Theile C, Maruyama T, Dougan S K, Ploegh H L and Lodish H F 2014 Engineered red blood cells as carriers for systemic delivery of a wide array of functional probes. *Proc. Natl. Acad. Sci. U. S. A.* **111** 10131–6

[305] Amouzegar A, Mittal S K, Sahu A, Sahu S K and Chauhan S K 2017 Mesenchymal Stem Cells Modulate Differentiation of Myeloid Progenitor Cells during Inflammation *Stem Cells* 1–12